

UNIVERSITY OF BIRMINGHAM

IMPACT OF LOW CARBON FUEL AND CATALYST ON GASOLINE DIRECT INJECTION ENGINE PARTICULATE MATTER

by

JUN HOE CHAN

A thesis submitted to

The University of Birmingham

for the degree of

DOCTOR OF PHILOSOPHY

School of Engineering

Mechanical Engineering

The University of Birmingham

March 2020

UNIVERSITY OF
BIRMINGHAM

University of Birmingham Research Archive

e-theses repository

This unpublished thesis/dissertation is copyright of the author and/or third parties. The intellectual property rights of the author or third parties in respect of this work are as defined by The Copyright Designs and Patents Act 1988 or as modified by any successor legislation.

Any use made of information contained in this thesis/dissertation must be in accordance with that legislation and must be properly acknowledged. Further distribution or reproduction in any format is prohibited without the permission of the copyright holder.

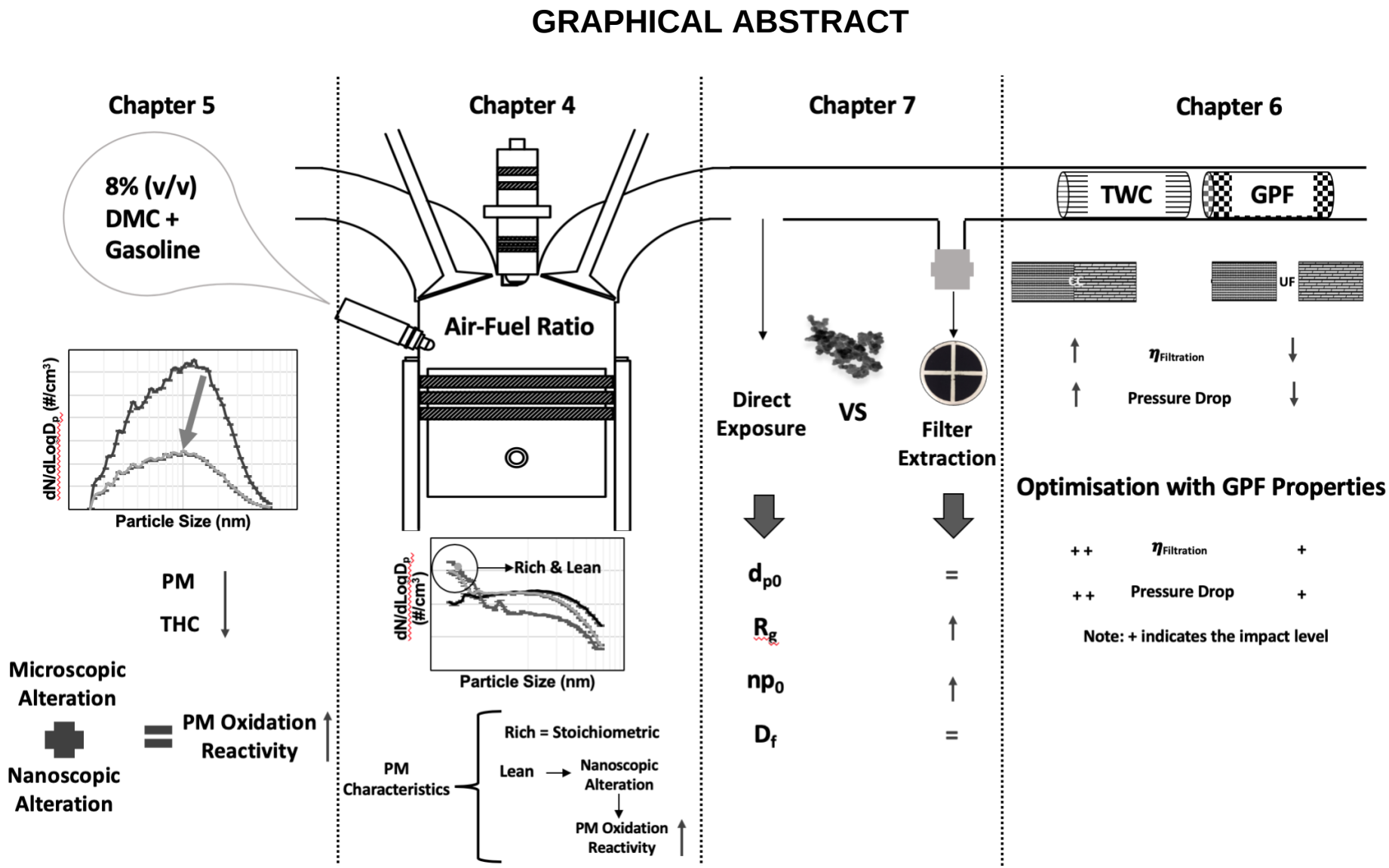
ABSTRACT

The increasingly concern of the impact of Particulate Matter (PM) emitted by Gasoline Direct Injection (GDI) engines on human health and the environment have led to the research community to look into various approaches to abate and to reduce the PM emissions in accordance to the permitted limits. A comprehensive understanding of PM behaviour and characteristics is required in order determine the appropriate approach for reducing PM emissions. This research thesis begins the investigation on PM with different stoichiometry at maximum brake torque condition. Results suggest rich combustions PM has similar characteristics to stoichiometric. Contrarily, PM was formed differently with lean combustion by showing about 30 °C earlier for the start of oxidation temperature (SOT) and maximum mass loss rate temperature (MMLRT). Secondly, the introduction of 8 % (v/v) Di-Methyl Carbonate (DMC) addition. DMC was capable of reducing PM up to 60 % and altering PM characteristics with indication of 15 °C earlier of oxidation temperatures. Most importantly, without significant negative impact on engine performance. Following the evaluation of aftertreatment architectural configurations. A gasoline particulate filter positioned underfloor to TWC shows better compromise between PM filtration efficiency and pressure drop in comparison to close-couple architectural configuration. The pressure drop was lower with slightly lessened filtration performance. In overall, the pressure drop can be reduced up to 32 % and filtration performance has dropped up to 6 %. However, GPF filtration performance in underfloor architectural configuration can be improved up to 3 % with the use of GPF with advantageous properties, yet the pressure drop remained below close-couple architectural configuration. The research thesis finalised with a small case study on TEM grids preparation methodologies demonstrating comparable microscopic analysis of PM

Abstract

agglomerates with several advantages; similar average primary particle size and fractal dimension.

Graphical Abstract



ACKNOWLEDGEMENTS

Firstly, I would like to express my sincerest gratitude to both my lead supervisor, Professor Athanasios Tsolakis and co-supervisor, Dr. Khamis Essa for their assistance through the application process for School of Engineering Postgraduate Scholarship. I am extremely grateful for the opportunity to conduct this research, and I would like to give a special mention to Professor Athanasios Tsolakis for his excellent guidance throughout the duration of my PhD.

Secondly, a big thank you to Dr. Jose Martin Herreros, Dr. Kyriakos Xenofon Kallis, Dr. Hadi Nozari, Dr. Nahil Serhan, Dr. Maria Bogarra Macias and Dr. Cruz Hergueta for their invaluable advice. Your technical knowledge of the laboratory equipment and analytical capabilities have helped me immeasurably with the completion of this project. Not forgetting Mr. Sak Sittichompoo and Mr. Ammar Wahbi, (despite you both being extremely annoying), I have really appreciated your continued support and helpfulness during my experiments!

A special thanks to the fellow technicians from the laboratory, who have assisted me countless times and have routinely solved complex technical tasks for me in order to produce high quality results. Special thanks to Mr. Jack Garrod and Mr. Kevan Charlesworth for making my days in the laboratory throughout my PhD.

Furthermore, many thanks to Johnson Matthey Technology Centre, LiqTech International and Shell Global Solutions for providing the catalysts, GPFs and gasoline used in the thesis.

Credit to my good friend of mine, Mr. Jonathan Shi Chai Loong for proofreading this thesis, despite his commitment to learning Mandarin in Taipei, Taiwan.

Acknowledgements

Last, but not certainly not least, I would like to extend my gratitude to my parents, my siblings and my spouse in Malaysia for their continuous support, encouragement and motivation to complete my thesis. I would also like to dedicate this thesis to them, and my little boy Xavier Chan Yu Hin.

TABLE OF CONTENTS

Abstract i
Graphical Abstract iii
Acknowledgements iv
Table of Contents vi
List of Figures ix
List of Tables xiv
Abbreviations xvi
Nomenclatures xix
Chapter 1 Introduction 1
1.1 Overview 1
1.2 Research Aims, Objectives and Novelty 7
1.2.1 Research Aim 7
1.2.2 Research Objectives 7
1.2.3 Research Novelty 7
1.3 Thesis Outline 8
Chapter 2 Background and Literature Review 11
2.1 Introduction 11
2.1.1 Introduction of Spark Ignition Engines 12
2.1.2 General Information and Types of GDI Engines 13
2.1.3 Main Drawback of GDI Engines 16
2.1.4 Exhaust Emissions Legislations 16
2.1.5 Gaseous Exhaust Emissions Formation 19
2.1.6 Gaseous Emissions Control and Aftertreatment 23
2.2 Particulate Matter (PM) 28
2.2.1 Introduction and Background of PM 28
2.3 State-of-the-Art 48
2.3.1 Combustion and Gaseous Emissions Characteristics 49
2.3.2 PM Characteristics 51
2.3.3 PM Abatement with GPF Application 73
2.3.4 Summary 75
Chapter 3 Experimental Setup and Facilities 78
3.1 Engine Test Bench 78

Table of Contents

3.2 Engine Instrumentation and Data Acquisition 80
3.3 Fuels Properties 83
3.4 Small Scale Aftertreament Architecture 84
3.4.1 Monolith Substrates Properties 84
3.4.2 Experimental Setup 85
3.5 Gaseous Emissions Instrumentation 87
3.5.1 Fourier Transform Infrared Spectroscopy (FTIR) Analyser 87
3.5.2 AVL Digas 400 88
3.6 Particulate Matter Characterisation Instrumentation 89
3.6.1 Scanning Mobility Particle Sizer (SMPS) 3936 89
3.6.2 Dilution System 90
3.6.3 Thermogravimetric Analyser (TGA) 92
3.6.4 Raman Spectroscopy (RAMAN) 95
3.6.5 Transmission Electron Microscope (TEM) 96
3.7 PM Loading Instrumentation 98
3.7.1 Microfiber Filters 98
3.7.2 PM Loading Setup 98
3.8 Data Processing 99
3.8.1 Combustion Analysis 99
3.8.2 Gaseous Emissions 102
3.8.3 PM Characterisation 102
3.8.4 GPF Performance Analysis 107
Chapter 4 Investigation of Combustion and PM Characteristics with Different Air-Fuel Ratio at MBT Condition 109
4.1 Introduction 109
4.2 Methodology and Test Conditions 110
4.3 Results and Discussion 112
4.3.1 Combustion Characteristics 112
4.3.2 Gaseous Emissions 116
4.3.3 PM Characteristics 119
4.4 Summary 139
Chapter 5 Study of Gasoline-Dimethyl Carbonate (DMC) Blend on Combustion and PM Characteristics 141
5.1 Introduction 141
5.2 Methodology and Test Conditions 141
5.3 Results and Discussion 144

Table of Contents

5.3.1 Combustion Characteristics 144
5.3.2 Gaseous Emissions 147
5.3.3 PM Characteristics 149
5.4 Summary 162
Chapter 6 Improving GPFs Performance by Architecture Optimisation 164
6.1 Introduction 164
6.2 Methodology and Test Conditions 164
6.3 Results and Discussion 168
6.3.1 Pressure Drop Analysis 168
6.3.2 Filtration Efficiency Analysis 172
6.4 Summary 177
Chapter 7 Enhancing TEM Analysis with Utilisation of Filter Extraction Method for GDI PM Reduction Investigation 179
7.1 Introduction 179
7.2 Methodology and Test Conditions 180
7.3 Results and Discussion 181
7.3.1 Advantages of Filter Extraction Method 181
7.3.2 Comparisons of d_{p0}, np_0, R_g and D_f. 181
7.4 Summary 184
Chapter 8 Conclusions and Future Works 186
8.1 Summary of Findings 186
8.1.1 Effect of Combustion Stoichiometry 186
8.1.2 DMC-Gasoline Blend 188
8.1.3 Aftertreatment Architectures 189
8.1.4 Filter Extraction TEM Grids Preparation 189
8.2 Future Work Reference 190
List of References 192
Appendix 1: Data Acquisition Channels 218
Appendix 2: Instrumentation Measurement Accuracy 219
Appendix 3: Author Publications and Awards 220
Publications 220
Awards and Scholarship 220
Appendix 4: Additional Information 221
In-House MATLAB Script 221

LIST OF FIGURES

Figure 1.1: λ vs Conversion Efficiency of THC, CO and NO_x of TWC [**10**]_____ 4

Figure 2.1: Homogenous and stratified charge combustion modes [**49**]. _____ 14

Figure 2.2: GDI engine (a) wall-guided (b) air-guided and (c) spray-guided [**54**]. _ 16

Figure 2.3: Euro I to Euro VI emissions limits. _____ 18

Figure 2.4: HCs emissions oxidation during post-combustion process [**39**]. _____ 20

Figure 2.5: Typical particulate size distribution (PSD) in mass and number found in exhaust emissions [**94**]. _____ 28

Figure 2.6: AED comparisons to aerosol particle size [**55**]. _____ 29

Figure 2.7: Suggested first benzene ring formation pathway [**126**]. _____ 35

Figure 2.8: Pathway for PAH growth via hydrogen abstraction–acetylene addition [**126**]. _____ 36

Figure 2.9: Ring to ring direct condensation pathway for PAH growth [**126**]. _____ 36

Figure 2.10: Schematics of wall-flow honeycomb of a particulate filter. _____ 43

Figure 2.11: Filtration mechanisms of particulate filter **(a)** Brownian diffusion **(b)** inertia impaction **(c)** direct Interception. _____ 44

Figure 2.12: Greenfield gap in typical particulate filter influenced by **(a)** filtration velocity **(b)** mean pore size and **(c)** is overall filtration efficiency of DPF [**172**], [**176**]. _____ 45

Figure 2.13: (a) Conventional PM layer formation on particulate filter **(b)** pressure drop concept of particulate during PM layer formation._____ 46

Figure 3.1: GDI engine used for experimental tests. _____ 79

Figure 3.2: (a) Rhenoik RM 015 Coriolis fuel mass flow meter and **(b)** fuel conditioning unit. _____ 81

Figure 3.3: Schematic of DAQ of engine test bench._____ 83

List of Figures

Figure 3.4: Small scale **(a)** TWC, **(b)** silicon carbide GPF and **(c)** cordierite GPF utilised in the research work. _____ 84

Figure 3.5: Stainless-steel reactor for small scale monolith substrates _____ 86

Figure 3.6: MKS Multigas 2030 FTIR gas analyser. _____ 87

Figure 3.7: AVL Digas 440. _____ 88

Figure 3.8: TSI SMPS 3969. _____ 89

Figure 3.9: Dilution system for PM sampling in the engine test cell. _____ 91

Figure 3.10: Perkin Elmer Pyris 1 TGA._____ 92

Figure 3.11: TGA temperature indication in ramp programme. _____ 93

Figure 3.12: Renishaw inVia Raman Microscopy. _____ 95

Figure 3.13: JEOL 2100 TEM with laB6 filament. _____ 96

Figure 3.14: PM dissolved in ethanol solution. _____ 97

Figure 3.15: Customised filter holder. _____ 98

Figure 4.1: Schematic of experimental setup. _____ 111

Figure 4.2: PM loaded filters of **(a)** stoichiometric (λ **=** 1), **(b)** lean (λ=1.1) and **(c)** rich (λ = 0.9) _____ 111

Figure 4.3: BSFC and BTE of λ = 0.9, 1 and 1.1. _____ 113

Figure 4.4: EGT and $\eta_{Combustion}$ of λ = 0.9, 1 and 1.1._____ 114

Figure 4.5: In-cylinder pressure and RoHR of λ = 0.9, 1 and 1.1. _____ 115

Figure 4.6: Specific **(a)** gaseous emissions and **(b)** HC species emissions of λ = 0.9, 1 and 1.1. _____ 118

Figure 4.7: (a) Number and **(b)** Mass PSD of λ = 0.9, 1 and 1.1._____ 120

Figure 4.8: PM Compositions for λ = 0.9, 1 and 1.1. _____ 122

List of Figures

Figure 4.9: (a) Soot oxidation mass profile, **(b)** derivatives of mass loss and **(c)** linear regression of Arrhenius plot for E_a of λ = 0.9, 1 and 1.1 with 7% oxygen concentration. _____ 124

Figure 4.10: (a) Soot oxidation mass profile, **(b)** derivatives of mass loss and **(c)** linear regression of Arrhenius plot for E_a of λ = 0.9, 1 and 1.1 with 1% oxygen concentration. _____ 127

Figure 4.11: TEM micrographs of PM agglomerate of λ = **(a)** 1, **(b)** 1.1 and **(c)** 0.9. _____ 129

Figure 4.12: Log-normal primary particles distribution for λ = **(a)** 1, **(b)** 1.1 and **(c)** 0.9. _____ 130

Figure 4.13: (a) Average d_{p0} **(b)** np_0 and R_g and (**c)** D_f of λ = 0.9, 1 and 1.1.____ 133

Figure 4.14: Average RAMAN spectra for λ = 0.9, 1 and 1.1. _____ 136

Figure 4.15: (a) Intensity ratio for band D1 and D3 **(b)** area ratio for band D1 and D3 **(c)** D1 FWHM for λ = 0.9, 1 and 1.1._____ 138

Figure 4.16: Estimated L_a using modified Knight and White's formula for λ = 0.9, 1 and 1.1. _____ 138

Figure 5.1: Schematic of engine bench test. _____ 143

Figure 5.2: PM loaded filters for **(a)** gasoline and **(b)** D8. _____ 143

Figure 5.3: MFB plot of gasoline and D8. _____ 144

Figure 5.4: BSFC, BTE and COV of IMEP of gasoline and D8._____ 145

Figure 5.5: EGT and $\eta_{Combustion}$ of gasoline and D8._____ 146

Figure 5.6: In-cylinder pressure and RoHR of gasoline and D8. _____ 146

Figure 5.7: Specific **(a)** gaseous emissions and **(b)** HC species emissions of gasoline and D8._____ 148

Figure 5.8: (a) Number and **(b)** Mass PSD of gasoline and D8. _____ 149

List of Figures

Figure 5.9: PM composition of gasoline and D8 _____ 151

Figure 5.10: (a) Soot oxidation mass profile, **(b)** derivatives of mass loss and **(c)** linear regression of Arrhenius plot for E_a of gasoline and D8. _____ 153

Figure 5.11: TEM micrographs of PM agglomerate of **(a)** gasoline and **(b)** D8.__ 154

Figure 5.12: Log-normal primary particles distribution for **(a)** gasoline and **(b)** D8. _____ 154

Figure 5.13: (a) Average d_{p0} **(b)** np_0 and R_g and (**c)** D_f of gasoline and D8. ____ 157

Figure 5.14: Average RAMAN spectra of gasoline and D8._____ 159

Figure 5.15: (a) Intensity ratio for band D1 and D3 **(b)** area ratio for band D1 and D3 **(c)** D1 FWHM of gasoline and D8. _____ 161

Figure 5.16: Estimated L_a using modified Knight and White's formula for gasoline and D8_____ 161

Figure 6.1: Schematic of the experimental setup. _____ 165

Figure 6.2: Schematic of aftertreatment architectures for CC (top) and UF (bottom). _____ 167

Figure 6.3: Pressure drop of aftertreatment architectures for 4800 seconds. ___ 168

Figure 6.4: Number PSD at 60 nm / 2100 rpm for standard calibration and advanced fuel injections._____ 169

Figure 6.5: Pressure drop difference during advanced fuel injection for all architecture configurations. _____ 170

Figure 6.6: Average $\eta_{Filtration}$ for all aftertreatment architectural configurations. __ 173

Figure 6.7: $\eta_{Filtration}$ **(a)** 600^{th} second (Fresh) **(b)** 1800^{th} second (30 mins) **(c)** 3600^{th} second (60 mins) (**d)** 4200^{th} second (Advanced Fuel Injection Timing) **(e)** 4800^{th} second (Post Advanced Injection Timing). _____ 176

List of Figures

Figure 7.1: TEM micrographs of **(a)** broken formvar-carbon coating and **(b)** PM agglomerates adhered on TEM grid wall. _____ 179

Figure 7.2: TEM Micrographs from filter extraction method at low, medium and high magnifications. _____ 181

Figure 7.3: Log-normal primary particles distribution for **(a)** direct exposure and **(b)** filter extraction methods. _____ 182

Figure 7.4: d_{p0}, np_0, R_g and D_f for direct exposure and filter extraction methods. 183

Figure 7.5: D_f of PM agglomerates for direct exposure and filter extraction. ____ 184

LIST OF TABLES

Table 1.1: Oxygen concentration in exhaust stream _____ 4

Table 2.1: The current enforceable Euro VI emission limits [**63**]. _____ 17

Table 2.2: Summary of PM source and proposed improvement. _____ 32

Table 3.1: GDI Engine specification. _____ 80

Table 3.2: Specifications of fuels used [**32**], [**191**], [**192**], [**265**], [**305**], [**306**]. _____ 84

Table 3.3: TWC and GPF monolith substrate properties._____ 85

Table 3.4: Technical specification of MKS Multigas 2030 gas analyser. _____ 88

Table 3.5: Technical specification for AVL Digas 440 for oxygen measurement.__ 89

Table 3.6: Technical specification for TSI SMPS 3969. _____ 90

Table 3.7: Technical specifications for Perkin Elmer Pyris 1 TGA._____ 93

Table 3.8: TGA conditions and settings in ramp programme. _____ 94

Table 3.9: Properties of LLG GF/F. _____ 98

Table 4.1: Experimental matrix and engine condition. _____ 110

Table 4.2: COV_{IMEP}, ignition duration, MFB50 and combustion duration of λ = 0.9, 1 and 1.1. _____ 112

Table 4.3: Statistical normality test for λ = 0.9, 1 and 1.1. _____ 130

Table 4.4: R_2 of linear regression for D_f (R_g) and D_f (LW) methodology. _____ 133

Table 5.1: Experimental matrix and engine condition. _____ 142

Table 5.2: Statistical normality test for gasoline and D8. _____ 155

Table 5.3: R_2 of linear regression for D_f (R_g) and D_f (LW) methodology. _____ 157

Table 6.1: Experimental engine condition._____ 165

Table 6.2: Experimental matrix and procedure for aftertreatment architecture. __ 167

Table 7.1: Statistical normality test for TEM grids prepared by direct exposure and filter extraction._____ 182

List of Tables

Table 7.2: R_2 of linear regression for D_f (R_g) and D_f (LW) methodology. _____ 183

ABBREVIATIONS

AED	Aerodynamic Equivalent Diameter
aGPF	after Gasoline Particulate Filter
AI	Analogue Input
AO	Analogue Output
aTDC	after Top Dead Centre
aTWC	after Three Way Catalyst
BDC	Bottom Dead Centre
bGPF	before Gasoline Particulate Filter
BSFC	Brake Specific Fuel Consumption
bTDC	before Top Dead Centre
BTE	Brake Thermal Efficiency
bTWC	before Three Way Catalyst
CAN	Controller Area Network
CC	Close-Coupled
cGPF	Catalysed Gasoline Particulate Filter
CI	Compression Ignition
Cord.	Cordierite
COV_{IMEP}	Coefficient of Variations of IMEP
CPC	Condensation Particle Counter
CPC	Condensation Particles Counter
D8	8%(v/v) of DMC blended in gasoline
DAQ	Data Acquisition
DI/O	Digital Input/Output
DI/O	Digital Input/Output Channel
DMA	Differential Mobility Analyser

Abbreviations

DMC	Di-Methyl Carbonate
EDC	European Driving Cycle
EGR	Exhaust Gas Recirculation
EGT	Exhaust Gas Temperature
ETBE	Ethyl Ter-Butyl Ether
EVC	Exhaust Valves Closing
FTIR	Fourier Transform Infrared
FWMH	Full Width Half Maximum
GHG	GreenHouse Gas
GNMD	Geometric Number Mean Diameter
GPF	Gasoline Particulate Filter
HEGO	Heated Exhaust Gas Oxygen
HEPA	High Efficiency Particle Arrestance
IEGR	Internal Exhaust Gas Recirculation
IMEP	Indicated Mean Effective Pressure
IVO	Intake Valves Opening
LHV	Lower Heating Value
MBT	Maximum Brake Torque
MFB	Mass Fraction Burn
MFB0	Mass Fraction Burned at 0%
MFB10	Mass Fraction Burned at 10%
MFB50	Mass Fraction Burned at 50%
MFB90	Mass Fraction Burned at 90%
MMLRT	Maximum Mass Loss Rate Temperature
MON	Motor Octane Number
MPS	Mean Pore Size
O/C	Oxygen to Carbon Ratio

Abbreviations

PEMS	Portable Emissions Measurement Systems
PM 0.1	Particulate Matter below 0.1 µm
PM 10	Particulate Matter below 10 µm
PM 2.5	Particulate Matter below 2.5 µm
PM	Particulate Matter
P_{Max}	Maximum In-Cylinder Pressure
PSD	Particle Size Distribution
RAMAN	Raman Spectroscopic
RDE	Real Driving Emissions
Redox	Reduction and Oxidation Process
REGR	Reformed Exhaust Gas Recirculation
RFF	Root Form Factor
RoHR	Rate of Heat Release
RON	Research Octane Number
SiC	Silicon Carbide
SMPS	Scanning Mobility Particle Sizer
SOT	Start of Oxidation
SPSS	Statistical Package for Social Science
SSA	Specific Surface Area
TDC	Top Dead Centre
TEM	Transmission Electron Microscope
TGA	Thermogravimetric Analyser
UF	Underfloor
VOM	Volatile Organic Materials
WGS	Water Gas Shift
WLTC	Worldwide Harmonised Light-duty Test Cycle
WLTP	Worldwide Harmonised Light-duty Test Procedure

NOMENCLATURES

χ^2	Curve fitting error
A	Area of agglomerate is projected in micrograph
a	Exponential factor for particle overlap
A_{D1}	Area under curve for Band D1
A_{D3}	Area under curve for Band D3
A_G	Area under curve for Band G
A_p	Area of primary particle
CO_2	Carbon Dioxide
C_p	Specific heat of constant pressure
C_{edge}/C_{basal}	Ratio of carbon in edge site to carbon in basal plane
C_v	Specific heat of constant volume
D_f	Fractal dimension
$D_f(LW)$	Fractal dimension using Minimum Bounding Rectangle method
$D_f(R_g)$	Fractal dimension using Power Law Relationship method
d_p	Particulate Matter Agglomerate Diameter
d_{p0}	Primary Particle Diameter
E_a	Activation Energy
γ	Ratio of specific heats
I_{D1}	Intensity for Band D1
I_{D3}	Intensity for Band D3
I_G	Intensity for Band G
k_f	Pre-factor or structural coefficient
L	Length of rectangle containing minimum area
L_a	Fringe length
m	Number of pixels per agglomerates
np_0	Number of primary particles per agglomerate

Nomenclatures

OH	Hydroxyl Radicals
ϕ	Equivalence Ratio
$\phi_{Critical}$	Equivalence Ratio for Critical Soot Threshold
R	Hydrocabon Radical
R_g	Radius of gyration
R_2	Coefficient of correlation
r_i	Distance between the centre of a primary particle and the centroid of agglomerate
$U_{filtration}$	Filtration Velocity
W	Width of rectangle containing minimum area
α	Dilution ratio
$\eta_{Combustion}$	Combustion efficiency
$\eta_{Filtration}$	Filtration efficiency
λ	Engine combustion stoichiometry

CHAPTER 1 INTRODUCTION

This introductory chapter presents an overview of the investigative studies performed by the author throughout the duration of his PhD. This thesis is primarily focused on Particulate Matter (PM) emissions by Gasoline Direct Injection (GDI) engines. The research adopted various approaches including engine combustion strategy, alternative fuel and exhaust aftertreatment. The research overview, outline, aims and objectives, and research approaches are presented below.

1.1 Overview

Pollution and the effect of global warming are two major concerns over the past few decades. Hence, catalysts made up of precious metals and filters are used in the Internal Combustion Engine (ICE) sector to control the emission of pollutants. In Compression Ignition (CI) engines, Diesel Oxidation Catalyst (DOC) and Selective Catalytic Reduction (SCR) are methods applied for gaseous emission control, and Diesel Particulate Filter (DPF) is used for PM control. Meanwhile, a Three-Way Catalyst (TWC) is utilised in Spark Ignition (SI) engines to abate gaseous emissions, such as hydrocarbons (HCs), Carbon Monoxide (CO) and Nitrogen Oxides (NO_x). However, the focus was later shifted to Greenhouse Gas (GHG) emissions, which included Carbon Dioxide (CO_2), as vehicle emission legislation was refined. Previous findings show that CO_2 emissions were not reduced following the application of TWC as a result of the oxidation process of HCs and CO. Subsequently, researchers pursued fuel-efficient alternative automotive technologies such as Gasoline Direct Injection (GDI) in order to reduce carbon footprint. Continual (more stringent)

adjustments to GHG limits have increased the market size of the GDI engine in the SI vehicle industry.

Although CO_2 production is lower when using GDI technology in comparison to conventional Port Fuel Injection (PFI), it is clear that PM emissions are inevitable due to the combustion that takes place within ICE's. Due to the differing fuel delivery systems in GDI engines, these PM emissions were recently highlighted. It was reported that greater concentrations of PM were formed in the combustion chamber in comparison with PFI engines and CI engines equipped with DPF [**1**]–[**3**].

Many studies have been conducted in an effort to control and understand the formation of PM emissions in GDI engines. Previous research has adopted several approaches including the use of biofuels, internal and external Exhaust Gas Recirculation (EGR), Reforming Exhaust Gas Recirculation (REGR), injection strategies (such as injection timing, injection pressure, multiple injections, injection spray patterns), combustion phasing (spark timing), different equivalence ratio (ϕ) and recently Gasoline Particulate Filters (GPFs).

Under ideal conditions, SI engines should combust close to stoichiometric (slightly rich, stoichiometry (λ) approximately equal to 1) and steadily throughout each cycle to maximise the functionality of the TWC. TWC efficiency is measured by constantly monitoring the Oxygen (O_2) concentration before and after the TWC conversion. Values are measured through O_2 sensors controlled by a '*closed-loop feedback'* Engine Control Unit (ECU). AFR values constantly fluctuate (become richer and leaner) during daily driving, due to the '*limit cycle*' in the control system from signalling delay [**4**]. Rich combustion commonly occurs in SI engines during abrupt and sharp acceleration (elevated load). This occurs because delayed air intake,

leading to an inability to precisely control the air-fuel mixture [**5**]. Furthermore, rich mixture is purposely utilised during cold starts, to increase combustion stability, maximise engine power output and reduce combustion temperature and exhaust gas temperature (EGT). This minimises the thermal cracking effect on pistons and catalysts [**5**]. Meanwhile lean combustion takes place during deceleration and fuel cut events. Lean combustion appears to be an adoptable approach as it could prospectively improve the combustion process and subsequently minimise PM, THC and CO emissions. Moreover, it can benefit the GPF application by promoting passive regeneration, as it is expected to be positioned after TWC (aTWC) as a second brick substrate [**6**], ensuring the TWC light-off activity is not affected particularly at cold-starts. Over time, a PM cake layer is expected to develop on the GPF channel surface, subsequently inducing pressure drop in the exhaust stream. The latter deteriorates engine power output and fuel economy [**7**], [**8**]. Therefore, GPF regeneration is vital but passive regeneration with stoichiometric combustion is unlikely to take place due to the O_2 consumption by the TWC. Measurement of O_2 concentration before TWC (bTWC) and aTWC with λ at 1, 1.1 and 0.9 corresponding to the stoichiometric, lean and rich mixture from the GDI engine used for this research thesis is presented in ***Table* 1.1**. Regardless of excessive O_2 concentration aTWC with lean combustion, ***Figure* 1.1** shows a deteriorated NO_x conversion. Alternatively, the unconverted NO_x mainly Nitric Oxide (NO) could be advantageous for GPF regeneration. Based on a study conducted by *Jiao et al.* [**9**], NO can effectively improve the PM oxidation light-off temperature. Hence, PM oxidation in conjunction with O_2 and NO can be an alternative solution to pressure drop in the GPFs as a regeneration strategy.

Table 1.1: Oxygen concentration in exhaust stream

Stoichiometry, λ	O_2 Concentration bTWC (%)	O_2 Concentration aTWC (%)
Stoichiometric (λ=1)	0.80	0.00
Lean (λ=1.1)	2.32	2.05
Rich (λ=0.9)	0.28	0.00

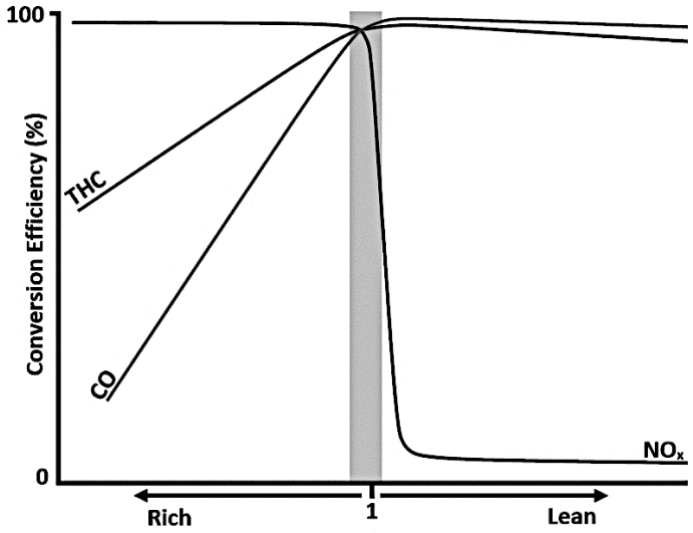


Figure 1.1: λ vs Conversion Efficiency of THC, CO and NO_x of TWC [**10**]

Biofuels are viewed to be potential sustainable source of fuel and are widely being used as a research octane number (RON) and a motor octane number (MON) enhancer for engines to increase compression ratios, output power and to promote cleaner combustion [**11**]–[**14**]. Di-Methyl Carbonate (DMC) is a methyl ester that can potentially be used as an alternative source of fuel, or as a fuel additive, as it was being reported to improve THC and CO emissions in SI and CI engines. Additionally, DMC addition demonstrated lower PM emissions in CI engines due to its molecular structure without C-C bonds and oxygen to carbon ratio (O/C) of 1 [**15**]. It hypothetically could be an alternative to reduce PM formation in GDI engines. DMC is a green chemical and is being produced at 90,000 tons per annum [**16**]. Furthermore, the

recent study proposed DMC can be produced via direct synthesis of CO_2 and methanol [**17**] but is still currently under research due to its poor conversion and low yield. This could provide an alternative method instead of the use of highly toxic chemical (phosgene) applied in conventional production methodologies such as phosgenation of methanol and carbonylation of methanol using NO_x [**16**]. DMC possesses numerous advantages over conventional biofuels that are blended with gasoline such as Methyl Ter-Butyl Ether (MTBE), Ethyl Ter-Butyl Ether (ETBE) and ethanol. The significantly Lower Heating Value (LHV) of DMC appears to be the only disadvantage which is hypothesised to deteriorate fuel economy as a penalty in fuel consumption. The main advantages are that DMC is able to convert energy more efficiently due to the combination of lower hydrogen to carbon ratio (H/C) of 0.168 and low LHV [**18**], [**19**]. MTBE and ETBE are less favourable due to their non-renewability and regarded as non-environmentally friendly [**20**], [**21**]. Moreover, MTBE is hazardous to the environment and humans via water contamination, and direct exposure at high dosage can be carcinogenic [**12**], [**22**]. Ethanol is a regarded as renewable as it can be produced from renewable feedstock and is currently being introduced in gasoline [**23**], up to 85 % (v/v) [**24**]. It was claimed to corrode with metals (engine parts) [**25**], [**26**] and have a tendency for phase separation with gasoline [**27**], [**28**]. Butanol was being comprehensively investigated as a potential candidate. However, a research study found that the physio-chemical properties of butanol have considerably higher latent heat of vaporisation and kinetic viscosity can negatively impact the engine cold-start and ignition [**29**]. A similar conclusion was also drawn regarding ethanol [**30**], [**31**] Conversely, the benefits of DMC over the aforementioned biofuels are similar kinematic viscosity and latent heat of vaporisation to gasoline, excellent solubility, non-reactivity with metals, low production cost, non-toxicity, and is renewable [**20**], [**21**],

[**28**], [**32**]–[**34**]. Finally, high oxygen content (approximately 53.3 wt %) is one of the main key benefits. Hence, combustion characteristics and PM emissions could be significantly improved with minimal volume blended with gasoline and is yet to be investigated on GDI engines.

Particulate filter application is expected in GDI engines based on the evidence showed that GPF is capable of efficiently trapping particles up to 99% in terms of number [**6**], [**35**]. Properties of GPF have been investigated in detail by other researchers in order to design an optimum GPF. Studies on aftertreatment architectural configurations, close-coupled (CC) and underfloor (UF) have also been evaluated for filtration efficiency and pressure drop with driving cycles. However, these investigations were much less thorough, particularly regarding the *Greenfield Gap* effect. Thus, the impact of architectures from fresh GPF to the PM layer formation is required to be comprehensively assessed.

A large range of microstructural and Nanostructural analyses have been conducted on PM formed by GDI engines, which can assist the designing of an optimum GPF. These characteristics can also be used as a reference to determine GPF regeneration strategies as well as the impact on human health. Microstructural and Nanostructural analyses are conducted with TEM grids which mostly are exposed directly to exhaust gas. Despite the conventional method for TEM grid preparation, an alternative method, filter extraction method was used in a preceding study [**36**]. However, the accuracy and precision in comparison with the conventional direct exposure approach has not been evaluated. A case study has been conducted to demonstrate a promising alternative for future application. Its comparison should be performed in relation to the conventional direct exposure method, to determine its feasibility and reliability.

1.2 Research Aims, Objectives and Novelty

1.2.1 Research Aim

This thesis aims to investigate effective approaches to reduce PM emissions. The primary aim is to evaluate PM characteristics formed during combustion in GDI engines. Methods include air-fuel ratio variation and utilisation of oxygenated fuel. In addition, the study aims to examine the performance of aftertreatment architectural configurations on particulate filters. The feasibility of filter extraction TEM grid preparation is also considered.

1.2.2 Research Objectives

1. Study the impact of air-fuel ratio on GDI engines by quantifying combustion performance, gaseous emission, PM emission and PM characteristics.
2. Demonstrate the feasibility of DMC additives in gasoline in GDI engines by assessing combustion performance, gaseous emission, PM emission and PM characteristics.
3. Understand how aftertreatment architectural configurations affect filtration performance and pressure drop in GPFs and are influenced by the GPF properties.
4. To identify result variation in TEM grids prepared via filter extraction methods comparable to conventional direct exposure.

1.2.3 Research Novelty

This research thesis addresses several original points, which aim to further understanding of PM formed in GDI engines. These are outlined below;

1. Performing PM oxidation reactivity formed by varied engine combustion stoichiometry at maximum brake torque (MBT) conditions using Thermogravimetric Analysis (TGA).
2. Assessment of PM characteristics using DMC-gasoline blends on GDI engines.
3. Development of a new TGA methodology capable of avoiding the mass effect and examination of the ratio of volatile organic material (VOM) to elemental soot in PM.
4. Demonstrating aftertreatment architectural configurations with correlation to the *Greenfield gap* effects in GPFs.
5. Highlighting the effect of GPF properties on the aftertreatment architectural configurations in filtration efficiency and pressure drop.
6. Determination of an filter extraction methodology for the use of PM Transmission Electron Microscope (TEM) samples, in comparison to the conventional direct exhaust exposure method in terms microstructure.

1.3 Thesis Outline

This thesis has a total of eight chapters. The outline of the thesis of each chapter is briefly explained below, beginning from ***Chapter 2***.

Chapter 2 presents relevant information on SI engines, focussing on GDI engine technology and its associated advantages and limitations over conventional PFI engines. This is followed by the fundamentals of emission formation, and the introduction of EU legislation with a focus on PM emissions. This is followed by a brief discussion on key concerns raised by PM emissions formed in ICE's on the environment and human health. Lastly, the chapter proceeds to a comprehensive

literature review on combustion characteristics, PM nature, PM characteristics with alternative fuels, engine operating conditions and PM aftertreatment.

Chapter 3 details the experimental facilities used during this research, including the engine test cell, the engine and data acquisition instrumentation, experimental instrumentation and setup, and specifications of TWC and GPFs. Brief theoretical explanations of the emission analysers are also included, as well as details of calculations used for post-processing.

Chapter 4 assesses the engine operation at stoichiometric, lean and rich AFR conditions corresponding to λ equal to 1, 1.1 and 0.9 respectively, with the engine condition at maximum brake torque (MBT) of 90 Nm / 2200 rpm. The experiments consist of combustion analyses and emissions, with particular attention to PM emission. Combustion analyses comprised of combustion stability, Mass Fraction Burned (MFB) analyses, fuel consumption, combustion efficiency, Brake Thermal Efficiency (BTE), in-cylinder pressure and Rate of Heat Release (RoHR). Emissions analyses assess emissions of THC, CO, CO_2, NO_x and PM. In PM, Particle Size Distributions (PSD's) are measured and PM is loaded on microfibre filters and TEM grids. The filters and TEM grids allow the evaluation of PM reactivity, PM compositions, primary particle size (d_{p0}) and, microstructural and Nanostructural analyses. Altogether, this allows examination of the nature of PM formed by different stoichiometry combustion in GDI engines.

The importance of ***Chapter 5*** is to demonstrate how DMC could be used as a suitable alternative fuel replacement for gasoline, with the objective of reducing emissions with minimal impact on engine performance. The same experimental setup and methodology stated in the previous chapter is applied in this chapter. The same

engine speed and torque (90 Nm / 2200 rpm) is applied with MFB50 phasing, and at homogenous-stoichiometric combustion throughout the course of the experiments. This study is performed using 8% (v/v) of DMC blended with commercial gasoline denoted as D8.

Chapter 6 investigates CC and UF architectural configurations of a TWC and GPFs executed with scaled-down substrates in a furnace-heated reactor. GPFs used are made up of Cordierite (Cord.) and Silicon Carbide (SiC) with different properties. The study evaluates the filtration efficiency and pressure drop in GPFs when influenced by varying architectural configurations. Additionally, the influence of GPF properties on architectural configurations is also examined. The *Greenfield gap* effect is analysed to identify the impact on performance of GPFs progressively from fresh, to post PM cake layer formation. The engine is conditioned at MBT of 60 Nm / 2100 rpm. The outcome of this chapter can be used as an indicator for optimisation of GPF applications in GDI engines.

Error! Reference source not found. focusses on PM micro-scale characteristics analysis. PM is obtained via microfibre filters loaded with an engine conditioned at MBT of 90 Nm / 2200 rpm. A comparison of TEM grid preparation methodologies are evaluated based on micro-scale analysis, including the d_{p0}, radius of gyration (R_g), number of primary particles (np_0) and fractal dimension (D_f).

Chapter 8 summarises key conclusions and recommendations for future work.

CHAPTER 2 BACKGROUND AND LITERATURE REVIEW

2.1 Introduction

This chapter intends to provide background knowledge for a state-of-the-art thesis. It begins with background information on SI engines, explaining the fundamental differences between conventional PFI and GDI engines. Subsequently, a brief overview of GDI engine technologies is provided, with an evaluation of the benefits of using GDI engines over PFI engines. The chapter also provides a discussion of emission-based legislation and the compatibility of GDI engines within the international framework.

The formation of gaseous emissions in SI engines is subsequently discussed, as well as the current methodologies and aftertreatment technologies used. The discussion is furthered into PM emissions including its formation and its impact on human health and the environment. Approaches to improve PM emissions through abatement alternatives are also discussed.

Finally, this chapter contains a comprehensive literature review. For the purpose of this thesis, the literature on combustion characteristics and gaseous emissions is only emphasised on air-fuel ratio and DMC. Instead, the literature focuses on PM formed in GDI engines, including; PM nature (oxidation reactivity, microstructure and Nanostructure), influential factors on PM oxidation reactivity and, the impact of fuels, engine parameters and aftertreatment on PM.

2.1.1 Introduction of Spark Ignition Engines

The era of four-stroke combustion engines was progressively utilised from 1876 and it has been the blueprint for SI engine design to this day [**37**]. Within a similar transit of time, the Diesel cycle was developed for CI engines in 1893 [**38**]. Fundamentally, the difference between SI and CI engines lie in the type of combustion that takes place. Spark-ignited engines burn with premixed flame, whilst contrarily, compression-ignited engines burn with diffusive-flame [**39**].

Spark-ignited engines began using carburettor injections, gradually switching to PFI and subsequently to GDI. Carburettor injections were rejected by automotive manufacturers due to their greater emissions, delayed engine response time and drivability [**40**], thus resulting in the adoption of PFI. Subsequently, since the 90's, GDI has become increasingly favourable for use by automotive manufacturers in the effort to reduce CO_2 emissions through its higher precision of fuel injection control [**40**].

The dissimilarity between PFI and GDI is distinguished by their fuel delivery systems due to the location of fuel injectors. For PFI, injectors are placed and mounted in the intake manifold, close to the intake valves, so that fuel can be delivered during the intake stroke as the valves are opened. In GDI, injectors are located on the cylinder head and fuel is directly injected into the combustion chamber. PFI is believed to be completely, or almost completely, mixed-charge due to the longer air-fuel mixing time. Therefore, the shorter mixing duration in GDI engines require a significantly higher injection pressure to ensure greater fuel vaporisation for better air-fuel mixing. This has led to the implementation of high-pressure fuel injection, with high-pressure mechanical fuel pumps feeding through common rails with pressure ranged between 50 to 200 bar.

2.1.2 General Information and Types of GDI Engines

The extensive utilisation of GDI engines is due to a suite of advantages. The first of these advantages is the superior cooling effect, as fuel is injected into the combustion chamber [**41**]–[**43**]. This allows an increase of the compression ratio, as the engine is less prone to knocking and pre-ignition due to the lower compression temperature. With GDI technology, engine downsizing is possible with the application of a turbocharger, resulting in lower emissions. It also improves the volumetric efficiency [**41**], [**42**] and peak engine output, therefore enhancing the engine fuel economy, particularly at mid-high load conditions [**44**]–[**46**]. Furthermore, better fuel economy is achievable due to higher precision and accuracy of the fuel injection into the combustion chamber [**47**]. As a consequence, this provides improved engine efficiency and a lower EGT, reducing the exertion of thermal effect on catalyst and exhaust components [**43**].

GDI engines have been continuously improved since the 1990s [**43**], leading to three designs namely, air-guided, wall-guided and spray-guided. These designs determine the combustion mode; either homogeneous or stratified (partially mixed) charge combustion. The combustion mode is controlled by fuel injection timing, either during the intake stroke or compression stroke respectively, as shown in ***Figure* 2.1**. The partially mixed-charge combustion is lean overall and can only be realised when injections take place at a very close vicinity to the spark plugs. The partially mixed-charged GDI engines usually operate in mixed modes. During low-mid load conditions, charge is stratified. Conversely, homogenous modes are applied during mid-high load conditions [**48**].

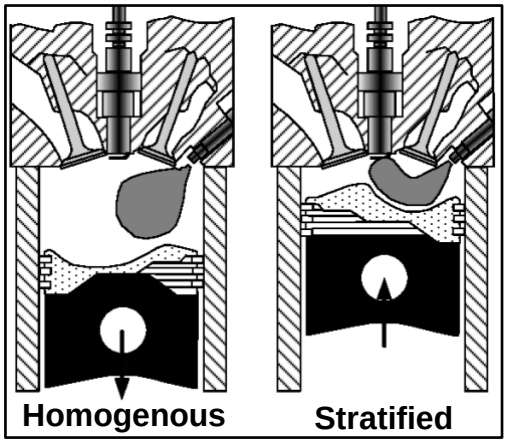


Figure 2.1: Homogenous and stratified charge combustion modes [**49**].

The initial design, or first generation, of GDI engines are known as *'wall-guided'* (***Figure* 2.2*a***). The charge motion depends heavily on the geometry of the piston, whereby a scooped design is implemented as the primary mechanism allowing for air-fuel mixing which is subsequently diverted towards the direction of the spark plug. However, a weakness of this approach is that injected fuel is unable to completely evaporate, leading to fuel impingement on the piston head and causing greater HC, CO and PM emissions [**43**], [**49**]. This phenomena increases the wall heat loss, limiting the use to low-mid load conditions with greater loss exhibited at high load conditions [**43**].

'Air-guided' GDI engines (***Figure* 2.2*b***) are an improved version of the first design, and were released to address the weaknesses in the '*wall-guided*' design by using a '*tumble charge*' motion to evaporate fuel injected prior being directed to spark plug [**50**]. Tumble or swirl charge motion is generated during the intake stroke [**51**], through specially designed intake ports which enable a desired amount of tumble charge motion relative to the speed and load range [**49**]. Occasionally, ECU controlled tumble flaps are utilised to provide the desired tumble charge motion [**52**]. A majority

of stratified-charge GDI engines adopt this design with the use of large-scale tumble motion to retain the compactness of spray (maintaining charge stratification) during the transportation towards the spark plug [**53**]. This design is also frequently used in homogeneous charge combustion mode engines [**43**].

Second-generation GDI engines later emerged using a *'spray-guided'* method, with fuel injection closely and centrally located on top of the combustion chamber as indicated in ***Figure* 2.2*c***. In comparison to *'wall-guided'* and *'air-guided'* designs, the injectors are positioned further away from the spark plug [**53**]. This design enables better stratification as well as obtaining the highest efficiency (lowest fuel consumption) [**53**]. The tumble charge motion and piston geometry have negligible influence [**53**], rather, the mixture is transported by its kinetic energy [**53**]. Under these conditions, the spray and atomisation of fuel by the fuel injectors are of greater importance [**51**], [**53**]. Piezoelectric injectors are often applied because of their rapid response and shorter minimum injection duration in comparison to conventional solenoid injectors [**49**], [**52**]. Fuel impingement can be reduced with a multi-injection (split injection) strategy. This allows shorter spray penetration and enhanced atomisation with the use of piezoelectric injectors [**52**]. The first injection takes place during the intake stroke, which is similar to the fuel injection timing of the engine operating at homogeneous charge combustion mode. The following injection occurs during the compression stroke, which creates a stratified-charge mixture. During this process, fuel-rich mixture is formed in the vicinity of the spark plug with a comparatively lean mixture surrounding the combustion chamber.

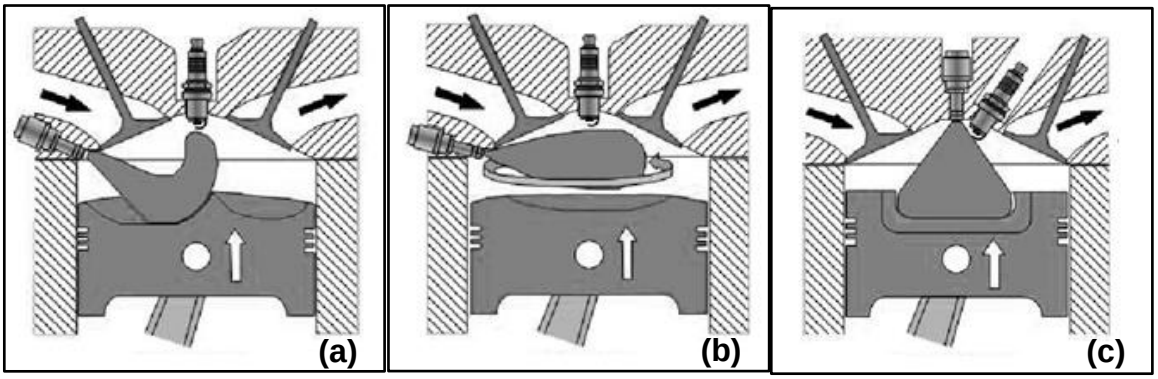


Figure 2.2: GDI engine (a) wall-guided (b) air-guided and (c) spray-guided [**54**].

2.1.3 Main Drawback of GDI Engines

The technological development of SI engines (GDI engines) have yielded numerous advantages in comparison to conventional PFI engines. These include; (i) a similar or lower magnitude of gaseous emissions in homogeneous combustion mode. (ii) Significantly fewer emissions during cold start operations, as fewer cycles are required for a stable operation due to faster warming up [**43**]. However, the formation of PM is inevitable in GDI engines. This becomes a major concern, as PM emissions are at considerably greater concentrations compared to conventional PFI engines [**43**], [**55**]. This is apparent during stratified-charge combustion operations, where PM concentrations were reported to be significantly higher than homogeneous charge combustion [**43**], [**56**], [**57**], as well as other gaseous emissions. Further discussions on gaseous and PM emissions will be discussed in later sections.

2.1.4 Exhaust Emissions Legislations

The European Union (EU) introduced its first legislation in 1970, imposing limits on HC and CO emissions. Tests were carried out with European Driving Cycle (EDC)

procedures comprising of three separate tests. NO_x emissions were included in 1976, and subsequently HC and NO_x emissions were combined due to the conflicting engine strategy in 1983 [**58**]. The first EU emissions standard (*Euro I*) was announced in 1992 to control HC, CO and NO_x emissions [**59**], followed by *Euro II* in 1996 with reduced emissions limits [**60**]. The enforceable standard in 2000, *Euro III*, replaced the combination of HC and NO_x to focus on individual emissions. This occurred in conjunction with the introduction of new test procedures (New European Driving Cycle (NEDC) [**61**]. In 2005, *Euro IV* was proposed, containing tightened emissions limits [**62**]. Subsequently in 2009, Non-Methane Hydrocarbons (NMHC) and PM mass emissions limits were included in *Euro V* [**63**] with the announcement of CO_2 reductions [**64**]. ***Table* 2.1** is the current enforceable *Euro VI* standard (announced in 2014) since September 2017. Worldwide Harmonised Light-duty Test Cycle (WLTC), which corresponds to Worldwide Harmonised Light-duty Test Procedures (WLTP), were introduced to replace NEDC. One of the highlights were that the PM emissions were tightened with PM number [**63**]. A full compilation of *Euro* emissions limits from 1992 to date is illustrated in ***Figure* 2.3**.

Table 2.1: The current enforceable Euro VI emission limits [**63**].

CO (g/km)	THC (g/km)	NOx (g/km)	NMHC (g/km)	PM Mass (mg/km)	PM Number (#/km)
1.0	0.1	0.06	0.068	4.5	6×10^6

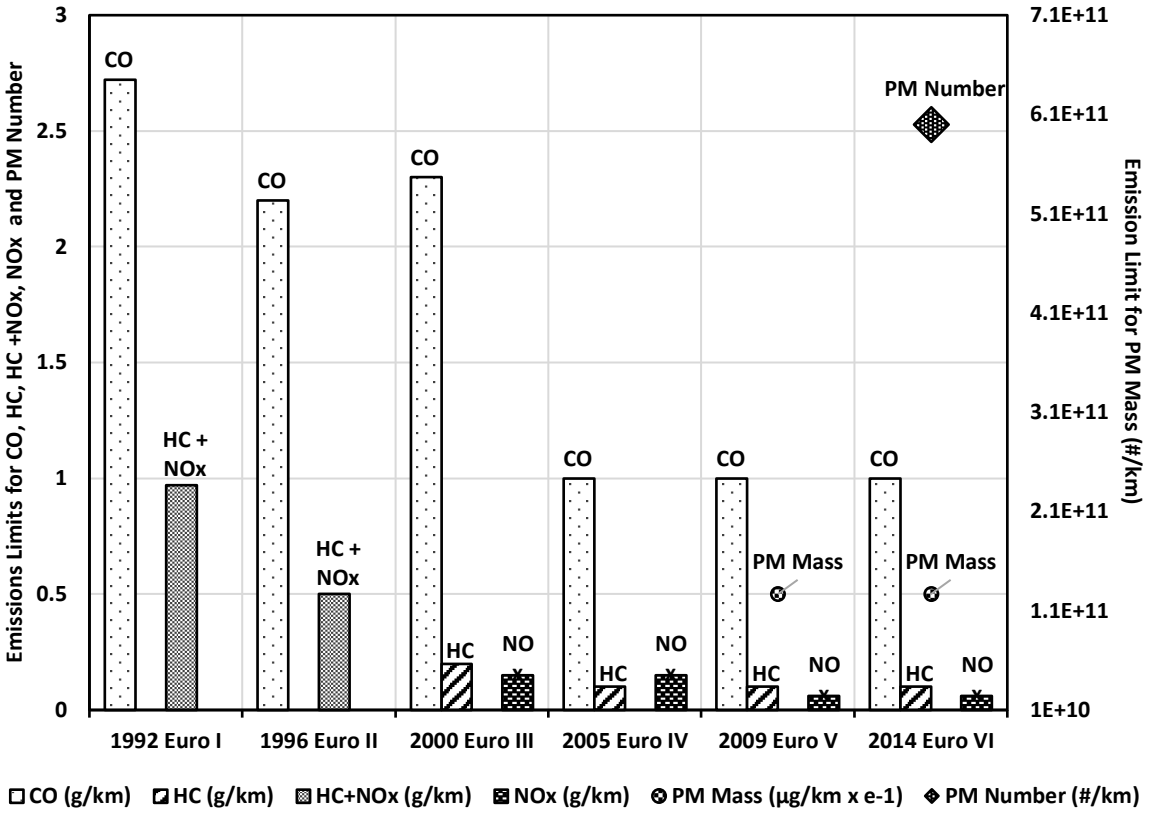


Figure 2.3: Euro I to Euro VI emissions limits.

In 2011, the research body of the Joint Research Center (JRC) of the EU research team has found discrepancies in the emissions emitted by ICE between on-road driving and laboratory test results [**65**]. For instance, NO_x emission emitted by CI vehicles were measured below permitted limit of 80 mg/km in the laboratory tests, but the emission exceeded up to 700 to 800 mg/km during on-road driving. This has led to the introduction of Real Driving Emissions (RDE) by the EU in 2017, imposing on the PN and NO_x emission limits [**65**], [**66**]. The emissions are monitored by the use of Portable Emissions Measurement Systems (PEMS), with conformity factors due to significantly lower repeatability of emissions measurement using PEMS [**65**]–[**67**]. In the RDE procedures, it is like the WLTP with consideration of low, medium and high-

speed conditions. But several extra factors are taken into account in the RDE tests, which includes (i) payload, (ii) altitude, (iii) ambient temperature, (iv) number and duration of stops, (v) speed and (vi) dynamic boundary conditions [**65**], [**67**].

2.1.5 Gaseous Exhaust Emissions Formation

2.1.5.1 Carbonaceous Emissions (HC, CO and CO_2)

The ideal combustion scenario in an engine. However, complete combustion in an internal combustion engine is almost impossible, resulting in undesirable emissions including unburned HC and CO in the exhaust stream.

Several factors have been identified explaining HC emissions due to incomplete combustion. The first factor includes '*flame quenching*'; causing a decrease in flame temperature whilst approaching the combustion chamber wall. This limits the flame range, particularly in crevice volumes (piston rings and valve seats). As a consequence, HC emissions are formed from the absorption and desorption of fuel vapor onto the cylinder wall and into air-fuel mixture. This forces the HCs into the crevice volumes during high in-cylinder pressure circumstances, evading the main combustion process [**4**], [**68**]. As the combustion stability (COV_{IMEP}) drops, the chance of misfiring and partial burning surges due to numerous slower burning cycles, leading to an increase of HC emissions [**4**]. Finally, partial oxidation is also identified as a source of HCs when the mixture is not well mixed (e.g. cold start and transient mode) [**39**]. However, HC oxidation takes place throughout the exhaust stroke in the combustion chamber and exhaust stream. This occurs at a lower temperature than CO oxidation. On average, ~ 47 % of HC emissions reach the exhaust stream, and ~ 53 % of total HC emissions are oxidised in the combustion chamber. Out of the remaining fraction, ~ 23 % that proceeds through to the exhaust is oxidised within the exhaust

stream and with the application of aftertreatment, it manages to oxidise up to ~ 23 %. Hence, only ~ 1 % of HC emissions are released into the atmosphere as tailpipe emissions [**39**], [**52**]. These figures may differ for stratified-charge combustion; as higher HC emissions are emitted into the atmosphere due to the lower in-cylinder temperature resulting in lower post-combustion oxidation [**43**]. ***Figure* 2.4** shows the distribution of how HC emissions are oxidised during post-combustion oxidation.

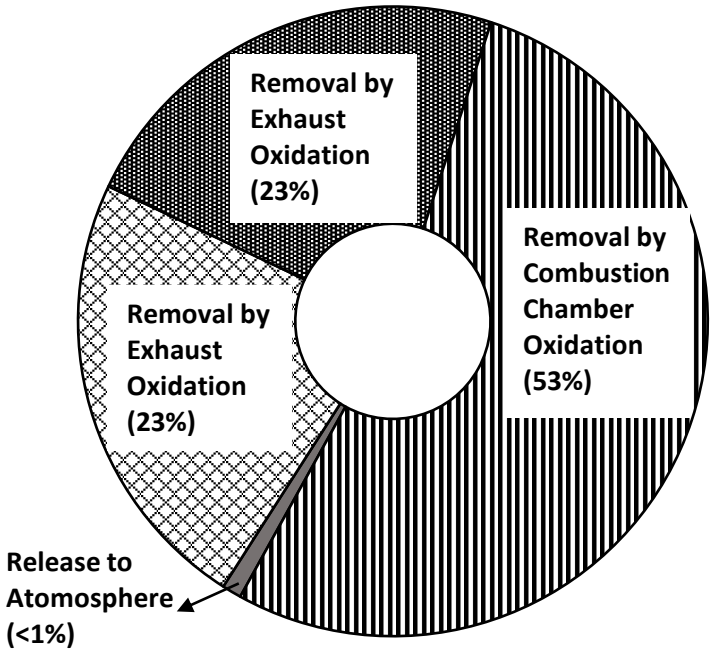


Figure 2.4: HCs emissions oxidation during post-combustion process [**39**].

The CO emission level acts an indicator for in-engine combustion completeness [**52**], and is mainly influenced by the ϕ of the mixture [**4**]. CO emissions spike as the mixture is enriched with fuel; and vice-versa as fuel is depleted [**69**] When the in-cylinder temperature is high enough with sufficient oxygen concentration, it can promote CO oxidation up to the expansion stroke. However, the rate of oxidation will become negligible as the temperature drops [**4**]. The oxidation process of CO into CO_2 can be referred to in ***Equation 2.1*** to ***Equation 2.4***. The primary oxidation reaction of

CO is ***Equation 2.3*** due to that ***Equation 2.1*** is a slower process. Hydroxyl radicals (OH) are continually produced by water, their formation is described through ***Equation 2.2*** and ***Equation 2.4***. Part of the CO emission contribution is by the dissociation of CO_2 at higher temperature due to the alteration of CO/CO_2 equilibrium shown in ***Equation 2.5*** [**4**].

Equation 2.1 $$CO + O_2 \rightarrow CO_2 + O$$

Equation 2.2 $$O + H_2O \rightarrow 2OH$$

Equation 2.3 $$CO + OH \rightarrow CO_2 + H$$

Equation 2.4 $$H + O_2 \rightarrow OH + O$$

Equation 2.5 $$CO + \frac{1}{2} O \leftrightarrow CO_2$$

Despite the *Euro* standards omission of CO_2 emission limits, the EU has set a target to achieve 130 and 95 g/km by 2015 and 2021 respectively for light-duty vehicles [**64**]. This was proposed to achieve the target by improving engine's fuel economy. Thus, an engine downsizing approach was adopted in the recent years. Additionally, an alternative approach was utilised in the UK using oxygenated fuel, although it compromises the fuel economy due to the lower LHV. It emits lower specific CO_2 emissions as a result of shorter carbon chains [**70**], [**71**].

2.1.5.2 Oxides of Nitrogen (NO_x) Emissions

In SI engines, NO_x emissions are generally defined as the mixture of NO and nitrogen dioxide (NO_2). Commonly, only NO will be formed from combustion. NO_2 is found in a minor proportion to NO, with NO_2 forming in the exhaust stream and

atmosphere through the oxidation process rather than during combustion in the flame. These NO_2 gases are corrosive and may cause smog pollution [**72**]. NO can be formed with four mechanisms; thermal NO, prompt NO, intermediate NO and fuel NO [**30**]. But in ICE, thermal NO is recognised as a significant contributor in exhaust tailpipe emissions. NO formation begins at temperatures of 1800 K and above. The NO formation is assumed based on Zeldovich mechanisms described in ***Equation 2.6*** to ***Equation 2.8*** [**4**] in which oxygen atoms, N_2 and OH are a part of the equilibrium concentrations.

Equation 2.6 $$O + N_2 \leftrightarrow NO + N$$

Equation 2.7 $$N + O_2 \leftrightarrow NO + O$$

Equation 2.8 $$N + OH \leftrightarrow NO + H$$

The primary pathways of NO formation is via oxidation of N_2 (***Equation 2.6*** and ***Equation 2.7***) [**73**]. These two mechanisms are dominant in lean and slightly rich mixtures [**74**] are not substantial if the reaction temperature is below 1500K [**75**]. Oppositely, NO formation in rich mixtures takes a different course, preferentially using OH radicals rather than oxygen atoms (***Equation 2.8***). NO formation rate can be assumed using the exponential equation in ***Equation 2.9*** [**4**]. Based on the equation, NO formation rate is dependent on temperature (T), oxygen (O_2) and nitrogen (N_2) concentrations, and residence time (t). Therefore, the engine operating parameters that influence NO formation are ϕ, valve overlapping, spark timing, engine speed and flame temperature.

Equation 2.9

$$\frac{d[NO]}{dt} = \frac{6\ x\ 10^{16}}{t^{1}/_{2}} . e^{-69{,}090/_{T}} . [N_2] . [O_2]^{1}/_{2}$$

2.1.6 Gaseous Emissions Control and Aftertreatment

2.1.6.1 Gaseous Emissions Control with Engine Parameters and Technologies

Various approaches have been adopted to improve tailpipe emissions from being released into the atmosphere. This includes the re-use of residual gas fraction from previous combustion cycles, known as EGR, which aims to improve engine performance, efficiency and emissions [**4**]. During this process, residual gas can be recirculated externally, using valves, or internally with engine valvetrain control [**76**].

IEGR retains exhaust gas by alternating the crank angle degree (CAD) of Intake Valve Opening (IVO) and Exhaust Valve Closing (EVC). Based on the duration and timing of overlap, various emission scenarios can be produced. Longer overlap can reduce NO_x emission efficiently by lowering the combustion temperature. A delayed overlap (later IVO) can improve the THC emission as the oxidation process is enhanced in the cylinder.

External EGR was initially implemented in CI engines by redirecting residual gas into the intake manifold. This process aimed to suppress thermal NO_x formation rate by reducing the combustion temperature [**77**]. Subsequent research was performed for GDI engines [**71**], [**77**]–[**80**]. Research demonstrated with the addition of EGR, most of the gaseous emissions, except for THC (lower combustion temperature worsened HC oxidation during and post combustion), were improved [**44**], [**81**]. Furthermore, as combustion temperatures were lower, CO and NO_x emissions were improved due to decreased CO_2 dissociation [**81**], [**82**], as well as slower NO_x production rate. EGR also

enhanced the engine fuel economy. As a subsequent effect, CO_2 emissions were reduced through reduced fuel mass injected into the combustion chamber. However, a limitation of external EGR includes worsening of engine combustion stability beyond controllable boundaries after a certain percentage of dilution [**83**].

Recently, a current trend in SI engine technology to improve CO_2 emissions involves the application of turbochargers to GDI engines. This method is seen as the most promising approach to reduce fuel consumption, as engines can be downsized to a smaller displacement (cubic centimetre or volume), but with equal performance [**43**], [**84**], [**85**]. Various car manufacturers have downsized their engines from naturally aspired (NA) four-cylinder engines, to smaller displacement turbocharged four-cylinder GDI engines, and recently, replacing with turbocharged three-cylinder GDI engines. *Eichhorn et al.* [**86**], demonstrated 50% downsizing from 1.6 L NA to 0.85 turbocharged two-cylinder engines was archivable with the same engine performance, with an improved fuel economy up to 25%, thus lowering CO_2 emissions. THC emissions were also lowered with this approach, as less crevice volume was available. The study also suggests that it was beneficial for NO_x emissions, as combustion temperature dropped. Adversely, slightly more CO was emitted as the oxidation rate reduced and delayed catalyst light-off time during cold-start [**43**].

Another approach used to achieve CO_2 reduction is utilising the aforementioned stratified-charge combustion mode. This combustion mode intended to reduce fuel consumption [**87**], whilst simultaneously improving THC and CO emissions. Despite better THC, CO and CO_2 emissions, a substantial amount of NO_x was produced during the oxygen and N_2 enrichening process (lean mixture) and it was not possible to meet

the scheduled emissions standards. Therefore, an aftertreatment catalyst is required to ensure emissions standards are met. This will be discussed in later in this section.

Split injection is an alternative method used in GDI engines that can improve combustion and emissions. The first injection takes place during the intake stroke in order to create lean homogenous charge, allowing combustion within an acceptable combustion stability limit. The following second injection, a stratified-rich fuel is created surrounding the spark plug vicinity. With the rich mixture, the ignition duration is reduced, enhancing the combustion stability during ignition. As a consequence, fuel consumption remains minimal during cold-start, pre-catalyst light off [**88**]. The overall combustion is stoichiometric, which leads to the higher in-cylinder temperature. Subsequently, the THC and CO emissions are improved by oxygen located in the homogenous-lean layer. This approach is currently adopted by Mercedes-Benz, achieving 5 injections per cycle with their current engine technology [**89**].

2.1.6.2 Gaseous Emissions Aftertreatment Technologies

Controlling emissions through engine parameter modification can be achieved, but a '*ceiling effect*' was observed, meaning having effect on emissions to a certain extent based on literature reviewed. Therefore, exhaust gas aftertreatment (catalytic converter) is implemented in internal combustion engines to effectively reduce the HC, CO and NO_x to meet the emissions limits. TWC is currently the most valuable technology in SI engines for emissions control since it can effectively remove THC, CO and NO_x emissions from the tailpipe [**4**], [**39**]. The removal is completed by reactions, mainly via oxidation and reduction (Redox), which is promoted by applying precious metals as catalysts such as Rhodium (Rh)-Platinum (Pt) or Palladium (Pd) only. TWC can be made from cordierite or metal monolith substrate as a base, and is

subsequently washcoated before the catalyst application using metal oxides. The function of the washcoat is to produce a metal-support interaction between catalyst and substrate, and to prevent or decrease the rate of catalyst ageing. TWC mainly applies a porous-ɣ-alumina (Al_2O_3) washcoat to support precious metals as it is high in porosity, providing a high specific surface area (SSA). Other metal oxides such as ceria (Ce_2O_3), zirconia (ZrO_2) etc. can be used as washcoat or as additives to enhance or stabilise the catalyst. Ceria is a widely used washcoat enhancer, therefore washcoat applied on the TWC has the capacity to store oxygen, which is vital for an excellent TWC operation [**90**].

For maximum TWC conversion efficiency, a narrow range exists in AFR for engine combustion, with maximum chemical equilibrium required to operate as indicated in ***Figure* 1.1**. AFR in the engine periodically fluctuates, hence different conversions happen during different engine conditions. During rich conditions, oxygen stored in ceria will be released and oxidation of CO and HCs will take place (***Equation 2.10*** and ***Equation 2.11***). Concurrently, CO and HCs are eliminated via Water Gas Shift (WGS) and steam reforming respectively, forming CO_2 as a end-product as shown in ***Equation 2.12*** and ***Equation 2.13***. In lean conditions, NO reduction into N_2 occurs through the reaction with CO, HCs and H_2 (***Equation 2.14*** to ***Equation 2.16***) [**4**], [**39**], [**90**].

Utilisation of TWC is possible for stratified-charge combustion but it is only extended to THC and CO emissions due to its overall lean condition. Hence, additional catalytic converters specifically for NO_x emissions must be installed. Two general NO_x aftertreatments have been introduced, the first being a lean-NO_x catalyst and the second, an NO_x trap. Lean-NO_x has a conversion efficiency range between 30 % and

50 % and, restrictively, has operating temperature range is narrow between 180 to 300℃. Given these restraints, the approach has not been considered as workable to achieve the emissions standards in the future [**43**]. Thus, NO_x trap seems to be the preferable approach, with greater conversion efficiency (above 90%) and a wider range of operating temperatures (200 to 550℃). The basic operation of the NO_x trap is to convert NO to NO_2, which is achieved by catalytic absorption during lean conditions. Subsequently NO_2 is released during rich conditions and react with HC, CO and H_2 to produce nitrogen, water and CO_2 as end-products. These processes are periodical, similar to a TWC operations [**91**]. Most importantly, it has close-coupled compatibility to a TWC, allowing control of the cold-start emissions [**43**].

Oxidation

Equation 2.10 $2CO + O_2 \rightarrow 2CO_2$ (**CO Oxidation**)

Equation 2.11 $C_xH_y + \left(x + \frac{y}{4}\right) O_2 \rightarrow xCO_2 + \frac{y}{2} H_2O$ (**HCs Oxidation**)

Equation 2.12 $CO + H_2O \rightleftharpoons CO_2 + H_2$ (**WGS**)

Equation 2.13 $C_xH_y + xH_2O \rightarrow xCO + \left(x + \frac{y}{2}\right) H_2$ (**Steam Reforming**)

Reduction

Equation 2.14 $2CO + 2NO \rightarrow 2CO_2 + N_2$ (**Reduction by CO**)

Equation 2.15 $4HC + 10NO \rightarrow 4CO_2 + 2H_2O + 5$ (**Reduction by HCs**)

Equation 2.16 $2NO + 2H_2 \rightarrow N_2 + 2H_2O.$ (**Reduction by H_2**)

2.2 Particulate Matter (PM)

2.2.1 Introduction and Background of PM

Since the announcement of the *Euro V,* attention has been drawn towards the newly introduced PM mass emission limits. Further revisions of PM emissions were subsequently tightened in *Euro VI* through limiting the PM number, following measurements of PM concentration eight-to-ten times greater in GDI engine tailpipes than PFI engines [**43**], [**92**]–[**94**]. This was emphasised in stratified-charge combustion scenarios, which can emit up to 40 times more PM than homogeneous charge combustion in GDI engines [**43**]. Furthermore, PM was discovered to be smaller in agglomerate size than CI engines PM; considered hazardous to human health [**95**], [**96**]. The hazards pose to human health and environment will be reviewed in *section 2.2.1.2.*

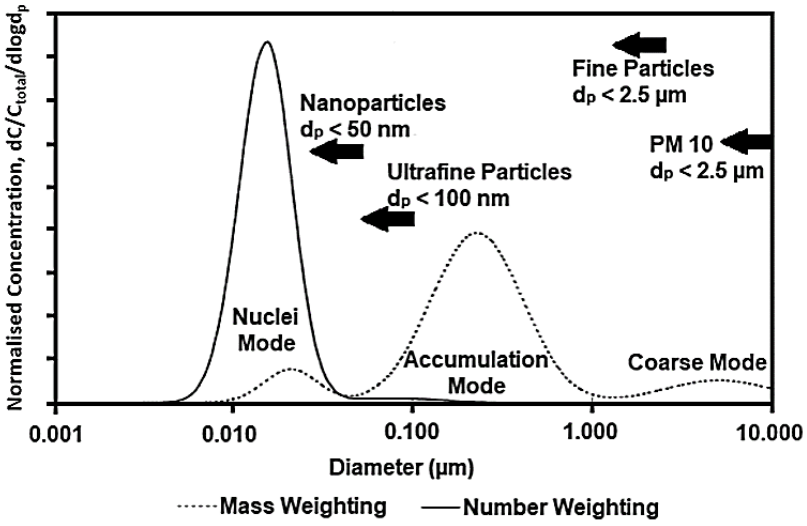


Figure 2.5: Typical particulate size distribution (PSD) in mass and number found in exhaust emissions [**97**].

PM is composed of volatile and non-volatile fractions. Non-volatile fractions are composed of components such as carbonaceous (mainly soot particles) and ash.

Volatile fractions consist of nitrates, sulphates and HCs (organics) which are condensed into particles or absorbed into solid soot particles [**55**], [**97**], [**98**]. According to Kettelson's finding [**97**], PM is categorised into three diameter (d_p) size ranges (***Figure* 2.5**). This includes nucleation mode (dp ≤ 50 nm) particles, mainly the condensed organic volatiles which usually occur in the exhaust system [**4**], may also contain some newly formed solid soot [**99**]–[**101**]. The adhesion of nucleation mode PM onto larger PM can intensify PM toxicity and smog pollution, and can contribute to secondary atmospheric PM formation [**102**]. It is about 1 to 20% of the PM mass, and 90% of PM numbers. Meanwhile, 5 to 20% of the PM mass is accounted by coarse mode (dp ≥ 100 nm), that primarily consists of multiple PM agglomerates. The accumulation mode (50 < dp < 100 nm) commonly seen in grape-like or aciniform form, with irregular shape, forming due to agglomeration of carbonaceous soot primary particles and absorption of volatile fractions.

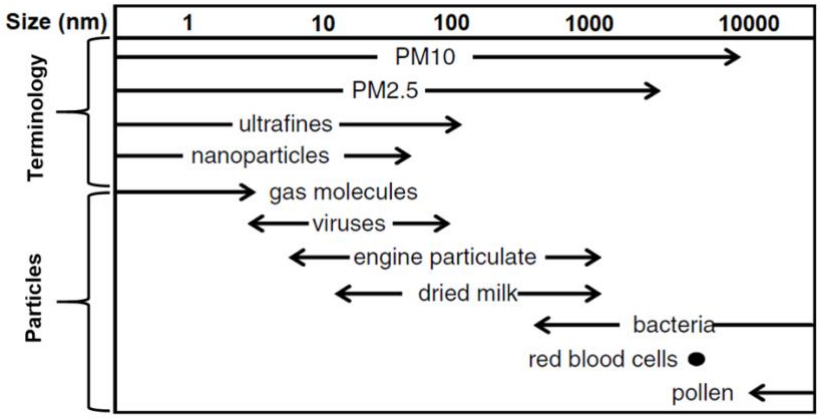


Figure 2.6: AED comparisons to aerosol particle size [**55**].

In the atmospheric aerosol quantitative method, PM agglomerate size is characterised by its aerodynamic equivalent diameter (AED). They are labelled as PM 10, PM 2.5 and PM 0.1 corresponding to d_p < 10 µm, < 2.5 µm and < 0.1 µm

respectively. According to ***Figure* 2.6**, engine PM emissions are one of the major contributors to atmospheric PM. The World Health Organisation (WHO) suggests PM 2.5 is one of the primary causes for approximately 800,000 premature deaths recorded annually, ranking as the 13th leading cause of mortality around the globe [**100**]. Despite smaller PM size posing higher risk to humans, it was claimed that particles equivalent to or smaller than PM 0.1 can only reside for 15 mins in atmosphere. Whereas, particles within the range of PM 2.5 to PM 10 can typically reside for a week. However, smaller particles can prolong residence time by rapid diffusion and coagulation with larger particles [**103**], posing a greater risk to human health.

Typical PSDs measured in CI engines are usually seen in a very distinctive bimodal, with a mean particle size of 30 nm and 200 nm respectively for nucleation and accumulation mode particles [**90**]. Contrarily, SI engines are less defined, in a way that both nucleation and accumulation mode particles are overlap. This makes measuring PSD in GDI engines more challenging [**104**], as the PM nature is composed of a higher volatile fraction in comparison to PM emitted by CI engines [**92**], [**105**], [**106**]. This was demonstrated to increase with the use of second generation GDI engines (spray-guided), depending on the operating conditions [**56**], [**107**]. This was due to second-generation GDI engines being less prone to fuel impingement and hence, leading to reduced soot formation [**40**]. Consequently, leading to a greater concentration of nucleation mode PM, and altering the accumulation mode PM due condensation and adsorption of volatiles. These processes exclusively occur when the temperature drops below the dew point (saturation temperature) [**55**]. This frequently takes place in the exhaust system as EGT drops, or during dilution at post-tailpipe.

Therefore, it is extremely important to note the precise procedures during experimentation.

2.2.1.1 Formation of PM

The formation of PM originates from 4 types of sources; (*i*) fuel, (*ii*) lubricant, (*iii*) air and (*iv*) material breakdown in the engine [**104**]. The main source of PM is from fuel during elevated load, abrupt acceleration and cold start conditions [**5**], [**108**], [**109**]. Principally, PM is formed because of direct carbonisation of unburned fuel droplets [**56**] and incomplete combustion [**110**], [**111**]. This leads to yellow diffusive pool fires in the rich fuel pocket and fuel film [**80**], [**112**]–[**114**]. The droplets, rich fuel pockets and fuel films can be attributed to several factors including [**113**], (*i*) poor fuel vaporisation due to injector deposit choking, (*ii*) fuel impingement on the engine top, cylinder wall and piston top and (*iii*) inhomogeneous air-fuel mixing. There are suggestions to minimise the formation of PM, which can be performed through engine design and operations [**115**] (*i*) air delivery, (*ii*) fuel delivery, (*iii*) combustion control and (*iv*) engine parameters conditioning. The enhancement largely emphasises better air-fuel mixing processes. Additionally, the improvements can also be implemented at the exhaust system, such as installing hot exhaust manifolds to promote PM oxidation and the application of aftertreatment like particulate filters. ***Table* 2.2** is the summary of PM sources and potential strategies for improving PM emissions.

Thermodynamically, PM should only form when the carbon-to-oxygen ratio (C/O) exceeds unity, resulting in *m* becoming larger than *2y* as shown in **Equation *2.17*** [**116**].

Equation 2.17 $$C_m H_n + y\ O^2 \rightarrow \frac{n}{2} H_2 + (m - 2y)\ C_s$$

Table 2.2: Summary of PM source and proposed improvement.

Source [**56**], [**80**], [**110**]–[**114**]	**Proposed Improvement** [**115**]
Direct carbonisation of fuel and diffusive yellow flame combustions. (i) Poor Vaporisation (ii) Fuel Impingements (iii) Inhomogeneous Air-Fuel Mixing	(i) Air Intake - Ensure sufficient air for combustion - Increase intake air temperature - Optimising valve overlapping and residual gas mixture (ii) Fuel Injection - Optimising spray pattern - Increase injection pressure to reduce fuel impingements and to atomise into small droplets - Increase fuel temperature for better vaporisation - Adopting split injection strategy - Increase precision on global air-fuel ratio (iii) Combustion Control - Optimising charge motion level - Ensure sufficient air-fuel mixing to prevent rich mixtures - Increase intake charge temperature - Spark timing optimisation (iv) Engine conditioning - Warm cylinder wall - Reduce oil layers in cylinder - Preventing introduction of intake system deposits and oil residuals from venting system. (v) Exhaust System - Hot exhaust manifold for better PM oxidation - GPF application

Formation of PM is dependent on the surrounding temperature, as well as the equivalence ratio at the critical sooting threshold ($\phi_{Critical}$). Despite numerous

publications, no defined standard exists for the temperature range and $\phi_{Critical}$. *Steimle et al.* [**113**] suggested the PM formation process occurs in the temperature range of 1700 and 2600 K, and $\phi_{Critical}$ at approximately 2 [**117**]. *Hageman et al.* [**118**] observed PM is likely formed between 1400 K < T < 1700 K, and 1.3 < $\phi_{Critical}$ <1.4. However, PM formation is inhibited as soon as temperature exceeds 2200 K due to the oxidation of PM precursors. Contrarily, *Kittelson et al.* [**97**] proposed a temperature range of 1400 K < T < 2000 K and $\phi_{Critical}$ > 1.4. Additionally, PM oxidation outweighs PM formation during stoichiometric and lean conditions, at maximum rate for T > 2000 K. This indicates PM is unlikely to form during early combustion, and more likely to form at the end of combustion, or marginally after the main combustion by the reaction of PM precursors. These precursors are mainly HCs forced into the crevice volume during the compression stroke. As cylinder pressure is relieved, HCs re-enter the combustion chamber (in close proximity to the cylinder wall) within the temperature range. However, the PM formation process will not develop during the exhaust stroke, or in the exhaust system, due to insufficient energy (insufficient temperature) for oxidation or formation to take place [**98**]. Published results from the literature may not be contradictory but may reflect variation of engine speed and load. PM formation is affected by temperature, pressure and residence time [**119**]. Consequently, shifting the formation temperature and $\phi_{Critical}$ leads to compromise between oxidation rate of precursors, and PM formation [**120**].

PM emitted by SI engines are comparable to CI engines by evaluation of the chemical composition and morphological analysis [**121**]. Therefore, it was proposed that the formation of PM for both SI and CI engines are formed through similar processes [**122**]. Several publications advocate the same mechanisms for PM

formation [**112**], [**113**], [**118**]. These mechanisms include (*i*) inception, (*ii*) nucleation, (*iii*) growth, (*iv*) agglomeration, (*v*) carbonisation and (*vi*) oxidation [**4**], [**55**], [**80**], [**116**], [**123**], [**124**].

The ***Inception*** stage involves fuel pyrolysis occurring thermally and oxidatively. The process requires high pressure and temperature conditions to generate PM precursors, known as polycyclic aromatic hydrocarbon (PAH). Key intermediaries for formation of PM is the aromatic ring/benzene (C_6H_6). Thermal pyrolysis occurs when the surrounding conditions are anoxic (no oxygen) and the temperature exceeds approximately 673 K [**80**]. This is a dehydration reaction requiring high activation energy, resulting in H, OH, methyl (CH_3) radicals and some other aliphatic compounds. These compounds are composed primarily of various decomposed HCs from parent fuel molecule with low molecular weight fragments (lighter HCs ≤ C4 group) [**113**], [**116**], [**125**], such as methane (CH_4), acetylene (C_2H_2), ethylene (C_2H_4), propynyl (C_3H_3), propane (C_3H_6) and butadiene (C_4H_6) [**112**], [**116**], [**126**], [**127**]. Oxidative pyrolysis occurs during oxygen deficient conditions, within 1900 K < T < 2300 K [**112**]. Similar HCs aliphatic compounds are formed [**125**], [**128**], in conjunction with the formation of CH_3 and ethyl (C_2H_5) radicals [**113**] due to the reaction process with H, OH and O [**116**]. The HC aliphatic compounds and radicals are thermally stable but extremely reactive. This is proceeded by a Hydrogen Atom Transfer (HAT) reaction between small radicals and large molecules to form larger and higher stability radicals [**125**]. Following this reaction, the highly important acetylene forms the first aromatic ring, illustrated in ***Figure* 2.7** [**129**].

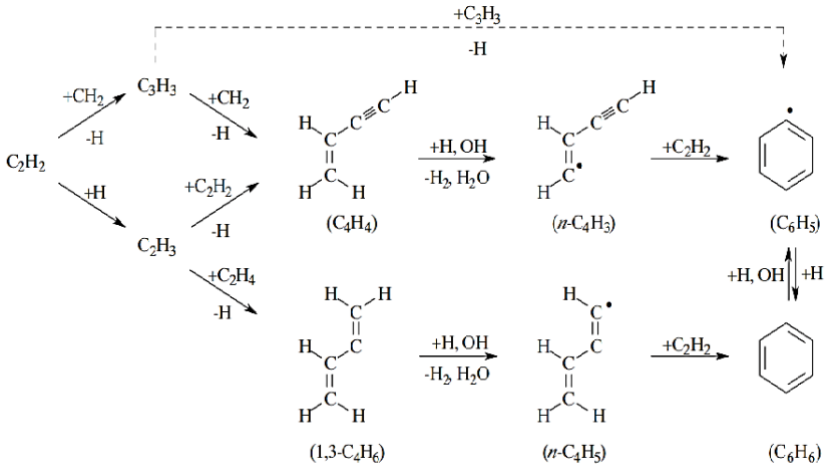


Figure 2.7: Suggested first benzene ring formation pathway [**129**].

The further growth of aromatic rings to PAHs is hypothesised to happen through two different processes; hydrogen abstraction–acetylene addition (HACA) and ring-ring direct condensation shown in ***Figure* 2.8** and ***Figure* 2.9** respectively. The HACA process requires activation by hydrogen abstraction to produce a PAH radical, and acetylene is subsequently added to aid the development and cyclisation of the aromatic ring into a larger PAH [**129**], [**130**]. Ring-ring direct condensation (PAH-PAH radical combination) takes place when the aromatic ring concentration is sufficient under limited acetylene conditions. The process requires the formation of biphenyl formed by benzene and phenyl, allowing it to proceed with HACA or benzene to form three-ring phenanthrene or four a ring aromatic [**129**]. However, the competition between the two processes is determined by the ratio of acetylene to benzene. When the ratio approaches or exceeds one, then HACA will be dominant and vice-versa.

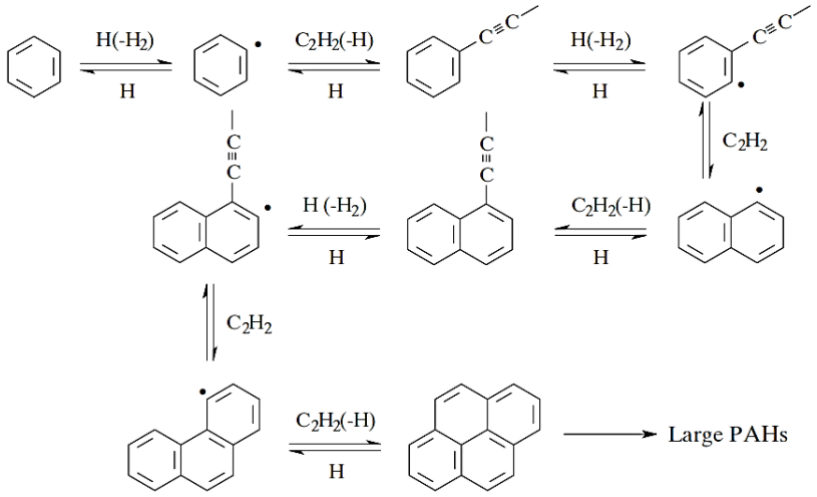


Figure 2.8: Pathway for PAH growth via hydrogen abstraction–acetylene addition [**129**].

Since the growth processes are reversible, decomposition of PAHs can be initiated when temperatures are greater than 1800 K. Not all PAHs are PM precursors. As reported *Mansurov* [**131**], only PAHs weigh between a molecular mass of 500 and 1000 atomic mass units (amu) are more likely to form PM.

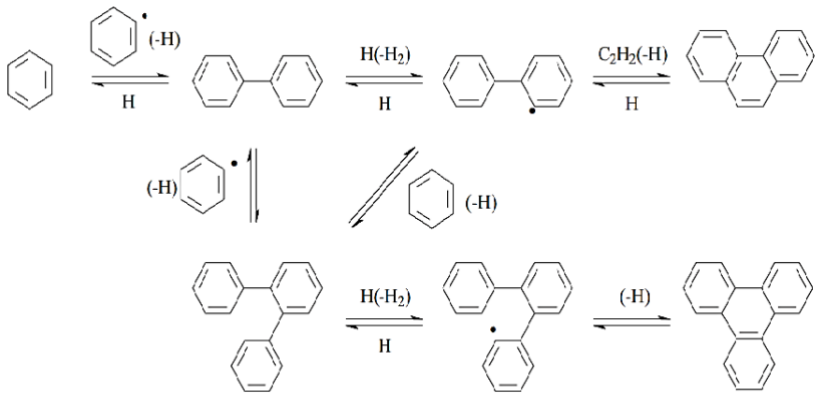


Figure 2.9: Ring to ring direct condensation pathway for PAH growth [**129**].

The following process is the ***nucleation*** stage. Once PAH growth exceeds four-ringed or larger [**80**], the first identifiable primary particle (formed around 5 nm to 30nm)

is observed and is referred to as the nuclei [**112**]. This can take place homogeneously or heterogeneously, corresponding to the same form (liquid and liquid) or mixed form (solid and liquid) [**132**]. Several theories exist on formation of PM nuclei; broadly categorised into direct or indirect routes [**4**]. The direct route is a condensation process and is usually more rapid, whist the indirect route requires a longer formation time - such as radical addition, PAH and polygene modelling theories. *Graham et al.* [**133**] suggested PAHs are condensed into graphite-like structures; occurring without alteration or breaks in the aromatic structure when T < 1800 K. Other studies propose an alternative course; through condensation of large PAHs in gas form into liquid microdroplets. This occurs due to the instability when approaching supersaturation point (during temperature decrease) and subsequent carbonisation into nuclei [**134**]. These two theories were believed to be associated to the PM formation due to direct carbonisation of fuel droplets as aforementioned (***Table* 2.2**).

Siegmann et al. [**135**], proposed nuclei formation under high pressure occurs via rapid chemical condensation of radicalic or reactive molecules, whilst the indirect PAHs model theory is more favourable for low pressure conditions. The commonly accepted hypothesis for nuclei formation is the indirect route, radical addition theory. The theory associates growth of PAHs into larger clusters by aliphatic HC compounds, forming nuclei once the cluster grows between temperatures of 1300 K < T < 1600 K [**126**], [**130**]. The PAH model and polyene model describe two indirect routes which depend on the molecular precursors present. In the PAH model, two large PAHs monomers are stacked together through collision, in sandwich-like form, by van-der-Waals forces to form a PAH-dimer [**130**], [**135**]. The dimers collide with PAH molecules or dimers to form PAH-trimers or PAH-tetramers, and rapidly turn into solid particles

as size increases [**136**]. Under the polyyne model hypothesis, every gas-phase radical has the capability to form polyyne complex. This occurs by fast polymerisation of supersaturated polyyne vapour, leading to PM nuclei. The polyyne complex is formed by the reaction between polyyne molecules and polyyne radicals, or both polyyne molecules [**130**], [**137**]. Despite these aforementioned theories, PM formation is a highly endothermic reaction. Physical condensation cannot explain the high activation energy [**138**], and it is believed that many chemical processes are simultaneously taking place during this stage of PM formation [**55**].

Particle growth is a process that occurs through two mechanisms; growth by surface and particle coagulation. The former involves addition or adhesion of gas phase species [**116**] (primarily acetylene and PAH species) [**112**], [**113**], [**130**]. These species exhibit a carbon-layered microstructure (graphene fringe layers) of the outer shell in nanoscopic magnification [**55**]. The outer-layer appears to be more ordered in structure in comparison to carbon layers in the core (nuclei) [**139**]; altering the surface reactivity of the particle [**140**]. Surface growth simultaneously occurs with the nucleation process [**141**]. The process significantly affects the PM mass, however does not affect the PM number [**113**], [**116**], [**134**]. To date, the process is not fully understood, however it appears that particles can be chemically bonded or physically adhered.

In the chemical bonding concept, *Frenklach et al.* [**142**] attributed surface growth to the HACA mechanism, similar to the inception process. It is thought that fresh nuclei are large molecules identical to PAH edge sites, covered with multiple C-H bonds. Hence, abstracting hydrogen will lead to the formation of active sites, forming surface

radicals. The release of the free radicals allow PAHs species to chemically bond, promoting surface growth [**130**].

Physical adhesion, known as direct condensation, is where gas-phase PAHs molecules are directly accumulated onto the nuclei [**80**], [**140**], [**143**]. The collision is thought to take place during the nucleation/surface growth process, immediately after PM nuclei formation [**113**], [**144**]. It was thought to happen during nucleation/surface growth process immediately after PM nuclei formation [**134**], [**145**]. Occasionally, part of the primary particle is unobservable in TEM, due to the merging of two nuclei into one [**130**]. In this scenario, the overall PM number decreases whilst mass is maintained [**124**], [**130**] and the effective diameter of particles will increase [**116**].

Once the coagulated PM matures and becomes more viscous, ***agglomeration*** between coagulated nuclei is initiated. This forms an irregular, loose-structured, agglomerate with fractal like geometry (aciniform) [**112**], [**113**], [**138**], [**144**], without drastic changes to the total surface area [**144**]. Agglomeration is a synchronised process that occurs mainly within the exhaust stream, with surface growth and oxidation simultaneously taking place. The stages in which particle coagulation and agglomeration occur is distinctive. Coagulation takes place when particles are new, whereas agglomeration takes place during the later stages of maturation. Matured particles exhibit ‘non-coalescent’ form, whilst the viscid and tarry nature in newly formed particles result in the ability to fuse easily [**55**].

Carbonisation occurs during the later stages of PM formation, and is assumed to occur simultaneously with agglomeration [**146**]. This stage primarily increases the structural order of the graphene layer located on the outer shell of particles, leading to

some loss in PM mass without affected the PM number. Based on the theory proposed by *Xi et al.*[**130**], mass loss occurs due to elimination of the functional group, cyclisation, ring condensation and ring fusion. This is accompanied by the dehydrogenation process, and the growth and alignment of polyaromatic layers.

PM ***oxidation*** is a heterogenous, oxidising process for PAHs species and PM particles [**147**]. Oxidation is a kinetically controlled process, occurring any time between inception and agglomeration of a particle [**4**], [**55**]. Main oxidising agents are OH, O and O_2, some agents contributing to oxidation process are CO_2, NO, N_2O, NO_2 and H_2O [**113**], [**130**]. The dominant oxidiser is dependent on the ϕ [**148**]; OH is the main oxidiser in fuel-rich conditions ($\phi > 1$). Contrarily, O_2 is the main oxidiser for fuel-lean condition ($\phi < 1$). Generally, oxidation is a two-step process comprising of the transfer of oxygen atoms onto PM surfaces by chemical attachment, forming a solid complex. This is followed by a reaction with carbon atoms originating from PM, desorbing from the surface as by product (CO and CO_2) [**149**]. The full or partial oxidation of PM is a non-reversible process. This is especially relevant to CO, which will not reform into PM even under fuel-rich conditions [**113**]. The PM emitted by the engine is a direct compromise between oxidation and formation. Realistically, more than 90% of the PM formed is depleted by the process of combustion [**55**]

2.2.1.2 Impact of PM

The introduction of PM limits in the *Euro* legislation originates from concerns regarding the adverse impact on the environment and human health. In environmental terms, PM has been evidenced to lead to global warming [**150**]–[**152**]. It has been reported to be the second most important contributing factor after CO_2 [**153**]. A large quantity of published research details a large array of environmental impacts. Critically,

this includes evidence of increased absorption of solar radiation that has led to a net increase of atmospheric temperature. Moreover, accumulation mode PM and smaller (< PM 2.5) is broadly equivalent to the wavelength of light; resulting in light dissemination and the production of haze (low visibility) [**152**], [**154**]. Other negative environmental impacts include infrastructural damages through the effect of building soiling and acid rain from PM pollution [**152**], [**154**]. The environmental consequences of PM are also exacerbated, as pollutants can be dispersed very long distances through wind and water. The Environment Protect Agency (EPA) of the United States [**152**] reported increasing acidity in lakes and streams, disruption in water nutrient balance, reducing nutrients in soil, ecological disruption to fauna and flora, and reduced diversity of ecosystems..

The potential health repercussions of PM is assumed to be the primary driving factor that led to the emergence of *Euro VI* emissions legislation. As a response, the EU commission proposed defined limits based on PM concentration (6×10^6 #/km). Attempts to enforce these restrictions follow evidence that suggests that human health is directly impacted by PM number, rather than PM mass [**55**]. The evidence is based on emissions from CI engines [**112**], which have been labelled as carcinogenic in June 2014 by the WHO [**113**]. The degree of severity is highly dependent on the residence time in the atmosphere and lungs, the rate of penetration into the human body, penetration depth and its toxicity. These parameters are strongly influenced by the morphological and chemical characteristics of the PM, as well as particle size and specific surface area [**155**]–[**157**]. *Seaton et al.* [**158**] demonstrated that smaller PM is more hazardous, as it penetrates deeper than larger particles. The research illustrated that ultrafine PM can transfer into the bloodstream, penetrating deeper into the lungs

before deposition [**55**]. This results in subsequent spreading to other organs, such as the liver and brain [**159**], causing cardiopulmonary inflammations and diseases (respiratory and cardiovascular), which is evidenced to increase the likeliness of premature death and worsened allergies [**154**], [**160**], [**161**]. Respiratory problems such as asthma and bronchitis are also associated to respiratory diseases caused by PM [**160**], [**162**]–[**164**]. Research published by *R.Jahn* [**165**] evidenced that Nano sized PM can reach lung alveoli, leading to the failure of self-cleaning process by macrophages. In addition, cardiovascular complications such as heart and cerebrovascular diseases may occur if PM in the bloodstream result in blockages to the arteries [**166**]–[**169**]. Other publications cite direct correlation between PM and lung cancer, due to body cell mutations after long term exposure [**170**]–[**173**].

2.2.1.3 PM Control Technologies

Gasoline Particulate Filter

Possible approaches designed to reduce PM is tabulated in ***Table* 2.2**. Out of these approaches, GPF appears to be the most feasible. Generally, GPFs are modelled on the design of the diesel particulate filter (DPF). However, optimisation is required due to lower concentrations and smaller PM emitted by GDI engines. A particulate filter is usually made out of Cordierite and SiC, in the form of a wall-flow 'honeycomb' design consisting of many parallel channels alternatively plugged at the end of the monolith substrate (***Figure* 2.10**) [**174**]. The GPF design is based on a model of a unit collector filtration system, comprised of three main mechanisms [**174**]. These mechanisms are; *Brownian Diffusion*, *Inertia Impaction* and *Direct Interception* illustrated in ***Figure* 2.11** [**174**]–[**176**]. Although there are other mechanisms that occur during the filtration process, such as *Thermophoresis, Electrostatic Force Attractions*

and *Sedimentation* (gravitational force effect), they are neglected due to their negligible involvement [**175**].

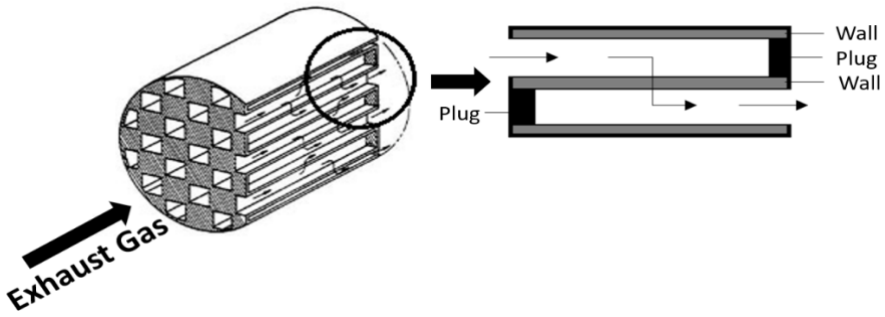


Figure 2.10: Schematics of wall-flow honeycomb of a particulate filter.

Particle movements formed from *Brownian diffusion* are characterised by *Peclet* number (Pe), occurring due to gradients in particle concentrations between the bulk flow and power walls of the filter [**174**]–[**176**]. This is experienced by smaller particles, and can be influenced by gas flow rate and particle size. This mechanism is due to adhesion of particles in random motion, induced by the *Brownian motion* - favouring low flow rates and smaller particle diameter. *Inertia impaction* is a mechanism caused by inertial force, when particles are unable to follow the abrupt streamline variation. Therefore, particles deviate from the streamline and into the filter. *Stokes' number* (Stk) is applied to characterise this mechanism, peaking when filter porosity is at a minimum under high flowrate conditions. Finally, *Direct Interception* is the ratio between particle diameter and the characteristic length of the filter. Particles under this mechanism are deposited in the filter when following the streamline but pass within one particle radius of the collection body.

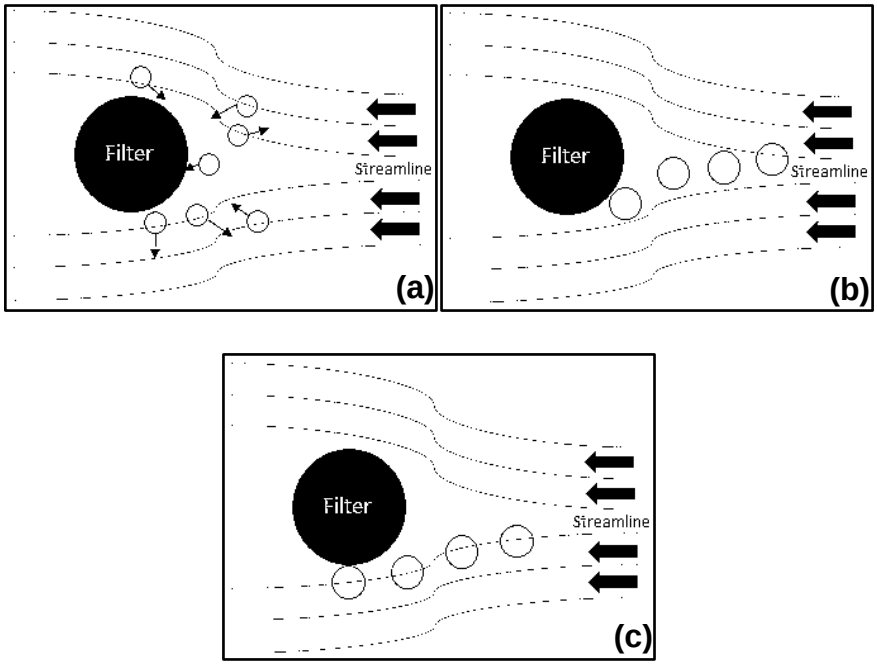


Figure 2.11: Filtration mechanisms of particulate filter **(a)** Brownian diffusion **(b)** inertia impaction **(c)** direct Interception.

A region exists where filtration efficiency is minimal, commonly reported within the accumulation mode PM range of 50 nm ≤ d_p ≤ 500 nm [**177**]. It is known as *Greenfield gap* (shown in ***Figure* 2.12**). It is claimed that particles within the mentioned range are too heavy for the *Brownian diffusion* mechanism to operate, and are too light to produce enough inertial force for *Inertia Impaction* or *Direct Interception* mechanisms to take place effectively [**35**], [**178**]. The *Greenfield gap* effect can be mitigated against by two factors; filtration velocity ($U_{filtration}$) and Mean Pore Size (MPS) [**179**]. Decrease in $U_{filtration}$ can lead to a longer residence time of particles in the filter and boost *Brownian diffusion*. Whereas, a filter designed with a small MPS can also improve the filtration through decreased particle penetration. However, the peak of the *Greenfield gap* may vary.

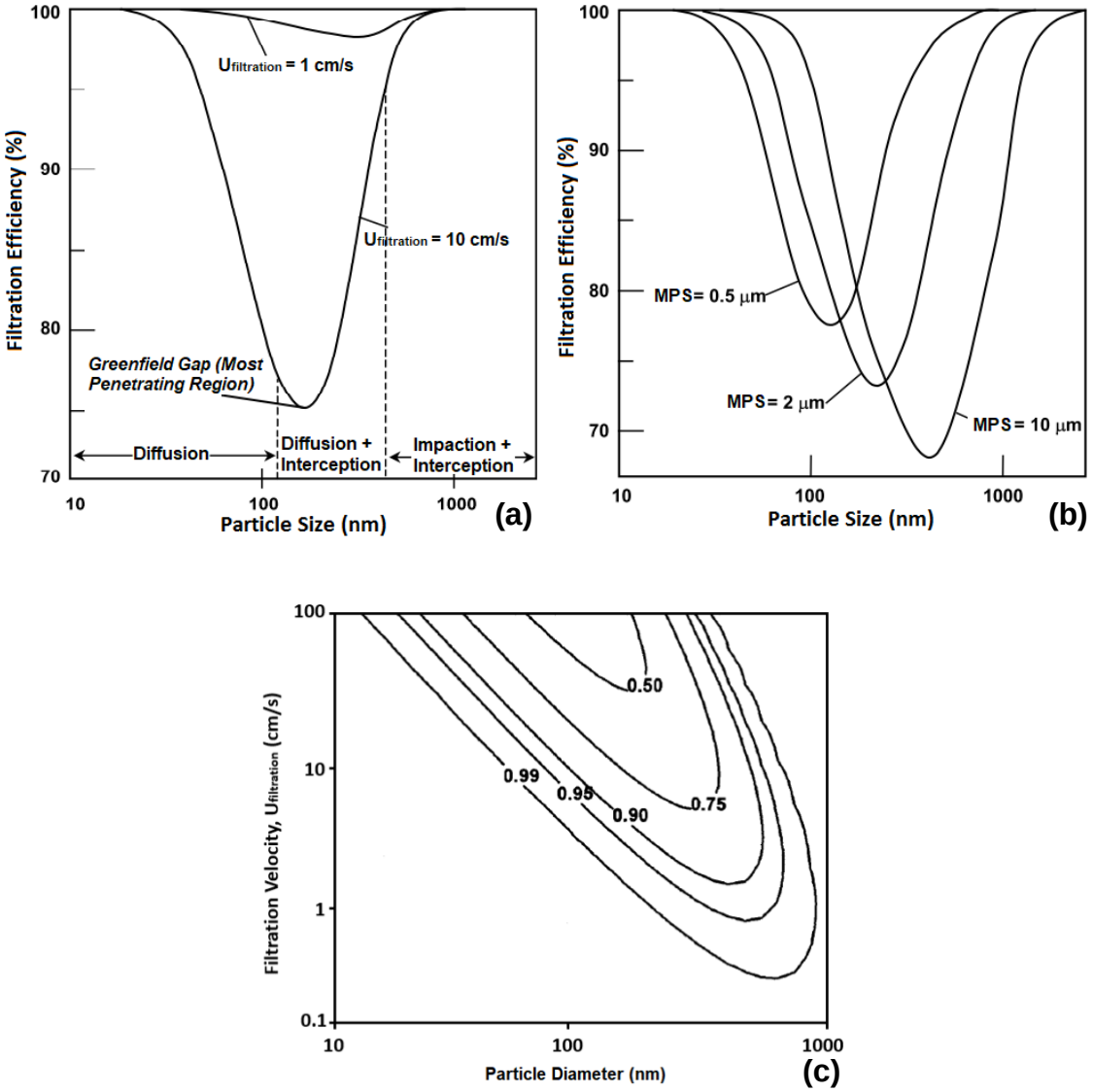


Figure 2.12: Greenfield gap in typical particulate filter influenced by **(a)** filtration velocity **(b)** mean pore size and **(c)** is overall filtration efficiency of DPF [**175**], [**179**].

Even if the *Greenfield gap* region does exist, it will gradually reduce, and later disappear proportionally to exhaust gas exposure time. The improvement is associated to PM accumulation on the filter. Accumulations fill the porous medium, resulting in the creation of a PM cake layer on wall channel surface that takes over the filtration function [**7**]. ***Figure* 2.13*a*** illustrates 4 accumulation phases for PM layer formation.

These phases are also directly correlated to the induced back pressure, known as pressure drop (***Figure* 2.13*b***).

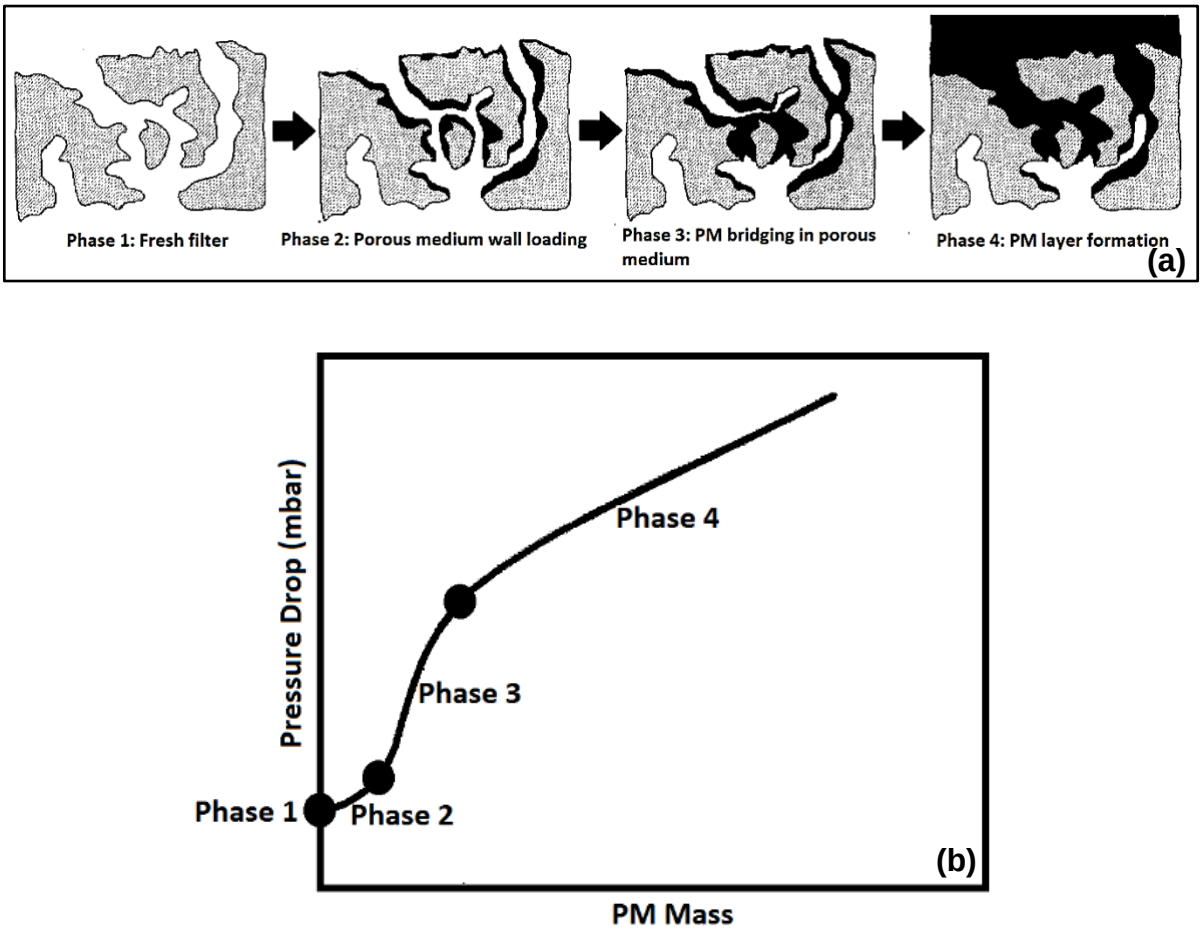


Figure 2.13: (a) Conventional PM layer formation on particulate filter **(b)** pressure drop concept of particulate during PM layer formation.

Phase 1 illustrates the interval where the particulate filter is fresh and the lowest back pressure is induced. Subsequently, phase 2 and 3 reflects the loading of the porous medium wall; where PM starts to form a bridge across the pores. These two phases are the primary factors influencing the non-linear rapid increase of back pressure, due to flow restriction as pores become plugged.

A thin PM cake layer begins to form in phase 4, shortly after phase 3. As the thickness of the PM cake layer grows, a greater pressure drop is induced and continues in a linear fashion throughout phase 4; from which the thickness can be estimated. The PM cake layer enhances the filtration process by subsiding the particle penetration. However, this can be undesirable due to the increase of back pressure, leading to deterioration of engine performance (fuel economy and power output). For example, *Saito et al.* [**7**] observed a drop in fuel economy during high speed and load conditions. *Richter et al.* [**180**] reported no difference in fuel consumption under NEDC and United States Federal Test Procedures (FTP). Whereby, *Ito et al.* [**181**], found a loose correlation between pressure drop and fuel economy under NEDC and WLTC tests. The power output was measured to be marginally lower, as the pressure drop magnitude increased [**180**], [**181**]. However, studies suggest that the application of turbochargers in engines can compensate for power loss caused by the pressure drop effect [**181**]. Based on the previous research, the importance of maintaining a balance between excellent filtration and low pressure drop of a particulate filter is key to maintaining vehicle performance at its peak in accordance with *Euro* emissions legislation.

Multiple Injections Strategy

The aforementioned multiple injection strategy can be used to reduce gaseous emissions. It is also capable of reducing PM emissions in accordance with the *Euro VI* limits in the absence of a GPF; namely *BlueDIRECT* engines by Mercedes-Benz [**89**]. Many previous publications have demonstrated reductions of PM emissions emitted by GDI engines across the engine map [**182**] as well as during warm-up conditions [**86**]. This has been regarded as a highly effective method [**183**].

The theory behind this approach involves splitting a single injection into two, or several injections with a reduced fuel quantity. This can reduce the penetration length of the fuel injection spray, and achieve greater homogeneity in the fuel mixture [**80**]. As a consequence of these modifications, the methods intend to reduce fuel impingement on the cylinder top and wall, and develop fewer fuel-rich regions in the combustion chamber. *Whitaker et al.* [**184**] demonstrated that multiple injections can significantly lower PM formation during combustion, showing agreement with *He et al.* [**5**] who reported more than 50% reduction in PM formation. Other research conducted by *OudeNijeweme et al.* [**185**] reported more than 80% reduction in PM emissions during the first 200s of NEDC. A certain reduction was also observed during steady state testing. Additionally, the research illustrated that increasing the number of injections with decreased fuel quantity reduced PM emissions by 60% and 80%, as injections were split into two and three respectively [**186**].

2.3 State-of-the-Art

The following section will review relevant literature detailing combustion characteristics and gaseous emissions in air-fuel ratio and DMC. The main focus of the review is centred on recent technological advances and their influence on PM emissions and characteristics.

2.3.1 Combustion and Gaseous Emissions Characteristics

By the Effect of Air-Fuel Ratio

Generally, λ studies in SI engines are well established. Lean combustion is generally still favourable for its efficiency in fuel economy and engine efficiency [**187**]. There is a distinctive trend of combustion stability and gaseous emissions as the λ gets leaner or richer. Combustion stability improves (reduction of COV_{IMEP}) with decreasing λ. Conversely, combustion stability deteriorates when λ increases. A lean limit defined by the COV_{IMEP} at approximately 5%. Excess air in the combustion chamber dilutes the combustion process in a leaner mixture, leading to longer combustion duration [**4**], [**188**], [**189**]. It is attributed to the longer ignition duration (MFB0 to MFB10), indicating a slower flame speed and instability during early flame development. It is also reflected in the CAD of the rate of heat release (RoHR) [**190**]. Greater thermal efficiency is achieved under leaner combustion as the specific ratio of heat (ɣ) is increased [**191**] and impacted by the longer combustion duration [**192**]. Contrarily, the opposite effects are present during richer combustion.

In the case of gaseous emissions, CO_2 and NO_x will surge during lean combustion. An increase in CO_2 is expected when THC and CO emissions are reduced. This is due to excess air in the combustion chamber, (i) promoting a more complete combustion reaction and (ii) the enhancement of THC and CO during post-combustion oxidation [**189**], [**191**], [**193**]. The presence of excess oxygen in the combustion chamber, in conjunction with sufficiently high temperature, results in a higher rate of NO_x formation [**189**], [**191**], [**192**]. Furthermore, longer combustion duration increases the residence time in the combustion chamber, boosting formation rate [**189**].

By the Effect of Di-Methyl Carbonate

In the past, DMC has been comprehensively evaluated in CI engines. However, uncertainties still exist in SI engines due to limited literature. Studies show that use of DMC in SI engines can achieve positive results, by obtaining higher indicated mean effective pressure under lean combustion when compared to ethanol and ETBE [**194**]. It was attributed to a faster flame speed of DMC promoting isochoric combustion. Additionally, *Gopinath et al.* [**195**] achieved an improvement in thermal efficiency from enhanced combustion through increased oxygen and RON.

In the case of emissions, oxygen contributed by DMC promotes more complete combustion, resulting in less THC and CO production [**32**], [**195**]. Experiments conducted by *Wen et al.* [**32**], NO_x reduction is only observed during near stoichiometric combustion mode; justifying lower flame temperature. Contrarily, *Gopinath et al.* [**194**].] measured more NO_x emissions when in-cylinder temperatures were higher; attributed to improvement in combustion. In comparison, *Alzueta et al.* [**15**] kinetic modelling study reported no observable changes in NO_x during lean and stoichiometric combustion. This was attributed to the reaction between key species (ketenyl radicals (HCCO) and NO_x), which are only active during rich combustion. Although HCCO were also present during stoichiometric combustion, but the presence of oxygen resulted in the oxidation of HCCO.

2.3.2 PM Characteristics

2.3.2.1 PM Nature

PM Microstructure and Nanostructure

The visual nature of PM formed in GDI engines are usually aciniform, or grape-like, exhibiting similarity to PM formed in CI engines [**196**]. However, the microscopic and Nanoscopic assessments of PM varies according to engine conditions and the fuel blend used. From a micro-scale view, it is reported that PM can be composed of (i) fractal-like PM, (ii) spherical, or sub-spherical volatile droplets (formed by HCs), (iii) small agglomerates comprised of tiny primary particles (approximately dp_0 = 6 nm), (iv) fractal-like PM with presence of HCs and (v) small spherical PM [**8**], [**197**]–[**199**]. In addition, traces of other elements were detected such as P, S, Ca, Zn, Mg, Mo, Na, Fe, Cr, Al and Cu, which are sourced from engine additives, lubricants and metal wear [**200**], [**201**]. These agglomerates are made up of primary particles, formed by collisions, during the agglomeration stage of PM formation [**196**], [**197**], [**200**], [**202**], [**203**]. The range of dp_0 is between 5 nm and 65 nm [**204**], [**205**].

Radius of gyration (R_g) is the average distance between the centroid of agglomerate to the centre of each primary particle. The range of R_g acquired by the literature, is measured approximately between 5 nm and 400 nm for GDI engine PM [**8**], [**199**], [**202**], [**206**]. Fractal dimension (D_f) assesses the shape of PM agglomerates to determine the type of collision that has taken place during agglomeration process [**199**], [**207**]–[**209**]. There are two methods that have been proposed to study the D_f; (i) the linear regression method [**8**], [**199**], [**210**], [**211**] and (ii) root form factor (RFF) [**8**], [**199**], [**202**] which will be elaborated in *3.8.3.5 Fractal Dimension (Df)*. The range is reported; $1.44 < D_f < 2.39$ and $0.29 < RFF < 0.4$ respectively for both methods. In

regards to Nanostructure, PM primary particles are observed to have similar appearance to PM formed in CI engines [**212**]. The structure contains an (i) inner core (concentrated graphene layers with a turbostratic structure, or amorphous graphene layers), (ii) outer shell middle onion-like structure with orderly, structured graphene layers containing a minor fraction of amorphous graphene and (iii) a coating of amorphous ring (HCs layer) [**200**], [**202**], [**205**], [**213**]–[**216**]. PM primary particle formation is initiated with the inception of amorphous graphene layers. This is subsequently crystallised into more ordered structure of graphene layers, under the exposure of heat towards the nucleus from the 'outside-in'. This is followed by HC absorption and condensation, resulting in the final amorphous coating on the particle [**217**]. In general, the graphene layer characteristics are often assessed in Nanostructural analysis by the fringe length (L_a), fringe tortuosity, and fringe layer distance.

PM Oxidation Reactivity

Investigations into PM oxidation reactivity is measured by its activation energy (E_a), via a ramp programmed study, or measured by the time taken for PM to completely oxidise with an isothermal study. These methods are crucial for designing GPF regeneration strategies. Comparisons have been made between PM formed by GDI and CI engines, that have indicated that PM from GDI engines have greater reactivity [**196**],[**218**]. Publications have reported that E_a of CI PM falls into the range of 100 to 300 kJ/mol [**219**]. Whereas the window for GDI PM has been measured at 125 kJ/mol < E_a < 256 kJ/mol. The literature reports that E_a is subjected to engine operating conditions, fuel, PM collection methodology and evaluation [**205**], [**217**], [**218**], [**220**]. Therefore, other factors may influence oxidation reactivity. Through visual

assessment, theories relating to the influence of PM oxidation reactivity in CI engines can be adopted for GDI.

PM Oxidation Reactivity Effects upon Microstructural Characteristics

In terms of the microstructure scale, the effect of PM oxidation reactivity is related to specific surface area (SSA), linked to dp_0, R_g and D_f. Numerous studies have proposed that the alteration of dp_0, R_g and D_f is influenced by different engine operating conditions and fuel type used. Studies conducted by *Lapuerta et al.* [**211**] and *Rodriguez-Fernandez et al.* [**221**] reported an improvement in PM oxidation reactivity. The studies show that smaller average dp_0 and R_g have higher SSA for contact with oxidisers, resulting in enhanced oxidation. Moreover, lower D_f agglomerates (more chain-like agglomerates) also exhibit higher SSA, containing a more open configuration (more exposure) with respect to higher D_f (more compact clustered agglomerates) [**222**], [**223**].

PM Oxidation Reactivity Effects upon Nanostructural Characteristics

The Nanostructural effect on PM oxidation reactivity is strongly linked to the graphene layer variation in L_a, fringe tortuosity and fringe distance separation. Nanostructural analyses can provide an understanding on how the carbon atoms located in both basal plane and edge site can affect the oxidation reactivity. Carbon atoms at the edge site are found to have greater reactivity, approximately 100 to 1000 times more than carbon positioned in basal plane [**224**]. The metric value of L_a is an indication of the carbon atom ratio present at the edge site and basal plane (C_{edge}/C_{basal}). Therefore, PM with shorter L_a exhibits rapid oxidation compared to PM that possess longer L_a [**149**], [**224**]. The variation in oxidation rate is related to carbon atoms at the edge site being bonded by unpaired sp_2 electrons, which are prone to attachment

by oxygen molecules. Conversely, chemical bonds formed between atoms in the basal plane share π electrons (stronger bonds). Furthermore, the edge sites are more exposed; accessible for oxygen reaction.

Fringe tortuosity measures the curvature of the graphene layer. Amorphous concentrations of PM can be referred to the width of distribution and mean value of magnitude of curvature (fringe tortuosity) [**224**]. Curved fringes reflect an absence of a stable 6 membered ring, known as a layer defect [**202**], [**214**], [**225**], [**226**]. This phenomenon is known to reduce the stability of C-C bonds located in the basal plane, because of the overlap of atomic orbitals. This means that C-C bonds are weakened and are susceptible to oxygen attack, leading to more superior oxidation reactivity. Furthermore, *Lapuerta et al.* [**211**] demonstrated that curved fringes are more likely to be removed from the outer layer of PM compared to flatter fringes, providing better reactivity.

The separation distance of the fringe can improve PM oxidation reactivity, as it characterises the structure of graphene layers (magnitude of similarity to graphitic structure) [**227**]. Larger fringe separation distances represent instabilities in PM, which facilitates oxidation reactivity by promoting oxygen reaction with carbon atoms through access to the edge site.

Vander Wal et al. [**228**], [**229**] published that PM oxidation reactivity does not only depend on its initial Nanostructure. Another critical factor includes synthesis conditions, such as temperature and residence time during formation. Longer residence time and higher combustion temperature alters the Nanostructure of PM towards less reactive nature, regardless of the fuel utilised. This was also

demonstrated by *Appicella et al* [**230**] in their recent study, who demonstrated that as PM ages and matures, oxidation reactivity decreases. This is reflected by longer L_a and lower tortuosity.

PM Oxidation Reactivity Effects upon Composition, Ashes and Oxygen Functional Groups

The ratio of VOM to elemental soot can facilitate the oxidation of PM. VOM are composed of unburned HCs, oil-derived HCs, water and other fuel and lubricants. As the ratio of VOM increase in PM via absorption and condensation, it can create new micro-pores as new channel for oxygen attack during the post-devolatilisation process. New pores result in higher SSA, which subsequently promotes the oxidation kinetic mechanisms [**208**], [**231**], [**232**].

Studies have reported that the presence of ash can have positive effects regarding PM oxidation reactivity. In CI engines, the process of catalytic impact by ash has shown that PM oxidation reactivity was enhanced [**205**], [**218**]. The presence of Ca, Na, Mg, Na and Al elements in ash have shown positive effects on PM oxidation reactivity, with the most significant being Ca and Na [**205**].

The presence of oxygen on the PM surface contributed by the functional groups can impact the PM oxidation reactivity. The main components promoting oxidation reactivity are the functional groups C-O-C, C-OH and C=O [**208**], [**233**]–[**235**]. The oxygen molecules can alter the Nanostructure drastically through the addition on tortuous graphene layers. This is due to the increase of surface chemical reactivity by the electron affinity from the oxygen atom [**233**]. Additionally, the chemically adsorbed oxygen is easily linked to carbon atoms at edge sites due to the unpaired sp_2 electrons

of the carbon atoms, leading to easier oxidation [**236**]. It is proposed that oxygen attached to carbon from the curved graphene layer can reduce the energy required for oxidation. This is attributed to the lower oxygen desorption energy requirements at the PM surface [**237**]. Recently, *Serhan et al.* [**208**] studied PM oxidation reactivity, concluding that the oxygen functional groups at the PM surface are one of the most influential factors leading to higher oxidation reactivity.

2.3.2.2 Effect of Alternative Fuels on PM Characteristics

Fuel Properties

PM emission is highly influenced by the physical and chemical properties of the fuel [**238**]–[**240**]. The influencing factors of chemical properties include aromatic, olefins, paraffins, oxygen, sulphur, vapour pressure (volatility), heat of vaporisation, boiling points, distillation curves and viscosity, and the physical properties is the molecular structure [**80**], [**114**]. Fuels with complicated molecular structures such as cyclic, branched chain and double bonds have tendency to form accumulation mode PM [**241**]. In the chemical properties point of view, the oxygen effect has been widely acknowledged for being able to minimise PM emissions. Research has also established a correlation between higher sulphur content and greater PM emissions [**240**], [**242**]. Heat of vaporisation increases when blended with oxygenated fuels, leading to greater PM emission as more energy is required to break down fuel droplets injected into the combustion chamber [**243**]. Paraffins and olefins have demonstrated a decrease in PM formation to certain degree and appear to have a minimal impact on PM formation [**242**], [**244**]. Fuel volatility and the aromatic content have the greatest influence on PM emission [**240**], [**242**], [**244**]–[**248**]. Studies indicate that PM emissions increase when fuel volatility is too high or too low. High volatility can lead to flash

evaporation of fuel injected into the combustion chamber, resulting in heterogenous and locally fuel-rich regions. Contrarily, low volatility can lead to fuel impingements resulting in yellow diffusive flames [**80**]. While aromatic hydrocarbons are the PM precursors, greater aromatic content can contribute to greater formation of PAHs as aromatic compounds [**114**]. This is attributed to higher boiling points and stable benzene ring structures formed by sigma bonds and delocalised pi electrons. This process likely to form more fuel-rich regions for PM formation [**244**]. Recently, distillation curves were investigated and recognised as one of the primary factors leading to the formation of PM [**244**], [**249**], [**250**]. Distillation temperatures at 90 °C (T90) were found to impact both PM mass [**244**], [**249**], [**250**] and concentration [**244**], [**249**]. T90 corresponds to heavy aromatic compounds with high numbers of carbon atoms [**245**], [**246**], [**251**]. *Shi et al.* [**250**] revealed the negative impacts of T80 and T95 on PM formation with a particle mass index. T80 was also deduced to have stronger links than T90 and T95. Conversely, *Zhu et al.* [**244**] evidenced a direct link between T50 and PM mass but not in PM concentration.

Oxygenated Fuel

Commonly studied oxygenated fuels are typically alcohol-based chemicals. Oxygenated fuel is widely studied because of it is capability to reduce well-to-wheel CO_2 emissions in vehicles [**252**]. Ethanol, butanol and methanol have recently been studied as an alcohol-based oxygenated fuel replacement. Although MTBE and ETBE have previously been used, they currently are removed from the commercial gasoline EN228. Therefore, this section will focus solely on bio-alcohols (ethanol, butanol and methanol) and DMC (used in the thesis).

Ethanol's effect on PM in GDI engines is a controversial area despite its worldwide use. In some countries, it is currently being used up to 100% as a replacement fuel [**80**]. A majority of literature reports a positive effect, mainly with a high volume of replacement [**80**]. However, there are some studies that evidenced lower PM emission with low volume replacement. The positive effect of ethanol is mainly attributed to the oxygen-bonded molecule, able to reduce soot precursors and leading to reduced PM formation [**80**], [**114**], [**240**], [**251**], [**253**]–[**257**]. *Storey et al.* [**254**] utilised ethanol blends in FTP-75 and supplementary FTP (US06) driving cycles, observing a reduction of PM with 10 and 20 % (v/v) ethanol blending. Other literature also demonstrated PM reductions in part-load tests, using a low ethanol blend [**255**]–[**257**]. Contrarily, some results showed that ethanol replacement can increase PM emission, linked to the higher heat of vaporisation and lower vapour pressure of ethanol properties [**5**], [**206**], [**217**], [**239**], [**258**]. *Lee et al* [**206**] stated that greater PM emissions only extends to low percentage blends. PM was reduced at higher volume, because of the higher oxygen concentration in the blends. Consensus was published in an investigation by *Catapano et al.* [**239**], showing that PM emissions improved as the blend percentage increased up to 100 % (v/v) except at 10 (v/v)%. *Luo et al.* [**217**]*, Price et al.* [**253**] and *Wang et al.* [**258**] have also documented that PM number increases due to the higher concentration of nucleation mode PM. This is due to the reduction of accumulation mode PM (solid soot PM), limiting absorption and condensation on solid soot PM. Despite that, *Luo et al.* [**217**] did not acquire the same trend during higher speed conditions. This was attributed to the limited time for unburned HCs to condense, and improved turbulence intensity in the combustion chamber (less THC). *He et al.* [**5**] concluded 20 (v/v)% ethanol addition produced

higher PM emissions during high load conditions. This was related to an increased penetration length from the longer fuel injection duration (lower LHV). This caused impingements on cylinder wall and piston top. *Storch et al.* [**259**] hypothesised worsening PM emissions with ethanol blends can be due insufficient optimisation throughout the operating range. For microstructure and Nanostructure, *Lee et al.* [**206**] measured a drastic growth in dp_0 with 10 % (v/v) ethanol addition, causing larger agglomerates (R_g increment). The latter also obtained a larger average dp_0 and R_g formed during combustion with a 20 % (v/v) ethanol blend. It was speculated that increased fuel consumption leads to greater fuel impingement [**203**]. Furthermore, ethanol addition show to alter the Nanostructure to lesser graphitic structure (order of fringe arrangement) to more amorphous-like graphene layers [**203**], [**206**], [**260**]. This is the result of conversion from initially adsorbed or condensed unburned HCs. *Seong et al.* [**213**] demonstrated that the use of 20 % (v/v) ethanol addition resulted in insignificant changes in microstructure during richer and lean combustion, due to MFB50 phasing. Recently, *Hergueta et al.* [**8**] proposed an opposite trend in terms of micro-scale analysis with 25 % (v/v) ethanol. Smaller dp_0 and R_g were reported, which have been attributed to an improved oxidation rate of PM by excess oxygen from ethanol addition. Additionally, more chain-like agglomerates (lower D_f) were formed due to a fewer number of primary particles had altered the collision mechanism. A similar trend in microstructure was demonstrated by *Gao et al.* [**261**] up to 65 % (v/v). However, Nanostructure analysis indicated a monotonic trend, as more premature PM was speculated for the enhancement of PM oxidation reactivity. Subsequently, several publications have evaluated the PM oxidation reactivity formed by ethanol blends,

evidencing that more reactive PM was formed. This was attributed to smaller dp_0 and more amorphous graphene layers [**217**], [**220**]

Butanol is increasingly more popular as a fuel, due to several advantageous properties in comparison to ethanol. As it is relatively new, discrepancies exist within PM emission data. Unlike ethanol, a majority of studies indicate an improvement in PM emissions with the use of butanol [**71**], [**240**], [**248**], [**251**], [**255**], [**262**], [**263**]. Conversely, *Waller et al.* [**264**] hypothesised that butanol has negatively impacted PM emissions based on the observation of higher concentrations of aldehydes and benzene precursors. *Lee et al.* [**206**] cited an increase of PM emissions in their study, attributed by higher heat of vaporisation and viscosity properties of butanol. In contrast, PM improvements were attributed to the reduction of aromatic content and the oxygen-borne atoms in butanol [**71**], [**248**], [**255**], [**262**], [**263**]. *Herguerta et al.* [**8**] reported a greater reduction of PM emissions with butanol, in comparison to ethanol, when gasoline was replaced by 33 % (v/v) and 25 % (v/v) respectively with similar oxygen concentration in the blends. A majority of findings reported smaller PM were formed (lower geometric number mean diameter (GNMD)). It was associated to the effective reduction of solid soot PM (accumulation mode PM) and the increase in the ratio of nucleation mode to accumulation mode PM [**71**], [**255**], [**262**]. In another study by *Hergueta et al* [**71**] only observed this phenomenon during low-load conditions. The nucleation peak effect is more prominent when accumulation mode particles are reduced as butanol addition is increased [**262**]. However, *Gu et al.* [**263**] and *Zhang et al.* [**255**] did not observe nucleation mode PM during high-load conditions. This was speculated to be related to THC post-combustion oxidation, as the combustion temperature was sufficient to promote oxidation during high-load conditions.

Karavalakis et al. [**240**], [**251**] demonstrated an overall PM reduction under Unified Cycle and FTP tests with butanol. The improvement was gradually enhanced with higher concentration of butanol used. A limited literature base exists surrounding TEM micro and Nanoscale analyses of butanol PM. *Lee et al.* [**206**] found that 16 % (v/v) butanol addition has led to PM with a lower degree of fringe order than gasoline and 10 % (v/v) ethanol/gasoline. Furthermore, the measurement of dp_0 was larger. *Hergueta et al.* [**8**] and [**71**] found contrasting results, demonstrating that butanol/gasoline blends formed smaller dp_0 with respect to gasoline. This was due to the oxidation by oxygen contributed by butanol, leading to lower R_g. However, D_f remained similar to gasoline indicating the same type of collisions experienced by particles. In spite of that, reactivity characteristics have been not been studied up to date.

Methanol is popularly used in China as it is sourced from coal and natural gas [**80**]. Due to its unpopularity, research on PM emissions is scant. PM reduction was observed in low percentage methanol/gasoline blends, and reported to deteriorate as higher methanol volume was added [**265**], [**266**]. The same reasoning is applied in ethanol and butanol studies. *Wang et al.* [**267**] studied 15, 25 and 40 % (v/v) methanol/gasoline blends. The results showed that increasing the methanol volume can result in lower PM mass and higher PM concentration, as the result of greater nucleation mode PM. *Qin et al.* [**268**] did not report any changes in nucleation mode PM with the utilisation of methanol. Hence, the PM emissions were improved by both the reduction of PM mass and concentration. A clear PM reduction trend was witnessed with methanol addition. However, morphological evaluations have not been published in the literature.

With regards to the DMC effect on PM emissions, no studies have been conducted with engine combustion. Nonetheless, the effect of DMC on solid soot PM emissions was investigated through an ethylene diffusion flame studied by *Paladpokkrong et al.* [**269**]. The effect of DMC addition is more substantial as the percentage increases, regardless of the normal and inverse diffusion flame. The studies show DMC can effectively suppress the formation of soot. Furthermore, TEM analysis on soot formed by DMC addition illustrated alterations in the Nanostructure of PM, towards a more reactive nature in comparison to soot formed by pure ethylene. Thus, the soot graphene layers are more amorphous, lower magnitude of graphitisation, shorter L_a, higher fringe tortuosity and higher fringe separation. Subsequently, greater PM oxidation reactivity was firmly confirmed by the shorter oxidation time using isothermal tests in TGA. Additionally, DMC was considered as a better soot suppressor than the conventional alcohol ethanol, yielding less PM mass in a pyrolytic conditioned kinetic modelling study [**15**].

2.3.2.3 Effect of Engine Operating Conditions on PM Characteristics

Injection Pressure and Timing

Injection parameters also play important role in supressing the formation of particles. PM formation is incredibly sensitive to parameters such as injection pressure and timing [**270**], affecting the mixing process and fuel impingements on the cylinder wall and piston head. High injection pressure can lead to minimising fuel droplet size for easier vaporisation, subsequently promoting the charge mixing process for improvement in fuel jet momentum (turbulence) [**43**], [**80**], [**188**], [**271**]–[**273**]. In turn, the flame radiation is distributed more evenly due to the reduced prominence of the diffusive flame, improving PM emissions [**272**]. In spite that, the influence of fuel

injection pressure is more prominent during low load and speed engine conditions. [**188**]. It was also noted that increasing the fuel pressure is not equivalent to increasing the penetration length of injection. Therefore, it is unlikely for the PM to increase due to impingements [**274**]. The relationship between PM reduction and injection pressure is non-linear. Several publications [**5**], [**114**], [**188**] demonstrated that the non-linear trend has a major influence on accumulation particles. *Kittelson et al.* [**97**] recognised this relationship as the primary factor driving the higher fraction of nucleation mode PM, as there is reduced surface area for unburned HCs to condense and adsorb on to solid PM.

Injection timing plays a more important role than injection pressure, as it determines the formation of PM. In order to reduce PM formation, it vital for the fuel injection in the engine to take place at an optimum time [**5**], [**275**]. It is believed that an early fuel injection can give ample time for the air/fuel mixing process to create a more homogenous mixture, resulting in less PM formation [**80**], [**276**]. However, this is not the case. Several publications have found that early or late injection timing may result in a spike of PM emissions [**1**], [**5**], [**273**], [**276**], [**56**], [**115**], [**203**], [**253**], [**260**], [**261**], [**268**], [**271**]. When injection occurs too early, near or close to the TDC, impingements on cylinder wall and piston top can be induced, causing diffusive pool fire. In contrast, when injection timing is delayed from the optimum, PM formation is promoted due to the limited time for air/fuel mixing. This leads to formation of heterogeneous mixture and the locally fuel-rich regions. These phenomena are thought to result in for formation of PM. *Maricq et al.* [**56**] reported an incremental increase of PM emissions in both stratified-charge and homogenous combustion mode, as injections timings were varied out of the optimum range. *Pei et al.* [**276**] and *He et al.* [**5**] documented a

greater proportion of nucleation mode particles, as the GNMD shifted towards a smaller size when fuel injection is delayed. It is due to the limited mixing time that leads to the greater concentration of unburned HCs. When fuel injection is advanced, the GNMD increases as the result of greater concentration of accumulation mode PM. *Bogarra et al.* [**1**] observed a similar trend when experimenting with advanced injection timing, where accumulation mode PM was attributed to solid PM (soot). *Price et al.* [**253**] suggested an optimum injection timing is dependent on volatility of fuel. Higher volatility fuel can be injected towards the end of the compression stroke, because of its ease of fuel evaporation. Contrarily, fuel with lower volatility (with heavy aromatic hydrocarbons) requires mixing longer time. Hence, earlier injection timing is more favourable, which was proven using gasoline and 85 % (v/v) ethanol/gasoline blend. In microscopic analysis, *Barone et al.* [**197**] measured a significant amount of liquid droplets during early fuel injection experiments. This was due to the nucleation of impinged fuel film and fuel lubricating oil. Additionally, the average of dp_0 was larger due to the deterioration of air/fuel mixing compared to optimum injection timing. *Lee et al.* [**203**] performed a similar investigation but was unable to find any significant difference in dp_0 due to the broad range of diameters. Moreover, the Nanostructure analysis exhibited greater amorphous graphene layers due to unburned HCs adhered onto particles, caused by the advancement of injection timing. Conversely, *Seong et al.* [**260**] revealed a trend of larger dp_0 and R_g as the injection timing was advanced. They also exhibited Nano-size primary particles (< 10 nm) are more likely to attach onto the solid PM when injection is executed outside of optimum timing. *Gaddam et al.* [**202**] measured a smaller dp_0, in agreement with *Seong et al.*[**260**] regarding late injection timing. However, the agglomerates were more compact (higher D_f) than

baseline measurement, because of the more PM precursors present and rapid surface growth. The graphene layers illustrated higher tortuosity as a result of increased $\phi_{Critical}$ regions, promoting the formation of longer graphene fringes. *Bogarra et al.* [**199**], [**214**] assessed the microstructural and Nanostructural of PM formed with advanced injection timing. The results suggest non-statistical difference in dp_0, D_f and Nanostructure. However, lower n_{p0} and smaller R_g of PM were recorded due to the lesser presence of large PM agglomerates. The large agglomerates were attributed to different timing of PM formation. For baseline injection condition, PM is formed at earlier stage in the expansion stroke, whereas PM formed by advanced injection timing occurs later, close to end of expansion stroke. Subsequently, the particles collision time is reduced, forming smaller agglomerates compared to baseline condition.

Spark Timing

Literature consistently agrees that retardation of spark timing reduces PM emissions [**5**], [**56**], [**278**], [**98**], [**188**], [**253**], [**263**], [**268**], [**271**], [**276**], [**277**]. Delaying spark timing elongates the air-fuel mixing time (time between injection timing and spark timing), leading to a more homogeneously mixed charge [**253**], [**268**], [**276**], [**277**]. However, the enhancement of PM emissions is associated to retarding the spark timing can increase the EGT (higher in-cylinder temperature). In turn, it will boost the post-combustion oxidation and PM oxidation in combustion chamber [**116**], [**253**], [**263**], [**273**], [**276**], [**277**]. However, spark timing advance can induce higher in-cylinder temperature during pre-ignition, which can boost nucleation rate as more unburned HCs are present after combustion. This was reported by several publications, which evidence greater production in nucleation mode PM [**116**], [**188**], [**253**], [**263**], [**268**], [**277**]. *Pei et al.* [**276**] and *Xie et al.* [**278**] demonstrated a reduction of PM was attributed

to both accumulation and nucleation mode PM. These reductions were inhibited by post-combustion oxidation from higher exhaust temperature. *Maricq et al.* [**56**] demonstrated the trend is same for engine combusting in homogeneous and stratified-charge combustion modes. Meanwhile, *Xin et al.* [**5**] observed different influences of spark timing during cold start and warmed up conditions. Accumulation mode particles are more pronounced when the engine temperature is cold. When the engine is warmed up, the influence shifts to nucleation mode particles. *Price et al.* [**253**] hypothesised several extra CADs can improve the fuel droplet size as well as improving the air-fuel mixing process, leading to lesser PM emission. The same trend was concluded by combusting a methanol blend by *Qin et al.* [**268**]. Conversely, *Arsie et al.* [**277**] observed the effect of delayed spark timing. The results showed that the effect was diminished at higher engine speed conditions because of shorter time for oxidation.

Air-Fuel Ratio

Referring to the source of PM formation in ***Table* 2.2**, the influence of λ is foreseeable. A homogenously mixed charge and reduction of fuel-rich pockets can be achieved through homogenous lean combustion, the longer development of flame and excess air in the combustion chamber. Moreover, it promotes a more complete combustion due to more air available for mixing [**5**], [**98**], [**188**], [**190**], [**253**], [**271**], [**276**], [**277**], [**279**]. Thus, the magnitude of PM emission drastically drops in respect to stoichiometric and rich combustion. *Zhang et al.* [**188**] added that hydrogen abstraction was being suppressed by lower combustion temperatures during lean combustion, as another contributing factor for lower PM emissions. Although less PM is emitted during leaner combustion, the ratio of nucleation mode PM to accumulation mode PM

increases. *Pei et al.* [**276**] reported increasing of the ratio as λ transitioned towards leaner mixture. The leaner combustion inhibited accumulation mode PM, which are mostly comprised of solid soot PM. However, both nucleation and accumulation mode PM were reduced overall. Despite rich λ increases accumulation mode PM [**188**], [**190**], a nucleation peak is observed as the result of condensed HCs [**276**]. Hence, the ratio is less likely to be affected by rich combustion. However, this does not occur for stratified-charge combustion. In stratified-charge combustion, more PM is emitted [**56**], [**57**]. 80% is accounted for by smaller PM (d_p < 50 nm) [**57**]. It is believed that smaller PM is formed by condensation of unburned HCs due to the fuel impingements during the late injection timing. However, two different courses of PM formation were found during rich and stratified-lean combustion. Both are influenced by the combustion temperature and, HCs and oxygen concentrations [**98**]. In rich combustion, PM is likely to be produced via gas-phase reaction, where unburned HCs is the source of PM precursors. Whereas, stratified-lean combustion favours formation via heterogenous phase (liquid droplets and liquid pool). On the other hand, *He et al.* [**5**] validated the effect of rich combustion with warm and cold engine conditions. Results indicated that PM emissions reduced when operating under warmed conditions, as the vaporisation of fuel was improved, leading to reduced fuel impingement.

There is limited literature on PM microscale morphological and Nanostructural analyses; with publications containing many discrepancies in their results. *Gaddam et al.* [**202**] evaluated micro and Nano structures of emitted PM under constant spark and fuel injection timings. Conditions for λ were measured at 0.87, 1 and 1.13, corresponding to rich, stoichiometric and lean. The results showed that stochiometric and lean conditions produced similar PM characteristics. No drastic changes were

found in dp_0 from the impact of λ. The fuel-rich agglomerates were observed to be denser and more compact in stoichiometric and lean conditions. The agglomerates were more open and chain-like, reflecting a lower D_f. The rich condition produced significantly more particles and hence, the rate of agglomeration was increased. Similarly, the R_g was reported to be larger, due to more fuel injected into the combustion chamber (more particles are formed). For the Nanostructural analysis, only alterations to fringe tortuosity was observed, measured at a higher magnitude. This was attributed to more locally fuel-rich pockets above $\phi_{Critical}$ resulting in the formation of non-6 membered benzene rings. The fringe curvature is the integration of defected benzene rings, hence it was promoted under fuel-rich conditions. Additionally, *Seong et al.* [**213**] studied PM under MFB50 phased conditions, formed during λ at 1.13 and 0.98. Due to the MFB50 phasing, the trend of variation in dp_0 was not apparent. However, the concentration ratio of large primary particles to small particles was increased as λ was lowered to 0.98 from 1.13, increasing the unburned HC availability for condensation (surface growth). *Wu et al.* [**215**] tested the micro and Nanostructures of PM emitted under constant spark timing with a variation of λ between 0.88, 1, 1.08 and 1.22. The PM emitted during λ at 1 was found to have the highest D_f, as well as average dp_0. It was associated to the enhanced PM oxidation during the formation process in lean mixtures, as more excess oxygen was available when stoichiometry transitioned to a leaner mixture. Similarly, the rich condition also improved the oxidation rate by the higher combustion temperature. These led to smaller and less primary particle formation. Moreover, the Nanostructural results indicated the stoichiometric condition has the longest L_a and more tortuous fringe curvature than rich and lean PM. Thus, the greatest PM oxidation reactivity is speculated by the authors.

Engine Load and Speed

As the engine load increases, PM emissions monotonically increase due to more fuel mass is injected per cycle [**56**], [**71**], [**188**], [**217**], [**271**]. The increase of PM can be measured in terms of mass and concentration. The increase of PM mass is related to the formation of solid soot PM [**271**]. The PM concentration increase is due to higher in-cylinder peak temperature at higher loads, promoting nucleation mode PM [**116**]. Emission trends of PM in relation to engine speed is not consistent but explained by several studies. A study on PFI engines by *Arsie et al.* [**277**] found that PM was reduced at higher engine speed, attributed to enhancement of PM oxidation by higher combustion and in-cylinder temperatures. Other researchers have also measured greater PM emissions during increases engine speed [**56**], [**217**], [**273**]. This is mainly associated to the short mixing time and more fuel being injected during higher engine speed conditions. However, high speed conditions do not always gradually increase PM emissions, and may improve results due to better vaporisation of fuel from higher temperatures. *Haynes et al*. [**116**] concluded that the effect of speed is affected by the competition between PM formation and oxidation. During high speed, EGT is high enough to oxidise PM, but depends on the residence time. Therefore, PM will be reduced under high speed conditions only when residence time is sufficient for oxidation to take place. For oxidation reactivity, PM emitted by the higher speed and load conditions were reported more reactive and less reactive respectively [**217**], [**220**]. The less reactive PM formed during high speed conditions was due to less oxidation activity during the formation process, as there is shorter residence time for PM oxidation [**217**]. Hence, leading to larger dp_0 and R_g. This was also reported in findings by *Seong et al.* [**260**], where there was lower SSA for oxygen attack illustrating lower

PM oxidation reactivity [**260**]. As for the PM formed during higher load conditions, it was attributed to the Nanostructural variation as amorphous graphene were being heat-treated into more ordered graphene layers under higher in-cylinder temperatures [**217**], [**220**]. However, the Nanostructure reported by *Gaddam et al.* [**202**] did not observe any variation despite higher exhaust temperatures. The oxidation reactivity alteration reported was mainly associated with the PM composed of smaller dp_0 [**202**], [**260**] and R_g [**202**].

Exhaust Gas Recirculation

EGR can be executed internally (IEGR) and externally. IEGR can be controlled through valvetrain and an external EGR can be achieved with via a low- and high-pressure loop EGR valve. IEGR is controlled by opening and closing of the intake and exhaust valve. This traps residual gas and helps with the fuel vaporisation process by increasing the charge temperature regardless of the adjustments being made by the IVO or EVC [**5**], [**79**]. It was found effectively reducing PM during engine cold-starts [**5**], [**115**] and under low load conditions [**79**], [**115**] that mainly reduces accumulation mode PM [**5**]. Though, this reduction is difficult to observe during high load conditions [**115**]. It is thought that the heat from residual gas is not significant enough to supplement the high in-cylinder temperature during high load conditions. Furthermore, IEGR was found to be more efficient during low speed conditions in arresting PM formation than an external EGR [**79**].

The external EGR mainly consists of intake heating, dilution and thermal effects. During its use, the overall oxidant in the combustion chamber is reduced. This occurs whilst retaining the same oxygen concentration prior to EGR through the induction of higher air mass flow in conjunction with exhaust gas [**44**]. With less oxidant from the

dilution effect, both the flame propagation speed and combustion speed are slowed down, which improves the homogeneity of the charge mixture in combustion chamber. Despite this, the combustion is not entirely complete, leading to the promotion of solid PM (soot) formation and the decrease of oxidation rate. Thus, more accumulation mode PM is emitted [**280**]. Simultaneously, the thermal effect starts with the reduction of in-cylinder temperature (lower combustion temperature), which inhibits the PM formation by thermal pyrolysis and H-abstraction as the dominant processes [**142**], [**188**]. Generally, EGR utilisation is reported to reduce accumulation mode particles, with increasingly more nucleation mode particles [**188**], [**276**]. However, this not all always the case. *Pei et al.* [**276**] observed a constant reduction of accumulation mode PM. For nucleation mode PM, the results showed an upwards (up to 15 %) increase, subsequently followed by a downwards (< 15 %) trend as the EGR percentage increased. It was correlated to a higher EGR concentration, which tends to have slower exothermic process and higher EGT during the expansion stroke. These factors contributed to the oxidation of nucleation mode particles. Contrarily, *Lattimore et al.* [**281**] demonstrated that nucleation mode PM was constantly lowered, and accumulation mode PM was constantly increased when EGR was added up to 12 %. When EGR was added beyond 12 %, reduction of both nucleation and accumulation mode PM was observed. It was associated to two significant phenomena, the improvement of fuel economy resulted in reduced PM formation and a slower combustion rate enhanced the PM oxidation rate. *Hergueta et al.* [**71**] also documented that fuel consumption was reduced with EGR utilisation, which led to lower PM emissions. Cooled EGR has also been investigated [**79**], demonstrating an increase of accumulation mode PM. It was speculated that due to the diminished intake heating

effect, fuel vaporisation was worsened, leading to a more heterogenous charge mixture [**116**], [**263**], [**276**]. In the recent findings, REGR using gasoline, was evaluated experimentally, successfully reducing PM emissions particularly for accumulation mode particles [**1**], [**44**], [**282**]. This is mainly associated to the enhanced thermal effect and additional chemical effect. In REGR, the higher combustion temperature from hydrogen, and the excess CO, can promote PM formation and continuous growth [**142**]. This occurs simultaneously with the oxidisation of HC and PM precursors [**283**]. In terms of chemical effect, the hydrogen addition inhibits PM nuclei formation by slowing or reversing the HACA mechanism [**284**]. Additionally, as previously mentioned, PM and PM precursors can be oxidised by OH. However, the CO presence from REGR in the combustion chamber can reduce the oxygen and OH radical concentration, contributing to reduced PM oxidation [**285**]. The difference in micro and Nanostructure, can be neglected due to overlapping of error bars between measurements acquired between the baseline, EGR and REGR [**199**], [**214**]. Consequently, PM oxidation reactivity between the baseline, EGR and REGR are comparable and are reflected by similar activation energies and oxidation curve profiles from TGA [**92**].

2.3.2.4 Effect of Aftertreatment System on PM Characteristics

Influence of TWC

PM is concluded to deteriorate TWC performance in terms of lower conversion efficiency of gaseous species and higher light-off temperature. This is due to plugging by ashes or soot [**286**]. However, the effect of the TWC has been found to be able to minimise PM emissions up to a certain extent; more prominent for PM which are smaller in diameter. *Chen et al.* [**287**] observed a massive drop in nucleation mode PM

post-TWC, but the effect in accumulation mode PM was negligible. *Bogarra et al.* [**92**] reported smaller PM (d_p < 50 nm) can be more easily trapped and possibly oxidised in the TWC, resulting in a decrease of smaller particles post-TWC. The ability of a TWC in abating smaller PM, HC droplets and accumulation mode PM can lead to a PSD peak shift. The reduction of PM was attributed to diffusion losses and thermophoresis mechanisms [**214**]. *Samuel et al.* [**288**] associated the PM reduction with the oxidation and coagulation for PM with d_p < 25 nm. The results indicated that PM mass and number were drastically dropped post-TWC. On the other hand, TWC did not alter the morphological characteristics of the PM and was unable to oxidise HCs absorbed on the PM due to the limited residence time [**92**]. *Bogarra et al* [**92**], [**214**], [**282**] expanded their studies on PM characteristics, concluding that the TWC had an insignificant effect on the micro and Nanostructural nature of PM. This was attributed to the short residence time of PM in the TWC, which was not sufficient enough to alter the nature of PM.

2.3.3 PM Abatement with GPF Application

Influence of GPF Properties and Washcoat on GPF Performance

GPF is a very efficient approach to abate PM emissions in the tailpipe. However, due to the variation of emitted PM by CI and GDI engines, design optimisation is essential. Besides that, optimisation is vital for obtaining the equilibrium between filtration efficiency and pressure drop, ensuring high quality GPF filtration and regeneration. Several publications have assessed the effect of GPF properties on PM. Studies suggest increasing wall thickness, length to diameter ratio, cell density and substrate volume can enhance the filtration performance of a GPF. This is also

exhibited in GPF with smaller MPS and lower porosity [**7**], [**181**]. These properties specifications mainly exhibit lower $U_{filtration}$, which is linked to the *Brownian diffusion* filtration mechanism. This results in longer residence time for PM to absorb onto the pores and is followed by thicker PM cake layer formation per specific area [**7**]. Adversely, these properties specifications can cause an increase in pressure drop [**289**]. With the concern of performance decline in the TWC from plugging, a catalysed GPF (cGPF) has been developed to ensure excellent conversion efficiency of gaseous emissions. As for the cGPF, the filtration efficiency constantly outperforms the bare GPF, because the washcoat reduces the MPS [**180**], [**181**], [**290**]. Likewise in pressure drop [**290**], it is also consistently greater than a bare GPF.

Influence of Aftertreament Achitectural Configurations on GPF Performance

The implementation of a GPF in the exhaust system acts as a 'second brick' (upstream to a TWC), therefore the influence of these architectural configurations (CC and UF) are evaluated. UF architectural configuration is agreed by researchers to achieve better filtration efficiency in comparison to CC architectural configuration. *Saito et al.* [**7**] observed a 15% improvement adopting UF architectural configuration with NEDC. This was credited to the lower inlet EGT at GPF, enhancing *Brownian diffusion* due to the lower $U_{filtration.}$ This result was associated with the slower regeneration rate, maintaining a thicker PM cake layer for better filtration performance. It was also verified with PM regeneration tests, showing that the use of CC architectural configuration was significantly more effective than the UF architectural configuration. This theory further supported by an investigation performed by *Shimoda et al.* [**289**]. The study concluded that UF architectural configuration accrued thicker PM cake layer accumulations over several NEDC repetitions. Furthermore, they also investigated pressure drop within

both architectures using the NEDC test. As expected, CC architectural configuration induced higher back pressure than UF architectural configuration. It was believed the lower inlet EGT of the UF architectural configuration reduced volumetric flow rate, affecting $U_{filtration}$. On the other hand, PM filtration performance improved proportionally to the distance interval of the two substrates, as the distance varied between 10 cm, 50 cm, 100 cm and 150 cm. The variation of filtration efficiency in the architecture was mainly associated to the equilibrium between the PM cake layer formation and PM oxidation rate [**291**].

2.3.4 Summary

The aim of this thesis is to understand PM emissions formed by GDI engines and also potential ways to improve PM emissions. In general, PM formation is caused by the yellow diffusive flame and direct carbonisation of fuel, despite the fuel blends and engine operating conditions. However, the only transformative variation of PM by fuel, and engine operating conditions, exists in the PM characteristics during the formation process. This is due to synthetic conditions such as residence time and surrounding temperature.

In relation to case studies stated in this thesis, the air-fuel ratio effect on combustion and emissions characteristics have been investigated. PM characteristics in microstructure and Nanostructure have also been evaluated, but mainly conducted under constant spark timing or MFB50 phasing. Therefore, air-fuel ratio studies under MBT conditions is an area undocumented by the literature. Additionally, PM oxidation reactivity is yet to be analysed, despite assumptions being made based on its

microstructure and Nanostructure analyses. A comprehensive evaluation of rich and lean GDI PM characteristics will be revealed with comparisons to PM formed during stoichiometric combustion.

In regard to oxygenated fuel, it has proven that alterations in fuel properties and additional oxygen concentration can improve PM emissions, as well as PM oxidation reactivity. A positive effect in combustion characteristics has been documented with the use of DMC, as well as THC and CO emissions. At present, publications have produced varied NO_x emissions creating uncertainties regarding to the use DMC. Therefore, it will be evaluated as part of the case study. In addition to that, DMC has also indicated improvements in PM emissions and oxidation reactivity through kinetic modelling and diffusive flame studies. However, an affirmation is required in internal combustion engines. Therefore, PM characteristics evaluations are extended to microstructure, Nanostructure and its oxidation reactivity.

Although TWC and GPF architecture have been briefly studied, it appears that a comprehensive evaluation is required to provide a more in-depth understanding of the filtration process. This can facilitate the optimisation of GPF by the architectural configuration effect. One of the most important parameters is the effect of *Greenfield gap*, as it is considered under-reviewed in GPF-related investigations. Moreover, optimisation of the architecture should be tested with the influence of GPF properties. Determination of crucial GPF properties can assist GPF performance in architectural configuration studies. The experiments carried out can be useful in locating the equilibrium between filtration efficiency, pressure drop and regeneration of GPF. This has led to experiments on aftertreatment architectures. Furthermore, the influence of

GPF properties on aftertreatment architectures performance have also been demonstrated.

CHAPTER 3 EXPERIMENTAL SETUP AND FACILITIES

This chapter will present the instrumental and experimental setup used throughout this PhD. This includes a multi-cylinder GDI engine, analytical facilities, fuels properties, and the substrate properties of GPFs and the TWC. The working principles and specifications of the equipment will also be discussed. Additional information of the instrumentation used in scaled-down aftertreatment architecture in ***Chapter 6*** is also detailed. The procedure used for TEM grid preparation in *Error! Reference source not found.*. is discussed. In the final subsection of this chapter, the details of post-processing analyses are presented.

3.1 Engine Test Bench

The GDI engine used in the thesis is a first-generation, air-guided direct injection combustion system design. It is a four-cylinder turbocharged engine, with a displacement capacity of 2L. The engine is configured with solenoid fuel injectors side-mounted to combustion chamber, with spark plugs centrally located on top of combustion chamber. In order to reduce the detrimental pressure wave interactions between successively firing cylinders, the exhaust manifold is divided into the turbine entry. A close-coupled TWC is included as the default exhaust gas aftertreatment to ensure compliance with *Euro V* emission limits. The default combustion strategy used in this engine was homogenous-stoichiometric. The engine stoichiometry was maintained with feedback signals from the heated exhaust gas oxygen (HEGO) sensors. The sensors were also applied to ensure the TWC was performing effectively.

The fuel delivery system uses a 12V, electric low-pressure fuel pump regulated at 4 bar which is directed to the camshaft-driven, high-pressure fuel pump. The fuel

injection pressure is varied by the fuel rail pressure, using an integrated solenoid valve, which is controlled by the ECU. The ECU default operation includes the IEGR effect, through the control of dual VCT (valve overlapping). Two separate water heat exchangers are utilised for cooling purposes of the charged-air and the engine coolant. The charged-air temperature is cooled and controlled before directed into intake manifold as intake air. The oil engine is cooled by the engine coolant which is circulated by the power steering pump. The additional function of the pump is also to maintain the auxiliary drive-belt arrangement. Therefore, a water heat exchanger is required to maintain engine coolant temperatures below the permitted temperature. Further engine specifications are tabulated in ***Table* 3.1** and illustrated in ***Figure 3.1***.

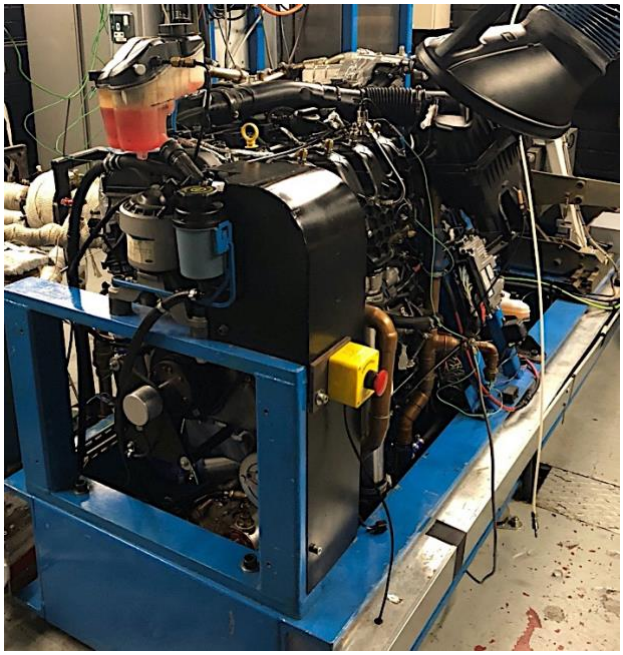


Figure 3.1: GDI engine used for experimental tests.

Table 3.1: GDI Engine specification.

Feature	Specification
Number of Cylinder	4
Displacement	1999 cc
Compression Ratio	10 to 1
Bore x Stroke	87.5 x 83.1 mm
Firing Order	1-2-4-3
Turbocharger	Borg Warner K03, variable wastegate
Rated Power Output	149 kW at 6000 rpm
Rated Torque Output	300 Nm at 1750 to 4500 rpm
Valvetrain System	Four valves per cylinder, dual variable electro-hydraulic phasing, dual overhead camshafts
Engine Management Unit	Bosch ME17
Exhaust Aftertreatment	Commercial TWC
Fuel Delivery System	Camshaft driven high pressure pump with solenoid actuated pressure control up to 200 bar
Fuel Injector	Side mounted multi-hole solenoid actuated injector
Spark Plug Location	Top centrally positioned
Piston Design	‘Flat’ top for air-guided design

3.2 Engine Instrumentation and Data Acquisition

The engine is coupled to a 75 kW alternative current (AC) dynamometer and an inverter drive with the capability to motor and absorp/regenerate. It is controlled by the CADET dynamometer control system, supplied by CP Engineering. The CADET has the ability to document the DAQ for engine load and speed, oil and coolant temperatures and variety of analogue and thermocouple inputs. In addition to that,

CADET is programmed with warning alarms and shut-down limits to avoid engine overloading.

The engine test bench is installed with a Rheonik RM 015 Coriolis fuel mass flow meter, along with a temperature conditioning unit sourced from CP Engineering. The instrument can provide continuous mass flowrate measurements within the range of 0 to 20 kg/h, with the tolerance of ± 0.12 %. The temperature of fuel delivery is constantly maintained at approximately 301.15 K (28 °C) prior to measurement by the mass flow meter.



(a) **(b)**

Figure 3.2: (a) Rhenoik RM 015 Coriolis fuel mass flow meter and **(b)** fuel conditioning unit.

In-cylinder pressure was measured with an AVL GM12D piezo-electric pressure transducer. The transducer is flush-mounted and positioned on top of the engine's fourth cylinder head via a machined hole. The measurement of in-cylinder pressure is charge-amplified. The measurements are continually referenced to the engine cycle at 720 pulses per revolution with the use of a Baumer magnetic rotary encoder. An additional pressure transducer is also positioned in the intake manifold, in order to

offset the in-cylinder pressure at the bottom dead centre (BDC) after the intake stroke. Two Variohm EPT3100 pressure transducers were also used to measure the absolute pressure pre and post-GPF. This allowed the evaluation of pressure drop in scaled-down aftertreatment architecture tests (***Chapter 6***)

The DAQ of pressure data was obtained with two National Instruments PCI-6251. These cards have sixteen analogue inputs (AI), two analogue outputs (AO), sixteen digital inputs/outputs (DI/O) and two onboard timers with maximum sampling rates up to 2 MS/s. Therefore, it is able support in-cylinder pressure data acquisition at intervals of 0.5° CAD when triggered by the crank encoder. The cards are utilised with a BNC-2090 breakout box. In-cylinder pressure data was used for the calculation of IMEP, COV of indicated mean effective pressure (COV_{IMEP}), maximum in-cylinder pressure (P_{Max}) and its CAD position. The absolute pressure data acquired during experiments conducted in ***Chapter 6*** was sampled at a frequency of 1 Hz throughout the experimental test, and post-processed for pressure drop analysis. These pressure data acquisitions were controlled by the LabVIEW application. Post-processing details are further explained in *section 3.8*.

The engine operating parameters are managed by a development specification ECU provided by Ford. Vision 5.2 software supplied by Accurate Technologies Inc. was used to access the ECU for engine calibration, sensor readings and additional calculated parameters. A minor fraction of DAQ was also obtained with a controller area network (CAN) hub via the interface software.

A full schematic of the DAQ system is illustrated in ***Figure* 3.3***.* A comprehensive list of DAQ from the engine test bench is shown in *Appendix 1: Data Acquisition Channels.*

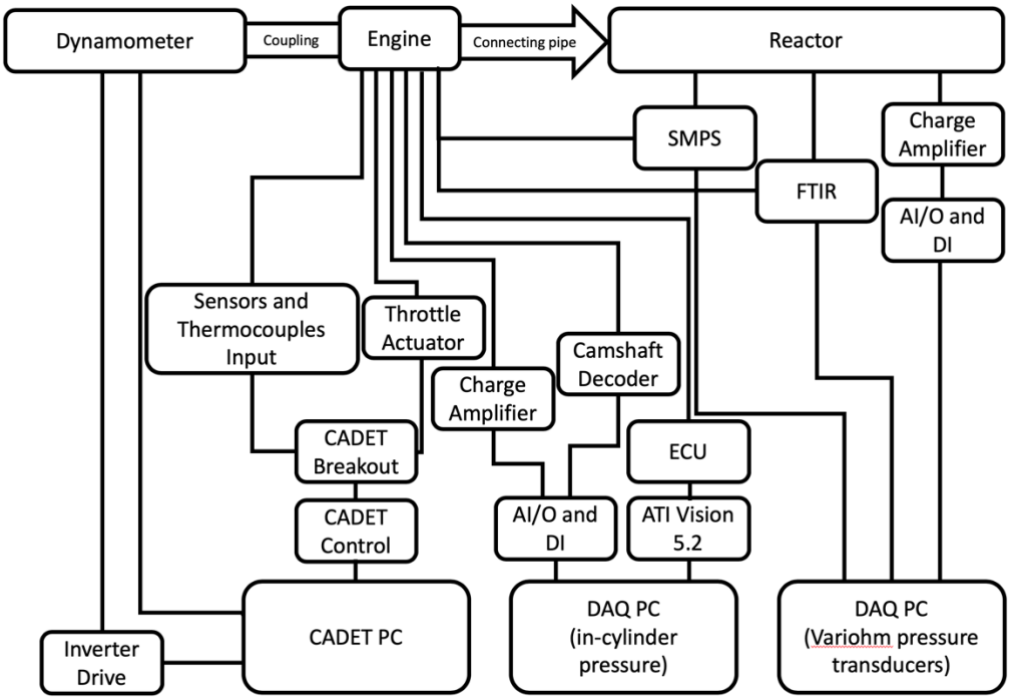


Figure 3.3: Schematic of DAQ of engine test bench.

3.3 Fuels Properties

The commercial pump-grade automotive gasoline (EN228) containing 10 % (v/v) of ethanol addition was used in this thesis; provided by Shell Global Solutions. DMC (CAS No. 616-38-6) utilised for the experimental work in ***Chapter 5*** was procured from Alfa Aesar UK, with a purity of 99%. Further specifications of the gasoline, DMC and DMC/gasoline blends are denoted as G, DMC and D8 respectively, and are provided ***Table* 3.2**.

Table 3.2: Specifications of fuels used [**32**], [**194**], [**195**], [**269**], [**292**], [**293**].

Properties	G (EN228) *	DMC	D8**
Chemical Formula	$C_{5.17}$ $H_{9.93}$ $O_{0.16}$	C_3 H_6 O_3	$C_{5.05}$ $H_{9.72}$ $O_{0.44}$ **
Research Octane Number (RON)	96.8*	101-120	97.2-98.7**
Lower Heating Value (MJ/kg)	41.65*	15.78	38.8**
Vapour Pressure @ 20˚C (kPa)	59.8-65.9*	5.3	-
Kinematic Viscosity @ 40˚C (mm_2/s)	0.8	0.6	-
Laminar Flame Velocity @1 bar, 375 K (cm/s)	33	36	-
Heat of Vaporisation (kJ/kg)	350	400	-
Initial Boiling Point (˚C)	35.5*	41.9	-
Final Boiling Point (˚C)	199.2*	203.7	-
T90 (˚C)	176*	-	-
O (m/m) %	3.48*	53.28	9.09**
Density @ 15°C (g/cm3)	0.7466*	1.076	0.7730**

* Properties provided by Shell Global Solution

** Properties based on theoretical calculations

3.4 Small Scale Aftertreament Architecture

3.4.1 Monolith Substrates Properties

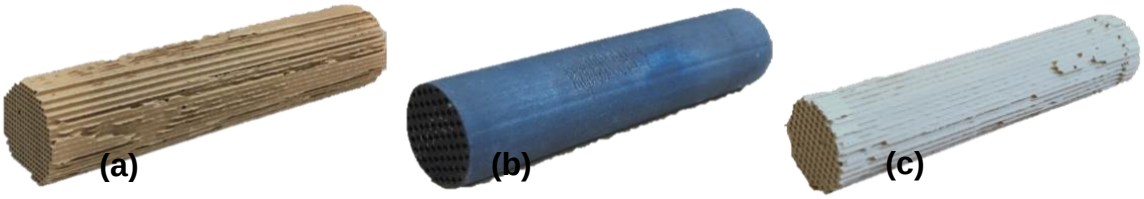


Figure 3.4: Small scale **(a)** TWC, **(b)** silicon carbide GPF and **(c)** cordierite GPF utilised in the research work.

A TWC and GPFs were supplied by Johnson Matthey Technology Centre. The size of the monolith substrates has the same length as commercial substrates (4.5 inches) and were scaled down to a diameter of 1 inch. The scaled down TWC has identical specification to a commercial TWC (***Figure* 3.4*a***). For GPF, two different materials of bare GPF were used namely, cordierite and silicon carbide (***Figure* 3.4*b*** and ***3.4c***) with properties varied which latter used to investigate its effect on aftertreatment architecture in ***Chapter 6***. Detailed properties are specified in ***Table* 3.3**.

Table 3.3: TWC and GPF monolith substrate properties.

Substrate Properties	TWC	SiC. GPF	Cord. GPF
Material	Cordierite	Silicon Carbide	Cordierite
Mean Pore Size, MPS (μm)	-	15.8	17 – 23
Porosity (%)	-	40	62 – 68
Cell Density (cell/in$_2$)	400	200	300
Wall Thickness (mil)	4.3	12	8.5
Washcoat Loading	Mid low	-	-
PGM Loading	Mid Low	-	-
Length (inch)	4		
Diameter (inch)	1		

3.4.2 Experimental Setup

The substrates were located inside a custom-built stainless-steel reactor (**Figure *3.5***). They were held in a large, vertical tubular electric furnace, constantly monitored by a K-type thermocouple located on top of the reactor. The thermocouple was located

close to the first monolith substrate (about 2 cm from the substrate) for accurate control of the exhaust inlet temperature, ranging between 450 to 500℃. External heating was applied to the inlet and outlet, in order to avoid condensation of water vapour and unburned HCs. An additional thermocouple was also positioned post-substrate at reactor outlet to monitor the temperature of EGT. Flow was diverted into the reactor with a by-pass from the main exhaust tailpipe, with the assistance of an in-line suction pump. Two EPT3100 Variohm pressure transducers were placed at P1 and P2 of the reactor, corresponding to the upstream and downstream of the substrates. This was in order to measure the absolute pressure. A valve was installed before the exhaust gas inlet to restrain any influence of PM formed during engine warm-up on the substrates.

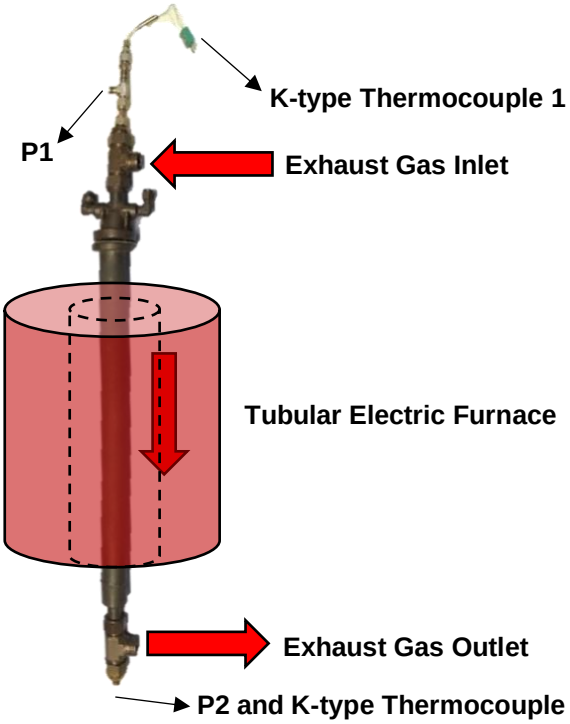


Figure 3.5: Stainless-steel reactor for small scale monolith substrates

3.5 Gaseous Emissions Instrumentation

3.5.1 Fourier Transform Infrared Spectroscopy (FTIR) Analyser



Figure 3.6: MKS Multigas 2030 FTIR gas analyser.

An MKS Multigas 2030 FTIR analyser (***Figure 3.6***) was employed to measure gaseous emissions (CO, CO_2, NO_x and THC). Additionally, it also has the ability to measure a range of hydrocarbons between C1 and C12. The concept of FTIR quantitative analysis is based on the molecular infrared (IR) spectroscopy absorption. FTIR analyses gas effectively, as every gas compound has a distinctive fingerprint. When the IR spectrum penetrates through the exhaust gas, an interaction between the exhaust gas and the spectrum takes place by absorption, reflecting the specific wavelength of a specific gas species. The standard gasoline engine emissions were predetermined in a database by the manufacturer, and was applied in the FTIR. The lowest detectable limits are 1.2 ppm, <1 ppm and 3.6 ppm for CO, HC species and NOx, respectively. The specification of the MKS Multigas 2030 gas analyser is tabulated in ***Table* 3.4**. PM in the exhaust gas is filtered prior to the inlet of FTIR in order to prevent any damage to the optical lens. Exhaust gas samples are transported with heating lines, maintaining temperature a 191°C in order to avoid water or unburned HCs condensation.

Table 3.4: Technical specification of MKS Multigas 2030 gas analyser.

MKS Multigas 2030 Gas Analyser	
Measurement Concept	IR Spectroscopy
Measurement Range	Between ppm and ppb
Spectra Resolution	0.5 cm^{-1} to 128 cm^{-1}
Scan Time	1 to 300 seconds
Scan Frequency	1 Hz
Infrared Source	Silicon Carbide at 1100 °C
Laser Reference	Helium – Neon
Detector	Liquid N_2 – cooled MCT, TE – cooled MCT
Pressure Transducer	MKS Baratron

3.5.2 AVL Digas 400



Figure 3.7: AVL Digas 440.

Although the AVL Digas 440 (***Figure 3.7***) has the ability to measure CO, CO_2, THC, NO and O_2, it was utilised for O_2 measurement. The measured concentrations were acquired at exhaust tailpipe, upstream and downstream of the TWC. Further measurements were taken in the combustion chamber of the TGA for different O_2 concentration tests. The AVL Digas 440 detects O_2 by diffusion with the R22A self-calibrated oxygen sensor. The sensor contains a circuit module comprised of an anode

and cathode, that breaks down O_2 into ions. In turn, electrons will be released, and the number of electrons passed from anode to cathode corresponds to O_2 concentration. Further technical information is included in ***Table* 3.5**.

Table 3.5: Technical specification for AVL Digas 440 for oxygen measurement.

AVL Digas 440 (Oxygen)	
Measurement Concept	Diffusion
Measurement Range	0 to 22%
Resolution	0.01%
Accuracy	If < 2%, ± 0.01 % Otherwise ± 5 %

3.6 Particulate Matter Characterisation Instrumentation

3.6.1 Scanning Mobility Particle Sizer (SMPS) 3936

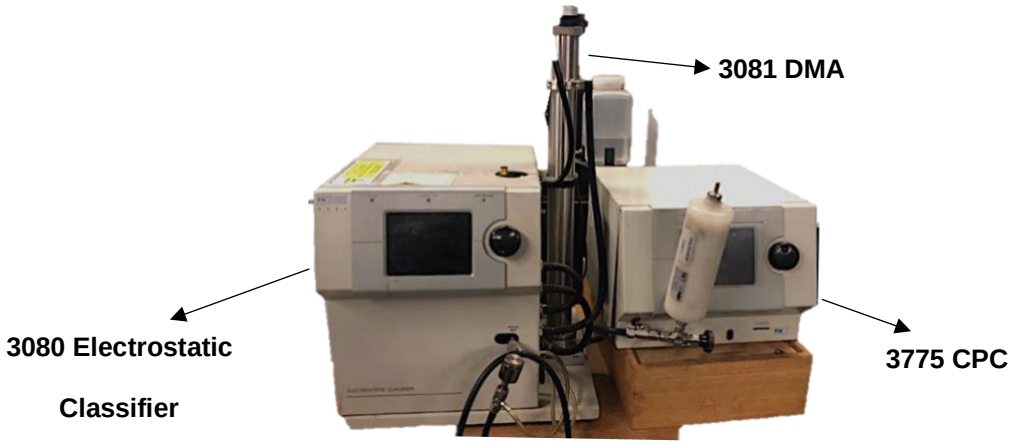


Figure 3.8: TSI SMPS 3969.

PM concentration and mass PSD were sampled with the employment of the TSI Scanning Mobility Particle Sizer (SMPS) 3936. It is comprised of a 3081 Differential Mobility Analyser (DMA), a 3080 electrostatic classifier and a 3775 Condensation

Particle Counter (CPC). The DMA and electrostatic classifier divides particles into their relative size and are subsequently counted by a CPC. The samples were acquired with an Aerosol Instrument Manager, supplied by TSI Instruments UK. The technical specification of the SMPS is detailed in ***Table* 3.6**. The sheath and sample flow rates were set at 10 and 1 litres / min respectively. A scan time of 120 seconds was set in order to obtain the PSD range of 7.77 nm to 294.3 nm.

Table 3.6: Technical specification for TSI SMPS 3969.

TSI SMPS 3969	
Measurement Range	0 to 10_7 (particles / cm_3) for both concentration and mass
Accuracy	If < 5 x 10_4, ± 10 %, otherwise ± 20 %

3.6.2 Dilution System

Prior to the sampling with the SMPS, dilution of exhaust gas was performed to mirror PM in the atmosphere. The dilution ratio (α) is calculated by measuring the NO or CO_2 emissions at the inlet and outlet of the dilutor (***Equation 3.1***). It was constantly monitored with the FTIR to ensure α remained approximately around 10 throughout the tests. The PSD plots were corrected by the factor of α across the range to accurately project the PSD of PM emissions.

Equation 3.1

$$\alpha = \frac{NO_{diluter\ inlet}\,(ppm)}{NO_{\ diluter\ outlet}\,(ppm)} = \frac{CO_{2\ diluter\ inlet}\,(ppm)}{CO_{2\ diluter\ outlet}\,(ppm)}$$



Figure 3.9: Dilution system for PM sampling in the engine test cell.

A single-stage temperature-controlled ejector dilution system was used, composed of an externally heated mixing chamber and an ejector diluter. A High Efficiency Particle Arrestance (HEPA) filter was installed before the mixing chamber to remove impurities in the air that could influence PM measurements. The dilutor was externally heated to 200 °C and fed with air heated to 150 °C from the heated mixing chamber. Exhaust gas samples were transported with a heating line, maintained at 191 °C. The setup of the dilution system is presented in ***Figure* 3.9**.

3.6.3 Thermogravimetric Analyser (TGA)

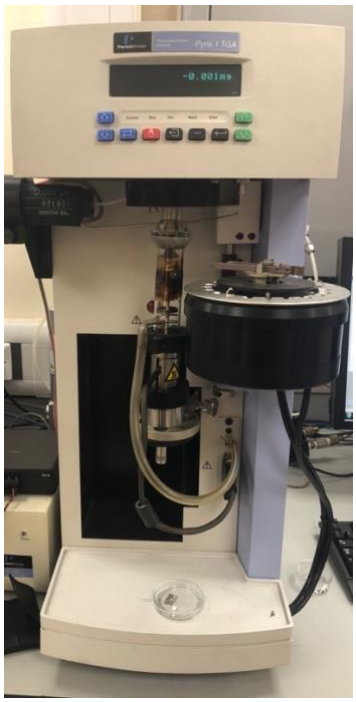


Figure 3.10: Perkin Elmer Pyris 1 TGA.

The Pyris 1 TGA (***Figure* 3.10**) created by Perkin Elmer UK was used to evaluate PM composition and PM oxidation reactivity. TGA is an instrument that has the ability to run with a programmable temperature function, that is highly sensitive to mass. Therefore, the tests are constantly observed and analysed based on the mass variations under the programmed temperatures. Samples can be analysed via ramp or isothermal studies. A ramp study was used in this thesis. Purge and sheath flowrates play an important role due to the residence time of gases, potentially affecting results. The purge flowrate was maintained at 60 ml / min by a flow meter. Meanwhile, a Thermal Analysis Gas Station (TAGS) was used to control the sheath flowrate at 40 ml / min. The TAGS also allowed switching between sheath gases; N_2, compressed air and 2% O_2 / N_2. These flowrates were calibrated with a microflow meter, supplied by Perkin Elmer, before tests were conducted. The temperature ramp tests were programmed at 3 °C / min. The programme is plotted and tabulated in

***Figure* 3.11** and ***Table* 3.8**. The program temperature was split into two stages; devolatilisation and oxidation stages. Devolatilisation (step 1 to 4) aimed to remove VOM, in order to avoid interference in the subsequent elemental soot analysis and to determine the ratio of VOM to elemental soot in the PM. The oxidation stage (step 6 and 7) was to identify the maximum mass loss rate temperature (MMLRT), start of oxidation temperature, oxidation temperature profile and E_a.

Table 3.7: Technical specifications for Perkin Elmer Pyris 1 TGA.

Perkin Elmer Pyris 1 TGA	
Temperature Range	Sub-ambient up to 1000 ˚C
Temperature Ramp Rate	Between 0.1 ˚C/ min to 200 ˚C/ min
Temperature Accuracy	± 2 ˚C
Mass Range	Up to 1.3 ± 2 µg
Mass Sensitivity	0.1 µg
Mass Accuracy	< 0.02 %

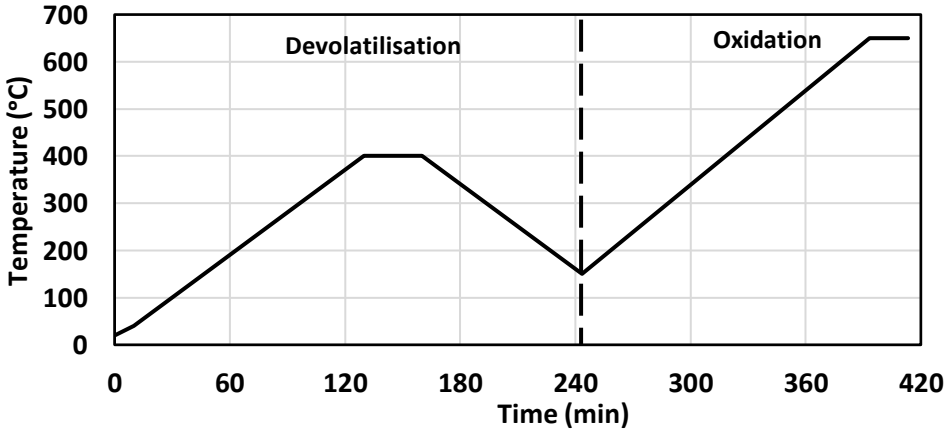


Figure 3.11: TGA temperature indication in ramp programme.

Table 3.8: TGA conditions and settings in ramp programme.

Step	Temperature	Flows
1	Hold for 10 minutes at 40 ˚C	(**Devolatilsation**) Purge: Inert gas at 60ml/min Sheath: Inert gas at 40 ml/min
2	Heat up to 400 ˚C at 3 ˚C/min	
3	Hold for 30 minutes at 400 ˚C	
4	Cool down to 150 ˚C at 3 ˚C/min	
6	Heat up to 650 ˚C at 3 ˚C/min	(**Oxidation**) Purge: Inert gas at 60ml/min Sheath: Oxidative gas at 40 ml/min
7	Hold for 30 minutes at 650 ˚C	
8	Cool down to 40 ˚C	(**Cool down**) Purge: Inert gas at 60ml/min Sheath: Inert gas at 40 ml/min

Gases utilised for the TGA tests were supplied by BOC UK. The inert gas used in the study was N_2 with N 5.2 (purity of 99.9992 %). The oxidative gases used were compressed air, containing 21 % of oxygen (± 0.5 %) and certified 2% O_2 / N_2. The PM loaded microfibre filters were used as test samples in the TGA (refer to *section 3.7.1*). The samples were prepared by cutting discs (5mm in radius) from a PM loaded microfibre filter. Prior to the actual tests, pre-tests were executed to obtain the approximate PM mass per disc. This procedure was to normalise the mass of the PM sample, in order to prevent the mass effect [**92**]. The mass of the PM was normalised to at least 0.12 mg, suggested by *Wang et al.* [**258**]. An alternative method was previously proposed for TGA sample preparation, which involves the extraction of PM from microfibre filters. However, this method was deemed unsuitable due to the influence of packing density in PM, as well as oxidation reactivity, that can lead to unreliable results [**294**] 7 pieces were used with a similar PM mass for all tests. Conditions with high PM mass loaded onto the filters required fewer loaded discs in

order to attain the normalised mass. The remaining discs were replaced with empty discs in order to avoid potential mass effect by the filter.

3.6.4 Raman Spectroscopy (RAMAN)

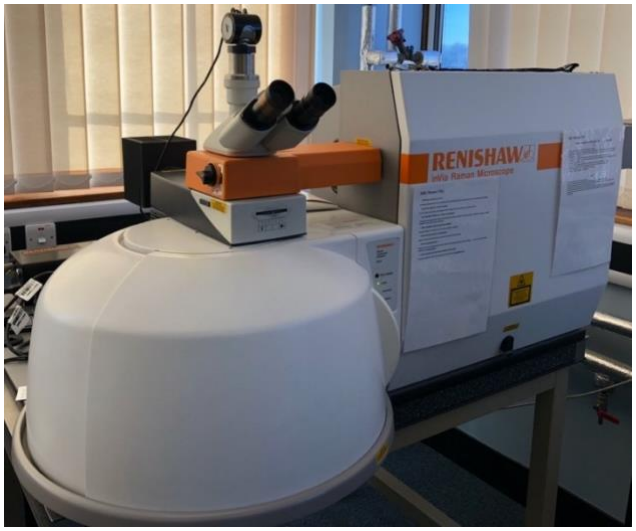


Figure 3.12: Renishaw inVia Raman Microscopy.

Renishaw inVia Raman Microscopy was used to study PM Nanostructure (***Figure* 3.12**). RAMAN is a tool that can provide information on chemical structure, phase and polymorphy, crystallinity and molecular interactions through its fingerprint spectrum (Raman shift). RAMAN uses a light scattering method from a high intensity laser. During the interaction with samples, it emits incident light, consisting mainly of Rayleigh scattering (same wavelength as the laser) and partly Raman scattering (different wavelength). The substance information lies within the Raman scattering, as every substance has distinctive wavelength, reflecting the intensity and wavelength position in the Raman spectra. RAMAN analysis was accomplished with PM loaded disc filters. Four PM disc samples were randomly prepared from the filters, and they were analysed in RAMAN by an Argon ion 532 nm edge laser. The laser intensity was

set at 1% to avoid Nanostructure alteration and PM oxidation (via burning). A 100x magnification lens was employed, precisely guiding the laser beam to a random PM spot on the disc. Five spectra were acquired from each disc, consisting of 10 accumulations, with 30 seconds exposure time on each sample spectrum. The range of the spectra was set between 800 cm^{-1} and 2000 cm^{-1}.

3.6.5 Transmission Electron Microscope (TEM)

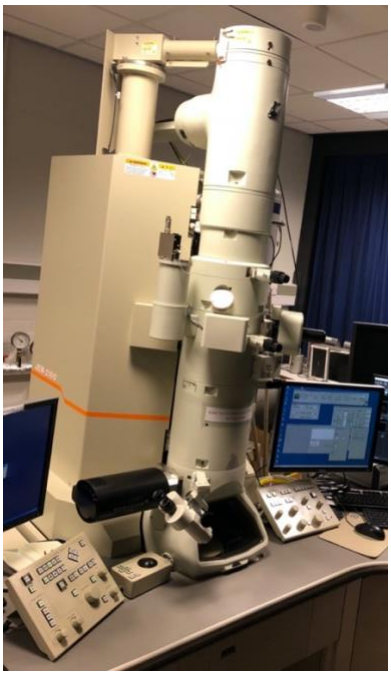


Figure 3.13: JEOL 2100 TEM with laB6 filament.

Microstructural analysis was acquired with the use of the JEOL 2100 laB6 TEM (***Figure* 3.13**). The analyses included the measurements of dp_0, number of primary particles (np_0), R_g and D_f. The TEM operation is similar to general light microscopes, but instead, electrons beam from a high voltage electron gun. Due to the extremely small wavelength of electrons, the TEM is able to obtain higher resolution images with clearer image boundaries and internal structures. TEM analysis was conducted with a

voltage setting of 200keV. Images of the agglomerates were captured in tagged-image-file-format (.tiff), in order to ensure no data loss in the images. TAAB formvar-carbon coated copper grids with a 3.05 mm diameter were utilised for the analysis. Two separate approaches were used for the TEM grid preparation; direct exhaust exposure and microfibre filter extraction. In direct exhaust exposure, TEM grids were held with a pair of tweezers and exposed to the exhaust tailpipe for 5 seconds on each side.



Figure 3.14: PM dissolved in ethanol solution.

Contrarily, the PM extracted from the microfibre filter is a longer method. A portion of loaded filters were cut and placed in an ethanol solution within a container. This was followed by extraction with an ultrasonic bath for 5 minutes. The final result of the PM-ethanol solution is presented in ***Figure* 3.14**. Finally, a micropipette was used to drop 1 ml of the PM-ethanol solution onto the TEM grids and left for drying in a contained environment. This was repeated 3 times to ensure PM were adhered onto the grids. An in-house MATLAB script, previously developed by Dr. Maria Bogarra Macias, was used for post-processing and will be discussed later.

3.7 PM Loading Instrumentation

3.7.1 Microfiber Filters

GF/F grade microfibre filters with 47 mm diameters (supplied by LLG) were used for the purpose of PM loading. The filters were tested with the TGA full ramp programme to ensure suitability, with no material loss during the test. Pre-treated and non-treated filters demonstrated that no significant difference was found, and no material loss occurred during the test. The properties of the filters are tabulated in **Figure 3.9**

Table 3.9: Properties of LLG GF/F.

LLG GF/F Microfibre Filters	
Diameter	47 mm
Pore Size	60 µm
Thickness	0.26 mm

3.7.2 PM Loading Setup

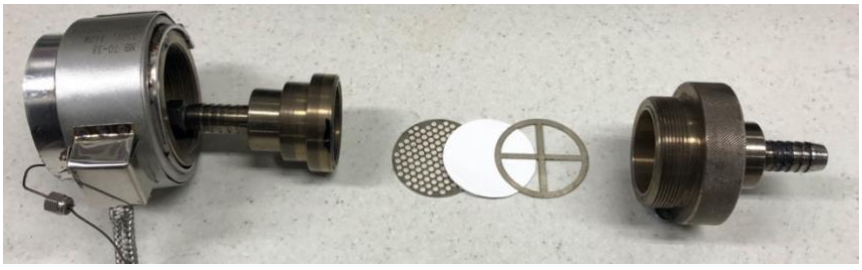


Figure 3.15: Customised filter holder.

Despite there being no material loss observed, filters were still pre-treated. The filters were baked in the oven for 6 hours at 500 ˚C in order to prevent moisture

absorption prior to the loading process. The filter was then placed in a customised filter holder (***Figure* 3.15***)*, and external heating was applied to the outside of the holder. This allowed an exhaust gas temperature to be maintained at 200 ˚C. Continual measurements were obtained by a K-type thermocouple, closely positioned on top of the filter. The process was assisted by a pump, with a flowrate of 15 l / min. The extraction processes used a heated line that extracted exhaust gas samples from the pre-TWC engine tailpipe to the holder. The loading duration was estimated by the PSD results. Less PM concentration and mass indicated in the PSD required a longer loading duration. This is to ensure sufficient PM mass samples for TGA and RAMAN analyses.

3.8 Data Processing

3.8.1 Combustion Analysis

3.8.1.1 Rate of Heat Release (RoHR) and Mass Fraction Burned (MFB)

Calculation of the RoHR and MFB was based on the average in-cylinder pressure acquired from 200 engine cycles. The RoHR was derived from ***Equation* 3.2** according to the theory published by *Heywood et al.* [**4**]. Where, P is the instantaneous in-cylinder pressure, V is the displaced instantaneous cylinder volume, $\frac{dQ}{d\Theta}$ is the apparent RoHR, and γ is the specific ratio of heat capacity. γ can be estimated by interpolation of the logarithm pressure-volume curves.

Equation 3.2 $$\frac{dQ}{d\Theta}\left(\frac{J}{deg}\right) = \frac{\gamma}{\gamma-1}.p(bar).\frac{dv}{d\Theta}\left(\frac{m^3}{deg}\right) + \frac{1}{\gamma+1}.v\ (\mathrm{m}^3).\frac{dp}{d\Theta}\left(\frac{bar}{deg}\right)$$

MFB was calculated by the ratio of cumulative heat release to total heat release. ***Equation* 3.3** was utilised for the MFB calculations and to plot the MFB curve. Where,

MFB_{Θ} is the MFB at a given CAD, $QR_{cumulative\ (\Theta)}$ is the cumulative heat release and QR_T is the total heat release. A normalised value was obtained between 0 and 1 for start and end of combustion, corresponding to 0% to 100% of MFB. Subsequently, MFB10 and MFB90 were used to estimate the ignition duration (MFB0 to MFB10) and combustion duration (MFB 10 to MFB90). Additionally, the MFB50 was used as the reference for combustion phasing.

Equation 3.3

$$MFB_{(\Theta)} = \frac{QR_{cummulative\ (\Theta)}}{QR_T}$$

3.8.1.2 Combustion Efficiency ($\eta_{combustion}$)

An indication of combustion efficiency was computed from the inefficiency of the exhaust gas species, mainly THC, CO and H_2, with ***Equation* 3.4**. It was estimated based on the residual energy that remained in the exhaust stream using the LHV_x and the mass flowrate, $\dot{m}_x$. The LHV_{THC} was assumed to be the LHV of the respective fuel blend.

Equation 3.4

$$\eta_{combustion} = 1 - \left[\frac{\left(LHV_{fuel}\left(\frac{kJ}{kg}\right) \times \dot{m}_{THC}\left(\frac{kg}{h}\right)\right) + \left(LHV_{CO}\left(\frac{kJ}{kg}\right) \times \dot{m}_{CO}\left(\frac{kg}{h}\right)\right) + \left(LHV_{H_2}\left(\frac{kJ}{kg}\right) \times \dot{m}_{H_2}\left(\frac{kg}{h}\right)\right)}{LHV_{fuel}\left(\frac{kJ}{kg}\right) \times \dot{m}_{fuel}\left(\frac{kg}{h}\right)}\right]$$

3.8.1.3 Combustion Stability

Combustion stability was determined by the COV_{IMEP} derived from ***Equation* 3.5.** Higher values indicate lower combustion stability. In order to calculate the standard deviation and mean of IMEP, the IMEP is calculated with ***Equation* 3.6**. The IMEP is the summation of all four individual strokes mean effective pressure (MEP). MEP is an important indication of the engine load, allowing comparisons between engines with alternative designs and configurations. The MEP was computed for each of the four-

cycle strokes, based on ***Equation* 3.7**. Where, $\bar{p}$ is the mean in-cylinder pressure during an interval of crank rotation, dV is the displaced volume by the piston and V_s is the total swept volume over the stroke.

Equation 3.5 $$COV_{IMEP}\ (\%) = \left(\frac{Standard\ Devieation\ of\ IMEP\ (bar)}{Mean\ IMEP\ (bar)}\right)$$

Equation 3.6 $$IMEP\ (bar) = MEP_1(bar) + MEP_2(bar) + MEP_3(bar) + MEP_4(bar)$$

Equation 3.7 $$\text{MEP}_x\ (bar) = \frac{\sum \bar{p}\ (\text{bar}) \times dV\ (m^3)}{V_s\ (m^3)}$$

3.8.1.4 Brake Specific Fuel Consumption (BSFC)

Brake specific fuel consumption (BSFC) is commonly referred to, to quantify the engine fuel economy and is stated in ***Equation* 3.8**. Where, P_{Brake} is the engine brake power, calculated from ***Equation* 3.9**. The denotation of T is the engine torque, measured by the dynamometer, and N is the engine speed.

Equation 3.8 $$BSFC\ \left(\frac{kg}{kW.h}\right) = \frac{\dot{m}_{fuel}\left(\frac{kg}{h}\right)}{P_{Br}\ (kW)}$$

Equation 3.9 $$P_{Brake}\ (kW) = \frac{T\ (n.m) \cdot 2\pi \cdot N(rpm)}{60000}$$

3.8.1.5 Brake Thermal Efficiency (BTE)

The brake thermal efficiency (BTE) is a quantification of the efficiency of an engine to convert fuel energy into mechanical work. A BTE value was obtained through ***Equation* 3.10**. Brake power value was derived from ***Equation* 3.9**, and subsequently divided by the total energy input by fuel ($\dot{m}_{fuel}$ x LHV_{fuel}).

Equation 3.10 $$BTE = \frac{P_{Brake}\ (kW)}{\dot{m}_{fuel}\left(\frac{\text{kg}}{\text{h}}\right) \cdot LHV_{fuel}\left(\frac{kJ}{kg}\right)}$$

3.8.2 Gaseous Emissions

3.8.2.1 Brake Specific Emissions for THC, CO, CO_2 and NO_x

For gaseous emissions, specific emissions were computed with molar mass to avoid density variation due to the influence of temperature. Specific emissions were derived from ***Equation* 3.11**. The exhaust mass flowrate is the summation of fuel mass and intake air mass flowrates, shown in ***Equation* 3.12**. The exhaust molar mass is the total of all gaseous species found in the exhaust gas, calculated by ***Equation* 3.13**. Where, M_x is molar mass and X_x is the relative concentration of gaseous emissions.

Equation 3.11
$$\dot{m}_{exhaust}\left(\frac{kg}{h}\right) = \dot{m}_{fuel}\left(\frac{kg}{h}\right) + \dot{m}_{air}\left(\frac{kg}{h}\right)$$

Equation 3.12
$$M_{exhaust}\left(\frac{g}{mol}\right) = \left(X_{THC}(\text{ppm}) \times M_{THC}\left(\frac{\text{g}}{\text{mol}}\right)\right) + \left(X_{CO_2}(\text{ppm}) \times M_{CO_2}\left(\frac{\text{g}}{\text{mol}}\right)\right) + \left(X_{CO}(\text{ppm}) \times M_{CO}\left(\frac{\text{g}}{\text{mol}}\right)\right) + \left(X_{NO_x}(\text{ppm}) \times M_{NO_x}\left(\frac{\text{g}}{\text{mol}}\right)\right) + \left(X_{N_2}(\text{ppm}) \times M_{N_2}\left(\frac{\text{g}}{\text{mol}}\right)\right)$$

Equation 3.13
$$Brake\ Specific\ Emission\left(\frac{g}{kW.h}\right) = \frac{\dot{m}_{exhaust}\left(\frac{kg}{h}\right) \times M_x\left(\frac{g}{mol}\right) \times X_x(ppm)}{M_{exhaust}\left(\frac{g}{mol}\right) \times P_{Brake}(kW)}$$

3.8.3 PM Characterisation

3.8.3.1 Particle Size Distribution (PSD)

The exhaust emissions were diluted during PSD measurements with SMPS. Therefore, a correction factor was applied based on α in the experimental work. The

PSD was calculated with ***Equation* 3.14** across a measurable diameter range (7.77nm < dp < 294.3 nm).

Equation 3.14 $$PSD\ (nm) = \alpha \times dp\ (nm)$$

3.8.3.2 Primary Particle Diameter (d_{p0})

The measurements for dp_0 were manually performed on MATLAB, digital imaging software, Image Tool (IMTOOL as codeword). Measurements were carried out on at least 450 primary particles from at least 20 agglomerates, randomly selected for each test condition. Measurements were taken exclusively on identifiable boundaries to ensure accuracy of estimation. The images were enhanced by background removal and contrast adjustment. This is crucial for the subsequent step in the morphological analysis, in order to reduce the analytical time by the MATLAB script. Additionally, log-normality statistical tests were performed on a representative number of primary particles measured from a TEM grid representing an individual condition. The test was performed with IBM SPSS statistical software, utilising the one-sample Kolmogorov-Smirnov significance test as accordance to literature [**1**], [**8**]. This was to ensure the results data were equally distributed, and to identify the significance of results when compared to baseline conditions. The test was also to limit subjectivity in recognition of primary particle boundaries within the diameter dimensions [**214**], [**295**].

3.8.3.3 Number of Primary Particles (np_0)

Estimation of the np_0 was achieved with the use of ***Equation* 3.15**. Where, A is the area of PM agglomerate (projected in TEM images), $A_p$is the area of primary particles assumed to be circular (obtained with ***Equation* 3.16**), and a is the

exponential factor that corresponds to particle overlap, that is constantly assumed to be 1.09 [**203**], [**228**].

Equation 3.15

$$np_0 = \left(\frac{A\,(nm^2)}{A_p\,(nm^2)}\right)^a$$

Equation 3.16

$$A_p(nm) = \frac{\pi}{4}.(dp_0(nm)^2)$$

3.8.3.4 Radius of Gyration (R_g)

R_g is a projection value based on ***Equation* 3.17** [**199**], [**246**], [**296**]. Where, m is the number of pixels per PM agglomerate, and r_i is the distance (nm) from the centre of a primary particle to the centroid of PM agglomerate.

Equation 3.17

$$R_g(nm) = \sqrt{\frac{1}{m}\sum r_i^2(nm)}$$

3.8.3.5 Fractal Dimension (D_f)

Agglomerates geometries are determined by the value of D_f. D_f allows the evaluation of primary particle compactness in an agglomerate [**199**], [**208**]. It also allows insight into the type of collisions experienced by PM agglomerates during the formation process [**297**]. The higher magnitude of D_f resembles compact, clustered PM agglomerates. Conversely, lower D_f means less compact, more chain-like PM agglomerates [**228**]. Chain-like PM agglomerates are formed by the collision between (i) primary particles and smaller agglomerates, or (ii) both smaller agglomerates [**209**]. This is known as the 'diffusion-limited' mechanism, which dictates the overall nature of collisions. This occurs in circumstances when the free path is smaller than the PM agglomerates [**298**]. The collisions occur at the tip of the agglomerates via *Brownian* motion. Conversely, clustered PM agglomerates are promoted when the mean free path is greater than the size of PM agglomerate. It is mainly dominated by a 'ballistic'

mechanism that occurs between primary particles and clustery PM agglomerates, penetrating directly into the clusters due to the ballistic trajectories.

Three different methodologies were used to estimate the D_f, including the minimum bounding rectangular method D_f (LW), the power law relationship D_f (R_g) and roof form factor (RFF). These methodologies were applied to ensure the consistency of D_f results. D_f (LW) and D_f (R_g) were acquired from the evaluation of the linear regression gradient line, derived from ***Equation* 3.18** and ***Equation* 3.19** respectively [**210**], [**296**]. RFF is a non-dimensional parameter, and is comparable to D_f based on the ratio of area to perimeter (***Equation* 3.20**) [**202**]. Where k_f is the pre-factor or structural coefficient [**210**] and L and W are the length and width of the minimum bounding method.

Equation 3.18
$$\ln n = \ln k_f + D_f \,.\ln\left(\frac{\sqrt{L(nm).W(nm)}}{dp_0\,(nm)}\right)$$

Equation 3.19
$$\ln n = \ln k_f + D_f \,.\ln\left(\frac{R_g(nm)}{dp_0(nm)}\right)$$

Equation 3.20
$$\mathrm{RFF} = \sqrt{\frac{4.\pi.A_p(nm^2)}{Perimeter\,(nm)^2}}$$

3.8.3.6 PM Composition and Oxidation Reactivity

PM composition is divided into VOM and elemental soot, and derived from ***Equation* 3.21** and ***Equation* 3.22**. Where, $Mass_{\,VOM}$ is the mass measured from TGA.

Equation 3.21
$$VOM\ (\%) = \frac{Mass_{\,VOM}\,(mg)}{Total\ PM\ Mass\ (mg)} \times 100\%$$

Equation 3.22
$$Elmental\ Soot\ (\%) = 100\% - VOM$$

The oxidation reactivity of PM is determined by two distinguished approaches; (i) MMLRT and (ii) E_a. MMLRT was identified as the peak temperature from the first

derivative of mass variation $\left(\frac{dm}{dT}\right)$ across the temperature axis. When PM is more reactive, a lower MMLRT value will be obtained. Furthermore, the $\frac{dm}{dT}$ was also used to compute the E_a using the Arrhenius equation through gradient evaluation of linear regression (***Equation* 3.23**). Where, E_a value is the energy required to oxidise PM, m is the instantaneous mass of the sample, T is the temperature in Kelvin (K), R is the universal gas constant (8.314 J/mol.K) and A_{pO_2} is the oxygen partial pressure. The weight loss of between 10 % to 50 % was considered in the calculation of E_a [**141**].

Equation 3.23 $$\ln\left(-\frac{1}{m\,(mg)}.\frac{dm\,(mg)}{dT\,(K)}\right) = \frac{-E_a\,(J.mol^{-1})}{R\,(J.mol^{-1}.K^{-1})}.\left(\frac{1}{T(K)}\right) + \ln A_{pO_2}(bar)$$

3.8.3.7 In-House MATLAB Script

As mentioned in *section 3.6.5 Transmission Electron Microscope (TEM)*, the in-house MATLAB script used can be reviewed in detailed at *Appendix 4: Additional Information*. The script comprised of several calculations, (i) images pixel calculation which was responsible for all morphological analyses, (ii) centroid calculation for obtaining R_g, (iii) binarization and projected area calculations for R_g and np_0 estimations respectively, (iv) minimum bounding rectangular calculation to obtain L and W for the use in ***Equation* 3.19**, (v) np_0 estimation which includes ***Equation* 3.15**, (vi) R_g calculation composed of ***Equation* 3.17**, and (vii) perimeter and RFF calculations derived from ***Equation 3.2***.

3.8.3.8 Nanostructure

The RAMAN spectra was post-processed with Renishaw Wire software. Several methodologies have been proposed by literature for deconvolution (curve fitting). However, 3 Lorentzian and 1 Gaussian (3L1G) fitting was chosen due its closest connection to PM oxidation and its lowest fitting error, χ^2 [**299**]. The 3L bands were

composed of G, D_1 and D_4, measured at 1590 cm^{-1}, 1360 cm^{-1} and 1180 cm^{-1} respectively. The G band was composed of D_3 and measured at 1500 cm^{-1}. Only the D_1 and D_3 bands were evaluated. The D_1 identified the graphene layer defects by measuring the magnitude of disordered graphene layers in the edge site. The D_3 measured the amorphous content in primary particles (non-graphitic carbon) comprising of organic molecules, fragments and functional group [**299**]. As the G band is the graphitic peak that corresponds to perfectly ordered graphene layers, it was taken as the benchmark for analysis. The evaluation was based on the intensity and area ratio of the D_1 and D_3 bands to G band, as following; I_{D1}/I_G, I_{D3}/I_G, A_{D1}/A_G and A_{D3}/A_G. Additionally, the full width half maximum (FWHM) of D1 was also used for estimating the disorder of graphene layers.

Furthermore, the 3L1G fitting method was demonstrated to be able to provide a similar estimation of L_a to the TEM examination. The formula introduced was modified by *Seong et al.*[**299**], using the area ratio of D_1 to G as indicated in ***Equation* 3.24.**

Equation 3.24

$$L_a(nm) = 4.4 \left(\frac{A_{D1}}{A_G}\right)^{-1}$$

3.8.4 GPF Performance Analysis

3.8.4.1 Filtration Efficiency ($\eta_{Filtration}$)

The GPF assessment is determined by the filtration efficiency ($\eta_{Filtration}$), calculated by the difference before and after the GPF as shown in ***Equation* 3.25**. Where, $PM_{before\ GPF}$ is the PM concentration before GPF and $PM_{after\ GPF}$ is the PM concentration after GPF.

Equation 3.25

$$\eta_{Filtration}\,(\%) = 100\% \times \left(\frac{PM_{before\ GPF} - PM_{after\ GPF}}{PM_{before\ GPF}}\right)$$

3.8.4.2 Pressure Drop

Equation* 3.26** was utilised to measure the pressure drop of the GPF, with two absolute pressure measurements acquired from pressure transducers. Where p_1 is the absolute pressure before the GPF, and p_2 is the absolute pressure after GPF, as illustrated in ***Figure 3.5.

Equation 3.26

$$Pressure\ Drop\ (bar) = p_2(\text{bar}) - p_1(bar)$$

CHAPTER 4 INVESTIGATION OF COMBUSTION AND PM CHARACTERISTICS WITH DIFFERENT AIR-FUEL RATIO AT MBT CONDITION

4.1 Introduction

As discussed in ***Chapter 2***, the effect of AFR was evaluated comprehensively in terms of combustion characteristics and gaseous emissions. Therefore, this investigation was performed briefly focusing on combustion and gaseous emissions under MBT conditions. Previously, PM has been understood in terms of concentration, mass and oxidation reactivity, as well as microstructure and Nanostructure. However, both micro and Nanostructural analyses have mainly defined PM characteristics; scarcely linking them to combustion characteristics, and therefore our understanding of PM formation is limited. Additionally, a limited PM oxidation reactivity has been studied by literature. This chapter includes several areas, including PM oxidation reactivity and composition with the use of TGA, and PM formation with reference to the combustion characteristics. Previous studies in the literature have executed combustion phasing (MFP50 phasing) or constant spark timing. This has led to the AFR investigation under the MBT conditions.

4.2 Methodology and Test Conditions

Table 4.1: Experimental matrix and engine condition.

Engine Condition			
Speed (rpm)		2200	
Torque/Load (Nm)		90	
Intake Valves Opening (CAD aTDC)		11	
Exhaust Valves Closing (CAD aTDC)		8	
Stoichiometry, λ	1	1.1	0.9
Air-Fuel Ratio, AFR	14.23	15.66	12.80
Injection Timing (CAD bTDC)	299	293	299
Spark Timing (CAD bTDC)	26	28	23

***Table* 4.1** tabulates the experimental matrix and engine conditions used in the study. The engine torque and speed were set at 90 Nm / 2200 rpm corresponding to a representative operating condition of the light-duty vehicle driving cycle in WLTP. The engine oil and coolant were warmed up to 90 ± 0.5 ˚C and 95 ± 2 ˚C respectively, prior to initiation of the test, to ensure engine stability for repeatability of results. The engine charged-air temperature was also warmed up to 40 ± 2 ˚C before the tests. The IEGR was removed by setting the IVO and EVC to 8 and 11 aTDC respectively to avoid influencing the acquired results. The ECU was mapped with MBT conditions, hence only the λ of the engine was varied between 0.9, 1 and 1.1, equivalent to rich, stoichiometric and lean conditions. The spark and fuel injection timing were default settings according to the MBT for each individual λ. ***Figure* 4.1** illustrates a schematic drawing of the experimental setup for this chapter. This diagram includes indications of sampling points for gaseous and PM emissions, PM loading and TEM grid

preparation. In order to ensure repeatability and reliability of results, gaseous emissions were measured for at least 300 seconds and PM measurements were conducted five times. PM was loaded for at least 90 minutes, as displayed in ***Figure 4.2***.

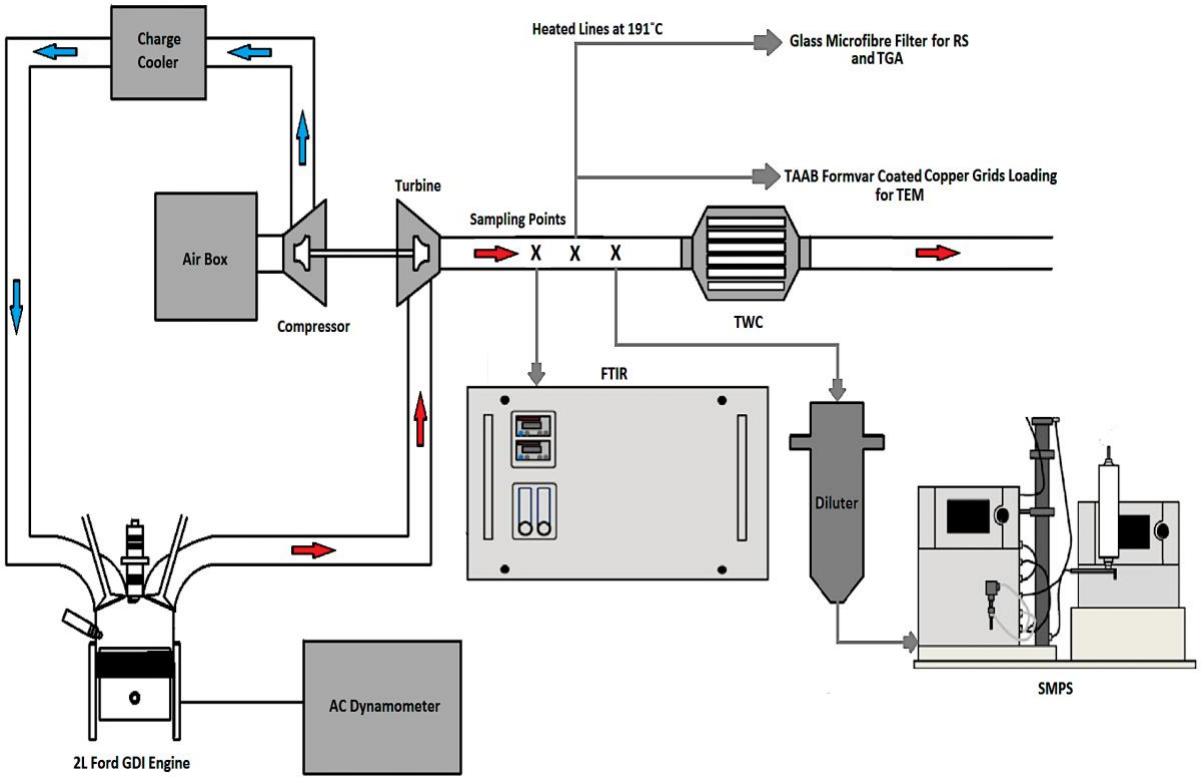
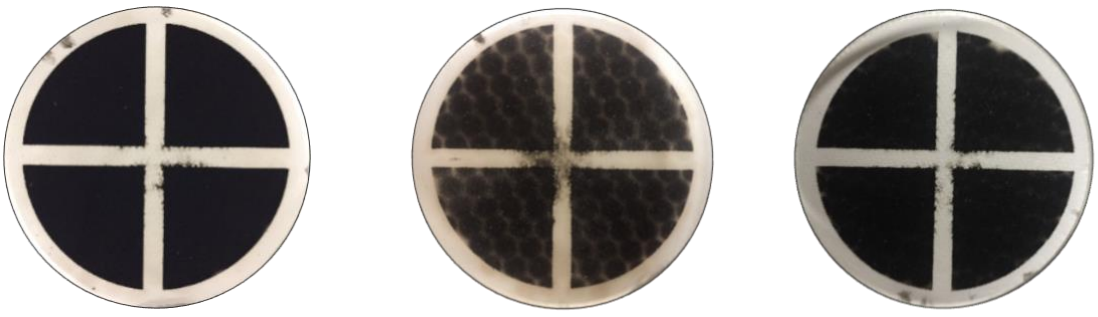


Figure 4.1: Schematic of experimental setup.



(a) **(b)** **(c)**

Figure 4.2: PM loaded filters of **(a)** stoichiometric (λ **=** 1), **(b)** lean (λ=1.1) and **(c)** rich (λ = 0.9)

4.3 Results and Discussion

4.3.1 Combustion Characteristics

Table 4.2: COV_{IMEP}, ignition duration, MFB50 and combustion duration of λ = 0.9, 1 and 1.1.

Stoichiometry, λ	COV_{IMEP} (%)	Ignition Duration (CAD)	MFB50 (CAD aTDC)	Combustion Duration (CAD)
Stoichiometric (λ = 1)	1.45	24.98	7.695	22.25
Lean (λ = 1.1)	2.02	28.01	10.65	`26.19
Rich (λ = 0.9)	1.21	23.78	10.19	25.86

The COV_{IMEP}, ignition duration, MFB50 and combustion duration are tabulated in ***Table* 4.2**. Combustion stability of each condition is reflected by the COV_{IMEP}. From the results, combustion stability is reduced, as the combustion mixtures transition to leaner AFR. This is linked to the prolonged ignition duration [**4**], [**189**], [**191**], [**192**]. The ignition duration is commonly used to evaluate flame kernel growth at the early flame development stage. The effect is due to the sensitivity of flame speed and RoHR during ignition period [**192**]. This is because the leaner mixture has a less severe chemical reaction during combustion, due to the higher dilution by air. This results in the reduction of energy transfer to the air-fuel mixture within the spark plug vicinity. Additionally, the leaner mixture has a locally inconsistent air-fuel mixing process from cycle-to-cycle, resulting the flame kernel growth is affected as the motions vary [**300**]. Oppositely, when more fuel is injected into the combustion chamber (rich condition), the higher cylinder temperature can improve the flame kernel growth. This is the consequence of a greater reaction within the spark plug vicinity, and the enhanced atomisation of fuel [**301**]. Despite having a shorter ignition duration with rich mixture,

the MFB50 is delayed due to extended combustion duration. This is the result of inadequate oxygen concentration in the combustion. Meanwhile, the delayed MFB50 for λ = 1.1 is due to the longer ignition duration. In general, the COV_{IMEP} of the varied λ is below the recommended stable combustion limit of 5% [**1**].

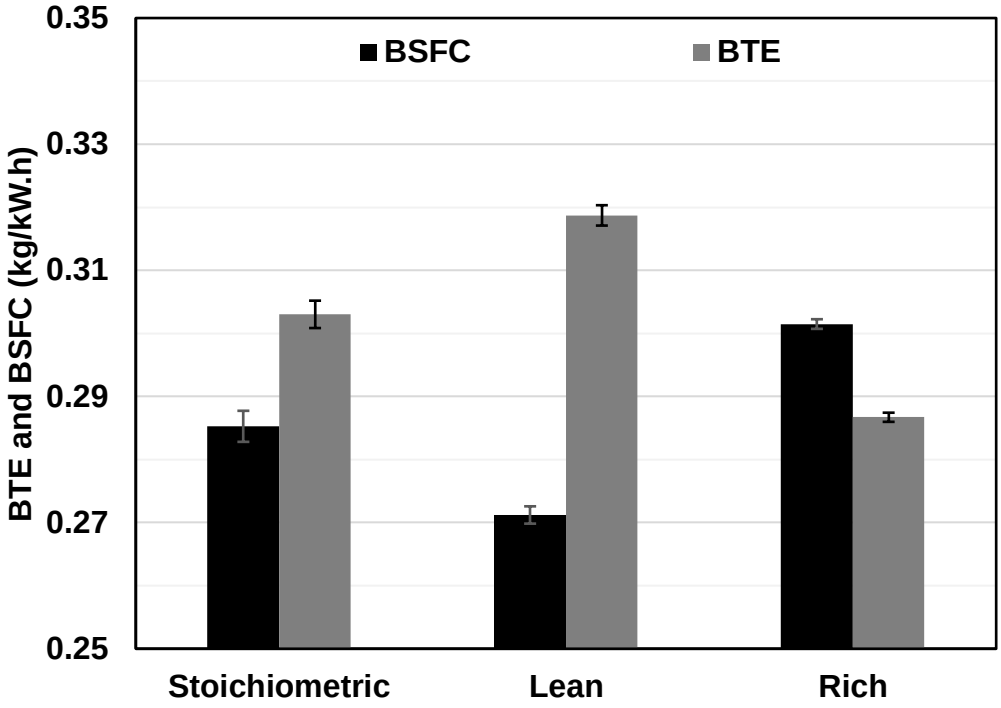


Figure 4.3: BSFC and BTE of λ = 0.9, 1 and 1.1.

BSFC and BTE are presented in ***Figure* 4.3**. In the lean mixture, the BSFC was reduced by 5.44 %, and the rich mixture increased by 5.96 %, in comparison to the stoichiometric value. The data indicates that leaner combustion results in enhanced fuel economy. Therefore, illustrating a relationship between engine efficiency and fuel economy. Both were improved concurrently as the mixture got leaner, as BTE is inversely proportional to BSFC. When the mixture became leaner, the lower BSFC increased the BTE, as more air was introduced into the engine, reducing the pumping loss. In turn, the volumetric efficiency was improved [**300**]. Secondly, the γ was also

increased as the result of more expansion work in the engine; leading to a greater work output by the engine [**192**], [**302**]. Therefore, BTE was seen to drop from 0.303 to 0.287 for the rich mixture, and improved to 0.319 for the lean mixture.

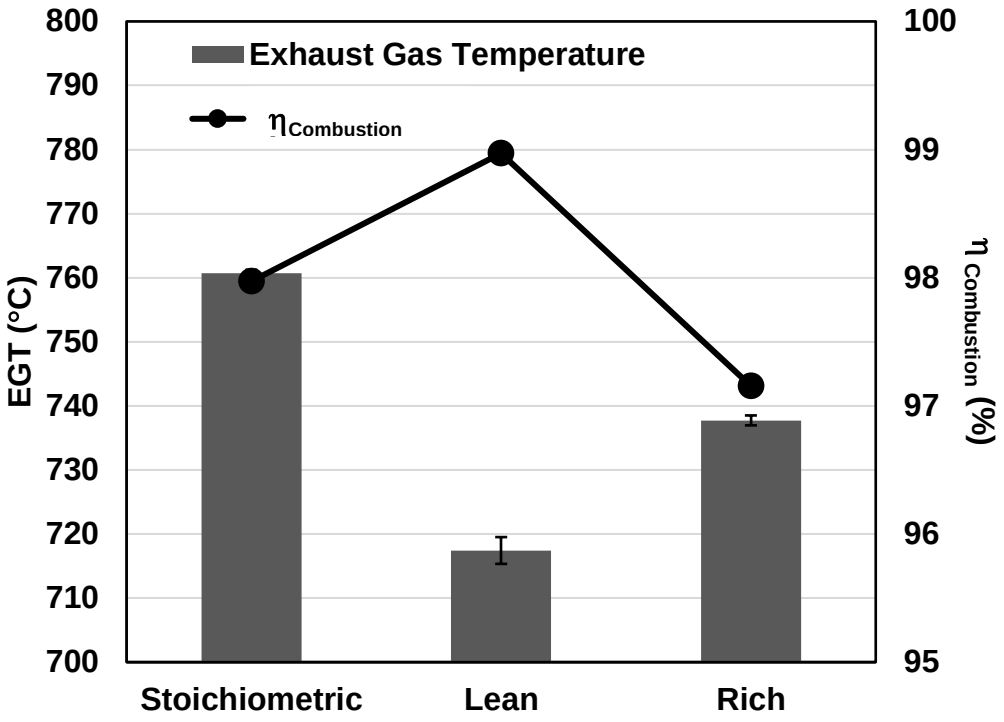


Figure 4.4: EGT and $\eta_{Combustion}$ of λ = 0.9, 1 and 1.1.

***Figure* 4.4** is the $\eta_{Combustion}$ and EGT. The trend of $\eta_{Combustion}$ has shown a similar trend to BTE, where excess air promotes better air-fuel mixing and subsequently more complete combustion. This demonstrated an increase of λ improved the $\eta_{Combustion}$ from 97.2 % to 98.9 %, as more combustion took place indicated by the lower THC and CO concentrations in the exhaust gas. In relation to the EGT, the lean condition had the lowest value of 717 °C in comparison to stoichiometric and rich conditions. This was a direct result of less heat loss via the coolant system and the exhaust. It was related to excess air acting as a diluent and therefore lowering the in-cylinder temperature [**190**]. For the rich condition, the EGT was measured at 738 °C (lower than

stoichiometric condition (760 °C). This was due to the limited oxygen in the combustion chamber, which consequently reduced the combustion reaction.

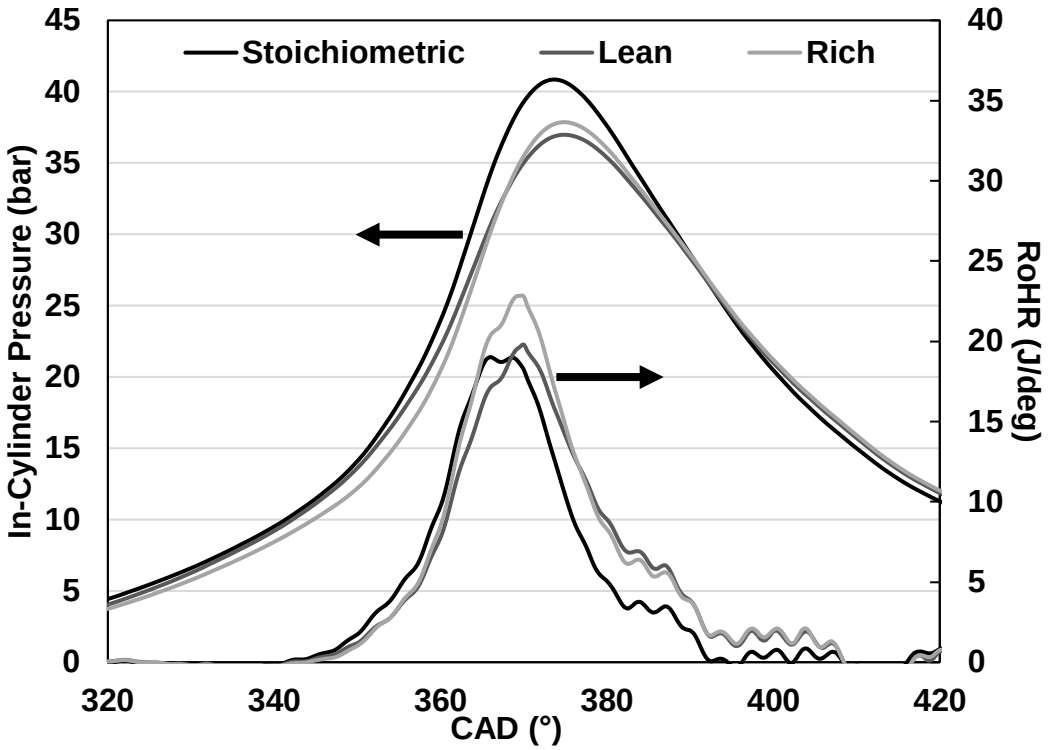


Figure 4.5: In-cylinder pressure and RoHR of λ = 0.9, 1 and 1.1.

In-cylinder pressure and RoHR are plotted in **Figure 4.5**. The trend of the acquired P_{Max} was as follows; stoichiometric > lean > rich (40.8, 37.9 and 37.0 bar respectively). The lower P_{Max} during lean combustion was because excess diluent had reduced the combustible vapour in the combustion chamber [**193**] and consequent to the loss of heat capacity in the mixtures [**300**]. In relation to the rich condition, the lower in-cylinder pressure profile was attributed to the incomplete combustion as a result of inadequate oxygen concentrations [**193**]. On the other hand, the highest peak value was measured under the rich condition in heat release plot, likewise for the total heat release (cumulative curve). Several reasons were identified. First, the quicker flame speed during flame ignition period had enhanced the flame propagation rate [**190**],

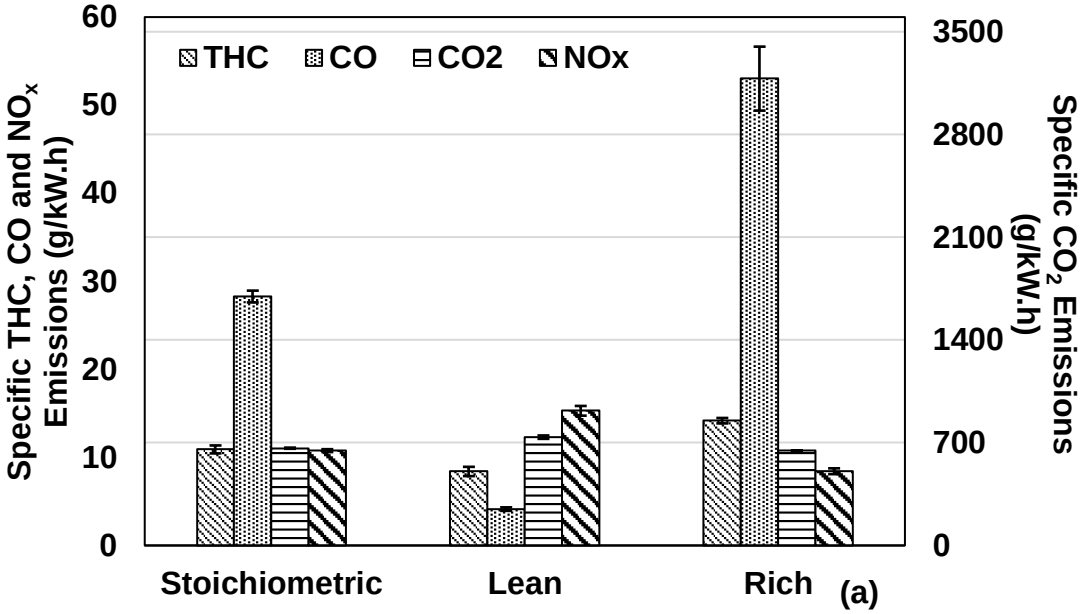
improving the combustion consistency. Secondly, the delayed spark timing (***Table* 4.1**) had increased the compression stroke. The longer compression stroke contributed to the higher in-cylinder temperature and greater surface area to volume ratio, resulting in greater heat transfer, as reflected in the RoHR profile [**4**]. Hence, this explains the comparatively higher exhaust gas temperature exhibited in the rich condition than the lean condition, despite a slighter combustion reaction. The lean condition has a similar RoHR peak to the stoichiometric condition, but with a higher total heat release. The peak value of RoHR was a direct result from substantial heat release after the TDC, due to the prolonged combustion duration. Concurrently, this promoted the work done by the engine and reduced the heat release from the mixture during the combustion process [**300**]. However, the greater total heat release has been attributed to more complete combustion aided by the excess oxygen in the combustion chamber.

4.3.2 Gaseous Emissions

Gaseous emissions composed of THC, CO CO_2 and NO_x emitted by λ are illustrated in ***Figure* 4.6*a***. THC is mainly produced by (i) the misfiring, incomplete combustion or high concentration of diluent leading to incomplete flame propagation, (ii) the flame quenching effect and (iii) fuel absorption in the crevice volume, as mentioned in *section 2.1.5.1*. The gradual improvement in THC emissions as λ increases was attributed to the availability of oxygen, enhancing the main combustion process (more complete combustion). This process led to lower THC mass trapped in the crevice volume [**300**]. Additionally, the presence of excess oxygen also aided post-combustion oxidation. Therefore, the difference of THC measured in the exhaust tailpipe under lean and rich conditions are at -22.9 % and +29.9 % in respect to

stoichiometric. ***Figure* 4.6*b*** illustrates the specific measurable HC species in the FTIR, confirming that the variation of the measured THC under all conditions were due to the variation of measurable HC species.

The relationship between CO and CO_2 demonstrates an inverted trend, associated with numerous factors. As λ became leaner, the combustion process was more complete due to the excess oxygen availability. This reduced CO, subsequently turning it into CO_2. Therefore, in comparison to the baseline condition (stoichiometric), CO emissions were highest under the rich condition (+87.0 %) and were lowest under the lean condition (-86.5 %). In contrast, CO_2 was highest under the lean condition (+2.5%) and lowest during the rich condition (-11.2%). The non-linear reduction of CO_2 during the lean condition may be related to lower fuel consumption.



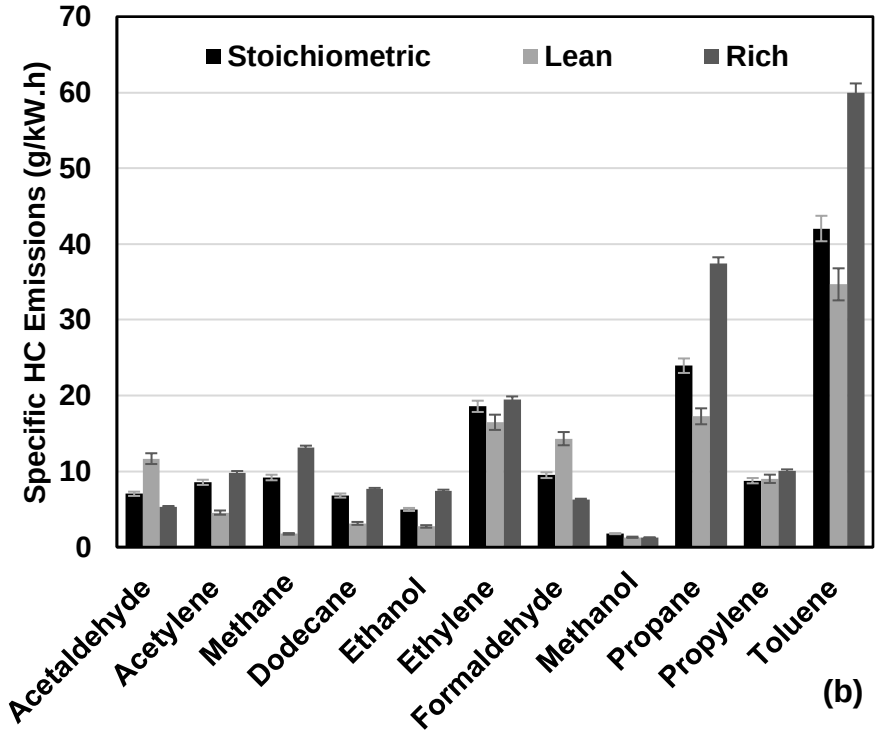


Figure 4.6: Specific **(a)** gaseous emissions and **(b)** HC species emissions of λ = 0.9, 1 and 1.1.

Thermal NO_x in the ICE is commonly associated with the Zeldovich mechanism, therefore has been used to justify NO_x emissions in this chapter [**30**]. Several factors were involved, such as (i) temperature, (ii) oxygen and nitrogen concentration and (iii) residence time [**4**]. The greatest concentration of NO_x was formed during the lean condition, which corresponded to an increase of approximately 42.0 % when compared to stoichiometric. The lowest concentrations were observed during rich conditions, exhibiting a decrease of 21.7%. It was presumed that the in-cylinder temperatures under all tested conditions were sufficient enough for the formation of NO_x. The longer residence time (combustion duration) and higher oxygen concentration during the lean condition impacted the formation of NO_x at a higher rate. Contrarily, despite the longer combustion duration during the rich condition, the limited

oxygen concentration in the combustion chamber reduced the NO_x formation. Additionally, NO_x was also suppressed by the decomposition of NO, which is increasingly more prominent during richer λ conditions [**303**]. This relation is expressed by the HCCO-NO reaction [**304**]. HCCO radicals are formed during combustion but are more likely to react with oxygen. Hence, this reaction is less prominent when λ is leaner, result of a greater presence of oxygen in the combustion chamber.

4.3.3 PM Characteristics

4.3.3.1 PM Emission

The number and mass PSDs are plotted in ***Figure* 4.7**. It is generally accepted that combustion during lower λ conditions can lead to higher concentrations of PM. Under the rich condition in this study, PM concentration was 32 % higher than the stoichiometric condition. Additionally, the lean condition had also shown an approximately 42 % increase in PM concentration. Referring to ***Figure* 4.7*a***, the greater PM concentrations were caused by nucleation mode PM (nucleation peaks). It has also been reported by *Zhang et al.* [**188**], that lean combustion can increase the fraction of nucleation mode PM. It is speculated that greater concentrations are attributed to water condensation from more complete combustion. For rich conditions, the peak in nucleation mode PM appears to be related to the condensation of unburned HCs (THC in ***Figure* 4.6*b***). The condensation that occurred in both lean and rich conditions was caused by the lower EGT. As the exhaust gas samples were fed into the diluter at a lower temperature, it resulted in the reduction of dilution temperature below the dew points of water and HC species. This subsequently led to the occurrence of condensation in the dilutor [**98**].

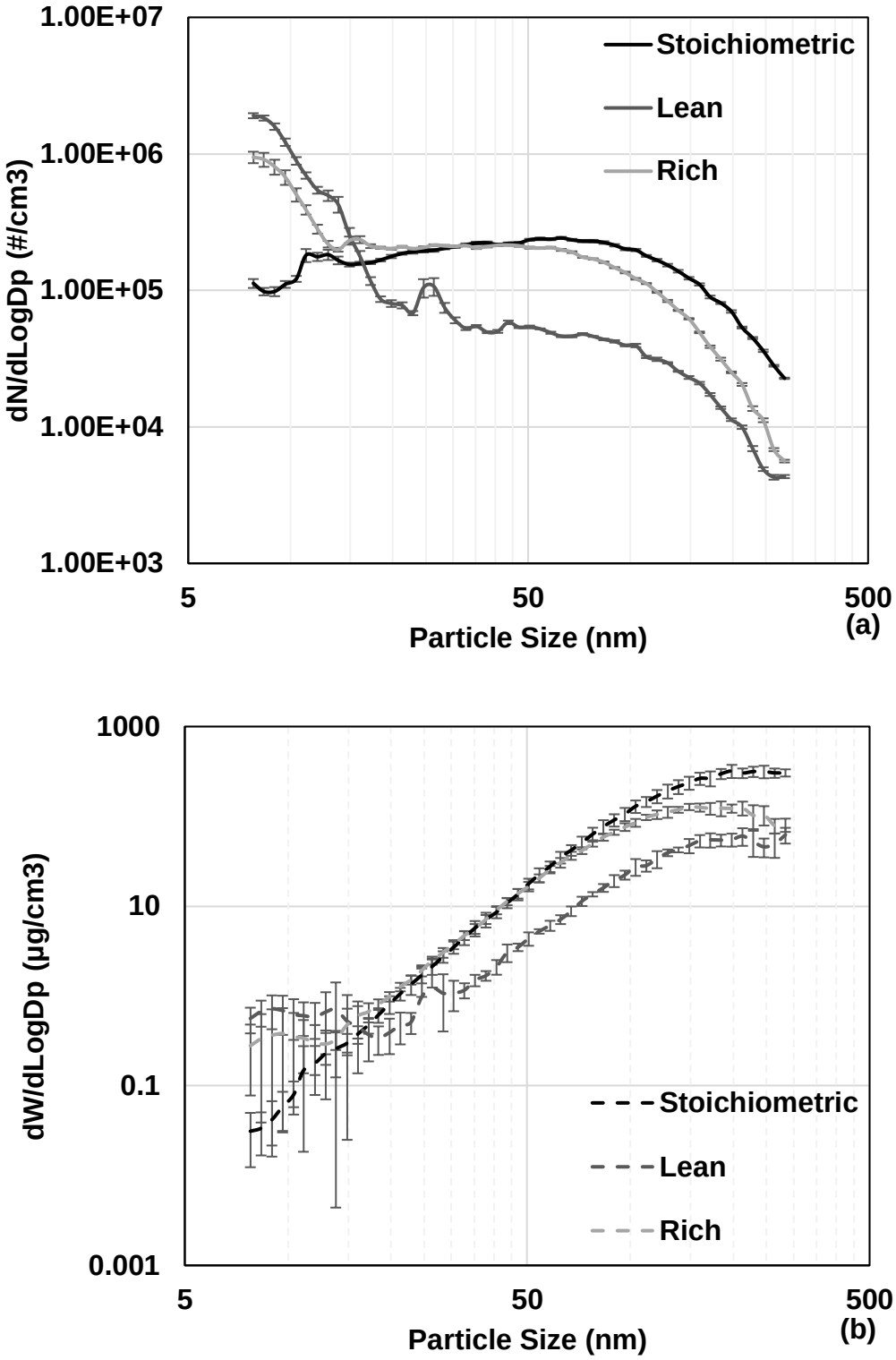


Figure 4.7: (a) Number and **(b)** Mass PSD of λ = 0.9, 1 and 1.1.

In relation to accumulation mode PM, excess oxygen in the lean condition had promoted the oxidation rate, and hindered the formation of intermediate species from their initial aromatic rings [**277**]. The lower fuel mass injected into the cylinder from the enhanced fuel economy (lower BSFC in ***Figure* 4.3**) resulted in the reduced concentration of solid PM [**44**]. Hence, the reduction was mainly seen across the diameter range between 17 nm and 284 nm.

In rich condition, the oxidation had dictated the competition between formation and oxidation. It was correlated to the higher combustion temperature (peak of the RoHR), altering the PM formation temperature and $\phi_{Critical}$. During the longer compression stroke (delayed spark timing), fuel vaporisation was enhanced, and the formation of soot by the diffusive flames (thinner fuel film impingements) was suppressed. The impinged fuel was broken down into shorter carbon chain HCs, that are more easily oxidised, leading to formation of fewer PM precursors. Under these conditions, shorter HC chains turn into CO by partial oxidation, which is a non-reversible process [**113**]. Due to less soot formation, surface area is reduced for unburned HC condensation or absorption [**107**]. Unreacted HCs were emitted in gaseous or VOM form (HC nuclei PM) by the process of condensation. This suggests that the measured PM concentration was contributed by the nucleation peak.

The greater nucleation mode PM, and the decreased accumulation mode PM, led to an overall reduction in GMND. This was observed under both lean and rich conditions, reducing from 41 nm to 30 nm and 11.6 nm respectively. ***Figure* 4.7*b*** presents the mass PSD. The data illustrates that under lean and rich conditions, a drop of approximately 81% and 52% respectively occurred, despite an increase in total PM concentration. This is attributed to nucleation mode PM having negligible impact

on the total PM mass. Additionally, the trend in the mass PSD also confirmed the decrease of GMND for both lean and rich conditions.

4.3.3.2 PM Composition and Oxidation Reactivity

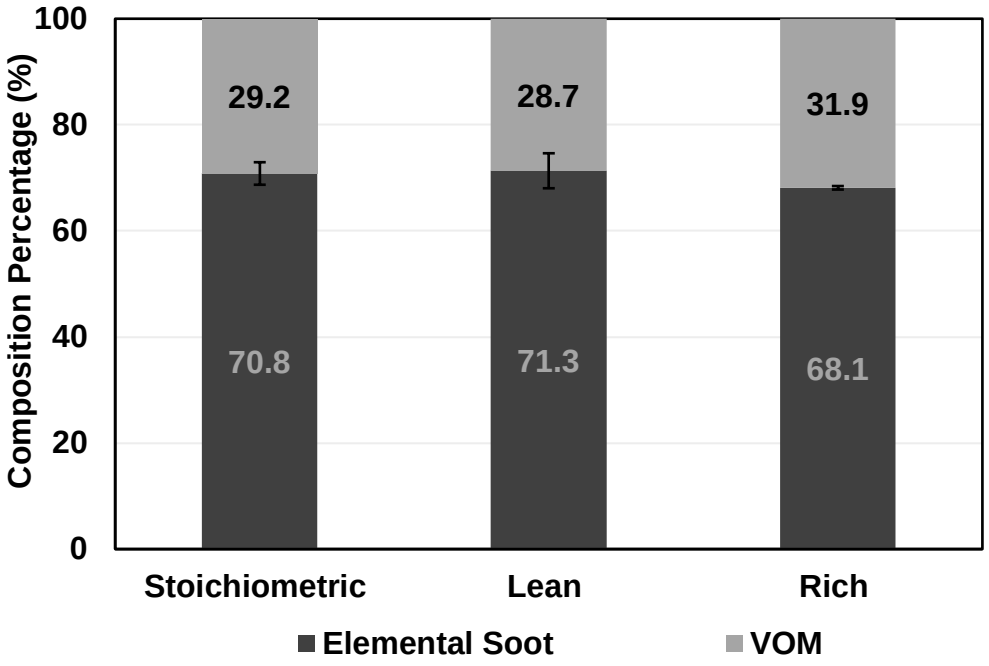
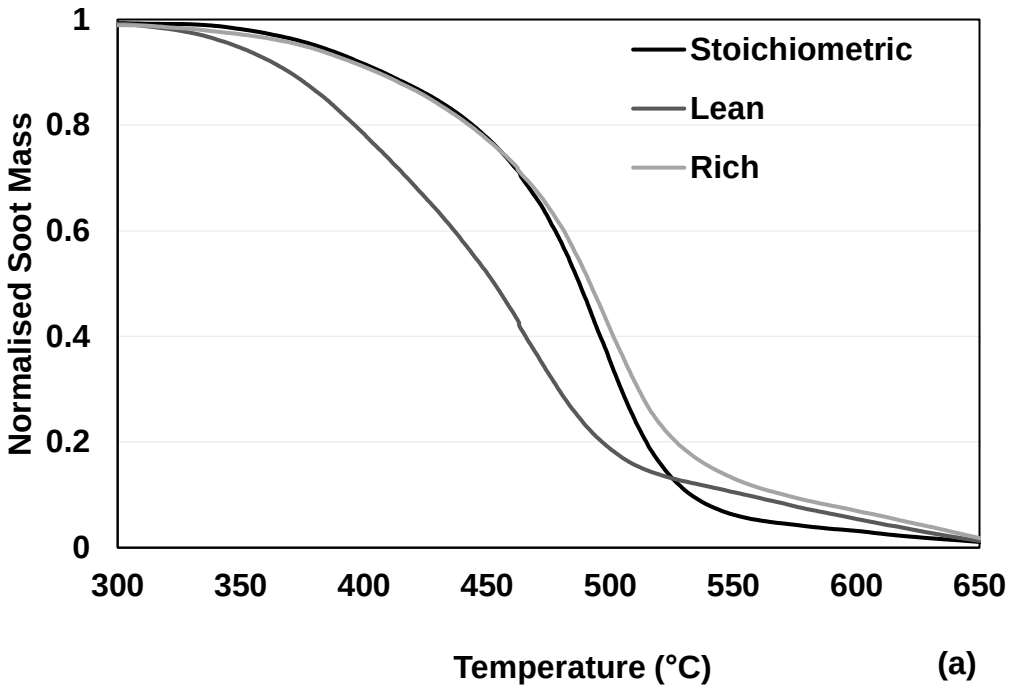
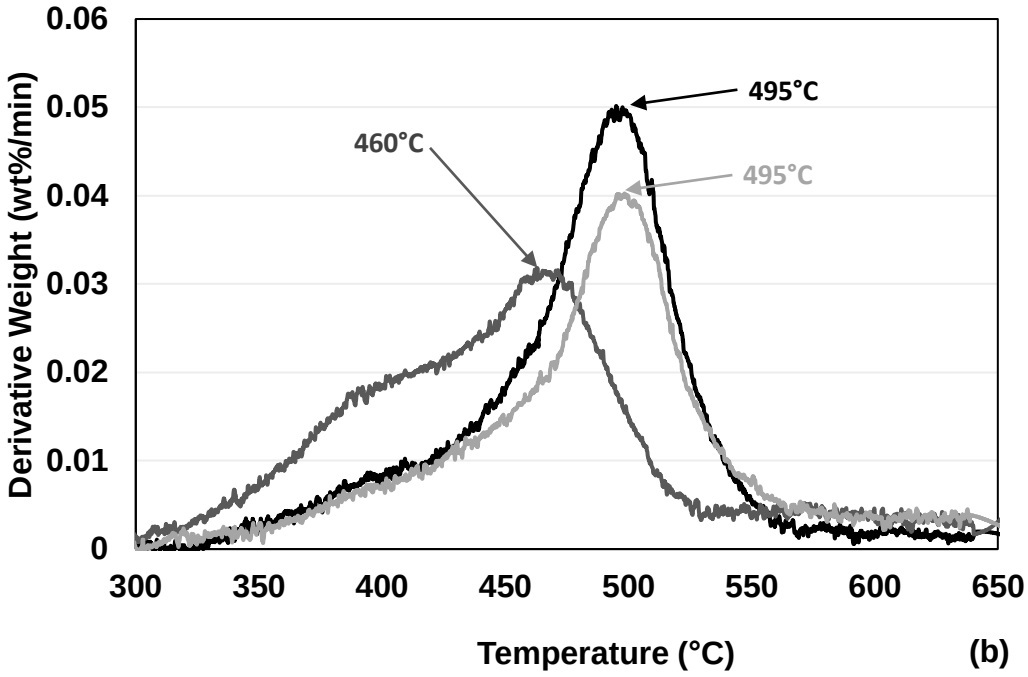


Figure 4.8: PM Compositions for λ = 0.9, 1 and 1.1.

The PM mass loaded on the filter varies between conditions, because of the variation of PM formation rate. Therefore, to normalise the mass of PM during TGA, 5 loaded discs, and 1 empty disc, was used for the stoichiometric condition. For the lean and rich conditions, 7 loaded discs were used, and 6 loaded dics and 1 empty disc were used respectively. ***Figure* 4.8** shows the PM composition for λ = 0.9, 1 and 1.1. The exhibited compositions for stoichiometric and lean conditions were similar. Hence, suggesting the nucleation peak in PSD was formed by water condensation. During the loading process, water condensation was unlikely to occur due to the sample flow temperature being constantly monitored at approximately 200 °C. The slightly higher

VOM to elemental soot ratio observed in the rich condition was consistent with the greater nucleation mode PM measurements in the PSD. This was attributed to the condensation of HCs from higher THC emissions. In theory, rich PM should enhance the PM oxidation reactivity, as higher VOMs can form new micropores for oxygen reaction after devolatilisation [**232**]. However, the overlap of error bars within the measurements indicates a insignificant difference in the results. Therefore, it is speculated the influence of PM composition has a negligible effect on PM oxidation reactivity.





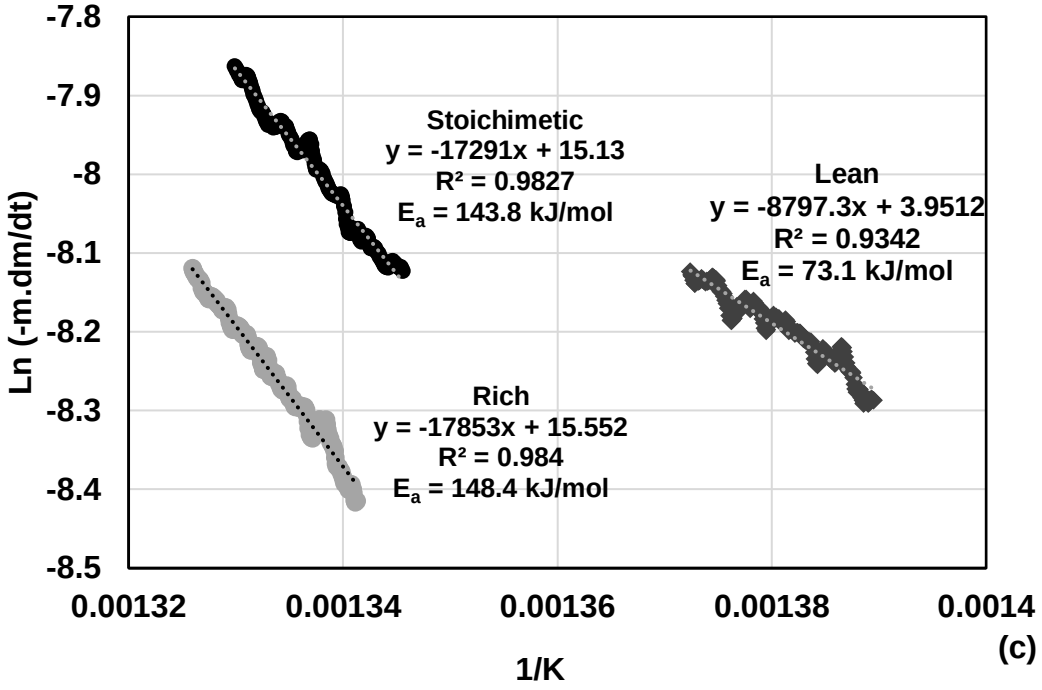
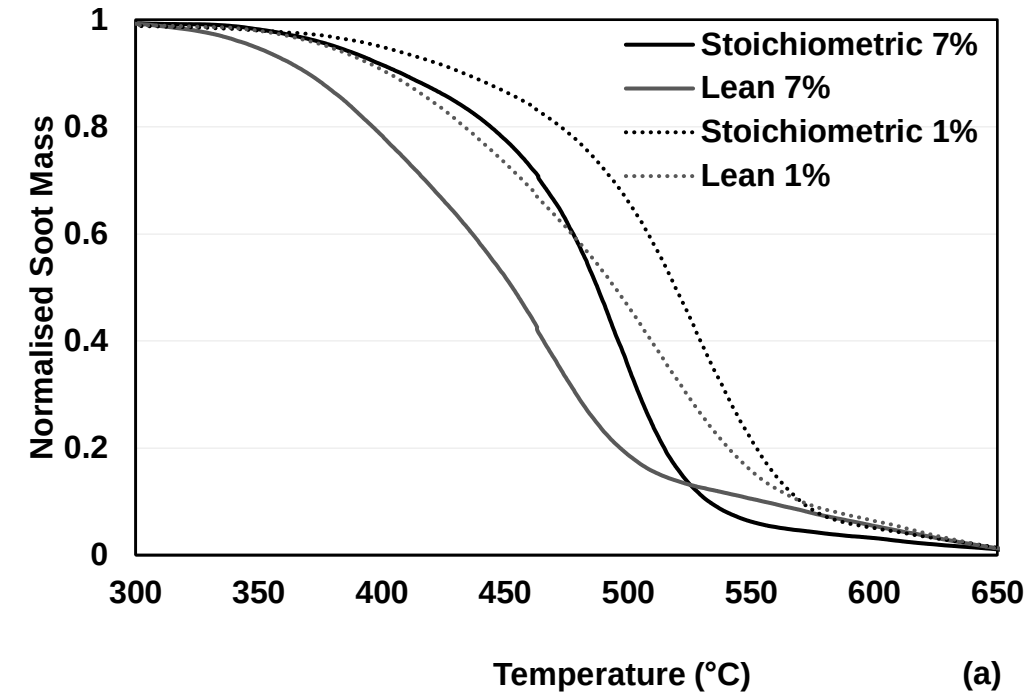
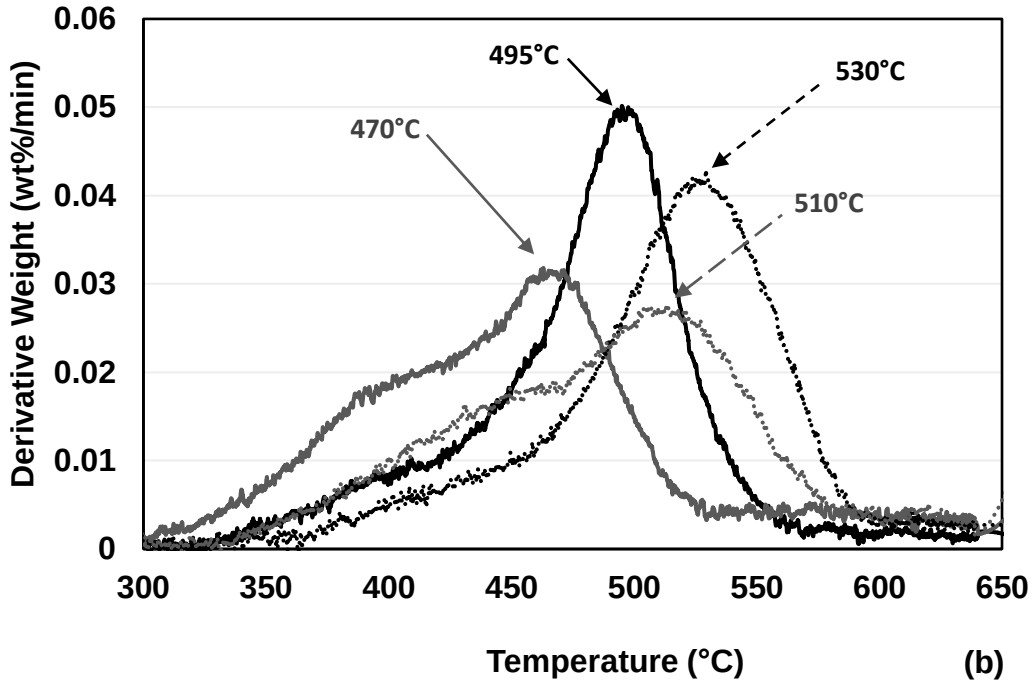


Figure 4.9: (a) Soot oxidation mass profile, **(b)** derivatives of mass loss and **(c)** linear regression of Arrhenius plot for E_a of λ = 0.9, 1 and 1.1 with 7% oxygen concentration.

In order to examine the PM oxidation reactivity, comparisons of the results were analysed through the soot oxidation mass profile, MMLRT and E_a (***Figure* 4.9**). The method is used to estimate micro and Nanostructural alterations [**202**], [**215**]. The soot oxidation mass profile (***Figure* 4.9*a***) shows the earlier start oxidation temperatures (SOT) for lean PM. This was measured at around 300 °C, where stoichiometric and rich PM were measured at 330 °C. Moreover, the mass loss derivatives in ***Figure* 4.9*b*** also illustrate an earlier shift in MMLRT to 470 °C for the lean PM, with both stoichiometric and rich PM remaining at a similar temperature of 500 °C. To further confirm the ameliorated oxidation reactivity of the lean condition, the E_a was calculated. To ensure the reliability of the linear regression, the coefficient of correlation (R_2) was above 0.9 for all cases exhibited in ***Figure* 4.9*c***. The trend of SOT was consistent with E_a. The lowest values were exhibited in the lean PM at 73.1 kJ/mol, and higher values were acquired for stoichiometric and rich PM at 143.8 kJ/mol and 148.4 kJ/mol respectively.


Normalised Soot Mass
1
0.8
0.6
0.4
0.2
0
300
350
400
450
500
550
600
650
Temperature (°C)
Stoichiometric 7%
Lean 7%
Stoichiometric 1%
Lean 1%

(a)


Derivative Weight (wt%/min)
0.06
0.05
0.04
0.03
0.02
0.01
0
300
350
400
450
500
550
600
650
Temperature (°C)
495°C
530°C
470°C
510°C

(b)

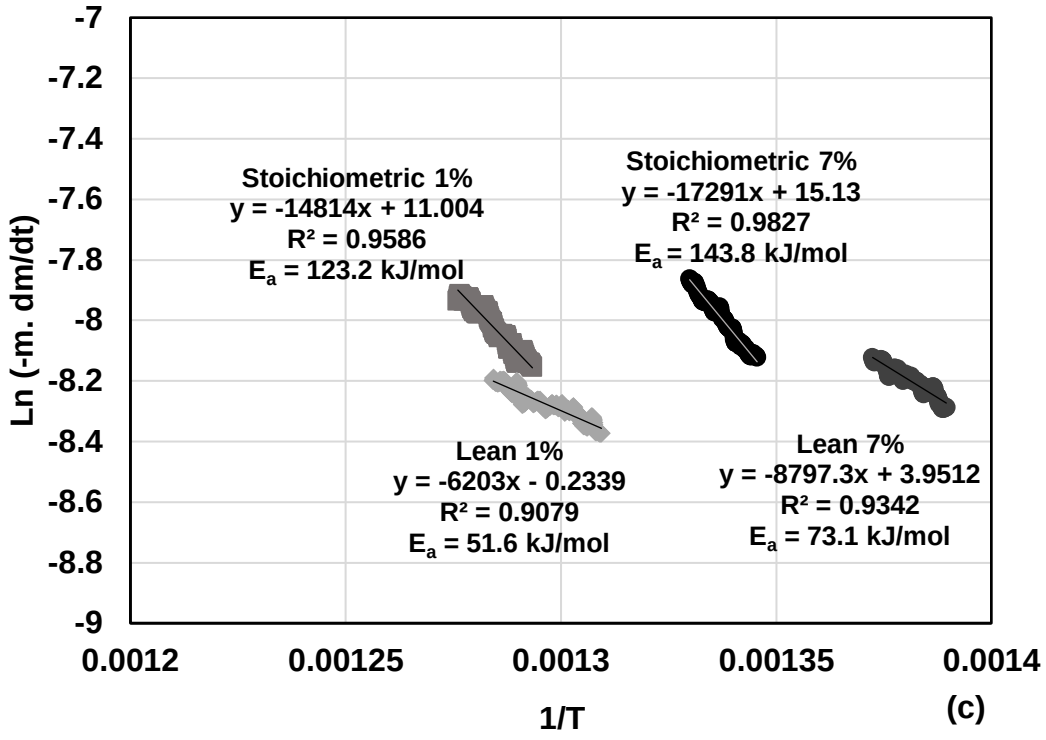


Figure 4.10: (a) Soot oxidation mass profile, **(b)** derivatives of mass loss and **(c)** linear regression of Arrhenius plot for E_a of λ = 0.9, 1 and 1.1 with 1% oxygen concentration.

As previously stated in ***Chapter 1***, oxygen concentration may vary according to the engine λ setting. Hence, a further study with TGA was conducted to mimic the lower oxygen concentration environment. Instead of using default compressed air as the oxidative gas (7% oxygen concentration), these sets of experiments were executed using 2% O_2/N_2, resulting in 1% oxygen concentration in the TGA combustion chamber. However, due to the non-difference in the PM oxidation reactivity between stoichiometric and rich PM, only stoichiometric and lean PM were tested to study the influence of low oxygen concentration on PM oxidation (***Figure 4.10***). For both lean and stoichiometric PM, SOT values shifted by approximately 30°C under the lower oxygen concentration environment (300 °C to 330 °C and 330 °C to

360 °C). Moreover, MMLRT peaks were also shifted slightly towards a lower temperature, from 470 °C to 510 °C and from 500 °C to 530 °C respectively, for lean and stoichiometric conditions. The shifts in temperature were because of the limited oxygen concentration, restricting the oxidation process, and leading to a longer PM oxidation time. It appeared that the lower oxygen concentration seemed to alter the activation energy (143.8 kJ/mol to 123.2 kJ/mol and 73.1 kJ/mol to 51.6 kJ/mol). However, it did not represent a higher oxidation reactivity. It was thought that the differing values obtained in the derivatives of mass loss had been influenced by the reduced oxygen concentration. This led to the change in activation energy. Regardless, PM formed under lean conditions consistently showed an enhanced PM oxidation reactivity. Compiling the evidence, it is speculated that lean PM possesses different PM characteristics. Thus, this chapter continues with micro and Nanostructural analyses, in order to study the PM characteristics influencing PM oxidation reactivity.

4.3.3.3 TEM for Primary Particle Diameter and Microstructure

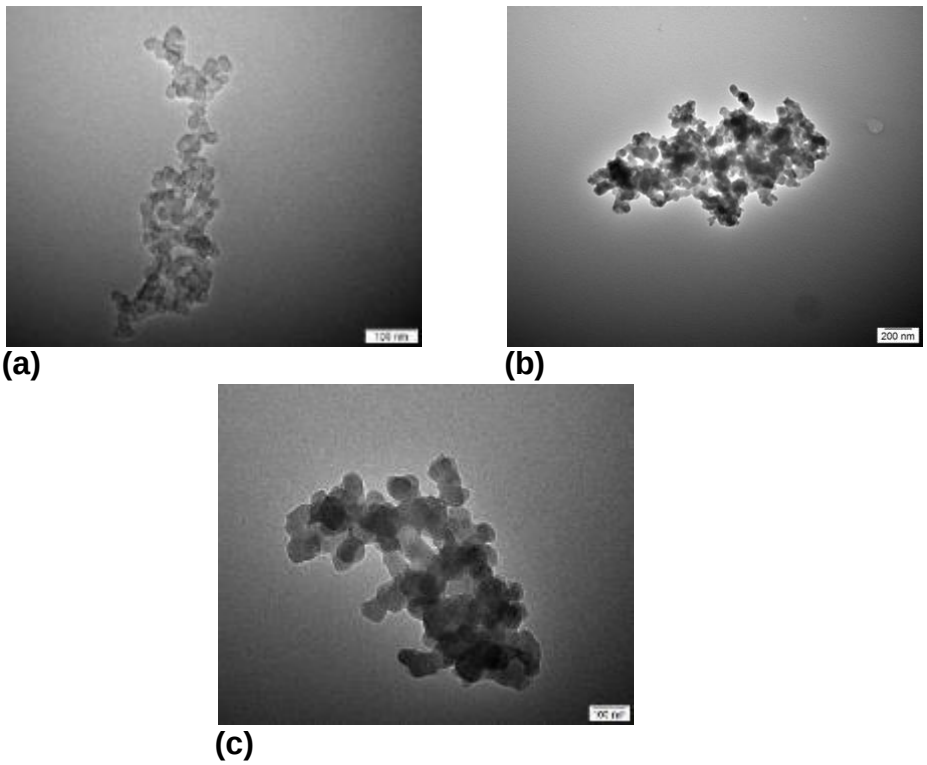


Figure 4.11: TEM micrographs of PM agglomerate of λ = **(a)** 1, **(b)** 1.1 and **(c)** 0.9.

TEM micrograph samples of PM agglomerates emitted by the GDI engine under stoichiometric, lean and rich conditions can be viewed in ***Figure* 4.11**. Agglomerates found from the TEM grids were in aciniform-shape, formed of large agglomerates, or occur in diesel-like particles formed of clustered or chain-like geometries [**71**], [**199**]. ***Figure* 4.12** illustrates the log-normality distributed histograms of primary particles for all the λ tested. The one-sample Kolmogorov-Smirnov statistical test was used for evaluation and satisfied the test (***Table* 4.3**).

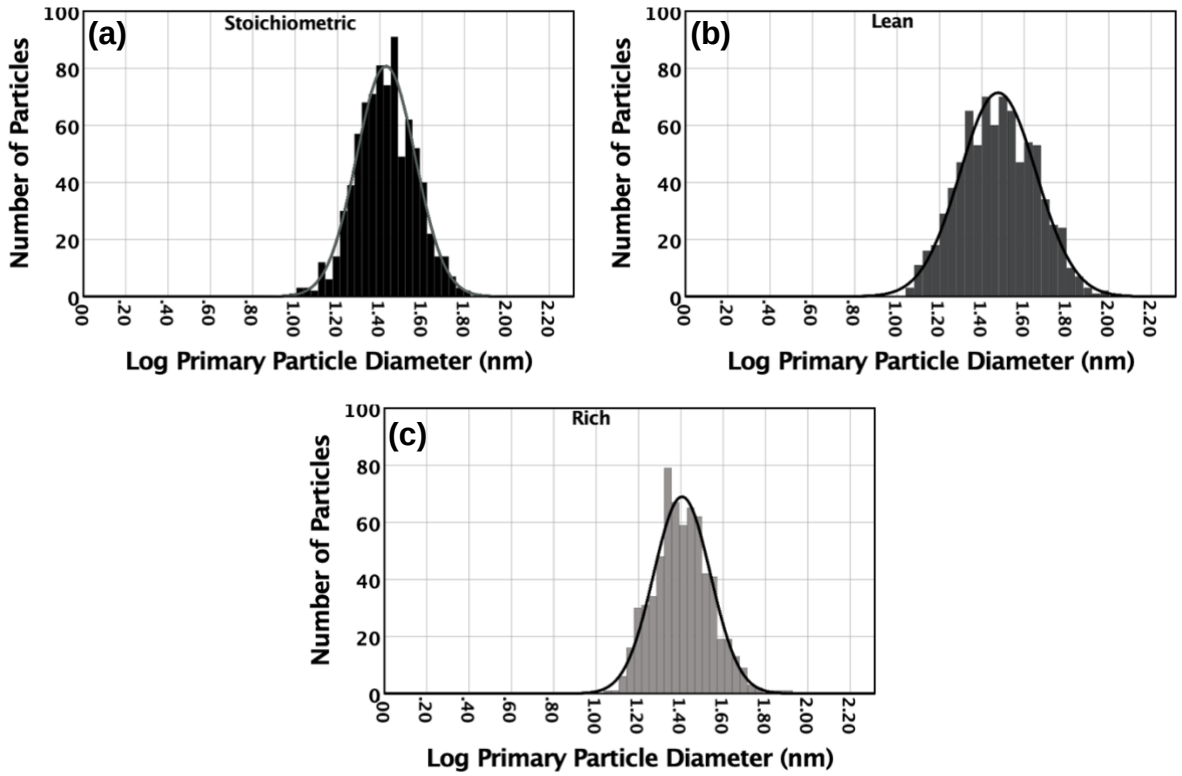


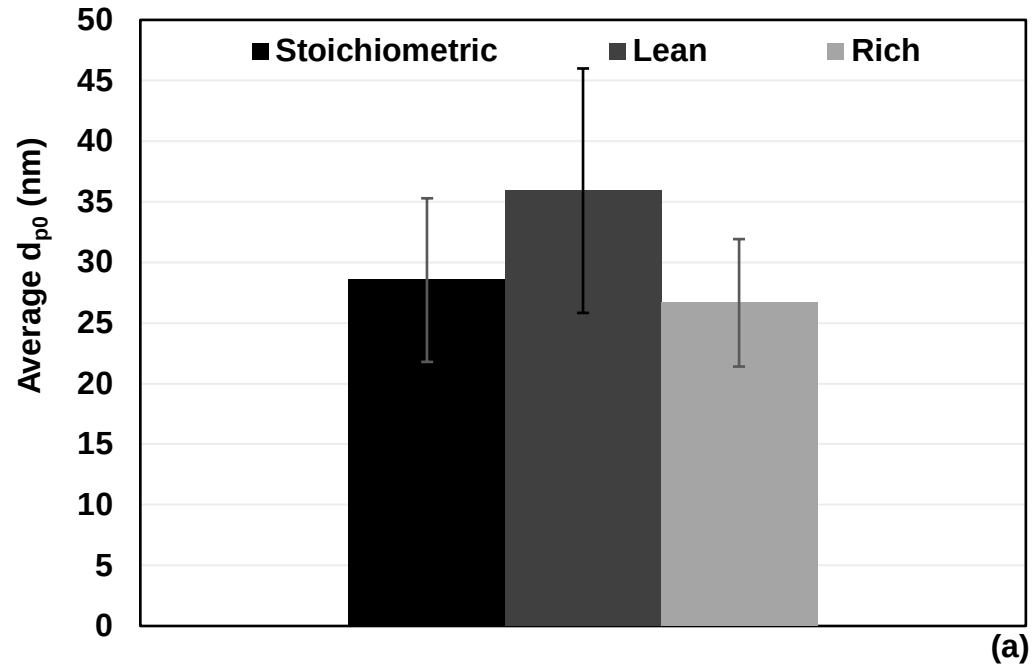
Figure 4.12: Log-normal primary particles distribution for λ = **(a)** 1, **(b)** 1.1 and **(c)** 0.9.

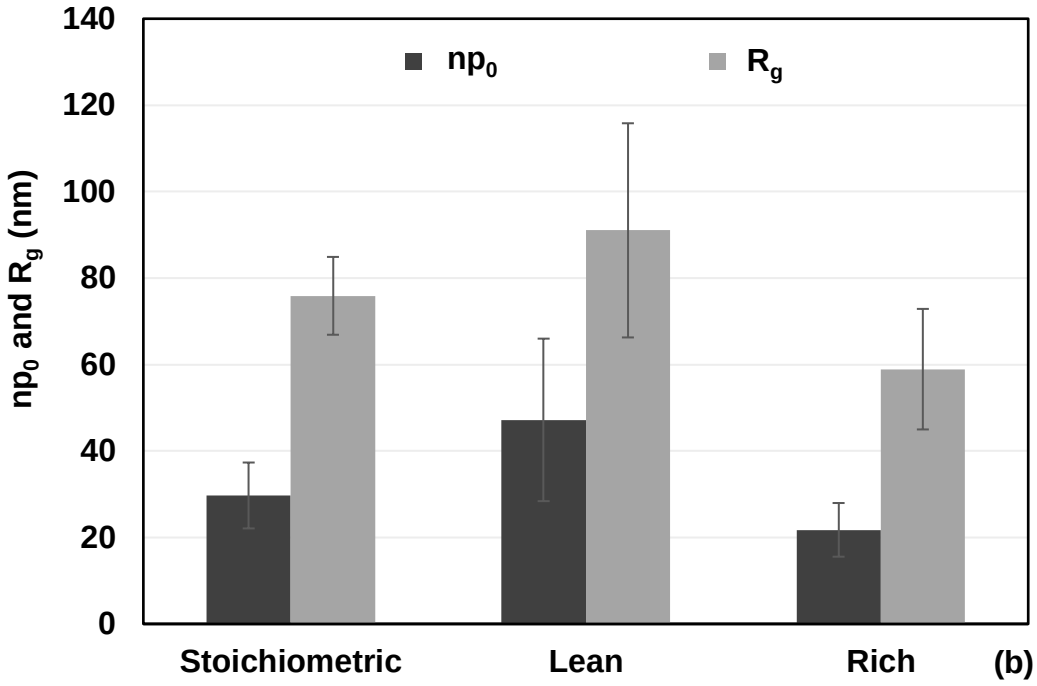
Table 4.3: Statistical normality test for λ = 0.9, 1 and 1.1.

Null Hypothesis	Significance	Results
The distribution of Log (Stoichiometric) is normal with mean 1.43 and standard deviation 0.138	0.200[a]	Retain null hypothesis
The distribution of Log (Lean) is normal with mean 1.48 and standard deviation 0.180	0.131[a]	Retain null hypothesis
The distribution of Log (Rich) is normal with mean 1.41 and standard deviation 0.134	0.183[a]	Retain null hypothesis
Asymptotic significances are displayed. The significance level is 0.05		

[a] Lilliefors corrected

The average d_{p0} for lean, stoichiometric and rich conditions were measured at 35.9 nm, 28.5 nm and 26.7 nm respectively (***Figure* 4.13*a***). Despite the lean condition having the largest d_{p0}, it also exhibited the most variation. This variation was associated with the default MBT conditioning of the engine. The later injection timing and earlier spark timing reduced the compression stroke, resulting in worsened fuel vaporisation and reduced air-fuel mixing time. Hence, this led to less uniformity in the mixture. As a result, some regions were richer, and some were leaner, but the overall λ was retained. Richer regions have higher formation rate (larger nuclei), and leaner regions have higher oxidation rate (smaller nuclei). Thus, surface growth processes of larger nuclei can form larger primary particles, resulting in higher d_{p0}. The smallest d_{p0} , formed by rich combustion, was attributed to the longer compression stroke (delayed spark timing). It was meant to compensate for the rapid flame propagation by the ECU during rich combustion [**253**]. The longer compression stroke increased the in-cylinder temperature, boosting the oxidation rate and slowing down the formation process. A similar trend was previously mentioned by *Wu et al.* [**119**]. Similar trend was previously mentioned by *Wu et al* [**215**]. Although, a smaller d_{p0} value is linked to improved oxidation reactivity of PM (higher SSA, greater surface area for a greater reaction with oxygen) [**208**], [**211**], [**217**]. Despite that, the PM oxidation reactivity indicated an opposite trend, inferring that d_{p0} was not the main reason. Furthermore, the difference in results between the conditions were insignificant due to the overlapping of error bars.


Stoichiometric
Lean
Rich
Average d_{p0} (nm)
50
45
40
35
30
25
20
15
10
5
0
(a)


np_0
R_g
np_0 and R_g (nm)
140
120
100
80
60
40
20
0
Stoichiometric
Lean
Rich
(b)

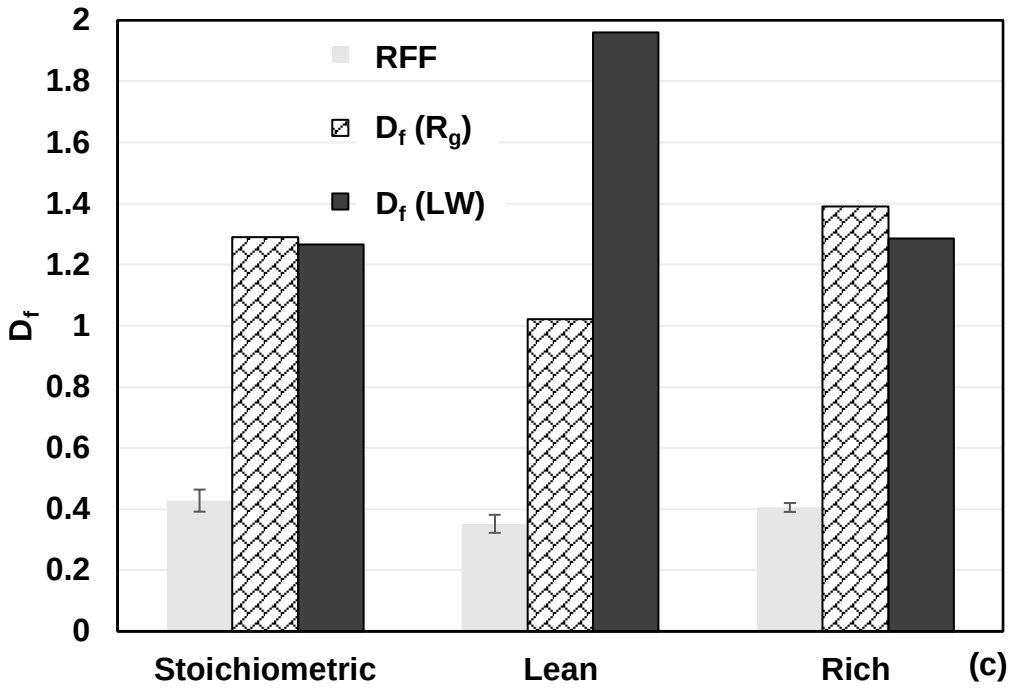


Figure 4.13: (a) Average d_{p0} **(b)** np_0 and R_g and (**c**) D_f of λ = 0.9, 1 and 1.1.

Table 4.4: R_2 of linear regression for D_f (R_g) and D_f (LW) methodology.

	D_f (R_g)	D_v (LW)
Stoichiometric (ʎ=1)	0.7511	0.8070
Lean (ʎ=1.1)	0.2102*	0.9640
Rich (ʎ=0.9)	0.8361	0.7419

* low accuracy

np_0 and R_g are presented in ***Figure* 4.13*b***. The np_0 and R_g exhibited increased magnitudes as λ transitioned to lean. The data shows that the PM agglomerates that were formed during rich conditions have the lowest np_0 and R_g with 21 and 59 nm. The np_0 also shows consistency with results discussed in PSD (lower accumulation mode PM) and lower elemental soot composition. The smaller R_g value represents fewer collisions between primary particles, due to the lower np_0 and smaller d_{p0}. However,

the highest R_g (91 nm) from the lean condition was not due to the higher np_0, as it is inconsistent to the PSD. The higher np_0 (47) may be attributed to inaccurate estimations by the large variation in of d_{p0} (wide error bar) (**Equation 3.15** and **Equation 3.17**). Hence, it was thought the higher R_g was caused by larger primary particles in the agglomerates. However, the error bars exhibited in the results suggest that PM oxidation reactivity was not due to the R_g alterations.

Three D_f methodologies were used to examine the geometrical structure, and to predict the type of collision that occurred in the agglomerates [**199**], [**208**], [**297**]. The D_f (LW) and D_f (R_g) are based on gradient evaluation of linear regressions. Thus, it is crucial to evaluate the R_2 prior to evaluating the results in order to confirm its reliability. The R_2 value is required to be above 0.5 to ensure the reliability of results [**305**]. According to R_2 for D_f tabulated in ***Table* 4.4**, the results demonstrated that D_f (R_g) for lean PM was negligible, with a value of 0.2102. Moreover, the RFF was eliminated due to the insignificance by the error bars. Therefore, only D_f (LW) was used to examine the agglomerates; reported to provide most accurate results amongst all methods [**8**], [**199**]. Stoichiometric and rich agglomerates, in general, are indifferent in nature, whilst lean agglomerates are compact and clustery-like. This was due to different collisions experienced under different λ conditions. The lower D_f agglomerates formed by stoichiometric and rich combustion mainly collided with the '*diffusion-limited'* mechanism. This occurs because the mean free path was reduced below the average PM agglomerate size. This results from the greater agglomerate concentrations (accumulation mode PM), shown in the PSD. Contrarily, the more compact and more clustery-like lean agglomerates were subjected to '*ballistic'* collisions, due to the lower accumulation mode agglomerate concentrations. This

process increased the mean free path, exceeding the average agglomerates size. Lower D_f is directly correlated to the oxidation reactivity, but the geometrical structure of lean agglomerates oppressed the PM oxidation trend, proposing the cause lies within Nanostructural alterations.

4.3.3.4 RAMAN for Nanostructure Analysis

The average RAMAN spectra are plotted in ***Figure* 4.14**. The spectra were deconvoluted with 3L1G and post-analysed, presented in ***Figure* 4.15**. The analyses comprised of the intensity ratio and area ratio for band D_1 and D_3, and the FWHM for band D_1. In the D_1 band, the intensity and area ratio show the magnitude trend according to rich < stoichiometric < lean. The lower magnitudes mean a higher order graphene layer structure. It also corresponds to the shorter fringe separation between graphene layers being less prone to oxygen attack [**227**]. In the case of the rich condition, the intensity and area ratio of the D_1 band has interrelating error bars, which indicates an insignificant effect. However, the FWHM of D_1 shows a more structured order of the graphene layers (lower value of FWHM D_1), which explains the slightly higher E_a than stoichiometric PM in ***Figure* 4.9*c***. It was caused by the higher combustion temperature under rich conditions, aiding the graphitisation process [**217**]. Furthermore, a similar amorphous concentration was inferred by the overlapping error bars from the results, derived by the intensity and area ratios of D_3. Meanwhile, the lean PM showed more disordered graphene layers, with a greater fringe separation distance and higher amorphous concentration. The greater amorphous content corresponds to a greater concentration of weak C-C bonds, that are easier to oxidise. This was attributed to the lower combustion temperature of the lean condition, slowing

down the graphitisation rate. Therefore, the greater oxidation reactivity of the lean PM was due to the highly disordered and amorphous graphene layers.

The L_a in ***Figure* 4.16** was derived with the modified Knight and White's formula (***Equation* 3.24**), as proposed by *Seong et al.* [**299**]. The shortest L_a was measured from lean PM, corresponding to a greater number of carbon atoms located at edge sites. It is strongly linked to the oxidation reactivity resulting from chemisorbed oxygen bonded carbons at edge sites, that are easier to oxidise. In contrast, the L_a from the rich condition has a similar magnitude to stoichiometric PM. Hence, it was evidenced that the differing PM oxidation reactivity during the lean condition was due to the transformation in the Nanostructures of PM.

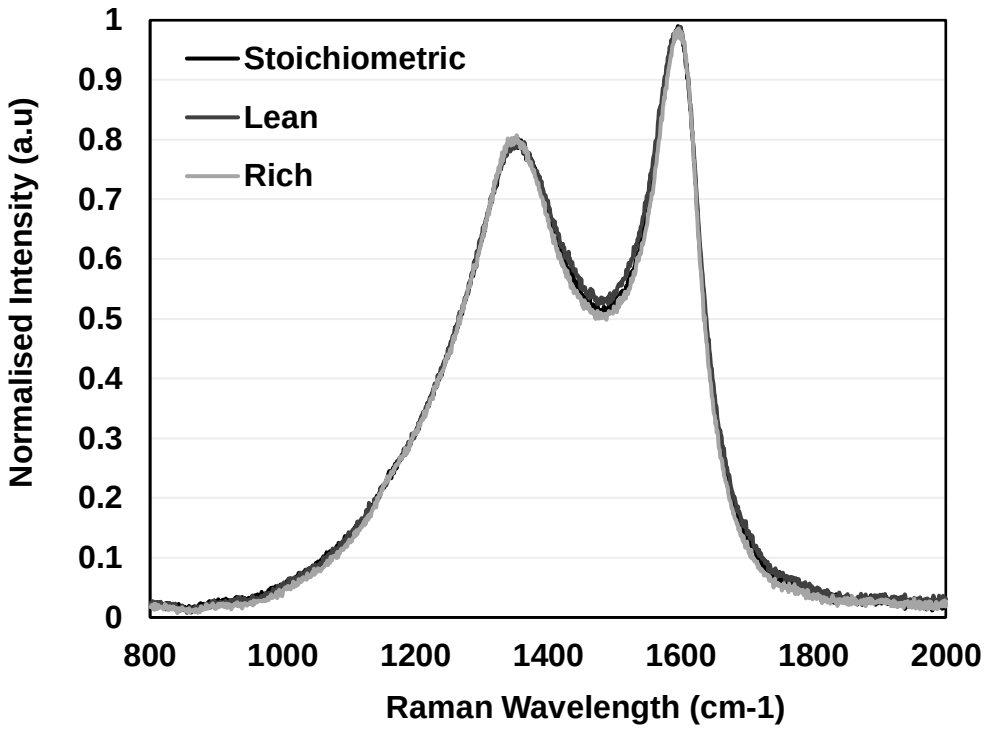
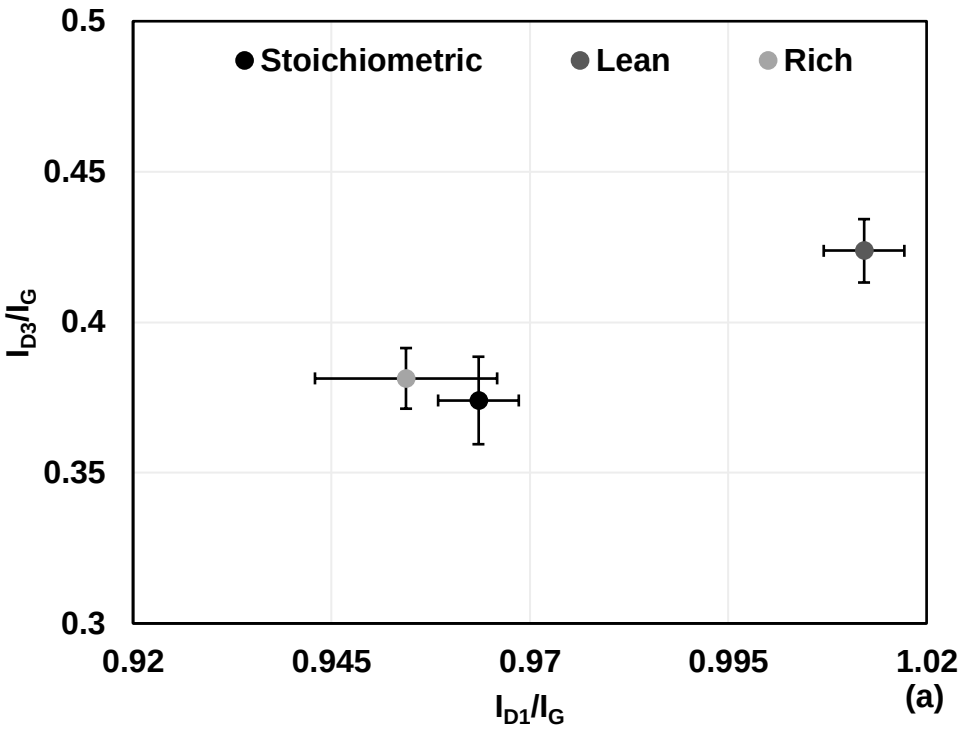
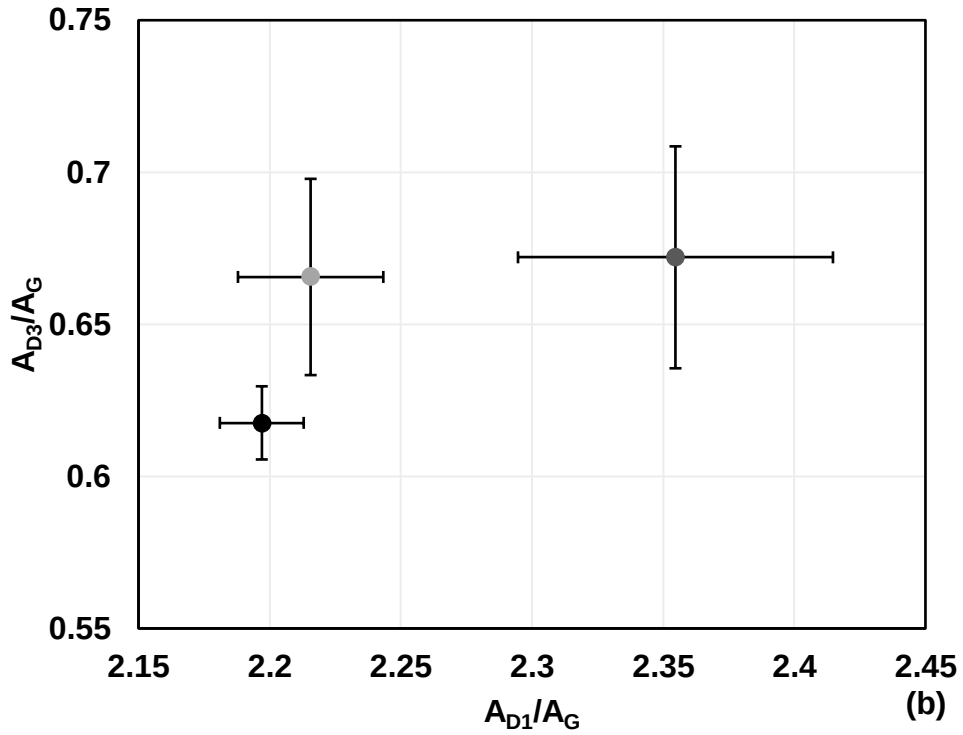


Figure 4.14: Average RAMAN spectra for λ = 0.9, 1 and 1.1.


Stoichiometric
Lean
Rich
0.5
0.45
0.4
0.35
0.3
I_{D3}/I_G
0.92
0.945
0.97
0.995
1.02
I_{D1}/I_G
(a)


0.75
0.7
0.65
0.6
0.55
A_{D3}/A_G
2.15
2.2
2.25
2.3
2.35
2.4
2.45
A_{D1}/A_G
(b)

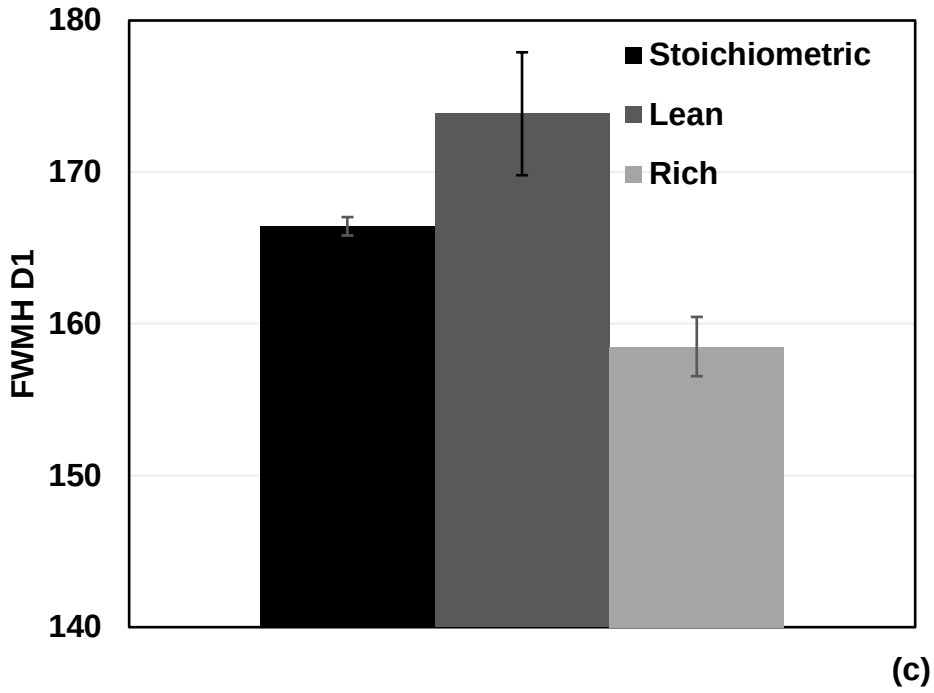


Figure 4.15: (a) Intensity ratio for band D1 and D3 **(b)** area ratio for band D1 and D3 **(c)** D1 FWHM for λ = 0.9, 1 and 1.1.

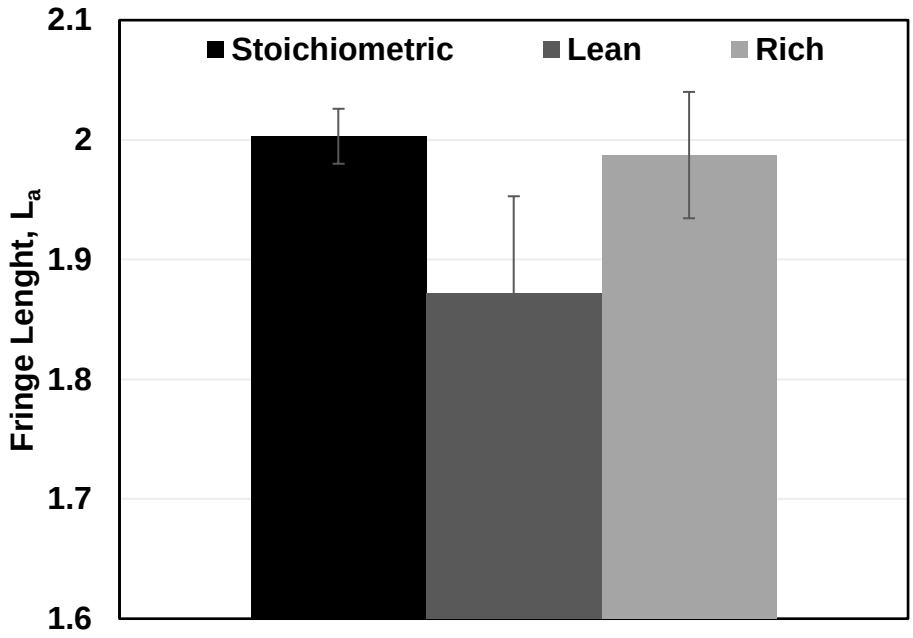


Figure 4.16: Estimated L_a using modified Knight and White's formula for λ = 0.9, 1 and 1.1.

4.4 Summary

This chapter investigated the AFR at MBT conditions in GDI engines. The study evaluated (i) combustion characteristics (ii) gaseous emissions, (iii) PM emissions and (iv) PM characteristics (PM oxidation reactivity, compositions, d_{p0}, microstructure and Nanostructure). The combustion and gaseous characteristics were as expected, aligning to results reported in the literature review.

In regard to PM, the concentration was increased during lean and rich combustion. The reduction in PM mass was because of the formation of higher nucleation mode PM, and lower accumulation mode PM. This was attributed to alterations resulting from the competition between PM formation and oxidation.

PM composition did not show any drastic differences, regardless of the λ condition. A majority of the microstructural analysis using TEM were similar for d_{p0}, R_g and np_0, and did not show any significant changes due to the overlapping of error bars. The variation in D_f was only observed in the lean PM due to different collision mechanisms. These results were believed not to be the reason for the greater PM oxidation reactivity under the lean condition. Meanwhile, rich and stoichiometric conditions demonstrated similar PM characteristics, as reflected in the oxidation reactivity. In the extended TGA study using 1% oxygen concentration, results indicated that the PM oxidation reactivity is not influenced under reduced oxygen conditions.

The Nanostructural analysis in RAMAN indicated the reasons for the observed changes in PM oxidation reactivity. No significant modifications were found between rich and stoichiometric conditions. The lean PM was composed of higher disordered

graphene layers and amorphous carbon concentrations. These graphene layers have an average L_a, shorter than both rich and stoichiometric PM.

CHAPTER 5 STUDY OF GASOLINE-DIMETHYL CARBONATE (DMC) BLEND ON COMBUSTION AND PM CHARACTERISTICS

5.1 Introduction

In the interest of abating PM emissions emitted by GDI engines, oxygenated fuels were widely investigated. With low production costs and numerous other advantages in terms of human health and environmental impact [**20**]–[**22**], [**28**], [**32**]–[**34**], DMC is seen as a potential candidate. Several publications in the literature have discussed the ability of DMC as an effective soot suppressor, as well as stating improvements in gaseous emissions in SI engines. However, the influence of DMC/gasoline blends in GDI engines has not yet been investigated. The aim of this chapter is to evaluate the combustion performance, gaseous and PM emissions in GDI engines. Furthermore, PM characteristics were extended to PM oxidation reactivity, micro and Nanostructural analyses. The outcome of this chapter will determine the feasibility of DMC as an oxygenated fuel replacement for gasoline.

5.2 Methodology and Test Conditions

The engine conditions and matrix are shown in ***Table* 5.1.** The engine torque and speed of 90 Nm / 2200 rpm were chosen as representative conditions for WLTP. The test was initiated after satisfying several pre-conditions; (i) the engine oil temperature was measured at 90 ± 0.5 ˚C, (ii) the engine coolant temperature was measured at 95 ± 2 ˚C and (iii) charged-air temperature was sustained at 40 ± 2 ˚C for reliability and

* This chapter is published as journal article.

.

repeatability of results. The IVO and EVC were pre-set at 8 and 11 aTDC respectively, in order to prevent any influence on the test results by the IEGR. The test was implemented under homogeneous-stoichiometric conditions. To ensure fair comparison between the fuels, MFB50 was phased due to the slightly faster flame speed of DMC. The D8 fuel spark timing combustion was varied in order to obtain an identical combustion profile gasoline at MBT condition (MFB50 phasing). ***Figure* 5.1**, illustrates the experimental setup, indicating sampling points for emissions measurements, PM loading and TEM grids sampling. Gaseous emissions and PM emissions were averaged at 300 seconds and 5 repetitions respectively. PM was loaded on filters for 30 minutes for gasoline, and 45 minutes for D8 (***Figure* 5.2**). This allowed adequate PM loading for further analysis by TGA and RAMAN. Prior to the main test, an integrity test was conducted on the D8 blend. This was achieved by leaving the blend in the fuel storage for 2 weeks to ensure no separation of phase.

Table 5.1: Experimental matrix and engine condition.

Engine Condition		
Stoichiometry, λ		1
Speed (rpm)		2200
Torque/Load (Nm)		90
Intake Valves Opening (CAD aTDC)		11
Exhaust Valves Closing (CAD aTDC)		8
Injection Timing (CAD bTDC)		300
Spark Timing (CAD bTDC)	**Gasoline**	27
	D8	26

* This chapter is published as journal article.

.

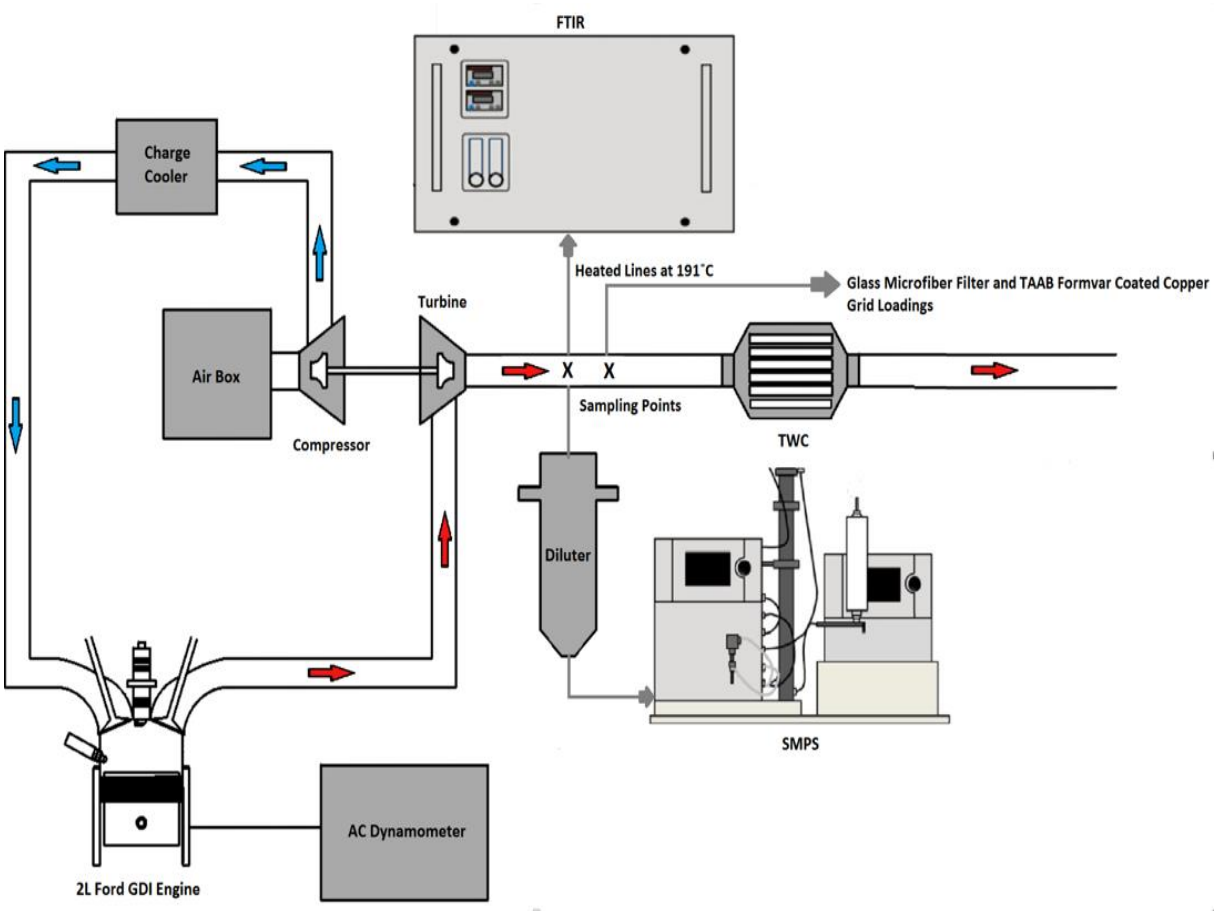


Figure 5.1: Schematic of engine bench test.



(a) **(b)**

Figure 5.2: PM loaded filters for **(a)** gasoline and **(b)** D8.

* This chapter is published as journal article.

.

5.3 Results and Discussion

5.3.1 Combustion Characteristics

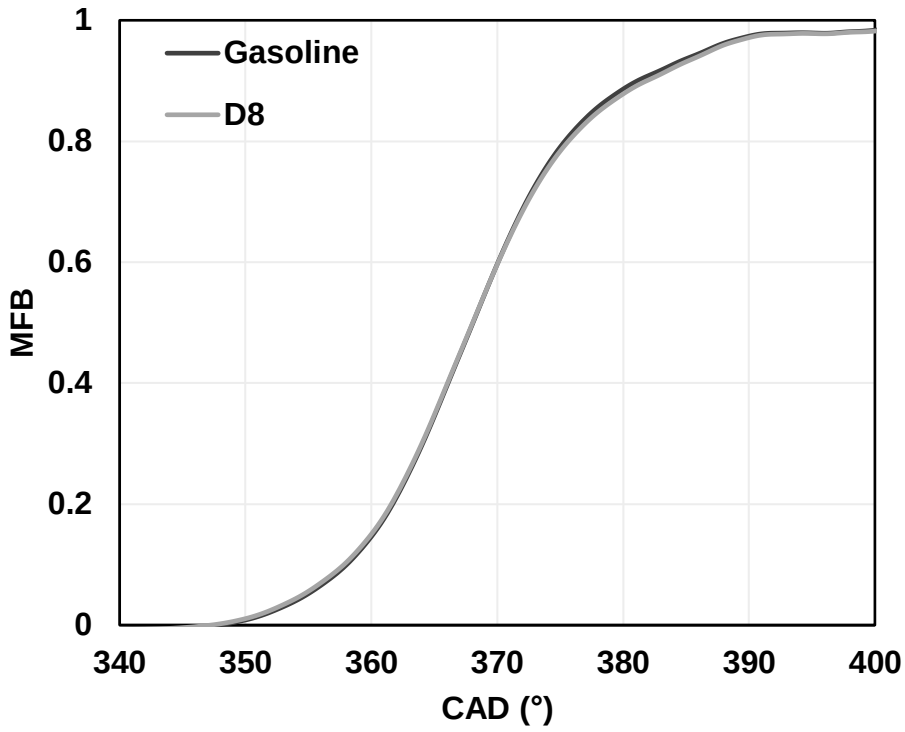


Figure 5.3: MFB plot of gasoline and D8.

The MFB plotted in ***Figure* 5.3** illustrates identical combustion profiles between the two fuels, due to the MFB50 phasing. The BSFC, BTE and COV of the IMEP during gasoline and D8 fuel engine combustion are shown in ***Figure* 5.4**. BSFC data shows that engine fuel economy deteriorated by 10% when DMC was added. The difference in BTE was insignificant, observing a 1 % reduction. Therefore, this indicates that the variation of BSFC was mainly attributed to the drastically lower energy density of DMC (approximately 15.78 MJ/kg, where gasoline was approximately 41.65 MJ/kg). The combustion stability using D8 was similar to the use of baseline gasoline, exhibiting a negligible increase of COV_{IMEP} from 1.4 % to 1.6 %. Both are below the recommended

* This chapter is published as journal article.

.

value of 5 % to assure stable combustion [**1**]. Hence, the in-cylinder pressure profile was unaffected, indicating a similar P_{Max} (***Figure* 5.5**) of 40.9 bar and 40.7 bar respectively, for gasoline and D8. The observed RoHR (***Figure* 5.5**) of D8 was lower than gasoline, due to the higher vaporisation heat of DMC that reduced the combustion chamber temperature [**306**]. This led to a lower combustion temperature and subsequently, dropped the EGT to 757 °C from 767 °C as presented in ***Figure* 5.6**. The $\eta_{Combustion}$ was improved from 97.9 % to 98.4 % with the use of D8, as a consequence of the oxygen borne in the DMC promoting the combustion process.

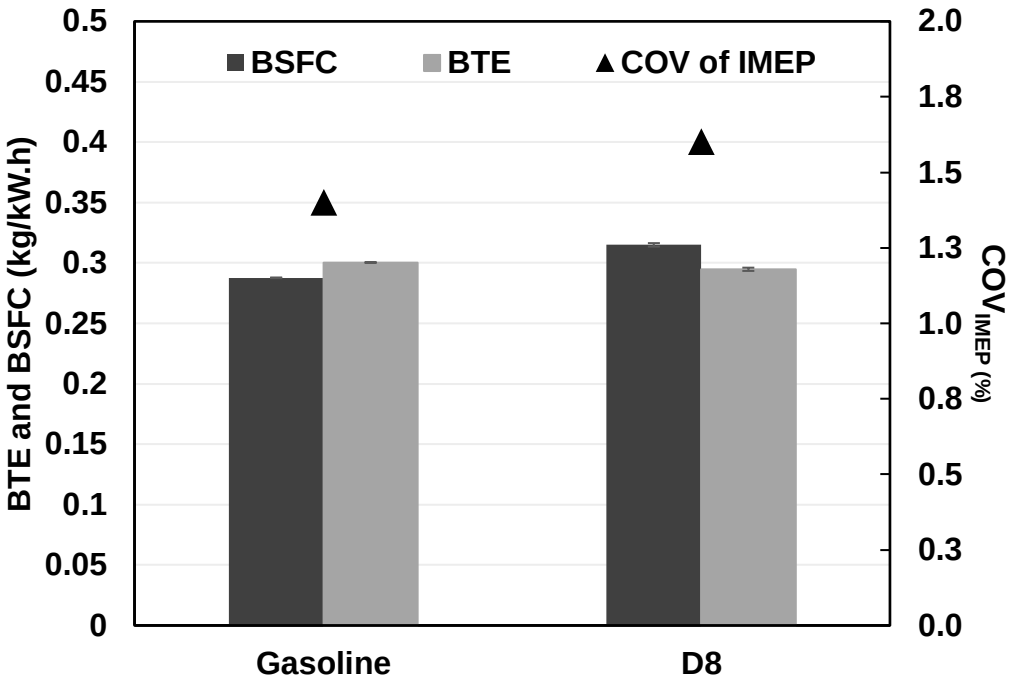


Figure 5.4: BSFC, BTE and COV of IMEP of gasoline and D8.

* This chapter is published as journal article.

.

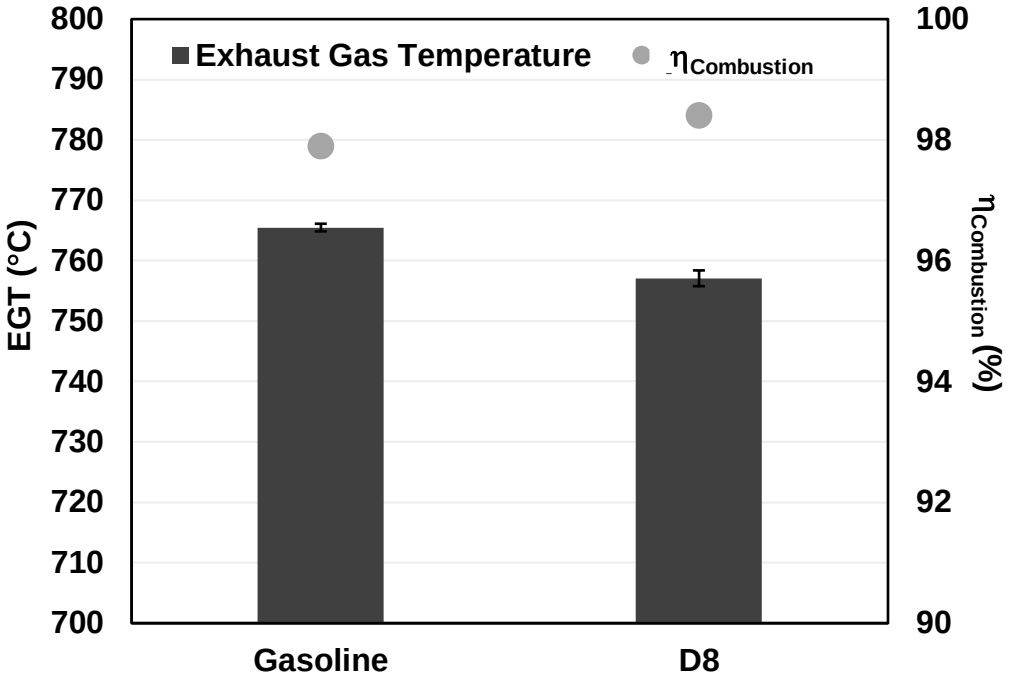


Figure 5.5: EGT and $\eta_{Combustion}$ of gasoline and D8.

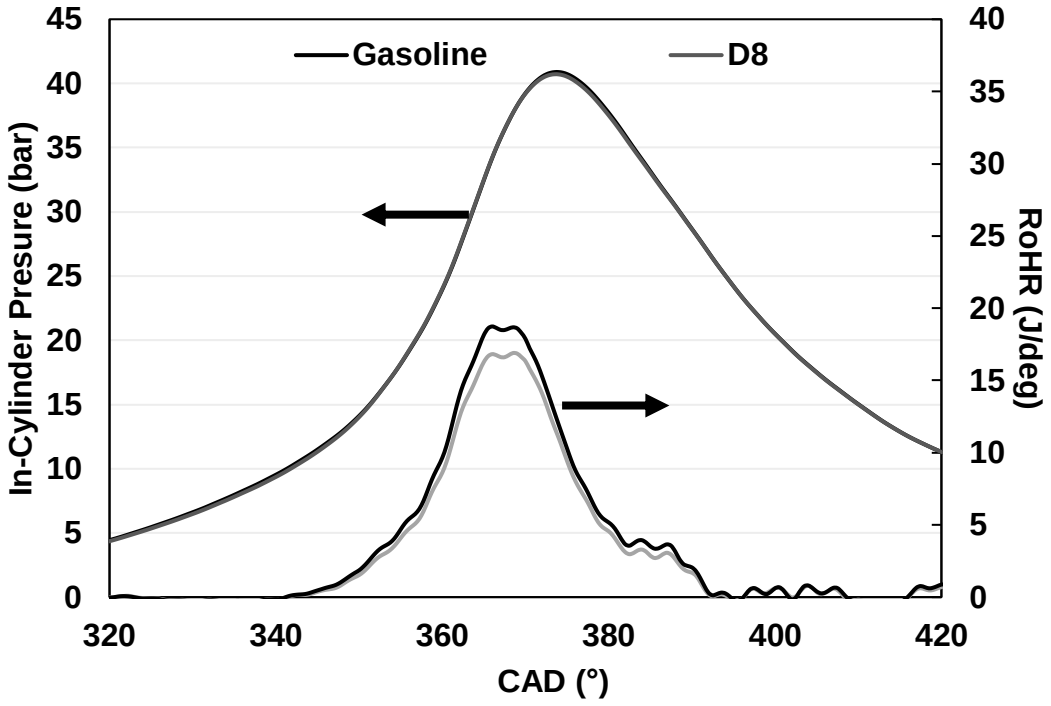


Figure 5.6: In-cylinder pressure and RoHR of gasoline and D8.

* This chapter is published as journal article.

.

5.3.2 Gaseous Emissions

D8 combustion drastically improved THC emissions, measuring a 30% reduction in comparison gasoline. It was the result of an overall reduction of all measurable HC species, with the exception of toluene, as shown in ***Figure* 5.7*a*** and ***Figure* 5.7*b***. In turn, CO and CO_2 emissions deteriorated, with an increase of 7% and 4% respectively. The increase of CO_2 was partly due to the oxygen contributed by the DMC, promoting more complete combustion. Additionally, the greater CO_2 also correlated to the higher BSFC, which led to greater CO_2 formation due to the greater fuel mass injected. In regard to CO, it was noted that the difference was not statistically significant, due to the overlapping error bars. The observed variation in CO concentration was because of the trade-off between THC and CO. This is because the post-combustion oxidation of some HCs species were enhanced, facilitated by the oxygen in DMC addition[**4**], [**307**]. However, the lower in-cylinder temperature during D8 combustion led to the partial oxidation of HCs, despite having higher oxygen concentration from the fuel blend.

NO_x demonstrated a negligible difference (1%) between D8 and gasoline, even though it was predicted to reduce based on Zeldovich thermal NO_x formation [**30**]. It was believed that the presence of oxygen from the DMC reacted with the HCCO radicals (HCCO oxidation reaction). This subsequently led to the suppression of the HCCO-NO reaction, and NO_x concentration remained comparable to gasoline [**15**], [**304**].

* This chapter is published as journal article.

.

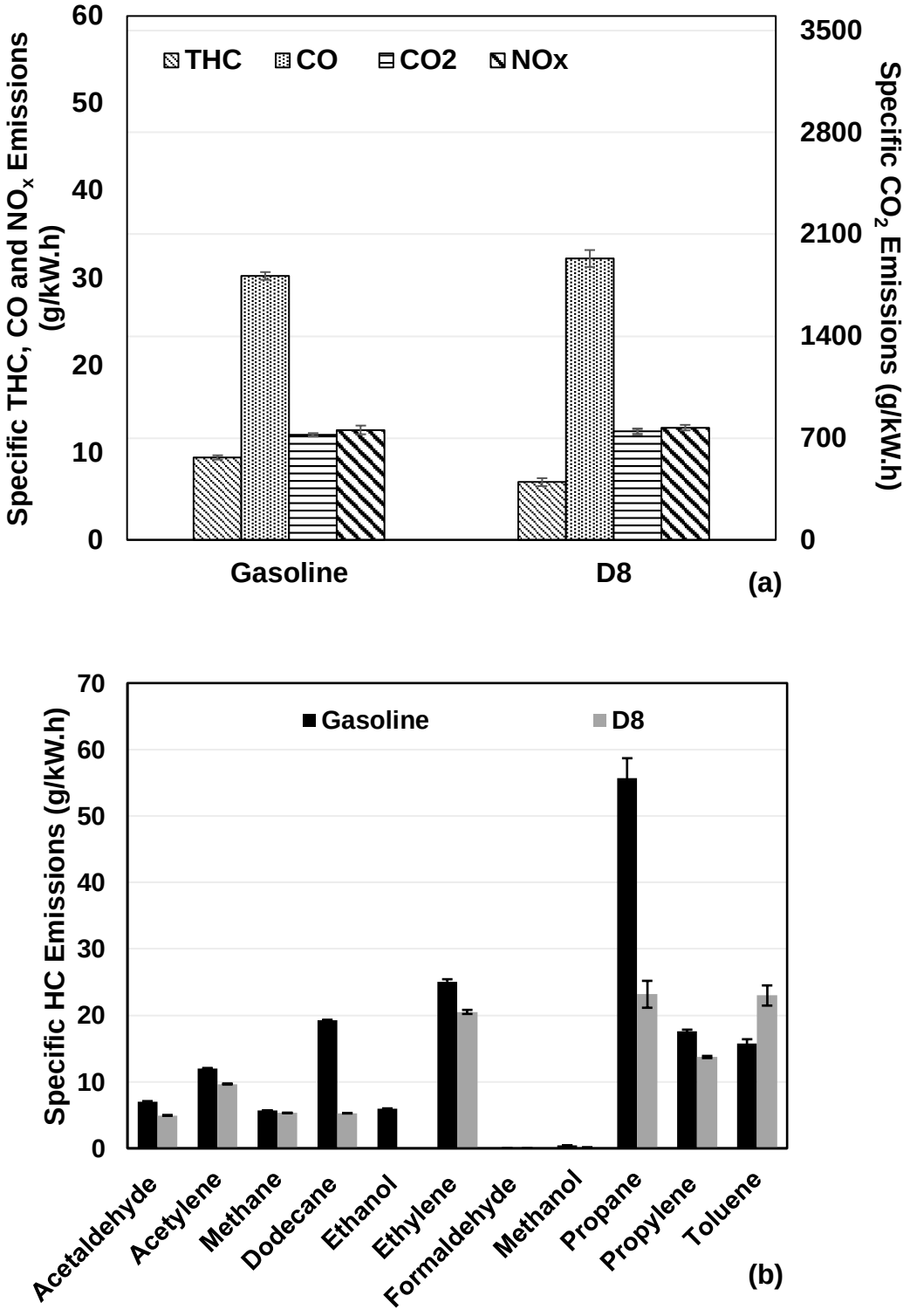


Figure 5.7: Specific **(a)** gaseous emissions and **(b)** HC species emissions of gasoline and D8.

* This chapter is published as journal article.

.

5.3.3 PM Characteristics

5.3.3.1 PM Emission

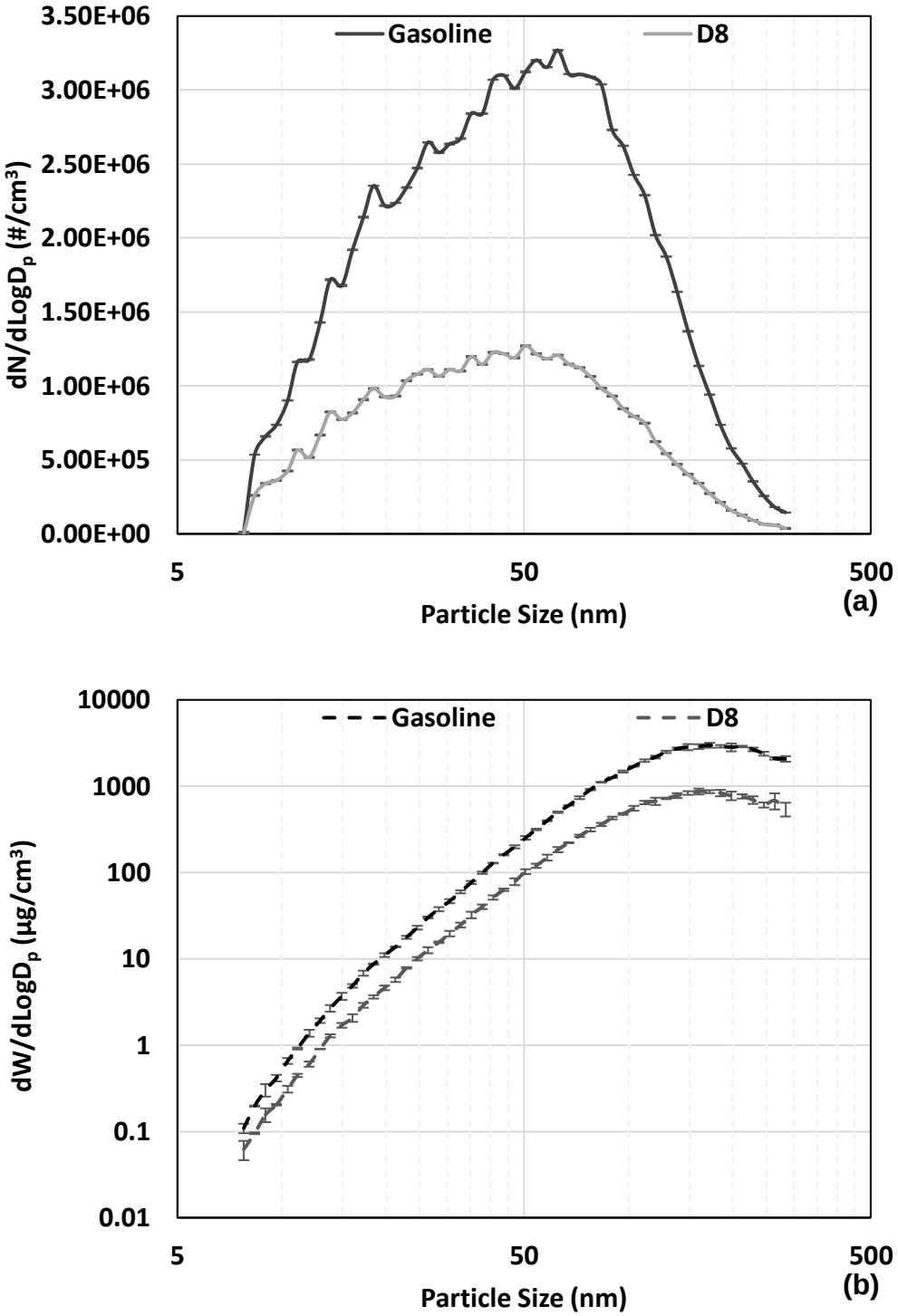


Figure 5.8: (a) Number and **(b)** Mass PSD of gasoline and D8.

* This chapter is published as journal article.

.

Figure* 5.8** illustrates the number and mass PSD from gasoline and D8 combustion. The PSD of all fuels were unimodal (Figure* 5.8*a***). The total PM concentration was reduced by approximately 60 % with use of the D8 blend in comparison to baseline gasoline. This led to the decline of GDNM from 46 mm to 41 mm. It was attributed to the reduction of PM across the diameter range, broadly related to the reduction of accumulation mode PM (soot). This phenomenon was confirmed by the mass PSD shown in ***Figure* 5.8*b***, showing a reduction across the diameter range [**44**]. With less PM concentration formed during D8 combustion, particle-to-particle interactions (coagulation, aggregation and agglomeration) were reduced [**44**], [**199**]. The explanation for lower nucleation mode PM is due to lower THC emissions which were aided by oxygen borne in DMC. Numerous factors were associated with the lower formation of soot PM (accumulation mode) with DMC addition. These factors included; the presence of oxygen in DMC, a greater oxygen/carbon ratio (O/C) [**308**], a lower C/H ratio, the absence of C-C bonds and fewer aromatic compounds in the D8 fuel blend [**244**]. Thus, hindering PM formation rates and promote PM oxidation during combustion process. These factors hindered PM formation rates and promoted PM oxidation during the combustion process. Furthermore, as proven by literature, DMC is effective in suppressing C_2 PM precursors such as acetylene, ethylene etc. (***Figure* 5.7*b***), slowing the PM formation and growth rates [**15**], [**309**].

5.3.3.2 PM Composition and Oxidation Reactivity

In addition to the PSD, a TGA was used to provide PM composition and to evaluate the oxidation reactivity. With less PM formed during D8 combustion, 3 loaded and 4 empty discs samples were used for gasoline. 5 loaded and 2 empty discs were

* This chapter is published as journal article.

.

used for D8 to normalise the mass in the TGA examinations. The PM composition in ***Figure* 5.9** the VOM to elemental soot ratio increased with D8 combustion. The higher percentage of VOM in the D8 PM suggested it was due to the reduction of solid soot PM.

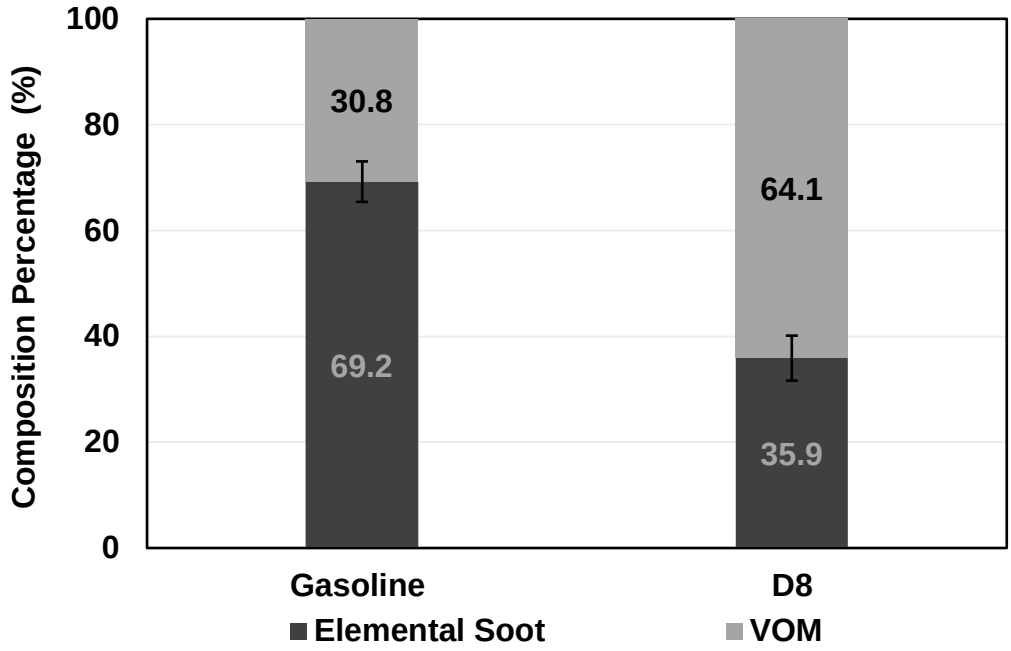


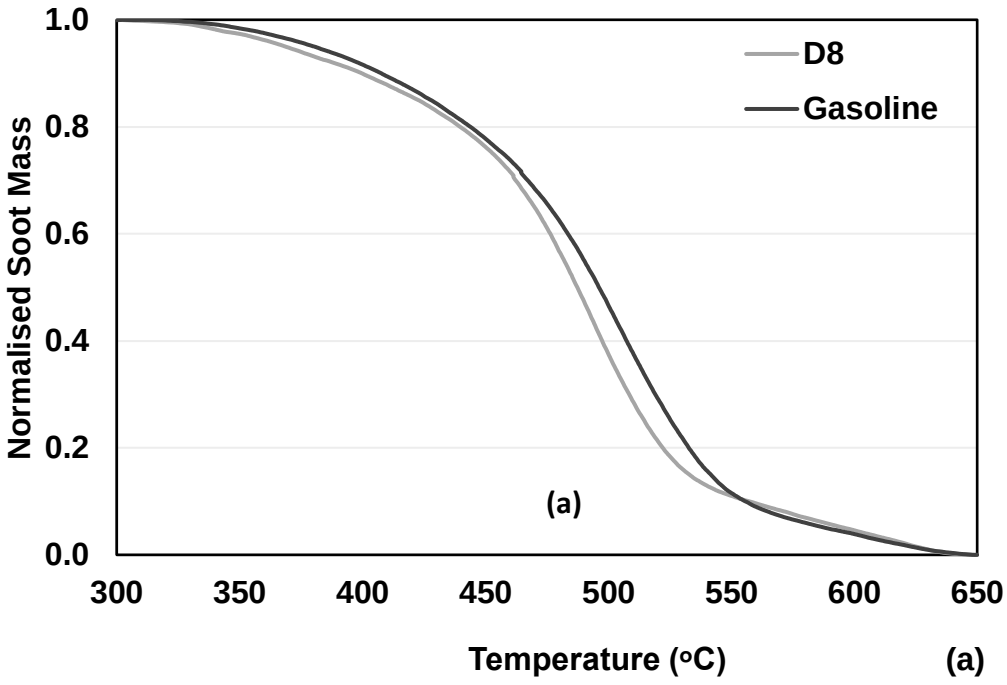
Figure 5.9: PM composition of gasoline and D8

Higher PM oxidation reactivity from the combustion of oxygenated fuels has been frequently reported in both SI and CI engines, as discussed in the *Oxygenated Fuel* section of the literature review. The same trend was observed between the two fuels in ***Figure* 5.10** as anticipated. Soot oxidation profile (***Figure* 5.10*a***) indicated the SOT of D8 was shifted about 15 °C earlier to around 300 °C in comparison to gasoline at 315 °C. Furthermore, the D8 has sharper, earlier gradient of MMLRT, shifting from 510 °C towards 495 °C in mass loss derivatives (**Figure 5.10*b***). The R_2 of linear

* This chapter is published as journal article.

.

regression in the Arrhenius plot (***Figure* 5.10*c***) were measured above 0.9 for both gasoline and D8. The E_a of D8 dropped from 130.4 kJ/mol to 85.1 kJ/mol demonstrating easier oxidation. Thus, the greater oxidation reactivity of PM emitted by D8 was confirmed. One of the reasons speculated for the improved D8 PM oxidation reactivity was the higher VOM content in PM. The creation of new pores during post-devolatilisation, makes the PM more vulnerable to oxygen penetration, increasing the oxidation rate [**208**]. It has been reported by the literature that other root-causes, such microstructure and Nanostructure, can affect the oxidation reactivity. Hence, TEM and RAMAN methods, designed for micro and Nano scale analyses, will be applied to further assess other causes for the oxidation reactivity between the two fuels.



* This chapter is published as journal article.

.

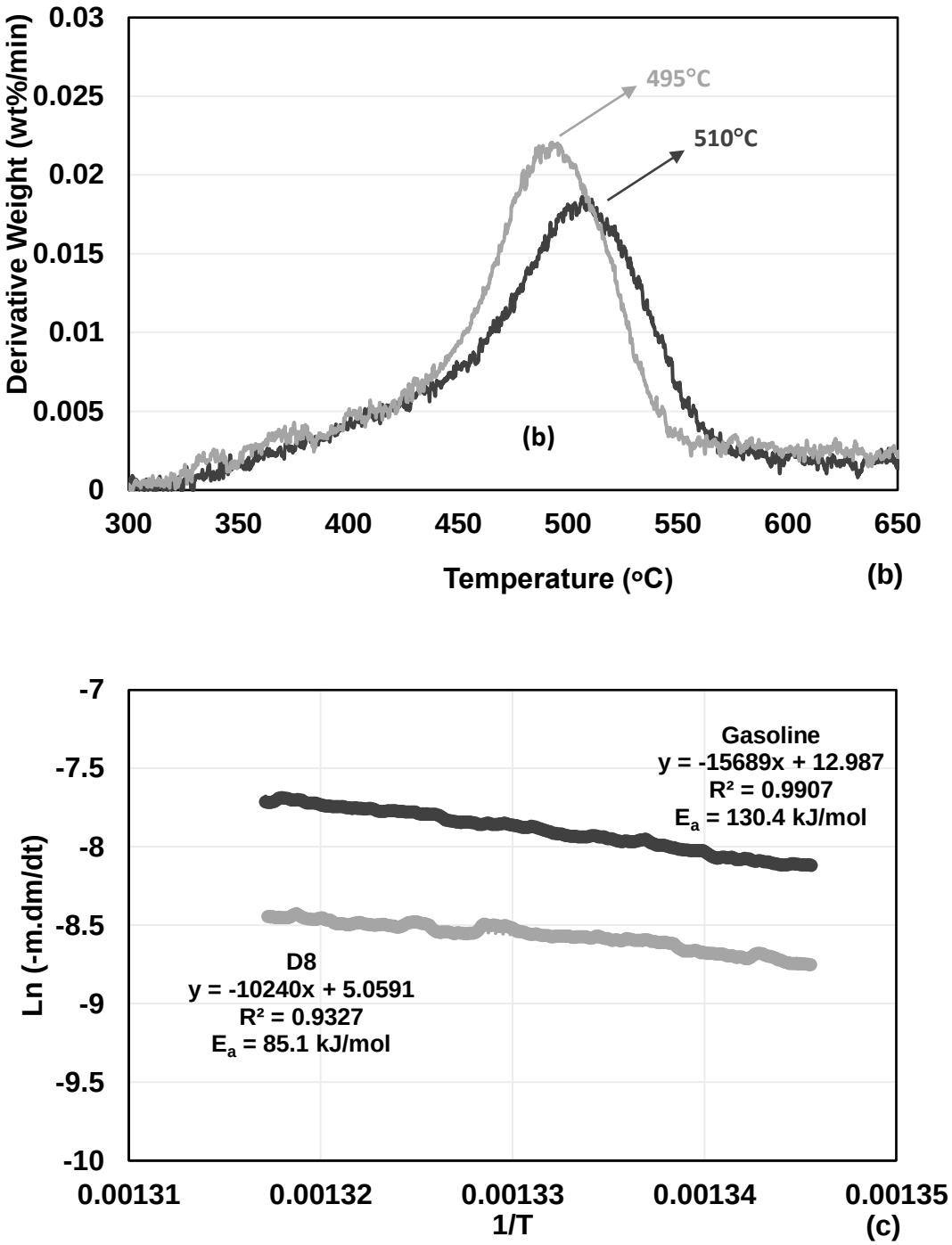


Figure 5.10: (a) Soot oxidation mass profile, **(b)** derivatives of mass loss and **(c)** linear regression of Arrhenius plot for E_a of gasoline and D8.

* This chapter is published as journal article.

.

5.3.3.3 TEM for Primary Particles Diameter and Microstructure

Figure* 5.11** presents the micrograph samples acquired from TEM for gasoline and D8. PM agglomerates on the TEM grids exhibited in an aciniform-shape, were in the form of large agglomerates or diesel-like particles, exhibiting clustered or chain-like geometries. Measured primary particles satisfied the log-normality one-sample Kolmogov-Smirnov test (Table* 5.2**). The histogram and log-normal distribution are plotted in ***Figure* 5.12.**

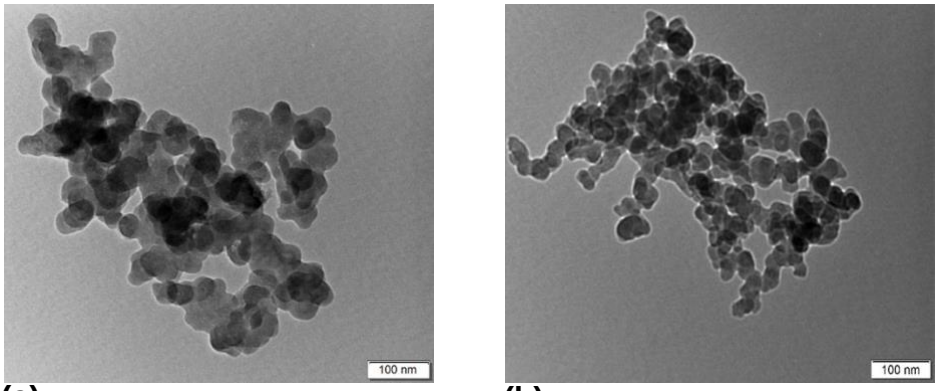


Figure 5.11: TEM micrographs of PM agglomerate of **(a)** gasoline and **(b)** D8.

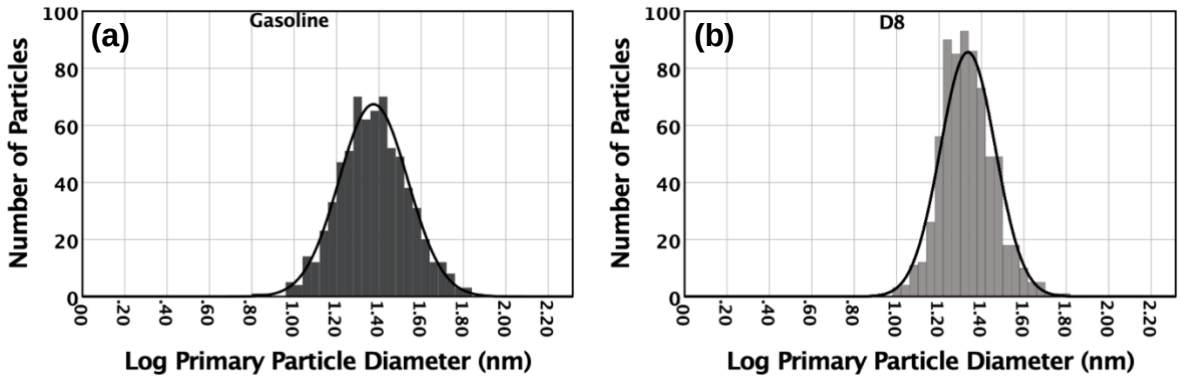


Figure 5.12: Log-normal primary particles distribution for **(a)** gasoline and **(b)** D8.

* This chapter is published as journal article.

.

Table 5.2: Statistical normality test for gasoline and D8.

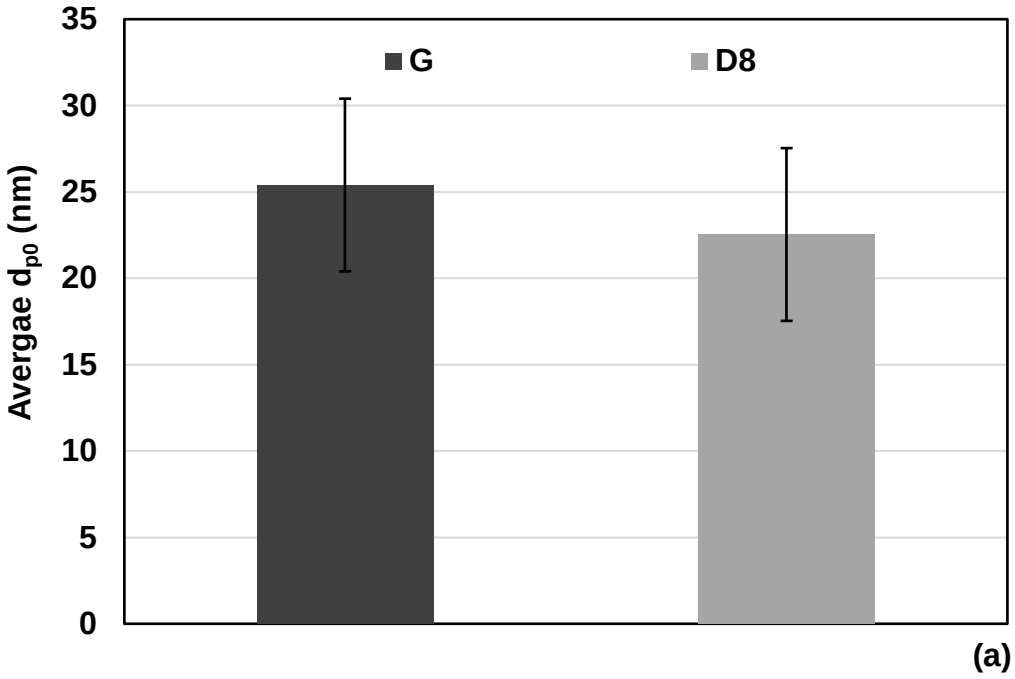
Null Hypothesis	Significance	Results
The distribution of Log (Gasoline) is normal with mean 1.37 and standard deviation 0.162	0.200[a]	Retain null hypothesis
The distribution of Log (D8) is normal with mean 1.34 and standard deviation 0.130	0.131[a]	Retain null hypothesis
Asymptotic significances are displayed. The significance level is 0.05		

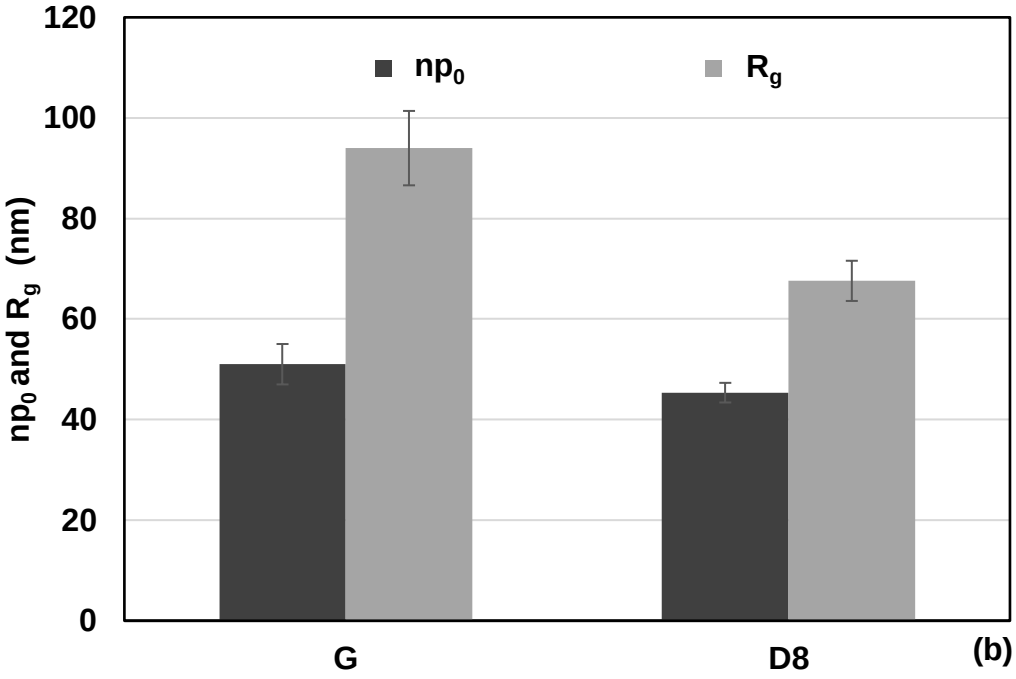
[a] Lilliefors corrected

D8 combustion has illustrated the tendency to form smaller primary particles sizes compared to the primary particles formed by gasoline combustion. As displayed in ***Figure* 5.13*a***, the average primary particles size is 25.4 nm and 22.5 nm respectively for gasoline and D8. The smaller d_{p0} of D8 was attributed to the presence of oxygen, lower C/H ratio and fewer aromatics within the DMC blend. Subsequently, these factors restricted surface growth by simultaneously suppressing formation, and promoting oxidation rates during combustion[**308**]. Secondly, the fewer C-C bonds in DMC suppressed the soot formation rate. The smaller average d_{p0} had increased the SSA, leading to more available surface area for oxygen reaction during the oxidation process. Therefore, the improvement observed in D8 PM oxidation reactivity is thought to have partially contributed to the alteration of d_{p0} because of the overlapping of error bars.

* This chapter is published as journal article.

.





* This chapter is published as journal article.

.

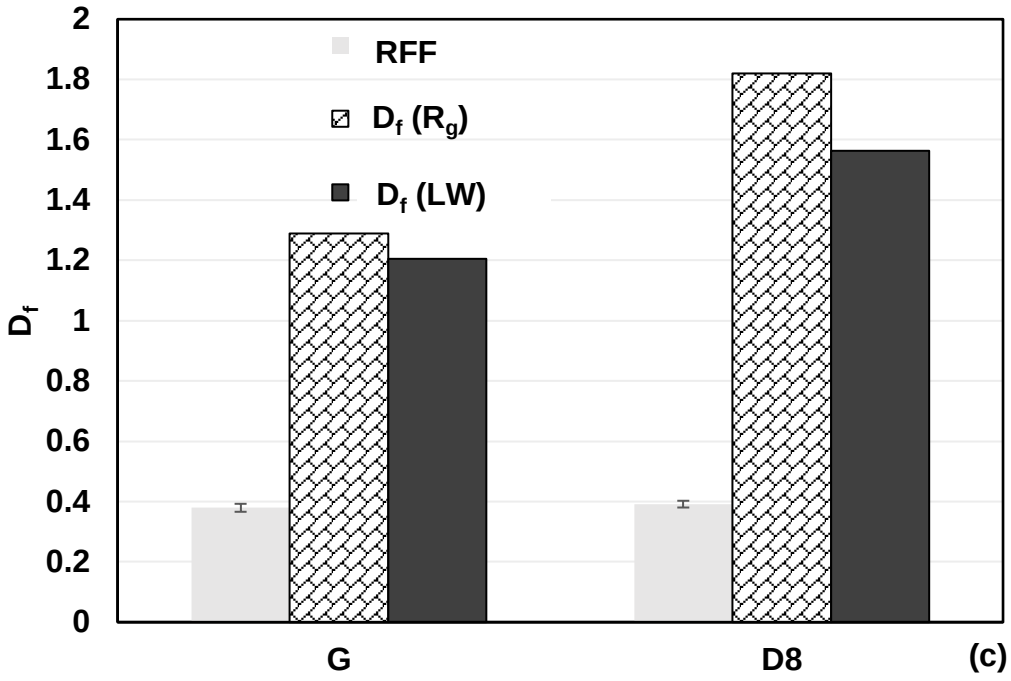


Figure 5.13: (a) Average d_{p0} **(b)** np_0 and R_g and (**c)** D_f of gasoline and D8.

Figure* 5.13*b illustrates the np_0 and R_g for gasoline and D8. As a subsequent effect of the suppression of PM forming with DMC, a lower np_0 was estimated in the PM agglomerates. Due to the lower np_0 and smaller average size of primary particles, smaller agglomerates were generated [**199**]. This resulted in the reduction of R_g size from 95 nm to 77 nm, showing an agreement with the PSD results (***Figure* 5.8**).

Table 5.3: R_2 of linear regression for D_f (R_g) and D_f (LW) methodology.

	D_f (R_g)	**D_f (LW)**
Gasoline	0.7132	0.6539
D8	0.8439	0.8395

* This chapter is published as journal article.

.

In relation to the D_f, three methods were used to evaluate the geometrical morphology of agglomerates. All the R_2 values for the linear regression of D_f (R_g) and D_f (LW) were above 0.5, and were adequate to provide accurate results [**305**]. All three methods consistently displayed that DMC addition altered the collision mechanisms with higher D_f [**298**]. The more compact nature and presence of cluster-like agglomerates were caused by the variation of mean free path. During D8 combustion, lower agglomerate concentrations and smaller R_g agglomerates increased the size of the mean free path, exceeding the average PM agglomerate size. Thus, aiding the '*ballistic*' collision mechanism leading to fewer chain-like agglomerates via cluster-cluster agglomeration. Oppositely, gasoline formed a greater concentration of agglomerates with a larger R_g, minimising the mean free path below agglomerates size. This aided the '*diffusion-limited*' collision mechanism, resulting in collisions by the tip of the agglomerates. Therefore, open and more chain-like agglomerates were formed. Based on the D_f results, the improved oxidation reactivity of PM formed by D8 combustion was not through the higher D_f, as clustery and compact agglomerates have lower SSA allowing a greater reaction with oxygen.

5.3.3.4 RAMAN for Nanostructure Analysis

Figure* 5.14** presents the average RAMAN spectra derived from the combustion of gasoline and D8. With the 3L1G deconvolution, the I_{D1}/I_G, A_{D1}/A_G, I_{D3}/I_G, A_{D3}/A_G and FWHM of the D1 band were evaluated for the Nanostructural analysis (Figure* 5.15**). Referring to ***Figure* 5.15**, the greater value of the D1 band measured in the D8 PM (I_{D1}/I_G, A_{D1}/A_G and FWMH D1), indicated a higher graphitic disorder magnitude in the graphene layers. Meanwhile, the D3 band also showed a similar trend, suggesting a

* This chapter is published as journal article.

.

higher concentration of amorphous graphene layers. As aforementioned, PM primary particles initially formed as an amorphous layered nucleus. Subsequently, amorphous graphene layers crystallised under heat exposure from the outer shell towards the nucleus of the primary particles. Hence, the lower in-cylinder temperature of D8 was thought to reduce the crystallisation process (graphitisation process) as less heat was released (***Figure* 5.6**). This resulted in a higher average tortuosity of graphene layer fringes (greater amorphous concentration) [**227**]. Therefore, are composed of weaker C-C bonds (breakdown easily due to lower resonance stability) in comparison to gasoline graphene layers. Overall, the improved D8 PM oxidation reactivity was due to the greater oxidation potential because of the larger fringe separation (band D1) and weaker C-C bonds of the amorphous graphene layer (band D3).

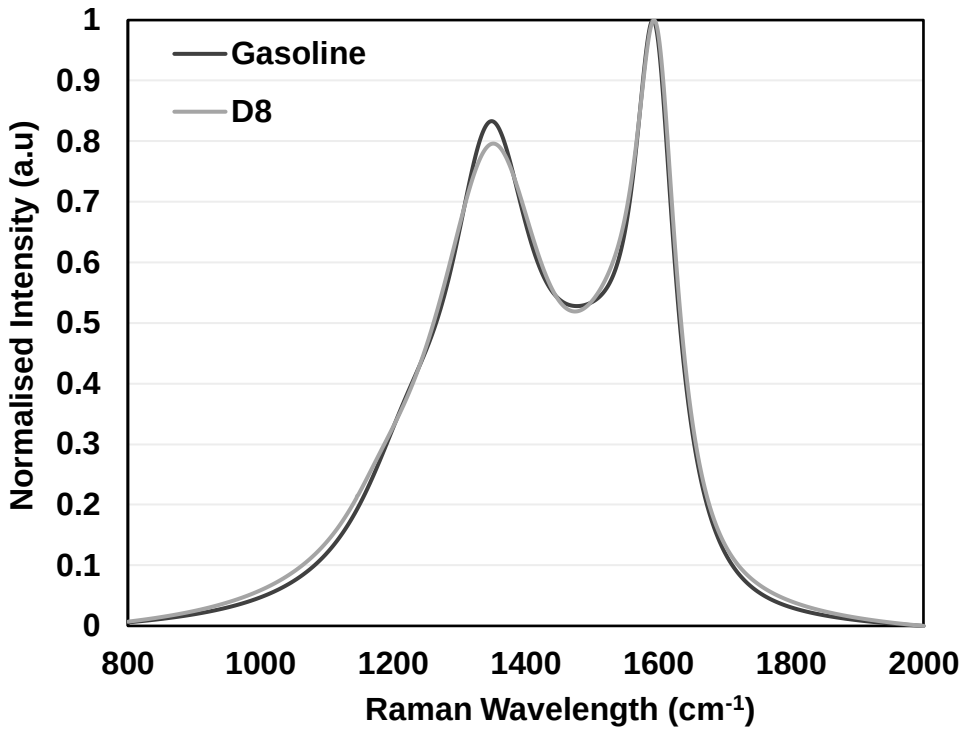
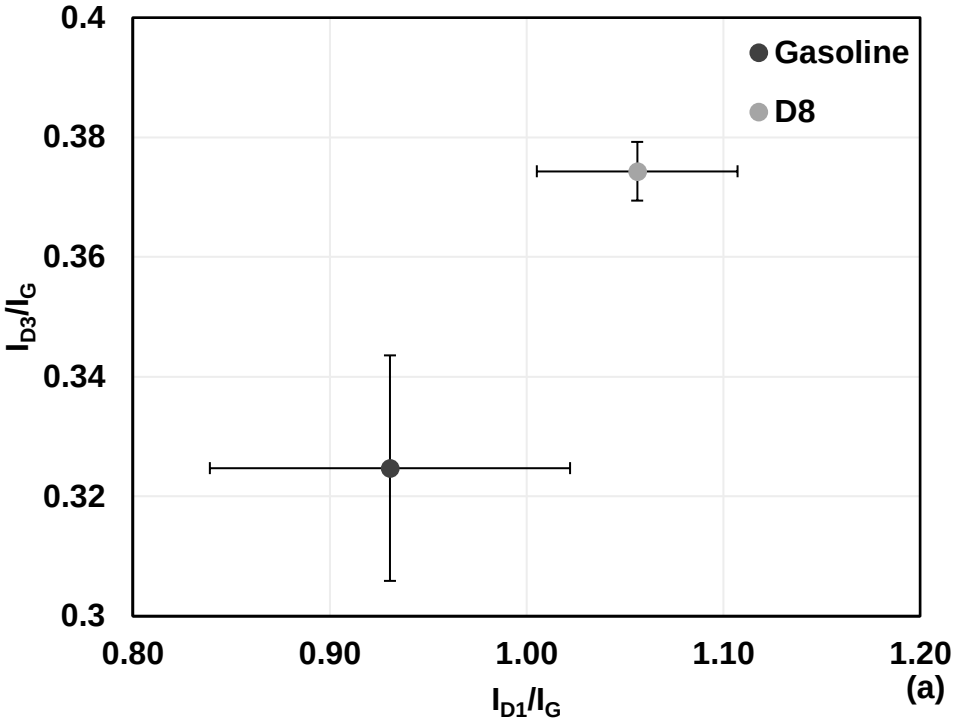
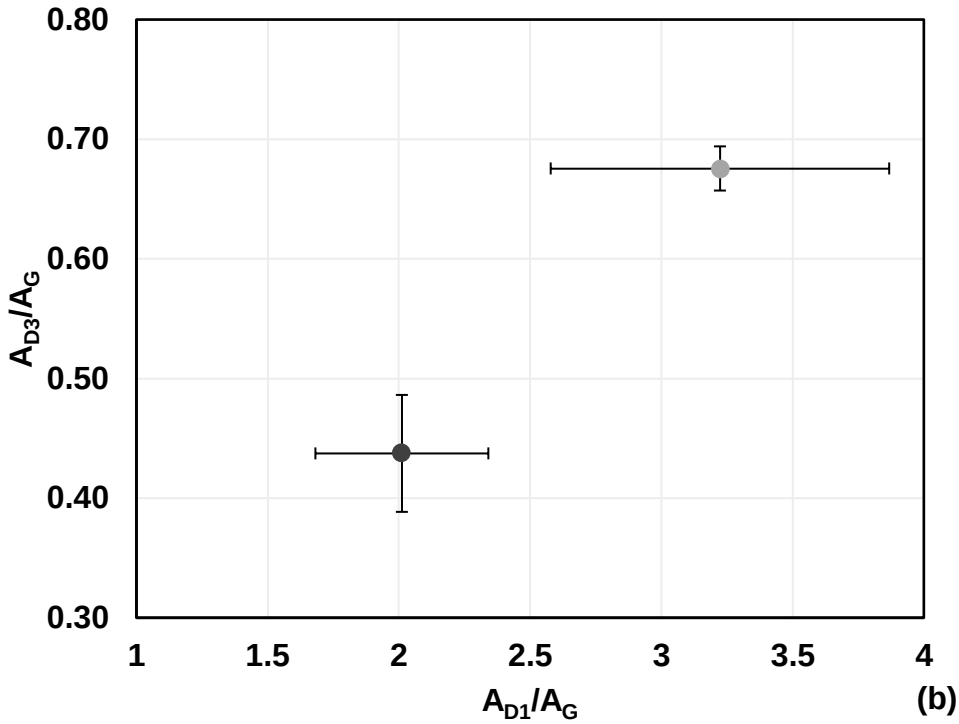


Figure 5.14: Average RAMAN spectra of gasoline and D8.

* This chapter is published as journal article.

.





* This chapter is published as journal article.

.

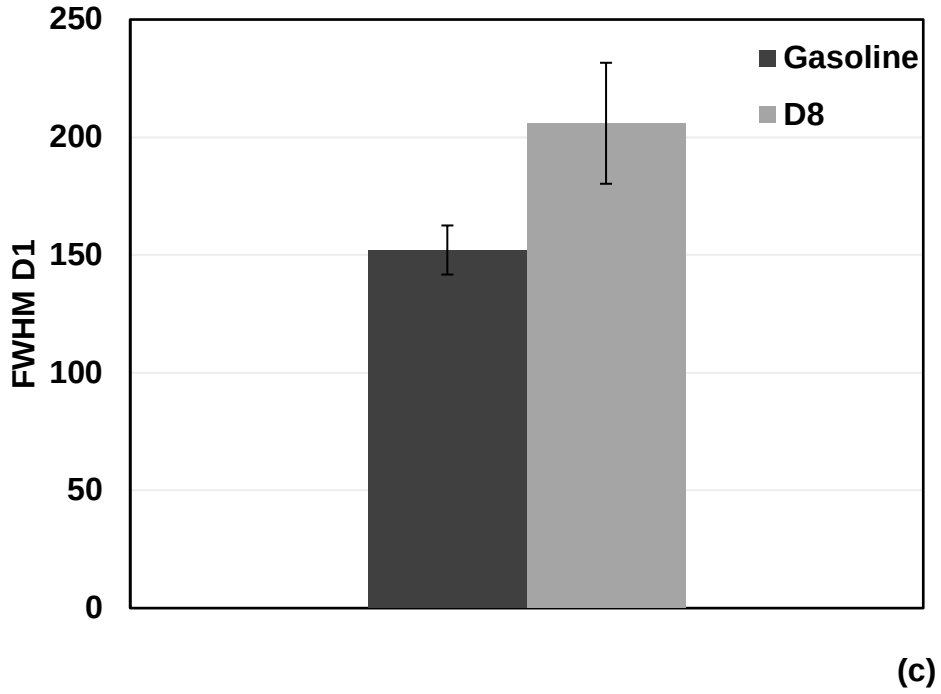


Figure 5.15: (a) Intensity ratio for band D1 and D3 **(b)** area ratio for band D1 and D3 **(c)** D1 FWHM of gasoline and D8.

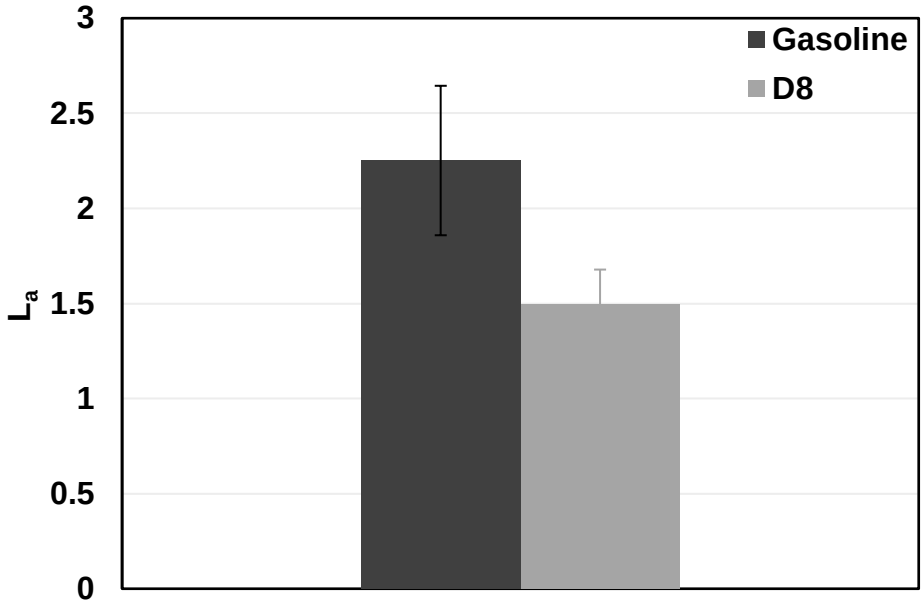


Figure 5.16: Estimated L_a using modified Knight and White's formula for gasoline and D8

* This chapter is published as journal article.

.

Based on the estimation of L_a derived from the modified Knight and White's formula (***Equation* 3.24**), gasoline exhibited a comparatively longer L_a to D8. The shorter L_a of D8 was attributed to a greater concentration of carbon atoms located at the edge site. This promoted the oxidation of PM due to easier access for oxygen [**208**]. This has also been identified as another factor responsible for the enhanced PM oxidation reactivity.

5.4 Summary

This chapter summarises the effect of 8% (v/v) DMC blended with EN228 commercial gasoline. The study evaluated the effect of DMC addition in GDI engines in terms of (i) combustion characteristics, (ii) gaseous and PM emissions and (iii) PM characteristics including the oxidation reactivity, compositions, dp_0, microstructure and Nanostructure.

A significant reduction of THC and PM was demonstrated by the addition of DMC, whilst maintaining the combustion characteristics and BTE. The improved THC and PM emissions were associated with the oxygen content in DMC, and its advantageous chemical structure. However, CO was slightly deteriorated due to less post-combustion oxidation. The addition of DMC also results in lower PM formation, a reduction in np_0 and average agglomerate size (smaller R_g). In conjunction with lower agglomerates concentrations, the collision mechanisms of the PM was altered, leading to the changes in the geometrical structure of the agglomerates.

* This chapter is published as journal article.

.

Furthermore, the D8 PM characteristics showed greater oxidation reactivity as a consequence from smaller average d_{p0}, greater amorphous concentration, disordered layering of graphene layers, and shorter L_a. This was the result of supplementary oxygen concentration and lower combustion temperature, from the DMC.

* This chapter is published as journal article.

.

CHAPTER 6 IMPROVING GPFS PERFORMANCE BY ARCHITECTURE OPTIMISATION

6.1 Introduction

To achieve the current enforceable *Euro VI* PM emissions limit, the application of GPFs are viewed as the most effective approach. Therefore, GPF properties are extensively evaluated, like DPF in the past, in order to search for a design with optimum performance (filtration efficiency and pressure drop). It is likely that the application of the GPF will be downstream to the TWC, forming a second brick in the exhaust system in GDI engines. Consequently, the literature is currently focussing on assessing aftertreatment architectural configurations and how it affects GPF performance. In order to optimise the aftertreatment architecture between substrates, two configurations were comprehensively evaluated from 'fresh state' to the formation of the PM cake layer. Furthermore, this chapter presents the integration of GPF properties into the architectural configurations in order to study its influence on the GPF performance for further optimisation.

6.2 Methodology and Test Conditions

***Figure* 6.1** illustrates a schematic of the experimental setup for this study. Tests were performed under steady state engine conditions, with torque and speed set at 60 Nm / 2100 rpm, corresponding to the medium-load point of WLTP. The engine IEGR was removed to avoid influencing PM emissions, hence the IVO and EVC were set at 11 and 8 CAD aTDC. Other engine conditions are shown in ***Table* 6.1**. Prior to the test, GPFs were regenerated in a furnace at 550 °C for 4 hours. The GFPs were subsequently pre-treated, using 5 L / min of air at 400 °C. The gas hourly space

velocity (GHSV) was set at 30 000 h^{-1} , similar to real-world vehicle operating conditions using ***Equation* 6.1** [**6**].

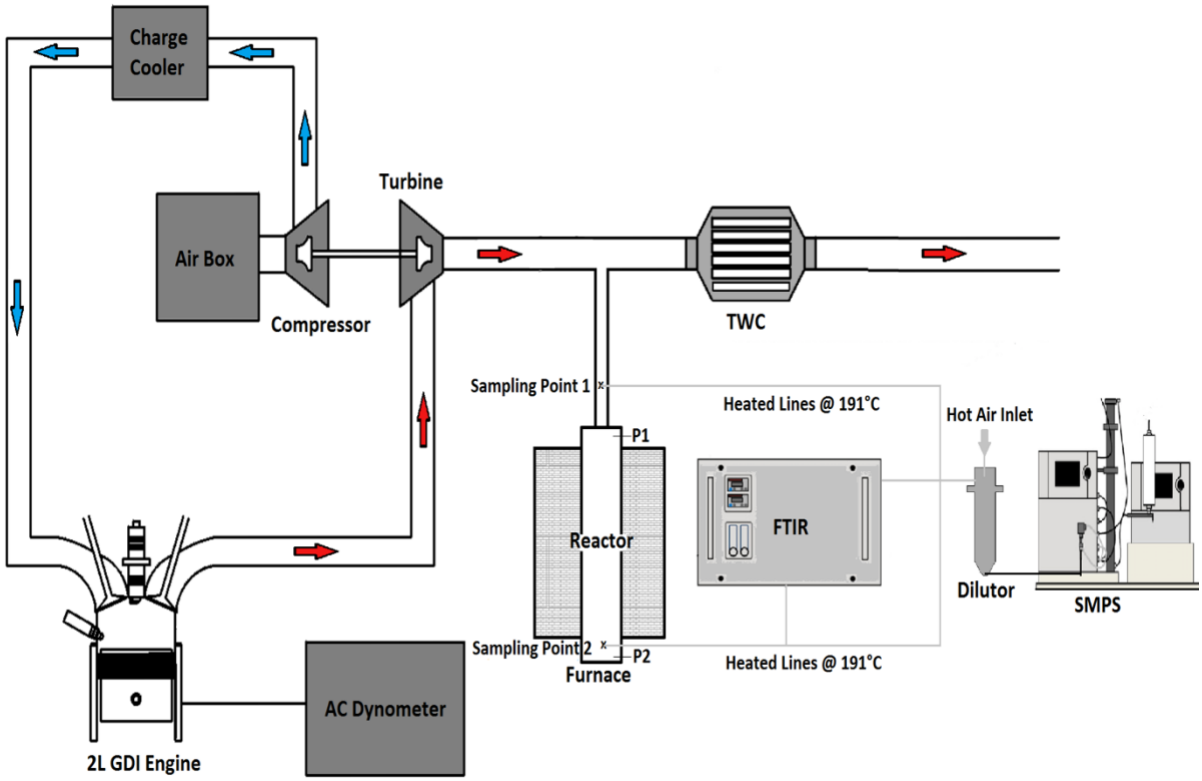


Figure 6.1: Schematic of the experimental setup.

Table 6.1: Experimental engine condition.

Engine Condition	
Stoichiometry, λ	1
Speed (rpm)	2100
Torque/Load (Nm)	60
Intake Valves Opening (CAD aTDC)	11
Exhaust Valves Closing (CAD aTDC)	8
Injection Timing (CAD bTDC)	303
Spark Timing (CAD bTDC)	30

Equation 6.1

$$GHSV\ (h^{-1}) = \frac{1}{Contact\ time\ (h)} = \frac{Feed\ rate\ (\frac{m^3}{h})}{Catalyst\ bed\ volume\ (m^3)}$$

The two GPFs utilised in this study were made out of cordierite and silicon carbide. Both GPFs had differing properties, which are tabulated in ***Table* 3.3**. The test consisted of CC and UF architectural configurations, corresponding to a 0 cm and 10 cm interval gap between the two substrates respectively. The UF configuration is displayed in ***Figure* 6.2**. The denotations of CC Cord., CC SiC, UF Cord. and UF SiC represent the CC cordierite, CC silicon carbide, UF cordierite and UF silicon carbide. Each individual test lasted for 4800 seconds, with variation in injection timing. Tests were initiated with standard calibration injection timing, for the first 3600 seconds. Filtration efficiencies were measured at the interval of 600 seconds (at 600th, 1800th and 3600th second) in order to assess the GPF from a fresh state, until 60 minutes after the exhaust gas exposure. Subsequently, the injection timing was advanced to 330 CAD bTDC for 600 seconds in order to mimic a cold-start and sudden elevated load conditions [**199**]. This interval was designed to study the performance of the GPF during high PM concentration events, with the filtration efficiency measured at 4200th second. Finally, the injection timing was reverted back to standard calibration in order to assess the post PM cake layer formation. The filtration efficiency measurement was acquired at the 4800th second. The experimental matrix is tabulated in ***Table* 6.2**. Pressure drop was based on the continuous absolution pressure measurements at sampling point 1 and 2, throughout the duration of the experiments.

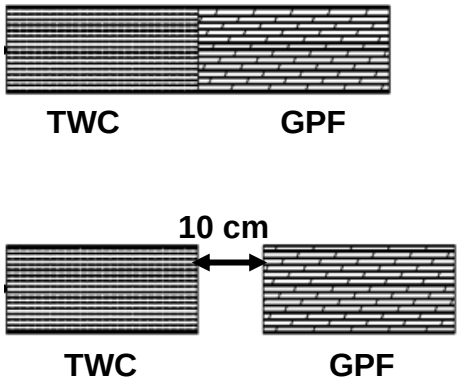


Figure 6.2: Schematic of aftertreatment architectures for CC (top) and UF (bottom).

Table 6.2: Experimental matrix and procedure for aftertreatment architecture.

Architecture Configurations					
CC Cord.	TWC + Cordierite GPF				
UF Cord.	TWC + Cordierite GPF				
CC SiC	TWC + SiC GPF				
UF SiC	TWC + SiC GPF				
Experimental Procedures	Fresh GPF	30 mins	60 mins	Advanced 330	Post Advanced 330
Time (second)	600th	1800th	3600th	4200th	4800th
Fuel Injection	Std.	Std.	Std.	Adv.	Std.

Std – Standard Calibration Injection Timing (303 CAD bTDC)
Adv – Advanced Injection Timing (330 CAD bTDC)

6.3 Results and Discussion

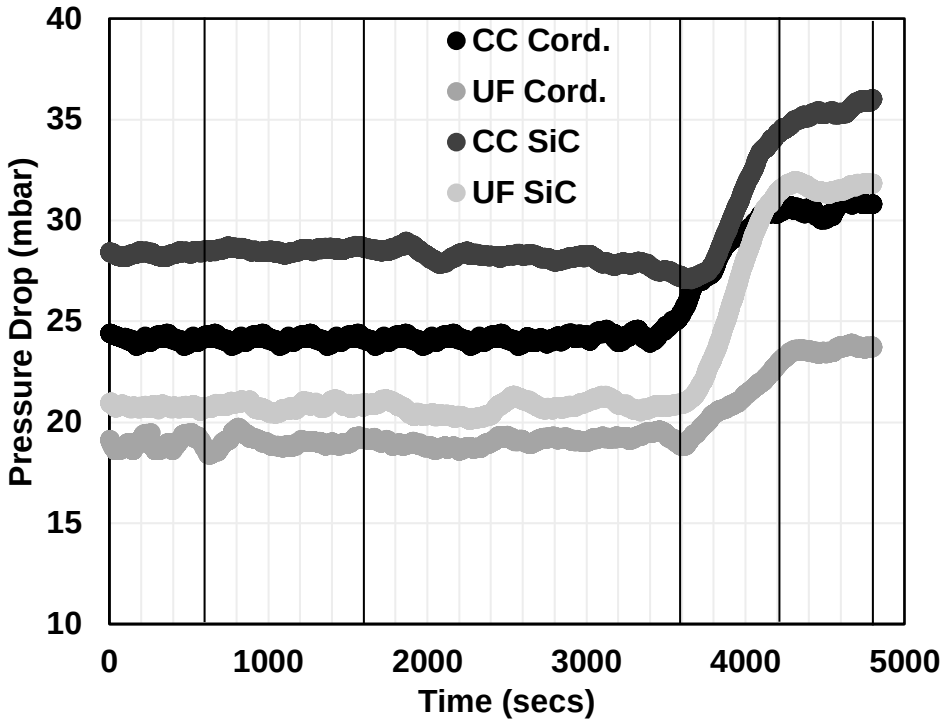


Figure 6.3: Pressure drop of aftertreatment architectures for 4800 seconds.

6.3.1 Pressure Drop Analysis

Figure* 6.3** illustrates the pressure drop measured throughout all the experimental work for 4800 seconds. In the examined aftertreatment architectural configurations, no observable pressure drop was observed during the standard calibrated fuel injection period (first 3600 seconds). This was evidenced by the PM emitted during this engine condition; composed of comparatively higher volatile content and smaller agglomerate size (Figure* 6.4**) to PM formed during advanced fuel injection condition [**92**], [**105**], [**106**]. Thus, the PM adhered in the GPF was not sufficient to induce observable back pressure in the system. When the fuel injection was advanced (3600 to 4200 seconds), a PM cake layer was formed, reducing the

permeability of the GPF and resulted in a linear surge in pressure drop. This occurred because flow was restricted through the filter walls and channels. As illustrated in ***Figure* 6.4**, a greater PM concentration and larger agglomerates were the cause. As soon as fuel injection timing reverted back to standard calibration at the 4200th second, the pressure drop did not display noticeable changes. Hence, this suggests that PM bridging (phase 3) and the PM cake layer (phase 4) were only formed during the sooty event (advanced fuel injection).

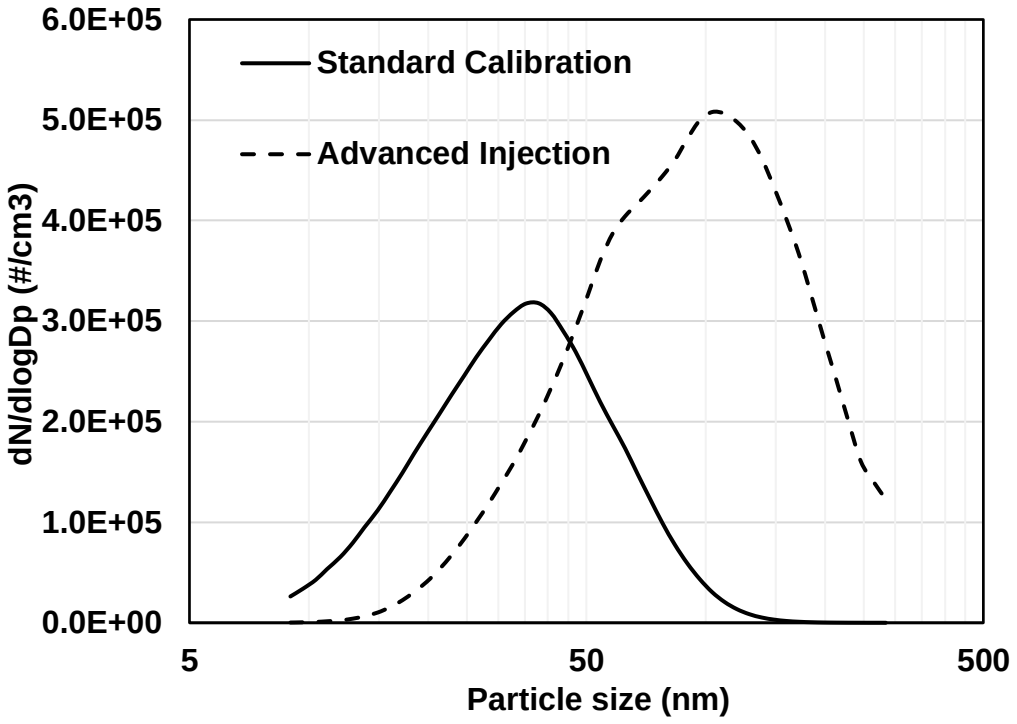


Figure 6.4: Number PSD at 60 nm / 2100 rpm for standard calibration and advanced fuel injections.

6.3.1.1 Effect on GPFs Properties on Pressure Drop

Pressure drop was observed at a consistently higher level with the use of a SiC based GPF, in comparison to cordierite based GPF, regardless of the architectural

configuration used. This was related to the advantageous properties of SiC GPF, including lower porosity, smaller MPS, lower cell density and thicker wall, that contributed to the restriction of gas flow. In spite of the negative impact on pressure drop, these properties can be beneficial in efficiently trapping PM (to be discussed in the later subsection). As observed in ***Figure* 6.3**, the pressure drop difference during the standard calibration fuel injection is negligible. The pressure drop difference was only induced during the advanced fuel injection timing.

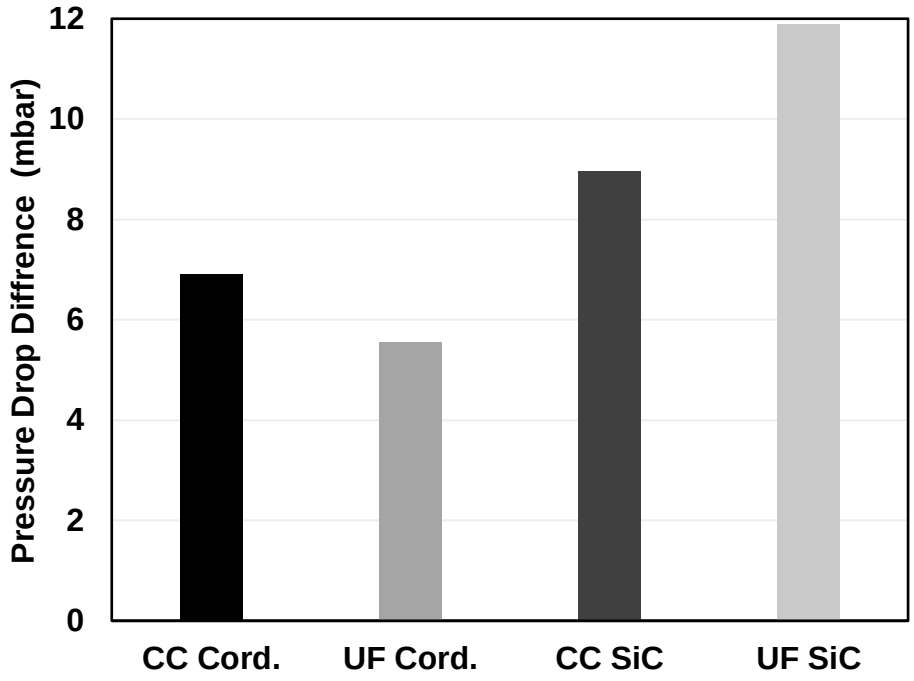


Figure 6.5: Pressure drop difference during advanced fuel injection for all architecture configurations.

The pressure drop difference computed during the advanced injection timing stage is presented in ***Figure* 6.5**. This can be used to estimate the thickness of PM on the GPF channel surface. The SiC GPF results exhibited a higher pressure drop difference (9 and 11 mbar) and steeper pressure drop gradient than Cord. GPF (6.9 and 5.5 mbar. This indicated that a thicker PM cake layer was formed. Moreover, the

steeper gradients of the pressure drop in ***Figure* 6.3** indicates a higher rate of PM wall-loading and bridging than the cordierite GPF. Therefore, it was believed that the higher effectiveness in PM filtration with the SiC GPF resulted in a reduction of GPF permeability, leading to greater pressure drop differences.

6.3.1.2 Influence of Aftertreament Architecture on Pressure Drop

In regards to the architectural configurations, the CC configuration showed a greater magnitude of pressure drop (28 and 24 mbar) in the system compared to the UF configuration (21 and 19 mbar) regardless of GPF properties (***Figure* 6.3**). The greater pressure drop was associated with greater gas temperatures at the inlet of the GPF [**289**]. Despite the temperature of the furnace being controlled between 450 to 500 °C, the local gas temperature at the inlet of GPF in CC architectural configuration was higher. This was due to the closer proximity to the TWC. The temperature at the TWC increased as a result of an exothermic reaction, generated by the oxidation of THC and CO. Consequently, a reduction in the exhaust gas density boosted the volumetric flowrate, leading to the more back pressure. In the case of the UF architectural configuration, the effect of supplemental heat from the TWC did not have a significant impact due to the heat loss in the interval gap. This led to a lower pressure drop, as there was no increase of flow resistance through the GPF wall due to the flow rate remaining unchanged. However, the pressure drop of UF SiC was measured at 31 mbar, surpassing CC Cord. (30 mbar) at the post-advanced fuel injection stage (4200 to 4600 second) despite having a lower pressure drop during earlier stages of the experiment. This was attributed to the advantageous properties of the SiC, which allowed swifter PM bridging in the porous medium (phase 3) and thicker PM cake layer formation (phase 4) from the improvement of the filtration performance. Despite that,

the pressure drop remained consistently lower in comparison to the CC SiC (35 mbar). However, PM collisions were thought to occur in between the interval gap of substrates, increasing the agglomeration process. This increased the concentration of larger d_p PM, which falls within the *Greenfield gap*. Consequently, the *Greenfield gap* effect was promoted with the less advantageous characteristics of the Cord. GPF, leading to the PM bridging at a slower rate. As a consequence, a thinner PM cake layer was formed on the GPF wall channel surface, during the event of the advanced fuel injection.

6.3.2 Filtration Efficiency Analysis

Figure* 6.6** is a plot of average $\eta_{Filtration}$ across the PSD diameter range (7.77 nm to 294.3 nm) for all aftertreatment architectural configurations. A mutual trend was observed where all architectural configurations gradually improved in filtration performance ($\eta_{Filtration}$), achieving around 100% $\eta_{Filtration}$, except for UF Cord (98%). The improvement was due to the PM cake layer forming on the GPF surface wall channel. This replaced and enhanced the filtration process, during high PM concentration events (advanced fuel injection) [**7**]. This was associated with the PM cake layer, which is the key factor for effective trapping of PM within the *Greenfield gap* [**6**], [**289**]. Therefore, both CC and UF presents a possibility of enhancing PM filtration with minimum thickness and density of the PM cake layer. The reason for the lower filtration efficiency with UF Cord. was clearly related to an inadequate PM cake layer thickness and density formed during stage 4. This was evidenced by the lowest pressure drop difference of 5.5 mbar (Figure* 6.5**). Although the pressure drop cannot be observed before the advanced fuel injection stage, progressive improvements in the filtration process were shown by all architectural configurations (***Figure* 6.3**). This

was attributed to the low fraction of the porous wall medium being filled, which was not sufficient to significantly impact pressure drop.

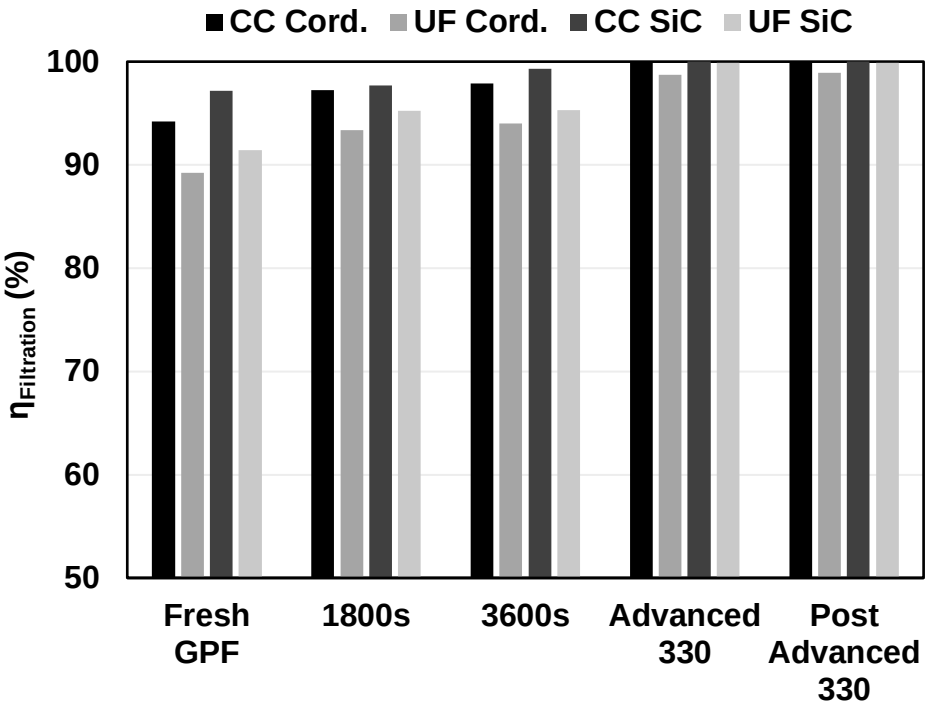
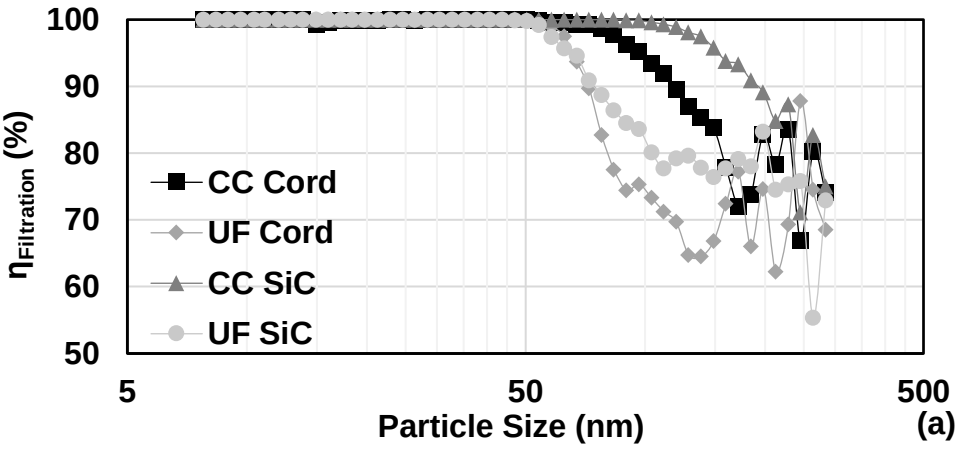


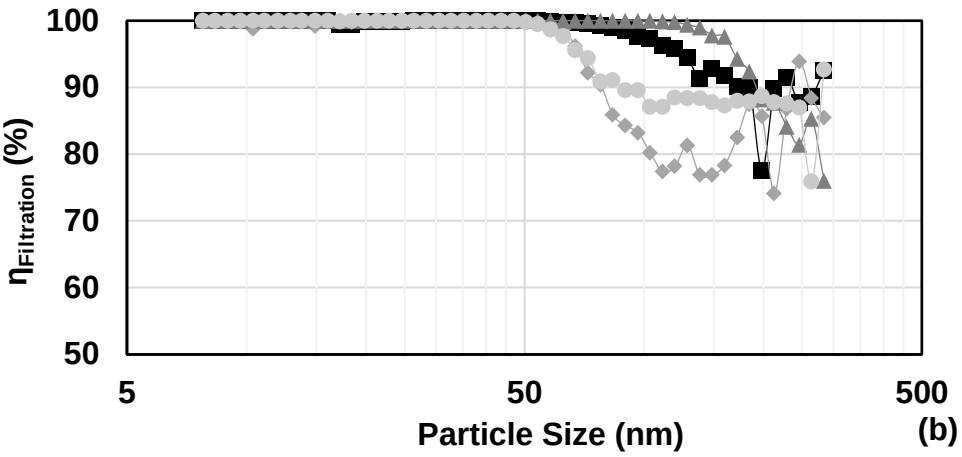
Figure 6.6: Average $\eta_{Filtration}$ for all aftertreatment architectural configurations.

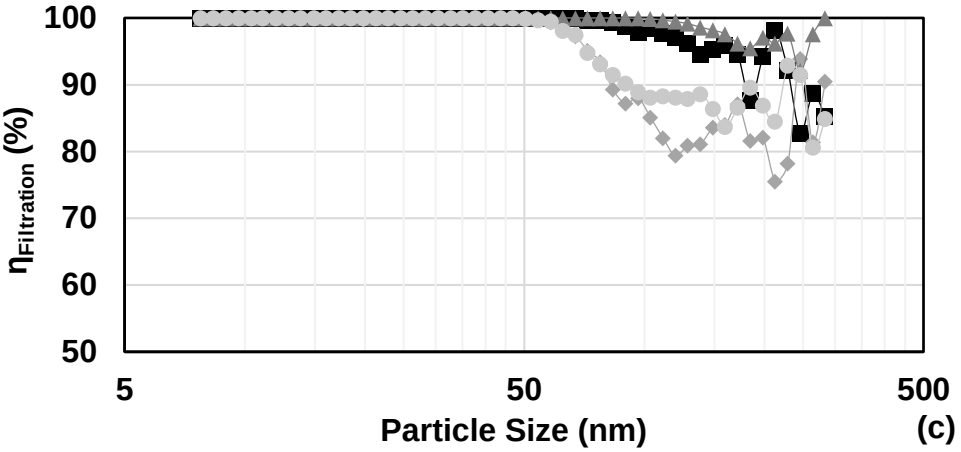
6.3.2.1 Effect of GPFs Properties on Filtration Performance

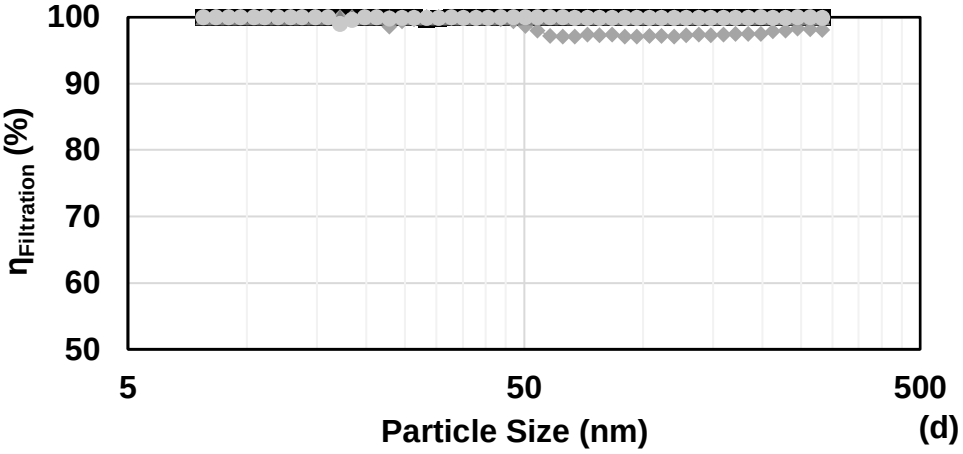
The $\eta_{Filtration}$ of all tested aftertreatment architectural configurations were measured for the duration of the experiments shown in ***Figure* 6.7**. The majority of nucleation mode PM showed about 100% $\eta_{Filtration}$ during the test for all architectural configurations due to the *Brownian Diffusion* mechanism. However, there was a range of d_p with the highest penetration, leading to the lowest $\eta_{Filtration}$ before the formation of PM cake layer (*Greenfield gap*). As explained in the literature review section, PM in that diameter range is too large for *Brownian Diffusion* mechanism, and the mass was insufficient for *Inertia Impaction or Direct Interception* mechanisms to take place

(***Figure* 6.7*a*** to ***Figure* 6.7*b***) [**35**], [**178**]. However, the effect of the *Greenfield gap* was improved with a SiC based GPF within CC and UF architectural configurations. This was due to the advantageous properties affecting both filtration velocity and MPS effects as shown in ***Figure* 2.12*a*** and ***Figure* 2.12b**. The gas flow was restricted more in the SiC GPF by the lower porosity and cell density, and thicker walls enhanced the filtration velocity effect. In conjunction with the smaller MPS of the SiC GPF, the PM filtration process was promoted through the enhancement of *Inertia Impaction and Direct Interception* mechanisms. Thus, this explains the narrower and lower peak of the *Greenfield gap* effect prior to the PM cake layer formation (advanced fuel injection stage) in comparison to the Cord. GPF. Subsequently, a greater volume of the GPF porous medium was filled. This led to a more rapid, and thicker PM cake layer formation during the highly sooty events in both CC and UF architectural configurations. This was reflected by greater pressure drop differences in ***Figure* 6.5** and a steeper pressure drop gradient in ***Figure* 6.3**).




100
90
80
70
60
50
ηFiltration (%)
5
50
500
Particle Size (nm)
(b)


100
90
80
70
60
50
ηFiltration (%)
5
50
500
Particle Size (nm)
(c)


100
90
80
70
60
50
ηFiltration (%)
5
50
500
Particle Size (nm)
(d)

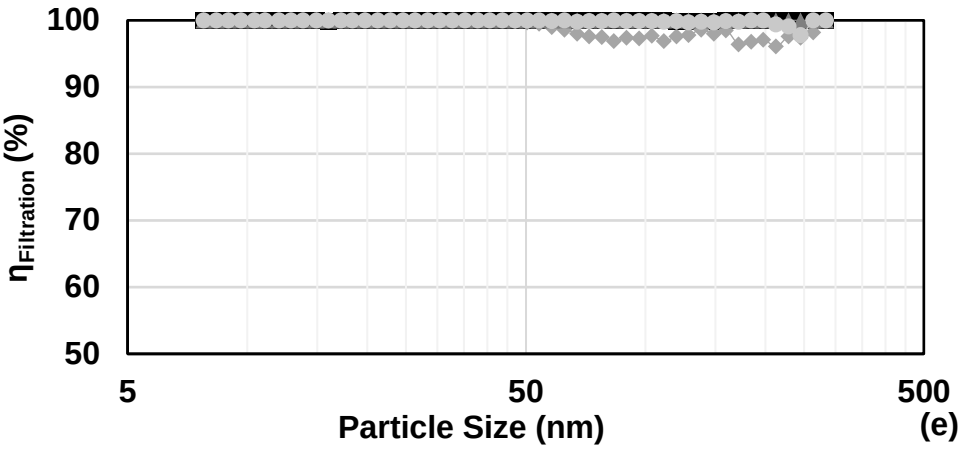


Figure 6.7: $\eta_{Filtration}$ **(a)** 600th second (Fresh) **(b)** 1800th second (30 mins) **(c)** 3600th second (60 mins) (**d)** 4200th second (Advanced Fuel Injection Timing) **(e)** 4800th second (Post Advanced Injection Timing).

6.3.2.2 Influence of Aftertreament Architecture on Filtration Performance

The data charted in ***Figure* 6.7** illustrated the CC architectural configuration has a better filtration performance in comparison to the UF architectural configuration (highest average filtration efficiency in ***Figure* 6.6**). Referring to the $\eta_{Filtration}$ prior to formation of PM (advanced fuel injection timing), the *Greenfield gap* was narrower and lower in peak using the CC architectural configuration. The peak d_p of the *Greenfield gap* for both Cord. and SiC GPFs in the CC architectural configuration are lower, measured at around 130 nm and 150 nm (200 nm and 250 nm for UF architectural configuration). As aforementioned, the higher gas flow rate in the CC architecture was predicted to have lower filtration performance than the UF architectural configuration. However, an opposite trend was exhibited in the results. This was attributed to the interval gap between substrates in the UF architectural configuration. The interval gap in the UF architectural configuration has led to PM growth, promoting the agglomeration process of PM. Therefore, increasing the PM agglomerate size and the concentration which falls within the *Greenfield gap* (wider and longer peak) [**55**], [**310**],

[**311**]. The use of the GPF with advantageous properties (SiC), resulted in an improvement in filtration performance (narrower and lower *Greenfield* gap), which was observed in the UF architectural configuration. The GPF improved the $\eta_{Filtration}$, as the penetration of PM within the Greenfield *gap* was reduced. Additionally, this justifies the lowest filtration performance with the Cord. GPF. This was particularly prominent in the UF Cord. architectural configuration, as it was unable to achieve 100 % $\eta_{Filtration}$, despite the formation of the PM cake layer. The higher PM concentrations within the *Greenfield* gap (higher penetration), resulted in a smaller fraction of GPF wall porous medium filled before the advanced fuel injection stage. Subsequently, a thinner and less dense PM cake layer was formed on the channel wall surface during the high PM concentration event. This resulted in a lower ability to trap PM efficiently. Comparing all the architectural configurations, the CC SiC has the highest $\eta_{Filtration}$, and the UF Cord. has the lowest $\eta_{Filtration}$ overall, based on the assessment of the measurement intervals.

6.4 Summary

The aftertreatment architectural configurations of the CC and UF were assessed on a scaled-down TWC-GPF. Assessment included pressure drop and $\eta_{Filtration}$. Furthermore, the influence of GPF properties were also evaluated in the aftertreatment architectural configuration. The results demonstrated a capability of reducing PM emissions efficiently up to 90%, displaying a potential to meet current *Euro VI* legislation. However, a major drawback was revealed, due to the trade-off between pressure drop and $\eta_{Filtration}$.

The pressure drop in the CC architectural configuration was constantly higher than the UF architectural configuration prior to the PM cake layer formation, regardless of the GPF used. Additionally, the CC architectural configuration also had better $\eta_{Filtration}$. The effect was more significant when using a GPF with more advantageous properties characteristics (SiC). In turn, the pressure drop was increased, notably in the UF SiC architectural configuration. The induced pressure drop during the advanced fuel injection stage surpassed CC Cord. and slightly below CC SiC. In conclusion, the aftertreatment architectural configurations are ranked as following: UF SiC, CC Cord., CC SiC and UF Cord, based on the balance between pressure drop and $\eta_{Filtration}$.

The application of the UF architectural configuration, using a GPF with similar properties to the SiC GPF, is the most promising combination for controlling GDI engine PM emissions. The trade-off shown was more optimum compared to other architectural configurations. It can minimise the deteriorating effects of the engine fuel economy and output power, due to the pressure drop (lower magnitude overall). Simultaneously, it can achieve similar $\eta_{Filtration}$ to CC Cord. and CC SiC after the PM cake layer formation. Furthermore, the proposed architectural configuration can also benefit the GPF passive regeneration strategy. This is achieved by lowering the frequency of regeneration, due to the comparable pressure drop after the PM cake layer was formed. Therefore, these results should be further verified with a commercial scale TWC and GPF.

CHAPTER 7 ENHANCING TEM ANALYSIS WITH UTILISATION OF FILTER EXTRACTION METHOD FOR GDI PM REDUCTION INVESTIGATION

7.1 Introduction

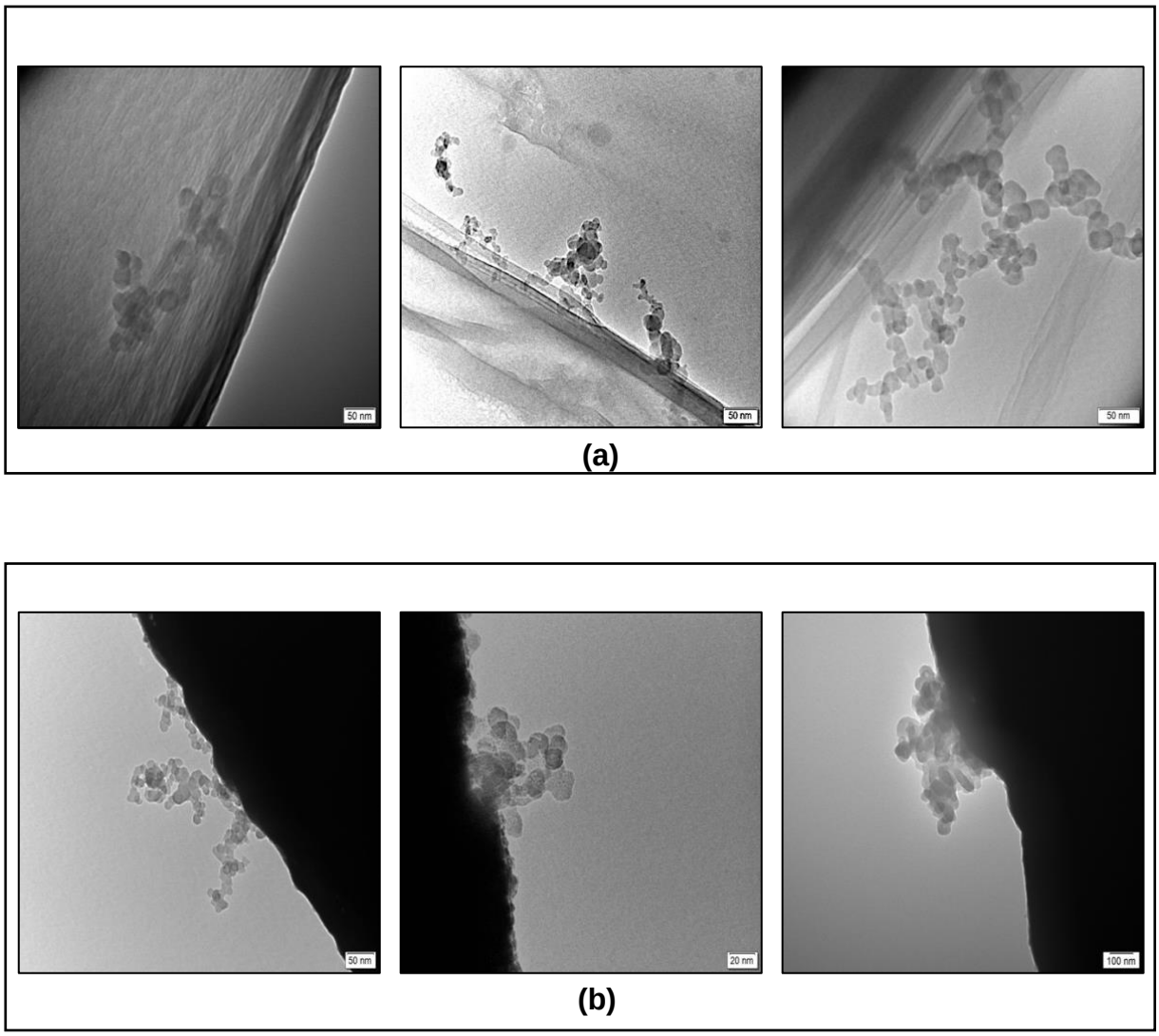


Figure 7.1: TEM micrographs of **(a)** broken formvar-carbon coating and **(b)** PM agglomerates adhered on TEM grid wall.

TEM analyses have been widely performed on PM that has been emitted by both CI and SI engines. Most studies have prepared TEM grid samples via direct exposure

thermophoretic sampling. In this chapter, an alternative method is proposed. Several reasons are associated with the proposal of alternative method, based on several limitations. One limitation includes the breaking of formvar-carbon coating on the TEM grids, leading to unrecognisable boundaries of PM agglomerates (***Figure* 7.1*a***). This limitation is thought to be related to the high flow rate and high EGT. Secondly, PM agglomerates were adhered to the TEM grid walls (***Figure* 7.1*b***), leading to alteration of the geometric dimension (D_f) of PM agglomerates. It also caused difficulty in detecting clear boundaries for the primary particle diameter measurements. However, a limited number of PM agglomerates were adhered onto the TEM grids. This consequently increases the difficulty in locating an adequate number of PM agglomerates for the microstructural and Nanostructural analyses. Therefore, filter extraction method proposed in this study is hypothesised to be able to improve the analytical process. Hence, this chapter demonstrates the advantages of the proposed method through visual comparison. Additionally, the comparison in the microstructure scale between the two methodologies was performed including d_{p0}, np_0, R_g and D_f.

7.2 Methodology and Test Conditions

The engine condition was set to MBT conditions of torque and speed, measuring at 90 Nm / 2200 rpm. The direct exposure TEM grids and PM loaded filters were used for the case study in ***Chapter 4***. TEM grids were prepared according to the *Transmission Electron Microscope (TEM) section* discussed in ***Chapter 3***. Subsequently, the same procedures and post-processing processes were used with the in-house MATLAB script.

7.3 Results and Discussion

7.3.1 Advantages of Filter Extraction Method

***Figure* 7.2** shows TEM micrographs captured from TEM grids prepared by the filter extraction method. The concentration of PM agglomerates on the TEM grids were significantly increased, improving the reliability and repeatability of the microstructural results. Furthermore, there was no occurrence of broken TEM coatings or PM agglomerates that adhered onto the TEM grid wall. Through visual assessment, some drastically larger agglomerates (course mode PM) and filter microfibers were present. For the purpose of confirming the comparability between the methods, an evaluation was performed on d_{p0}, np_0, R_g and D_f; discussed in the next subsection.

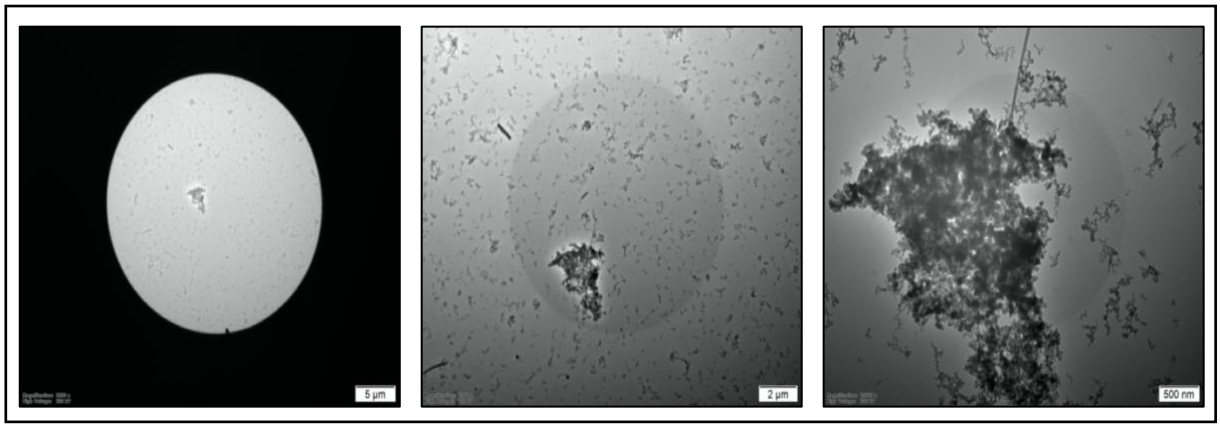


Figure 7.2: TEM Micrographs from filter extraction method at low, medium and high magnifications.

7.3.2 Comparisons of d_{p0}, np_0, R_g and D_f.

The d_{p0} measurements for the PM extracted from the loaded filter satisfied the log-normality test (***Table* 7.1**), and is plotted in ***Figure* 7.3**. The average d_{p0} measurements are similar between both methodologies, 28.5 nm and 28.2 nm

respectively (***Figure* 7.4**), for direct exposure and filter extraction methods. This indicates no alteration (e.g. surface growth or oxidation) to the primary particles during the loading process.

Table 7.1: Statistical normality test for TEM grids prepared by direct exposure and filter extraction.

Null Hypothesis	Significance	Results
The distribution of Log (DirectExposure) is normal with mean 1.43 and standard deviation 0.138	0.200[a]	Retain null hypothesis
The distribution of Log (FilterExtraction) is normal with mean 1.44 and standard deviation 0.107	0.097[a]	Retain null hypothesis

Asymptotic significances are displayed. The significance level is 0.05

[a] Lilliefors corrected

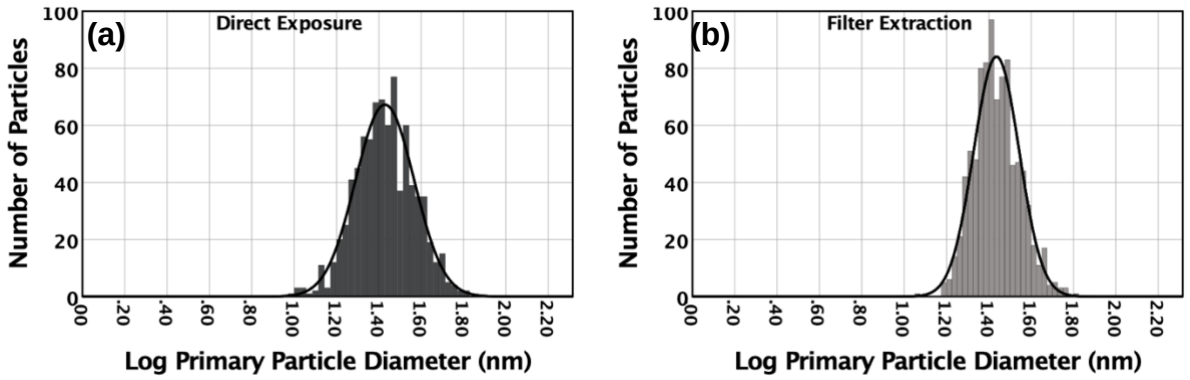


Figure 7.3: Log-normal primary particles distribution for **(a)** direct exposure and **(b)** filter extraction methods.

It is expected for growth to take place in PM agglomerates. Therefore, the measured R_g was increased from 75.9 nm to 126.2 nm in the filter extraction method. PM growth is attributed to the increase of residence time during the loading process in the filter. Although the same sampling point was used for TEM grid preparation

during the direct exposure method and PM loading, the use of an external heating line during the loading process has promoted the interaction between particles. During the process, the particles collided forming larger agglomerates. As a consequence, the np_0 also increased, which is consistent with the R_g trend.

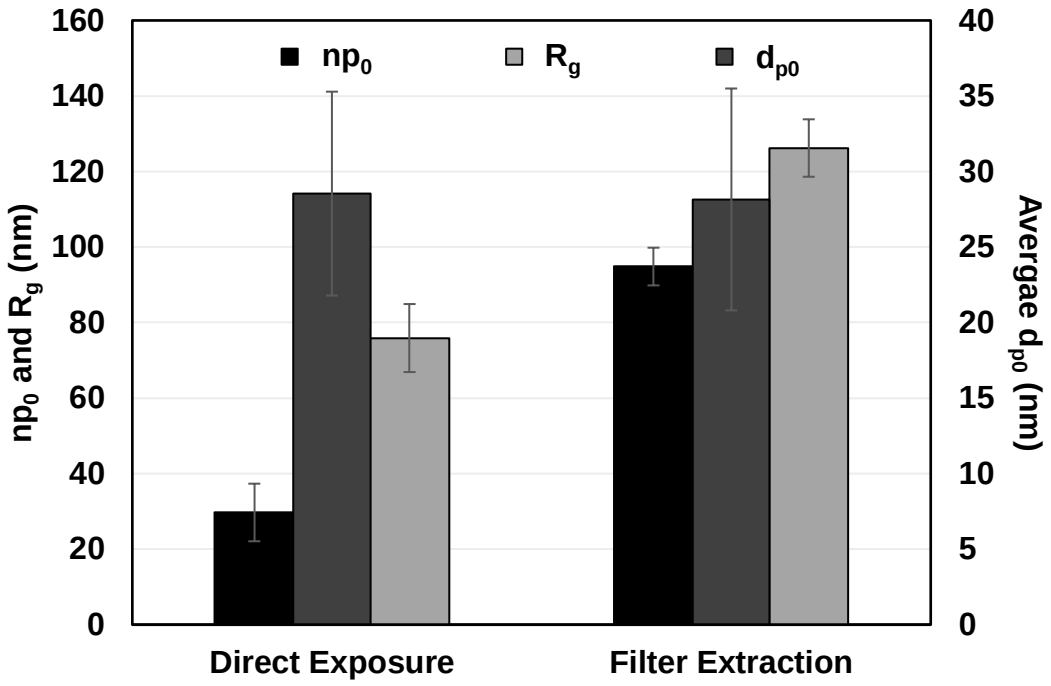


Figure 7.4: d_{p0}, np_0, R_g and D_f for direct exposure and filter extraction methods.

Table 7.2: R_2 of linear regression for D_f (R_g) and D_f (LW) methodology.

	D_f (R_g)	D_v (LW)
Direct Exposure	0.7511	0.8070
Filter Extraction	0.6866	0.7875

Prior to the comparison of D_f, R_2 was evaluated, indicating the filter extraction method has a magnitude above 0.5. Thus, the results were deemed comparable.

Referring to the D_f in ***Figure* 7.5**, both D_f (R_g) and D_f (LW) do not show a significant difference between the two methodologies used for TEM grid preparation. However, the RFF shows a slightly lower value, reflecting sensitivity to changes in agglomerate size [**199**]. According to the ***Equation* 3.20**, the average perimeter of agglomerates increased in the filter extraction method, due to the larger R_g of the PM agglomerates and similar d_{p0}. Overall, the geometrical dimensions were similar for both methods, proving that longer residence times during agglomeration does not change the type of collisions.

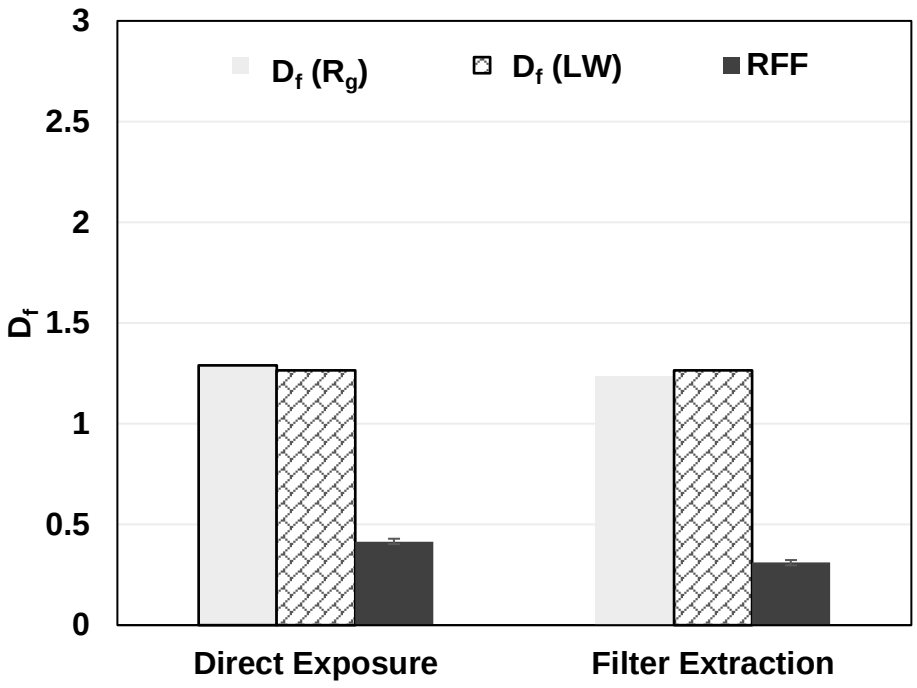


Figure 7.5: D_f of PM agglomerates for direct exposure and filter extraction.

7.4 Summary

A microscale evaluation of PM agglomerates was performed with direct exposure and filter extraction methods. The proposed methodology demonstrated to be more

advantageous in comparison to the conventional direct exposure method from the visual assessment. The assessment did not show any limitations using the proposed alternative method. It can increase PM adhesion on TEM grids, allowing a greater number of agglomerates to be analysed for better reliability and repeatability.

With regards to the microscale analysis, similar d_{p0} and D_f values were measured, except for R_g and n_{p0}. This indicates no major alterations to the PM during the loading process, other than increased collision frequency (larger R_g). This proves comparability between the two methods. Furthermore, the validation of the direct exposure method in this study can be used as a reference for future utilisation.

CHAPTER 8 CONCLUSIONS AND FUTURE WORKS

8.1 Summary of Findings

This research thesis has extensively studied PM emissions and characteristics, utilising several approaches. These approaches include the combustion stoichiometry, DMC/gasoline blends, and aftertreatment architectural configurations. Moreover, filter extraction TEM grid preparation methodology was introduced and validated. Experimental results were obtained using a 2L turbocharged GDI engine. The summary of this research thesis is as follows:

8.1.1 Effect of Combustion Stoichiometry

Regarding the effects of combustion stoichiometry at MBT conditions, the engine operation during lean conditions was found to be beneficial in many ways. This was with the exception of the deteriorating combustion stability (higher COV_{IMEEP}). The BTE, $\eta_{Combustion}$ and fuel economy were gradually improved up to 3%, 2% and 5.44% respectively as the λ transitioned towards lean. Although THC and CO showed improvement (reduced by 23% and 87%), as combustion was leaner, 42% more NO_x was formed. However, this condition can be advantageous in conjunction with excess oxygen, allowing easier GPF regeneration.

With regards to the PM emissions, the lowest concentration was measured during the stoichiometric condition. This was due to greater nucleation mode PM forming during lean and rich combustion, which did not occur during the stoichiometric condition. Contrarily, both lean and rich conditions had a lower concentration of solid soot PM in comparison to stoichiometric. Regardless, both lean and stoichiometric PM have a similar composition ratio of VOM to elemental soot at approximately of 29% to

71%. The rich condition exhibited a slightly higher PM composition ratio of 32% to 68%.

The overall PM characteristics indicated a similarity between rich and stoichiometric conditions. An improvement in PM oxidation reactivity was only observed in the lean PM with about 20 °C earlier. This was attributed to Nanostructural changes observed in RAMAN. Shorter, more disordered graphene fringes exhibiting more curvature, were the reason for the aforementioned changes. The study suggests rich and stoichiometric PM agglomerates were formed in the same course, however were formed differently in the lean condition. The lower D_f of rich and stoichiometric PM have a similar impact on human health. The D_f similarities exhibited under rich and stoichiometric conditions have a similar influence on GPF performance. Although the higher D_f in lean PM can reduce the negative effects on human health, it also reduces the effectiveness of trapping by the GPF. In terms of advantages, lean PM is easier to oxidise in comparison to rich and stoichiometric PM. Furthermore, periodic combustion under lean conditions can benefit the regeneration strategy of the GPF. This is due to the higher NO_x further enhancing PM oxidation reactivity. The higher oxidation reactivity of NO_x (lower start of oxidation temperature for PM) can reduce the regeneration time of the GPF at a lower temperature. Therefore, the duration of engine combustion in the lean condition can be reduced (reducing duration of low combustion stability). Lean combustion can be proposed during idle or low load conditions, as it can simultaneously reduce unnecessary carbonaceous emissions (THC, CO, CO_2 and PM emissions).

8.1.2 DMC-Gasoline Blend

The alternative fuel, 8% (v/v) DMC-gasoline blend, did not show any significant deteriorations in engine performance. Similar in-cylinder pressure and combustion stability were measured. The engine combustion temperature was estimated lower, demonstrated by lower RoHR and EGT. This led to reduced post-combustion oxidation (with 7% greater of CO emission) and impacted the PM Nanostructure. The alteration of Nanostructure includes shorter L_a graphene fringe layers were more disorderly and consisted of higher amorphous concentration. The excess oxygen contributed by DMC reduced the THC (30%), PM emissions (60%) and the average d_{p0} (3 nm reduction). Improvements exhibited in PM emissions were due to the lower elemental soot formation, and as consequence, resulted in less np_0 and lower R_g. Consequently, these effects altered the collisions of PM, emitting more compact and clustery agglomerates (higher D_f). Generally, the influence of DMC on PM agglomerates agreed with higher oxidation reactivity.

The enhanced oxidation reactivity is beneficial for GPF regeneration strategies, by reducing the required energy and the frequency of regeneration. Additionally, lower PM concentration and smaller agglomerates (lower R_g) emitted by D8 can reduce the pressure drop of GPFs. This minimises the deteriorating effect of the engine by the back pressure. Therefore, DMC is considered as a potential candidate as a fuel replacement for GDI engines, which can potentially achieve the *Euro VI* emissions limits. This can aid the reduction of hazardous emissions that affect humans and the environment.

8.1.3 Aftertreatment Architectures

Aftertreatment architectural configurations were assessed, suggesting that there is trade-off between pressure drop and $\eta_{Filtration}$. The CC architectural configuration induced up to 32% higher back pressure (pressure drop), although a maximum of 6% improvement on filtration performance was promoted. As a subsequent effect, a thicker PM cake layer was formed, rapidly promoting $\eta_{Filtration}$ close to 100%. Despite the lower pressure drop and filtration performance exhibited with the UF architectural configuration, it was learned that using a GPF with advantageous properties can improve the $\eta_{Filtration}$. The increase of filtration efficiency was observed to be as high as 3%. The pressure drop was slightly increased, along with a slower PM cake layer formation. This was evidenced in the UF SiC architectural configuration, demonstrating the ability to form an adequate PM cake layer thickness at nearly 100 % $\eta_{Filtration}$.

The trade-off shown in the UF SiC architectural configuration was optimum in comparison to other architectural configurations. Its use can minimise the deteriorating effects of the engine (fuel economy and output power) due to the pressure drop (lower magnitude overall) yet exhibited a similar $\eta_{Filtration}$ to CC Cord. and CC SiC after the PM cake layer formation. Furthermore, the proposed architectural configuration can also benefit the GPF passive regeneration strategy. This can be achieved by lowering the frequency of regeneration, due to the comparable pressure drop after the formation of the PM cake layer.

8.1.4 Filter Extraction TEM Grids Preparation

The filter extraction TEM grid preparation methodology shows no defects or other limitations found in conventional direct exposure method. The microscale analysis for both methodologies were similar (difference below observable magnitude, lesser than

5%), with the exception of np_0 and R_g, due to PM agglomerate growth and maturation. This leads to larger np_0 and R_g values measured in the PM agglomerates, when the TEM grids were prepared by filter extraction method. With the validated results, the direct exposure TEM grid preparation method demonstrates potential to be used for further TEM experimentation. However, the investigation should proceed into Nanostructural analysis for further validation.

8.2 Future Work Reference

1. In relation to the AFR, combustion analysis, gaseous emissions and PM characteristics have been understood. The unlikelihood of GPF regeneration during stoichiometric combustion was predicted in this research thesis. Therefore, it is important to understand the regeneration process during lean combustion. Additional tests should be performed with a PM-loaded-GPF, positioned upstream to a TWC at idle and low load conditions. During the tests, stoichiometry should be optimised between the values of 1.01 and 1.1. The results will provide valuable information, allowing regeneration strategies for GPF applications in GDI engines to be determined.

2. In regard to the DMC case study; an evaluation of the engine performance, emissions and PM characteristics were presented. However, these tests were carried out without the application of a TWC. Therefore, the emissions should be assessed with the application of a TWC to ensure compatibility, as well as to investigate its influence over PM characteristics derived from DMC-gasoline blends. Furthermore, an assessment on the GPF filtration performance should be performed with DMC-gasoline blends. The differing PM characteristics and PM concentrations may have an influence on the GPF. It is proposed that further studies

should be conducted in the WLTC and RDE tests, to ensure compliance with current *Euro VI* legislation and future emissions schedules.

3. Aftertreatment architectural configurations have demonstrated more promising applications with the use of UF SiC. A full size TWC and GPF should be utilised with complete WLTC and RDE tests in order to validate architectural configurations. Moreover, optimisation of the UF architectural configuration is required, prior to its commercial application. Particular attention should be focussed on the distance of the interval gap, and the influence of GPF properties on architectural configurations. The future experimental work should also include an assessment of cGPF, that includes varying the distribution of the catalyst load between the TWC and cGPF.

4. A microscale TEM analysis has been performed, indicating filter extraction method is capable of producing similar results. However, an extended analysis on Nanostructure (graphene fringe length, tortuosity, separation distance) would be required to further verify the methodology. A similar comparative analysis should also be performed on PM, formed by different fuels or engine conditions. This will provide a final validation of the methodology. In addition, a novel 'burn-off' investigation can be presented, using the proposed alternative methodology to study GDI engines PM. This can provide a broader understanding of PM characteristics during the oxidation process, which can be exceptionally useful in the determination of GPF design and regeneration strategies.

LIST OF REFERENCES

[1] M. Bogarra, J. M. Herreros, A. Tsolakis, A. P. E. York, and P. J. Millington, "*Study of particulate matter and gaseous emissions in gasoline direct injection engine using on-board exhaust gas fuel reforming,*" *Appl. Energy*, vol. 180, pp. 245–255, 2016, doi: 10.1016/j.apenergy.2016.07.100.

[2] C. L. Reddington *et al.*, "*Primary versus secondary contributions to particle number concentrations in the European boundary layer,*" *Atmos. Chem. Phys.*, vol. 11, no. 23, pp. 12007–12036, 2011, doi: 10.5194/acp-11-12007-2011.

[3] M. Braisher, R. Stone, and P. Price, "*Particle Number Emissions from a Range of European Vehicles,*" *SAE Tech. Pap. 2010-01-0786*, 2010, doi: https://doi.org/10.4271/2010-01-0786.

[4] J. B. Heywood, *Internal combustion engine fundamentals*. New York: McGraw-Hill, 1988.

[5] X. He, M. A. Ratcliff, and B. T. Zigler, "*Effects of gasoline direct injection engine operating parameters on particle number emissions,*" *Energy and Fuels*, vol. 26, no. 4, pp. 2014–2027, 2012, doi: 10.1021/ef201917p.

[6] C. Hergueta, M. Bogarra, and A. Tsolakis, "*Catalyst Coated Gasoline Particulate Filters : Filtration Efficiency and Activity,*" 2017.

[7] C. Saito, T. Nakatani, Y. Miyairi, K. Yuuki, M. Makino, H. Kurachi, W. Heuss, T. Kuki, Y. Furuta, P. Kattouah, and C.-D. Vogt, "*New Particulate Filter Concept to Reduce Particle Number Emissions,*" *SAE Tech. Pap. 2011-01-0814*, 2011, doi: 10.4271/2011-01-0814.

[8] C. Hergueta, A. Tsolakis, J. M. M. Herreros, M. Bogarra, E. Price, K. Simmance, A. P. E. York, and D. Thompsett, "*Impact of bio-alcohol fuels combustion on particulate matter morphology from efficient gasoline direct injection engines,*" *Appl. Energy*, vol. 230, pp. 794–802, 2018, doi: 10.1016/j.apenergy.2018.08.076.

[9] P. Jiao, Z. Li, B. Shen, W. Zhang, X. Kong, and R. Jiang, "*Research of DPF regeneration with NOx-PM coupled chemical reaction,*" *Appl. Therm. Eng.*, 2017, doi: 10.1016/j.applthermaleng.2016.08.184.

[10] T. Leroy, J. Chauvin, N. Petit, and G. Corde, "*Motion planning control of the airpath of a S.I. engine with Valve Timing Actuators,*" *Proc. Fifth IFAC Symp. Adv. Automot. Control*, 2007.

[11] R. Cataluña, D. Dalávia, R. da Silva, E. Menezes, V. Venturi, and R. Wagner, "*Acceleration tests using gasolines formulated with di-TAE, TAEE and MTBE ethers,*" *Fuel*, vol. 90, no. 3, pp. 992–996, 2011, doi: 10.1016/j.fuel.2010.10.031.

[12] F. Nadim, P. Zack, G. E. Hoag, and S. L. Liu, "*United States experience with gasoline additives,*" *Energy Policy*, vol. 29, no. 1, pp. 1–5, 2001, doi: Doi 10.1016/S0301-4215(00)00099-9.

[13] R.-H. Chen, L.-B. Chiang, C.-N. Chen, and T.-H. Lin, "*Cold-start emissions of*

an SI engine using ethanol–gasoline blended fuel," *Appl. Therm. Eng.*, vol. 31, no. 8–9, pp. 1463–1467, 2011, doi: 10.1016/j.applthermaleng.2011.01.021.

[14] Z. H. Huang, H. Miao, L. Zhou, and D. Jiang, "*Combustion characteristics and hydrocarbon emissions of a spark ignition engine fuelled with gasoline-oxygenate blends,*" *Proc. Inst. Mech. Eng. Part D-Journal Automob. Eng.*, vol. 214, no. D3, pp. 341–346, 2000, doi: Doi 10.1243/0954407001527466.

[15] M. U. Alzueta, P. Salinas, Á. Millera, R. Bilbao, and M. Abián, "*A study of dimethyl carbonate conversion and its impact to minimize soot and NO emissions,*" *Proc. Combust. Inst.*, vol. 36, no. 3, pp. 3985–3993, 2017, doi: 10.1016/j.proci.2016.07.086.

[16] S.-H. Pyo, J. H. Park, T.-S. Chang, and R. Hatti-Kaul, "*Dimethyl carbonate as a green chemical,*" *Curr. Opin. Green Sustain. Chem.*, vol. 5, pp. 61–66, 2017, doi: 10.1016/j.cogsc.2017.03.012.

[17] P. Kongpanna, V. Pavarajarn, R. Gani, and S. Assabumrungrat, "*Techno-economic evaluation of different CO2-based processes for dimethyl carbonate production,*" *Chem. Eng. Res. Des.*, vol. 93, pp. 496–510, 2015, doi: 10.1016/j.cherd.2014.07.013.

[18] I. Schifter, U. González, L. Díaz, G. Sánchez-Reyna, I. Mejía-Centeno, and C. González-Macías, "*Comparison of performance and emissions for gasoline-oxygenated blends up to 20 percent oxygen and implications for combustion on a spark-ignited engine,*" *Fuel*, vol. 208, pp. 673–681, 2017, doi: 10.1016/j.fuel.2017.07.065.

[19] A. Abdalla and D. Liu, "*Dimethyl Carbonate as a Promising Oxygenated Fuel for Combustion: A Review,*" *Energies*, vol. 11, no. 6, p. 1552, 2018, doi: 10.3390/en11061552.

[20] A. Arteconi, A. Mazzarini, and G. Di Nicola, "*Emissions from Ethers and Organic Carbonate Fuel Additives: A Review,*" *Water Air Soil Pollut.*, vol. 221, no. 1–4, pp. 405–423, 2011, doi: 10.1007/s11270-011-0804-y.

[21] R. R. Ginting, A. Mustain, and G. Wibawa, "*Determination of Ternary Liquid–Liquid Equilibria for Dimethyl Carbonate + 2-Methyl-1-propanol or 2-Methyl-2-propanol + Water Systems at T = 303.15 and 313.15 K,*" *J. Chem. Eng. Data*, vol. 62, no. 1, pp. 463–468, 2017, doi: 10.1021/acs.jced.6b00763.

[22] F. Belpoggi, M. Soffritti, and C. Maltoni, "*Methyl-tertiary-butyl ether (MTBE)--a gasoline additive--causes testicular and lymphohaematopoietic cancers in rats,*" *Toxicol Ind Heal.*, vol. 11, no. 2, pp. 119–149, 1995, doi: 10.1177/074823379501100202.

[23] S. Yunoki and M. Saito, "*A simple method to determine bioethanol content in gasoline using two-step extraction and liquid scintillation counting,*" *Bioresour. Technol.*, vol. 100, no. 23, pp. 6125–6128, 2009, doi: https://doi.org/10.1016/j.biortech.2009.06.027.

[24] X. Nie, X. Li, and D. O. Northwood, "*Corrosion Behavior of Metallic Materials in Ethanol-Gasoline Alternative Fuels,*" *Mater. Sci. Forum*, vol. 546–549, pp. 1093–

1100, 2007, doi: 10.4028/www.scientific.net/MSF.546-549.1093.

[25] X. Lou, D. Yang, and P. M. Singh, "*Effect of ethanol chemistry on stress corrosion cracking of carbon steel in fuel-grade ethanol,*" *Corrosion*, 2009, doi: 10.5006/1.3319105.

[26] L. M. Baena, M. Gómez, and J. A. Calderón, "*Aggressiveness of a 20% bioethanol-80% gasoline mixture on autoparts: I behavior of metallic materials and evaluation of their electrochemical properties,*" *Fuel*, 2012, doi: 10.1016/j.fuel.2011.12.002.

[27] H. Jafari, M. H. Idris, A. Ourdjini, H. Rahimi, and B. Ghobadian, "*Effect of ethanol as gasoline additive on vehicle fuel delivery system corrosion,*" *Mater. Corros. Und Korrosion*, vol. 61, no. 5, pp. 432–440, 2010, doi: 10.1002/maco.200905459.

[28] C. L. Peng, K. C. Lewis, and F. P. Stein, "*Water solubilities in blends of gasoline and oxygenates,*" *Fluid Phase Equilib.*, vol. 116, no. 1–2, pp. 437–444, 1996, doi: Doi 10.1016/0378-3812(95)02916-8.

[29] G. Broustail, F. Halter, P. Seers, G. Moréac, and C. Mounaim-Rousselle, "*Comparison of regulated and non-regulated pollutants with iso-octane/butanol and iso-octane/ethanol blends in a port-fuel injection Spark-Ignition engine,*" *Fuel*, vol. 94, pp. 251–261, 2012, doi: https://doi.org/10.1016/j.fuel.2011.10.068.

[30] B. M. Masum, H. H. Masjuki, M. A. Kalam, I. M. Rizwanul Fattah, S. M. Palash, and M. J. Abedin, "*Effect of ethanol–gasoline blend on NOx emission in SI engine,*" *Renew. Sustain. Energy Rev.*, vol. 24, pp. 209–222, 2013, doi: 10.1016/j.rser.2013.03.046.

[31] R. B. Gupta and A. Demirbas, *Gasoline, Diesel, and Ethanol Biofuels from Grasses and Plants*. Cambridge University Press, 2010.

[32] L. bin Wen, C.-Y. Y. Xin, and S.-C. C. Yang, "*The effect of adding dimethyl carbonate (DMC) and ethanol to unleaded gasoline on exhaust emission,*" *Appl. Energy*, vol. 87, no. 1, pp. 115–121, 2010, doi: 10.1016/j.apenergy.2009.06.005.

[33] P. Tundo, "*New developments in dimethyl carbonate chemistry,*" *Pure Appl. Chem.*, vol. 73, no. 7, pp. 1117–1124, 2001, doi: DOI 10.1351/pac200173071117.

[34] M. A. Pacheco and C. L. Marshall, "*Review of Dimethyl Carbonate (DMC) Manufacture and Its Characteristics as a Fuel Additive,*" *Energy & Fuels*, vol. 11, no. 1, pp. 2–29, 1997, doi: 10.1021/ef9600974.

[35] T. W. Chan, E. Meloche, J. Kubsh, D. Rosenblatt, R. Brezny, and G. Rideout, "*Evaluation of a Gasoline Particulate Filter to Reduce Particle Emissions from a Gasoline Direct Injection Vehicle,*" *SAE Int. J. Fuels Lubr.*, vol. 5, no. 3, pp. 1277–1290, 2012, doi: 10.4271/2012-01-1727.

[36] J. Song, M. Alam, A. Boehman, and U. Kim, "*Examination of the oxidation behavior of biodiesel soot,*" *Combust. Flame*, vol. 146, no. 4, pp. 589–604, 2006, doi: 10.1016/j.combustflame.2006.06.010.

List of References

[37] C. Wu, *Thermodynamics and Heat Powered Cycles: a Cognitive Engineering Approach*. New York : Nova Science Publishers, 2006.

[38] S. Bennett, "*Medium/Heavy Duty Truck Engines, Fuel & Computerized Management Systems,*" *Ref. Res. B. News*, vol. 27, no. 5, p. 960, 2012, [Online]. Available: https://books.google.com/books?id=76H8T5UPC7QC&pgis=1.

[39] R. Stone, *Introduction to internal combustion engines / Richard Stone.*, 3rd ed. Basingstoke: Basingstoke : Macmillan, 1999.

[40] C. Wang, "*Combustion and Emissions of a Direct Injection Gasoline Engine Using Biofuels,*" PhD. Thesis, University of Birmingham, 2014.

[41] K. Shimotani, K. Oikawa, O. Horada, and Y. Kagawa, "*Characteristics of gasoline in-cylinder direct injection engine,*" *JSAE Rev.*, vol. 17, no. 3, pp. 267–272, 1996, doi: https://doi.org/10.1016/0389-4304(96)00021-5.

[42] J. Yang and R. W. Anderson, "*Fuel Injection Strategies to Increase Full-Load Torque Output of a Direct-Injection SI Engine,*" *SAE Tech. Pap. SAE 980495*, 1998, doi: https://doi.org/10.4271/980495.

[43] H. Zhao, *Advanced Direct Injection Combustion Engine Technologies and Development : Gasoline And Gas Engines.* Woodhead Publishing, 2009.

[44] D. Fennell, J. Herreros, and A. Tsolakis, "*Improving gasoline direct injection (GDI) engine efficiency and emissions with hydrogen from exhaust gas fuel reforming,*" *Int. J. Hydrogen Energy*, vol. 39, no. 10, pp. 5153–5162, 2014, doi: 10.1016/j.ijhydene.2014.01.065.

[45] T. Alger, M. Hall, and R. D. Matthews, "*Effects of Swirl and Tumble on In-Cylinder Fuel Distribution in a Central Injected DISI Engine,*" *SAE Tech. Pap. 2000-01-0533*, 2000, doi: https://doi.org/10.4271/2000-01-0533.

[46] J. Harada, T. Tomita, H. Mizuno, Z. Mashiki, and Y. Ito, "*Development of Direct Injection Gasoline Engine,*" *SAE Tech. Pap. 970540*, 1997, doi: https://doi.org/10.4271/970540.

[47] R. B. GmbH, *Gasoline-engine management.*, 3rd ed., c. Plochingen: Plochingen, 2006.

[48] J. Yi, "*7 - Design and optimization of gasoline direct injection engines using computational fluid dynamics,*" vol. 1, H. B. T.-A. D. I. C. E. T. and D. Zhao, Ed. Woodhead Publishing, 2010, pp. 166–198.

[49] Ç. Mustafa Bahattin and B. Ozdalyan, *Gasoline Direct Injection, Fuel Injection*. InTech, 2010.

[50] C. Preussner, C. Döring, S. Fehler, and S. Kampmann, "*GDI: Interaction Between Mixture Preparation, Combustion System and Injector Performance,*" *SAE Tech. Pap. 980498*, 1998, doi: https://doi.org/10.4271/980498.

[51] R. Ortmann, S. Arndt, J. Raimann, R. Grzeszik, and G. Würfel, "*Methods and Analysis of Fuel Injection, Mixture Preparation and Charge Stratification in Different Direct Injected SI Engines,*" *SAE Tech. Pap. 2001-01-0970*, 2001, doi:

https://doi.org/10.4271/2001-01-0970.

[52] F. Daniel, "*Exhaust Gas Fuel Reforming for Improved Gasoline Direct Injection Efficiency and Emissions,*" PhD. Thesis, University of Birmingham, 2014.

[53] C. Baumgarten, *Mixture Formation in Internal Combustion Engine*. Springer Berlin Heidelberg, 2006.

[54] S. Stefan, "*Optical Diagnostic on FSI Transparent Engine,*" *FISITA World Automot. Congr.*, 2004.

[55] P. Eastwood, *Particulate Emissions from Vehicles*. 2008.

[56] M. M. Maricq, D. H. Podsiadlik, D. D. Brehob, and M. Haghgooie, "*Particulate Emissions from a Direct-Injection Spark-Ignition (DISI) Engine,*" no. 724, 1999, doi: 10.4271/1999-01-1530.

[57] C. Park, S. Lee, and U. Yi, "*Effects of engine operating conditions on particle emissions of lean-burn gasoline direct-injection engine,*" *Energy*, 2016, doi: 10.1016/j.energy.2016.09.051.

[58] N. Brown, "*Characterisation of Emissions and Combustion Stability of a Port Fuelled Spark Ignition Engine,*" PhD. Thesis, University of Nottingham, 2009.

[59] "*Directive 91/441/EEC of European Parliament and of the Council,*" *Off. J. Eur. Committees*, 1992.

[60] "*Directive 96/44/EC of European Parliament and of the Council,*" *Off. J. Eur. Committees*, 1996.

[61] "*Directive 2001/1/EC of European Parliament and of the Council,*" *Off. J. Eur. Committees*, 2001.

[62] "*Directive 2003/76/EC2006/96/EC of European Parliament and of the Council,*" *Off. J. Eur. Committees*, 2003.

[63] "*Commission Regulations (EC) No 692/2008 of European Parliament and of the Council,*" *Off. J. Eur. Committees*, 2008.

[64] "*REGULATION (EC) No 443/2009 of European Parliament and of the Council,*" *Off. J. Eur. Committees*, 2009.

[65] International Council on Clean Transportation, "*Real-Driving Emissions Test Procedure for Exhaust Gas Pollutant Emissions of Cars and Light Commercial Vehicles in Europe,*" 2017. https://theicct.org/sites/default/files/publications/EU-RDE_policy-update_18012017_vF.pdf (accessed Jul. 13, 2020).

[66] European Comission, "*Clean Mobility: Commission tables proposal on car emissions testing in real driving conditions,*" *Eur. Comm. - Quest. answers*, 2019, [Online]. Available: https://www.google.com/url?sa=t&rct=j&q=&esrc=s&source=web&cd=&cad=rja&uact=8&ved=2ahUKEwjOrr3s68nqAhVNT30KHR0jDVkQFjABegQIAxAB&url=https%3A%2F%2Feuropa.eu%2Frapid%2Fpress-release_QANDA-19-2850_en.htm&usg=AOvVaw1eVM0z4LVGpw9FJ8phx8vY.

[67] "*What is Real Emissions Driving (RDE) Tests?,*" 2016. https://www.caremissionstestingfacts.eu/rde-real-driving-emissions-test/# (accessed Jul. 13, 2020).

[68] M. Tomita, Y. Iwakiri, E. Sakai, T. Urushihara, R. Inoue, and K. Kojima, "*Effects of Gas Flow and Mixture Properties on Engine-Out HC Emissions,*" *SAE Tech. Pap. 961952*, 1996, doi: https://doi.org/10.4271/961952.

[69] C. T. Bowman, "*Kinetics of pollutant formation and destruction in combustion,*" *Prog. Energy Combust. Sci.*, vol. 1, no. 1, pp. 33–45, 1975, doi: 10.1016/0360-1285(75)90005-2.

[70] D. Turner, H. Xu, R. F. Cracknell, V. Natarajan, and X. Chen, "*Combustion performance of bio-ethanol at various blend ratios in a gasoline direct injection engine,*" *Fuel*, vol. 90, no. 5, pp. 1999–2006, 2011, doi: 10.1016/j.fuel.2010.12.025.

[71] C. Hergueta, M. Bogarra, A. Tsolakis, K. Essa, and J. M. Herreros, "*Butanol-gasoline blend and exhaust gas recirculation, impact on GDI engine emissions,*" *Fuel*, vol. 208, pp. 662–672, 2017, doi: 10.1016/j.fuel.2017.07.022.

[72] A. H. Lefebvre, "*The Role of Fuel Preparation in Low-Emission Combustion,*" *J. Eng. Gas Turbines Power*, vol. 117, no. 4, pp. 617–654, 1995, doi: 10.1115/1.2815449.

[73] S. S. Gill, "*Controlling Diesel NOx & PM Emissions using Fuel Components and Enhanced Aftertreament Techniques,*" PhD. Thesis, University of Birmingham, 2012.

[74] F. N. Alasfour, "*NOx Emission from a spark ignition engine using 30% Iso-butanol–gasoline blend: Part 1—Preheating inlet air,*" *Appl. Therm. Eng.*, vol. 18, no. 5, pp. 245–256, 1998, doi: https://doi.org/10.1016/S1359-4311(97)00081-1.

[75] J. Allen, "*Low NOx burner systems,*" *Energy world*, no. 183, pp. 13–15, 1990.

[76] U. Kramer and P. Phlips, "*Phasing Strategy for an Engine with Twin Variable Cam Timing,*" *SAE Tech. Pap. 2002-01-1101*, 2002, doi: https://doi.org/10.4271/2002-01-1101.

[77] K. H. Yoo, J. Hoard, A. Boehman, and M. Gegich, "*Experimental Studies of EGR Cooler Fouling on a GDI Engine,*" *SAE Tech. Pap. 2016-01-1090*, 2016, doi: https://doi.org/10.4271/2016-01-1090.

[78] A. Cairns, H. Blaxill, and G. Irlam, "*Exhaust Gas Recirculation for Improved Part and Full Load Fuel Economy in a Turbocharged Gasoline Engine,*" *SAE Tech. Pap. 20016-01-0047*, 2006, doi: https://doi.org/10.4271/2006-01-0047.

[79] M. Hedge, P. Weber, J. Gingrich, T. Alger, and I. A. Khalek, "*Effect of EGR on Particle Emissions from a GDI Engine,*" *SAE Int. J. Engines*, vol. 4, no. 1, pp. 650–666, 2011, doi: 10.4271/2011-01-0636.

[80] M. Raza, L. Chen, F. Leach, and S. Ding, "*A Review of particulate number (PN) emissions from gasoline direct injection (gdi) engines and their control*

techniques," *Energies*, 2018, doi: 10.3390/en11061417.

[81] J. M. Luján, H. Climent, R. Novella, and M. E. Rivas-Perea, "*Influence of a low pressure EGR loop on a gasoline turbocharged direct injection engine,*" *Appl. Therm. Eng.*, vol. 89, pp. 432–443, 2015, doi: https://doi.org/10.1016/j.applthermaleng.2015.06.039.

[82] T. Alger, T. Chauvet, and Z. Dimitrova, "*Synergies between High EGR Operation and GDI Systems,*" *SAE Int. J. Engines*, vol. 1, no. 1, pp. 101–114, 2009, doi: https://doi.org/10.4271/2008-01-0134.

[83] W. Zeng, M. Sjöberg, and D. L. Reuss, "*Combined effects of flow/spray interactions and EGR on combustion variability for a stratified DISI engine,*" *Proc. Combust. Inst.*, vol. 35, no. 3, pp. 2907–2914, 2015, doi: https://doi.org/10.1016/j.proci.2014.06.106.

[84] D. Petitjean, L. Bernardini, C. Middlemass, and S. M. Shahed, "*Advanced Gasoline Engine Turbocharging Technology for Fuel Economy Improvements,*" *SAE Tech. Pap. 2004-01-0988*, 2004, doi: https://doi.org/10.4271/2004-01-0988.

[85] L. Guzzella, U. Wenger, and R. Martin, "*IC-Engine Downsizing and Pressure-Wave Supercharging for Fuel Economy,*" *SAE Tech. Pap. 2000-01-1019*, 2000, doi: https://doi.org/10.4271/2000-01-1019.

[86] A. Eichhorn, D. Lejsek, A. Hettinger, and A. Kufferath, "*Challenge Determining a Combustion System Concept for Downsized SI-engines - Comparison and Evaluation of Several Options for a Boosted 2-cylinder SI-engine,*" *SAE Tech. Pap. 2013-01-1730*, 2013, doi: https://doi.org/10.4271/2013-01-1730.

[87] H. Ando, "*Combustion Control Technologies for Gasoline Engines,*" United Kingdom, 1996. [Online]. Available: https://www.osti.gov/etdeweb/servlets/purl/22151718.

[88] R. Krebs, J. Boehme, R. Dornhoefer, R. Wurms, K. Friedmann, J. Helbig, and W. Hatz, "*The New Audi 2.0T FSI Engine,*" Germany, 2004. [Online]. Available: https://www.osti.gov/etdeweb/servlets/purl/22151718.

[89] Daimler AG, "*The Petrol Engines: Powerful, Responsive and Super-Clean,*" 2012. https://media.daimler.com/marsMediaSite/en/instance/ko/The-petrol-engines-Powerful-responsive-and-super-clean.xhtml?oid=9904067 (accessed Oct. 15, 2019).

[90] P. Eastwood, *Critical Topics in Exhaust Gas Aftertreatment*. Research Studies Press, 2000.

[91] Y. Ikeda, K. Sobue, S. Tsuji, and S. Matsumoto, "*Development of NOx Storage-Reduction Three-way Catalyst for D-4 Engines,*" *SAE Tech. Pap. 1999-01-1279*, 1999, doi: https://doi.org/10.4271/1999-01-1279.

[92] M. Bogarra-Macias, J. M. M. Herreros-Arellano, A. Tsolakis, A. P. E. York, and P. Millington, "*Reformate Exhaust Gas Recirculation (REGR) Effect on Particulate Matter (PM), Soot Oxidation and Three Way Catalyst (TWC)*

Performance in Gasoline Direct Injection (GDI) Engines," *SAE Int. J. Engines*, vol. 9, no. 1, pp. 305–314, 2015, doi: 10.4271/2015-01-2019.

[93] C. L. Myung and S. Park, "*Exhaust nanoparticle emissions from internal combustion engines: A review,*" *Int. J. Automot. Technol.*, vol. 13, no. 1, pp. 9–22, 2012, doi: 10.1007/s12239-012-0002-y.

[94] R. Zhu, J. Hu, X. Bao, L. He, Y. Lai, L. Zu, Y. Li, and S. Su, "*Tailpipe emissions from gasoline direct injection (GDI) and port fuel injection (PFI) vehicles at both low and high ambient temperatures,*" *Environ. Pollut.*, vol. 216, pp. 223–234, 2016, doi: 10.1016/j.envpol.2016.05.066.

[95] K. Donaldson, X. Y. Li, and W. MacNee, "*Ultrafine (nanometre) particle mediated lung injury,*" *J. Aerosol Sci.*, vol. 29, no. 5–6, pp. 553–560, 1998, doi: 10.1016/S0021-8502(97)00464-3.

[96] M. Riedl and D. Diaz-Sanchez, "*Biology of Diesel Exhaust Effects on Respiratory Function,*" *Journal of Allergy and Clinical Immunology*, vol. 115, no. 2. pp. 221–228, 2005, doi: 10.1016/j.jaci.2004.11.047.

[97] D. B. Kittelson, "*Engines and nanoparticles,*" *J. Aerosol Sci.*, vol. 29, no. 5–6, pp. 575–588, 1998, doi: 10.1016/s0021-8502(97)10037-4.

[98] D. Kayes and S. Hochgreb, "*Mechanisms of particulate matter formation in spark-ignition engines. 1. Effect of engine operating conditions,*" *Environ. Sci. Technol.*, 1999, doi: 10.1021/es9810991.

[99] T. Lähde, T. Rönkkö, A. Virtanen, A. Solla, M. Kytö, C. Söderström, and J. Keskinen, "*Dependence between Nonvolatile Nucleation Mode Particle and Soot Number Concentrations in an EGR Equipped Heavy-Duty Diesel Engine Exhaust,*" *Environ. Sci. Technol.*, vol. 44, no. 8, pp. 3175–3180, 2010, doi: 10.1021/es903428y.

[100] D. Lee, A. Miller, D. Kittelson, and M. R. Zachariah, "*Characterization of metal-bearing diesel nanoparticles using single-particle mass spectrometry,*" *J. Aerosol Sci.*, vol. 37, no. 1, pp. 88–110, 2006, doi: https://doi.org/10.1016/j.jaerosci.2005.04.006.

[101] A. De Filippo and M. M. Maricq, "*Diesel Nucleation Mode Particles: Semivolatile or Solid?,*" *Environ. Sci. Technol.*, vol. 42, no. 21, pp. 7957–7962, 2008, doi: 10.1021/es8010332.

[102] L. A. Sgro, P. Sementa, B. M. Vaglieco, G. Rusciano, A. D'Anna, and P. Minutolo, "*Investigating the origin of nuclei particles in GDI engine exhausts,*" *Combust. Flame*, vol. 159, no. 4, pp. 1687–1692, 2012, doi: https://doi.org/10.1016/j.combustflame.2011.12.013.

[103] Deaprtment of the Environment, "*Airborne Particulate Matter in the United Kingdom - Third QUARG report,*" 1996. [Online]. Available: https://uk-air.defra.gov.uk/library/reports?report_id=48.

[104] M. Anbari Attar, H. M. Xu, M. A. Attar, H. M. Xu, M. Anbari Attar, and H. M. Xu, "*Correlations between particulate matter emissions and gasoline direct injection*

spray characteristics," *J. Aerosol Sci.*, vol. 102, pp. 128–141, 2016, doi: 10.1016/j.jaerosci.2016.09.006.

[105] Q. Jiao and R. D. Reitz, "*The Effect of Operating Parameters on Soot Emissions in GDI Engines,*" *SAE Int. J. Engines*, vol. 8, no. 3, pp. 1322–1333, 2015, doi: 10.4271/2015-01-1071.

[106] E. Stevens and R. Steeper, "*Piston Wetting in an Optical DISI Engine: Fuel Films, Pool Fires, and Soot Generation,*" *SAE Tech. Pap. 2001-01-1203*, 2010, doi: 10.4271/2001-01-1203.

[107] P. Price, R. Stone, D. OudeNijeweme, and X. Chen, "*Cold Start Particulate Emissions from a Second Generation DI Gasoline Engine,*" *SAE Tech. Pap. 2007-01-1931*, 2007.

[108] J. D. Andersson, B. G. A. Wedekind, D. Hall, R. Stradling, and G. Wilson, "*DETR/SMMT/CONCAWE Particulate Research Programme: Light Duty Results,*" *SAE Tech. Pap. 2001-01-3577*, 2001, doi: https://doi.org/10.4271/2001-01-3577.

[109] M. S. Peckham, A. Finch, B. Campbell, P. Price, and M. T. Davies, "*Study of Particle Number Emissions from a Turbocharged Gasoline Direct Injection (GDI) Engine Including Data from a Fast-Response Particle Size Spectrometer,*" *SAE Tech. Pap. 2011-01-1224*, 2011, doi: https://doi.org/10.4271/2011-01-1224.

[110] M. Shimizu, K. Yageta, Y. Matsui, and T. Yoshida, "*Development of New 1.6Liter Four Cylinder Turbocharged Direct Injection Gasoline Engine with Intake and Exhaust Valve Timing Control System,*" *SAE Tech. Pap. 2011-01-0419*, 2011, doi: https://doi.org/10.4271/2011-01-0419.

[111] M. Yamakawa, T. Youso, T. Fujikawa, T. Nishimoto, Y. Wada, K. S. K. Sato, and H. Yokohata, "*Combustion Technology Development for a High Compression Ratio Gasoline Engine,*" *Trans. Soc. Automot. Eng. Japan*, vol. 43, no. 1, pp. 81–87, 2012, doi: 10.11351/jsaeronbun.43.81.

[112] A. Überall, R. Otte, P. Eilts, and J. Krahl, "*A literature research about particle emissions from engines with direct gasoline injection and the potential to reduce these emissions,*" *Fuel*, vol. 147, pp. 203–207, 2015, doi: 10.1016/j.fuel.2015.01.012.

[113] F. Steimle, A. Kulzer, H. Richter, D. Schwarzenthal, and C. Romberg, "*Systematic Analysis and Particle Emission Reduction of Homogeneous Direct Injection SI Engines,*" *SAE 2013 World Congr. Exhib.*, 2013, doi: https://doi.org/10.4271/2013-01-0248.

[114] Y. Qian, Z. Li, L. Yu, X. Wang, and X. Lu, "*Review of the state-of-the-art of particulate matter emissions from modern gasoline fueled engines,*" *Appl. Energy*, vol. 238, pp. 1269–1298, Mar. 2019, doi: 10.1016/j.apenergy.2019.01.179.

[115] W. Piock, G. Hoffmann, A. Berndorfer, P. Salemi, and B. Fusshoeller, "*Strategies Towards Meeting Future Particulate Matter Emission Requirements in Homogeneous Gasoline Direct Injection Engines,*" *SAE Int. J. Engines*, vol. 4,

no. 1, pp. 1455–1468, 2011, doi: 10.4271/2011-01-1212.

[116] B. S. Haynes and H. G. Wagner, "*Soot formation,*" *Prog. Energy Combust. Sci.*, 1981, doi: 10.1016/0360-1285(81)90001-0.

[117] K. Akihama, Y. Takatori, K. Inagaki, S. Sasaki, and A. M. Dean, "*Mechanism of the Smokeless Rich Diesel Combustion by Reducing Temperature,*" *SAE Tech. Pap. 2001-01-0655*, 2001, doi: https://doi.org/10.4271/2001-01-0655.

[118] M. D. Hageman, S. S. Sakai, and D. A. Rothamer, "*Determination of soot onset and background particulate levels in a spark-ignition engine,*" *Proc. Combust. Inst.*, 2015, doi: 10.1016/j.proci.2014.06.105.

[119] A. Ergut, Y. A. Levendis, H. Richter, J. B. Howard, and J. Carlson, "*The effect of equivalence ratio on the soot onset chemistry in one-dimensional, atmospheric-pressure, premixed ethylbenzene flames,*" *Combust. Flame*, vol. 151, no. 1, pp. 173–195, 2007, doi: https://doi.org/10.1016/j.combustflame.2007.04.009.

[120] M. Bönig, C. Feldermann, H. Jander, B. Lüers, G. Rudolph, and H. G. Wagner, "*Soot formation in premixed C2H4 flat flames at elevated pressure,*" *Symp. Combust.*, vol. 23, no. 1, pp. 1581–1587, 1991, doi: https://doi.org/10.1016/S0082-0784(06)80429-7.

[121] D. Kittelson, "*Ultrafine Particle Formation Mechanisms,*" *South Coast Air Qual. Manag. Dist. Conf. Ultrafine Part. Sci. Technol. Policy Issues*, 2006.

[122] H. Beck, "*Technisher Abschlussbericht Projekt 00983: Partikelemissionen von Otto--DI-Motoren,*" *ADA Protoc.*, 2007.

[123] H. Hopf and H. Musso, "*Preparation of Benzene by Pyrolysis of cis- and trans-1,3-Hexadien-5-yne,*" *Angew. Chemie Int. Ed. English*, vol. 8, no. 9, p. 680, 1969, doi: 10.1002/anie.196906801.

[124] D. R. Tree and K. I. Svensson, "*Soot processes in compression ignition engines,*" *Prog. Energy Combust. Sci.*, vol. 33, no. 3, pp. 272–309, 2007, doi: https://doi.org/10.1016/j.pecs.2006.03.002.

[125] S. C. Moldoveanu, "*Chapter 2 - Pyrolysis of Hydrocarbons,*" S. C. B. T.-P. of O. M. (Second E. Moldoveanu, Ed. Elsevier, 2019, pp. 35–161.

[126] Shah.S, "*Experimental Study and Thermodynamical Analysis of Water Injection in the Intake Manifold of an Automotive Diesel Engine, for Pollutant Emission Reduction,*" EcoleCentrale de Nantes, 2011.

[127] O. I. Smith, "*Fundamentals of soot formation in flames with application to diesel engine particulate emissions,*" *Prog. Energy Combust. Sci.*, vol. 7, no. 4, pp. 275–291, 1981, doi: https://doi.org/10.1016/0360-1285(81)90002-2.

[128] I. Glassman, R. A. Yetter, and N. G. Glumac, "*Chapter 8 - Environmental combustion considerations,*" I. Glassman, R. A. Yetter, and N. G. B. T.-C. (Fifth E. Glumac, Eds. Boston: Academic Press, 2015, pp. 393–475.

[129] C. K. Law, *Combustion Physics*. Cambridge: Cambridge University Press, 2006.

[130] J. Xi and B.-J. Zhong, "*Soot in Diesel Combustion Systems,*" *Chem. Eng. Technol.*, vol. 29, no. 6, pp. 665–673, 2006, doi: 10.1002/ceat.200600016.

[131] Z. A. Mansurov, "*Soot Formation in Combustion Processes (Review),*" *Combust. Explos. Shock Waves*, vol. 41, no. 6, p. 727, 2005, doi: 10.1007/s10573-005-0083-2.

[132] G. P. Merker, C. Schwarz, and R. Teichmann, *Motorische Verbrennung BT - Grundlagen Verbrennungsmotoren: Funktionsweise, Simulation, Messtechnik*. Wiesbaden: Vieweg+Teubner Verlag, 2012.

[133] S. C. Graham, J. B. Homer, J. L. J. Rosenfeld, and T. M. Sugden, "*The formation and coagulation of soot aerosols generated by the pyrolysis of aromatic hydrocarbons,*" *Proc. R. Soc. London. A. Math. Phys. Sci.*, vol. 344, no. 1637, pp. 259–285, 1975, doi: 10.1098/rspa.1975.0101.

[134] G. Prado, J. Lahaye, and B. S. Haynes, "*Soot Particle Nucleation and Agglomeration BT - Soot in Combustion Systems and Its Toxic Properties,*" J. Lahaye and G. Prado, Eds. Boston, MA: Springer US, 1983, pp. 145–161.

[135] K. Siegmann, K. Sattler, and H. C. Siegmann, "*Clustering at high temperatures: carbon formation in combustion,*" *J. Electron Spectros. Relat. Phenomena*, vol. 126, no. 1, pp. 191–202, 2002, doi: https://doi.org/10.1016/S0368-2048(02)00152-4.

[136] M. Frenklach and H. Wang, "*Detailed Mechanism and Modeling of Soot Particle Formation,*" H. Bockhorn, Ed. Berlin, Heidelberg: Springer Berlin Heidelberg, 1994, pp. 165–192.

[137] A. V Krestinin, "*Detailed modeling of soot formation in hydrocarbon pyrolysis,*" *Combust. Flame*, vol. 121, no. 3, pp. 513–524, 2000, doi: https://doi.org/10.1016/S0010-2180(99)00167-4.

[138] I. M. Kennedy, "*Models of soot formation and oxidation,*" *Prog. Energy Combust. Sci.*, vol. 23, no. 2, pp. 95–132, 1997, doi: https://doi.org/10.1016/S0360-1285(97)00007-5.

[139] H. Song, "*Diesel Soot Oxidation under Controlled Conditions,*" PhD. Thesis, Brunel University London, 2003.

[140] J. Appel, H. Bockhorn, and M. Frenklach, "*Kinetic modeling of soot formation with detailed chemistry and physics: laminar premixed flames of C2 hydrocarbons,*" *Combust. Flame*, vol. 121, no. 1, pp. 122–136, 2000, doi: https://doi.org/10.1016/S0010-2180(99)00135-2.

[141] N. Serhan, "*Destruction of Diesel Soot Aggregates with the use of Fuel-Borne Oxygen and the Application of Hydrogen Assisted SCR Catalyst.,*" PhD. Thesis, University of Birmingham, 2019.

[142] M. Frenklach and H. Wang, "*Detailed modeling of soot particle nucleation and growth,*" *Symp. Combust.*, vol. 23, no. 1, pp. 1559–1566, 1991, doi: 10.1016/S0082-0784(06)80426-1.

[143] F. Bisetti, G. Blanquart, M. E. Mueller, and H. Pitsch, "*On the formation and early*

evolution of soot in turbulent nonpremixed flames," *Combust. Flame*, vol. 159, no. 1, pp. 317–335, 2012, doi: https://doi.org/10.1016/j.combustflame.2011.05.021.

[144] J. . Wen, "*Chemical and Physical Aspects of Soot/Nano-Particle Formation in Combustion,*" PhD. Thesis, University of Toronto, 2005.

[145] H. G. Wagner, "*Soot formation in combustion,*" *Symp. Combust.*, vol. 17, no. 1, pp. 3–19, 1979, doi: 10.1016/S0082-0784(79)80005-3.

[146] R. A. Dobbins and H. Subramaniasivam, "*Soot Precursor Particles in Flames,*" 1994, pp. 290–301.

[147] D. C. Siegla and G. W. Smith, *Particulate Carbon - Formation During Combustion*. Boston, MA: Springer US, 1981.

[148] C. P. Fenimore and G. W. Jones, "*Oxidation of soot by hydroxyl radicals,*" *J. Phys. Chem.*, vol. 71, no. 3, pp. 593–597, 1967, doi: 10.1021/j100862a021.

[149] H. Marsh and K. Kuo, "*Chapter 4 - Kinetics and Catalysis of Carbon Gasification,*" Butterworth-Heinemann, 1989, pp. 107–151.

[150] V. Ramanathan and G. Carmichael, "*Global and regional climate changes due to black carbon,*" *Nat. Geosci.*, vol. 1, no. 4, pp. 221–227, 2008, doi: 10.1038/ngeo156.

[151] T. C. Bond *et al.*, "*Bounding the role of black carbon in the climate system: A scientific assessment,*" *J. Geophys. Res. Atmos.*, vol. 118, no. 11, pp. 5380–5552, 2013, doi: 10.1002/jgrd.50171.

[152] Environmental Protection Agency (EPA), "*Health and Environment Effects of Particulate Matter (PM).*" https://www.epa.gov/pm-pollution/health-and-environmental-effects-particulate-matter-pm (accessed Oct. 30, 2019).

[153] M. Z. Jacobson, "*Strong radiative heating due to the mixing state of black carbon in atmospheric aerosols,*" *Nature*, vol. 409, no. 6821, pp. 695–697, 2001, doi: 10.1038/35055518.

[154] D. Y. H. Pui, S.-C. Chen, and Z. Zuo, "*PM 2.5 in China: Measurements, sources, visibility and health effects, and mitigation,*" *Particuology*, vol. 13, pp. 1–26, 2014, doi: 10.1016/j.partic.2013.11.001.

[155] B. Giechaskiel, B. Alföldy, and Y. Drossinos, "*A metric for health effects studies of diesel exhaust particles,*" *J. Aerosol Sci.*, vol. 40, no. 8, pp. 639–651, 2009, doi: https://doi.org/10.1016/j.jaerosci.2009.04.008.

[156] J. Löndahl, A. Massling, E. Swietlicki, E. V. Bräuner, M. Ketzel, J. Pagels, and S. Loft, "*Experimentally Determined Human Respiratory Tract Deposition of Airborne Particles at a Busy Street,*" *Environ. Sci. Technol.*, vol. 43, no. 13, pp. 4659–4664, 2009, doi: 10.1021/es803029b.

[157] R. I. Crane, L. Rubino, C. Arcoumanis, S. Golunski, J. M. McNamara, S. Poulston, and R. Rajaram, "*Strategies for Gasoline Particulate Emission Control - A 'Foresight Vehicle' Project,*" *SAE Tech. Pap. 2002-01-1894*, 2002, doi:

10.4271/2002-01-1894.

[158] A. Seaton, D. Godden, W. MacNee, and K. Donaldson, "*Particulate air pollution and acute health effects,*" *Lancet*, vol. 345, no. 8943, pp. 176–178, 1995, doi: 10.1016/S0140-6736(95)90173-6.

[159] C. A. Pope and D. W. Dockery, "*Health Effects of Fine Particulate Air Pollution: Lines that Connect,*" *J. Air Waste Manage. Assoc.*, vol. 56, no. 6, pp. 709–742, 2006, doi: 10.1080/10473289.2006.10464485.

[160] T. Mimura, T. Ichinose, S. Yamagami, H. Fujishima, Y. Kamei, M. Goto, S. Takada, and M. Matsubara, "*Airborne particulate matter (PM2.5) and the prevalence of allergic conjunctivitis in Japan,*" *Sci. Total Environ.*, vol. 487, pp. 493–499, 2014, doi: https://doi.org/10.1016/j.scitotenv.2014.04.057.

[161] B. Peterson and A. Saxon, "*Global Increases in Allergic Respiratory Disease: the Possible Role of Diesel Exhaust Particles,*" *Ann. Allergy, Asthma Immunol.*, vol. 77, no. 4, pp. 263–270, 1996, doi: https://doi.org/10.1016/S1081-1206(10)63318-2.

[162] K.-H. Kim, E. Kabir, and S. Kabir, "*A review on the human health impact of airborne particulate matter,*" *Environ. Int.*, vol. 74, pp. 136–143, 2015, doi: https://doi.org/10.1016/j.envint.2014.10.005.

[163] G. J. F., K. Petros, B. Kathleen, T. Elizabeth, H. T. R., B. M. B., and L. B. P., "*Symptoms and Medication Use in Children with Asthma and Traffic-Related Sources of Fine Particle Pollution,*" *Environ. Health Perspect.*, vol. 117, no. 7, pp. 1168–1174, 2009, doi: 10.1289/ehp.0800335.

[164] A. F. Behndig, I. S. Mudway, J. L. Brown, N. Stenfors, R. Helleday, S. T. Duggan, S. J. Wilson, C. Boman, F. R. Cassee, A. J. Frew, F. J. Kelly, T. Sandström, and A. Blomberg, "*Airway antioxidant and inflammatory responses to diesel exhaust exposure in healthy humans,*" *Eur. Respir. J.*, vol. 27, no. 2, pp. 359 LP – 365, 2006, doi: 10.1183/09031936.06.00136904.

[165] R. Jahn, "*Ultrafeinstaub überwindet alle Grenzen,*" *Schweizerische Natl.*, vol. 2006, pp. 14–5.

[166] B. R. D., R. Sanjay, P. C. Arden, B. J. R., B. Aruni, D.-R. A. V., H. Fernando, H. Yuling, L. R. V., M. M. A., P. Annette, S. David, S. S. C., W. Laurie, and K. J. D., "*Particulate Matter Air Pollution and Cardiovascular Disease,*" *Circulation*, vol. 121, no. 21, pp. 2331–2378, 2010, doi: 10.1161/CIR.0b013e3181dbece1.

[167] L. J. L. Forbes, M. D. Patel, A. R. Rudnicka, D. G. Cook, T. Bush, J. R. Stedman, P. H. Whincup, D. P. Strachan, and R. H. Anderson, "*Chronic Exposure to Outdoor Air Pollution and Markers of Systemic Inflammation,*" *Epidemiology*, vol. 20, no. 2, 2009, [Online]. Available: https://journals.lww.com/epidem/Fulltext/2009/03000/Chronic_Exposure_to_Outdoor_Air_Pollution_and.17.aspx.

[168] K. Donaldson, N. Mills, W. MacNee, S. Robinson, and D. Newby, "*Role of inflammation in cardiopulmonary health effects of PM,*" *Toxicol. Appl. Pharmacol.*, vol. 207, no. 2, Supplement, pp. 483–488, 2005, doi:

https://doi.org/10.1016/j.taap.2005.02.020.

[169] M. J. O'Donnell, J. Fang, M. A. Mittleman, M. K. Kapral, G. A. Wellenius, and on behalf of the I. of the R. of the C. S. Network, "*Fine Particulate Air Pollution (PM2.5) and the Risk of Acute Ischemic Stroke,*" *Epidemiology*, vol. 22, no. 3, 2011, [Online]. Available: https://journals.lww.com/epidem/Fulltext/2011/05000/Fine_Particulate_Air_Pollution__PM2_5__and_the.26.aspx.

[170] M. F. Denissenko, A. Pao, M.-S. Tang, and G. P. Pfeifer, "*Preferential formation of benzo[a]pyrene adducts at lung cancer mutational hotspots in P53,*" *Science (80-.).*, vol. 274, no. 5286, pp. 430–432, 1996, doi: 10.1126/science.274.5286.430.

[171] I. Kulhánová, X. Morelli, A. Le Tertre, D. Loomis, B. Charbotel, S. Medina, J.-N. Ormsby, J. Lepeule, R. Slama, and I. Soerjomataram, "*The fraction of lung cancer incidence attributable to fine particulate air pollution in France: Impact of spatial resolution of air pollution models,*" *Environ. Int.*, vol. 121, pp. 1079–1086, 2018, doi: https://doi.org/10.1016/j.envint.2018.09.055.

[172] G. Weinmayr *et al.*, "*Particulate matter air pollution components and incidence of cancers of the stomach and the upper aerodigestive tract in the European Study of Cohorts of Air Pollution Effects (ESCAPE),*" *Environ. Int.*, vol. 120, pp. 163–171, 2018, doi: https://doi.org/10.1016/j.envint.2018.07.030.

[173] F. J. Kelly and J. C. Fussell, "*Size, source and chemical composition as determinants of toxicity attributable to ambient particulate matter,*" *Atmos. Environ.*, vol. 60, pp. 504–526, 2012, doi: https://doi.org/10.1016/j.atmosenv.2012.06.039.

[174] A. G. Konstandopoulos, M. Kostoglou, E. Skaperdas, E. Papaioannou, D. Zarvalis, and E. Kladopoulou, "*Fundamental Studies of Diesel Particulate Filters: Transient Loading, Regeneration and Aging,*" *SAE Tech. Pap. 2000-01-1016*, 2000, doi: https://doi.org/10.4271/2000-01-1016.

[175] E. Wirojsakunchai, "*The effects of filtration velocities and particulate matter characteristics on diesel particulate filter wall loading performance,*" PhD. Thesis, University of Wisconsin-Madison, 2008.

[176] TSI, "*Mechanisms of Filtration for High Efficiency Fibrous Filters,*" *TSI Inc.*, vol. 041, pp. 1–4, 2012.

[177] T. T. Mercer, "*Aerosol Technology,*" *J. Aerosol Sci.*, vol. 14, no. 2, p. 175, 1983, doi: 10.1016/0021-8502(83)90049-6.

[178] Z. G. Liu, M. D. Skemp, and J. C. Lincoln, "*Diesel Particulate Filters: Trends and Implications of Particle Size Distribution Measurement,*" *SAE Tech. Pap. 2003-01-0046*, 2003, doi: 10.4271/2003-01-0046.

[179] W. Hinds, *Aerosol Technology: Properties, Behavior, and Measurement of Airborne Particles*. John Wiley & Sons, Ltd, 2012.

[180] J. M. Richter, R. Klingmann, S. Spiess, and K.-F. Wong, "*Application of*

Catalyzed Gasoline Particulate Filters to GDI Vehicles," *SAE Int. J. Engines*, vol. 5, no. 3, pp. 1361–1370, 2012, doi: https://doi.org/10.4271/2012-01-1244.

[181] Y. Ito, T. Shimoda, T. Aoki, K. Yuuki, H. Sakamoto, K. Kato, D. Thier, P. Kattouah, E. Ohara, and C. Vogt, "*Next Generation of Ceramic Wall Flow Gasoline Particulate Filter with Integrated Three Way Catalyst,*" *SAE Tech. Pap. Ser. 2015-01-1073*, 2015, doi: 10.4271/2015-01-1073.

[182] M. Zhang, J. Zhong, S. Capelli, and L. Lubrano, "*Particulate Matter Emission Suppression Strategies in a Turbo-Charged Gasoline Direct Injection (GDI) Engine,*" *J. Eng. Gas Turbines Power*, vol. 139, 2017, doi: 10.1115/1.4036301.

[183] L. de Francqueville, "*Effects of Ethanol Addition in RON 95 Gasoline on GDI Stratified Combustion,*" *SAE Tech. Pap. 2011-24-0055*, 2011, doi: https://doi.org/10.4271/2011-24-0055.

[184] P. Whitaker, P. Kapus, M. Ogris, and P. Hollerer, "*Measures to Reduce Particulate Emissions from Gasoline DI engines,*" *SAE Int. J. Engines*, vol. 4, no. 1, pp. 1498–1512, 2011, [Online]. Available: http://www.jstor.org/stable/26278238.

[185] D. OudeNijeweme, P. Freeland, M. Behringer, and P. Aleiferis, "*Developing Low Gasoline Particulate Emission Engines Through Improved Fuel Delivery,*" *SAE Tech. Pap. 2014-01-2843*, 2014, doi: https://doi.org/10.4271/2014-01-2843.

[186] J. Su, M. Xu, P. Yin, Y. Gao, and D. Hung, "*Particle Number Emissions Reduction Using Multiple Injection Strategies in a Boosted Spark-Ignition Direct-Injection (SIDI) Gasoline Engine,*" *SAE Int. J. Engines*, vol. 8, pp. 20–29, 2014, doi: 10.4271/2014-01-2845.

[187] M. Akif Ceviz, A. K. Sen, A. K. Küleri, and I. Volkan Öner, "*Engine performance, exhaust emissions, and cyclic variations in a lean-burn SI engine fueled by gasoline-hydrogen blends,*" *Appl. Therm. Eng.*, 2012, doi: 10.1016/j.applthermaleng.2011.10.039.

[188] M. Zhang, W. Hong, F. Xie, Y. Su, H. Liu, and S. Zhou, "*Combustion, performance and particulate matter emissions analysis of operating parameters on a GDI engine by traditional experimental investigation and Taguchi method,*" *Energy Convers. Manag.*, 2018, doi: 10.1016/j.enconman.2018.03.017.

[189] H. M. Cho and B. Q. He, "*Combustion and emission characteristics of a lean burn natural gas engine,*" *Int. J. Automot. Technol.*, vol. 9, no. 4, pp. 415–422, 2008, doi: 10.1007/s12239-008-0050-5.

[190] S. Sakai, M. Hageman, and D. Rothamer, "*Effect of Equivalence Ratio on the Particulate Emissions from a Spark-Ignited, Direct-Injected Gasoline Engine,*" *SAE 2013 World Congr. Exhib.*, 2013, doi: https://doi.org/10.4271/2013-01-1560.

[191] J. Kim, K. M. Chun, S. Song, H. K. Baek, and S. W. Lee, "*Hydrogen Effects on the Eombustion Etability, performance and emissions of a turbo gasoline direct injection engine in various air/fuel ratios,*" *Appl. Energy*, 2018, doi: 10.1016/j.apenergy.2018.06.129.

[192] Z. Ran, D. Hariharan, B. Lawler, and S. Mamalis, "*Experimental study of lean spark ignition combustion using gasoline, ethanol, natural gas, and syngas,*" *Fuel*, 2019, doi: 10.1016/j.fuel.2018.08.054.

[193] C. W. Wu, R. H. Chen, J. Y. Pu, and T. H. Lin, "*The influence of air-fuel ratio on engine performance and pollutant emission of an SI engine using ethanol-gasoline-blended fuels,*" *Atmos. Environ.*, vol. 38, no. 40, pp. 7093–7100, 2004, doi: 10.1016/j.atmosenv.2004.01.058.

[194] I. Schifter, U. González, and C. González-Macías, "*Effects of ethanol, ethyl- tert -butyl ether and dimethyl-carbonate blends with gasoline on SI engine,*" *Fuel*, vol. 183, pp. 253–261, 2016, doi: 10.1016/j.fuel.2016.06.051.

[195] E. G. S. D.Gopinath, "*Experimental Investigation on The Effect Adding Di-Methyl Carbonate to Gasoline in a SI Engine Performance,*" *Sci. Eng. Res.*, vol. 3, no. 6, pp. 92–96, 2012.

[196] D. Uy, M. A. Ford, D. T. Jayne, A. E. O'Neill, L. P. Haack, J. Hangas, M. J. Jagner, A. Sammut, and A. K. Gangopadhyay, "*Characterization of gasoline soot and comparison to diesel soot: Morphology, chemistry, and wear,*" *Tribol. Int.*, vol. 80, pp. 198–209, 2014, doi: 10.1016/j.triboint.2014.06.009.

[197] T. L. Barone, J. M. E. Storey, A. D. Youngquist, and J. P. Szybist, "*An analysis of direct-injection spark-ignition (DISI) soot morphology,*" *Atmos. Environ.*, 2012, doi: 10.1016/j.atmosenv.2011.11.047.

[198] P. Karjalainen, L. Pirjola, J. Heikkilä, T. Lähde, T. Tzamkiozis, L. Ntziachristos, J. Keskinen, and T. Rönkkö, "*Exhaust particles of modern gasoline vehicles: A laboratory and an on-road study,*" *Atmos. Environ.*, 2014, doi: 10.1016/j.atmosenv.2014.08.025.

[199] M. Bogarra, J. M. Herreros, A. Tsolakis, A. P. E. York, P. J. Millington, and F. J. Martos, "*Impact of exhaust gas fuel reforming and exhaust gas recirculation on particulate matter morphology in Gasoline Direct Injection Engine,*" *J. Aerosol Sci.*, vol. 103, pp. 1–14, 2017, doi: 10.1016/j.jaerosci.2016.10.001.

[200] A. La Rocca, F. Bonatesta, M. W. Fay, and F. Campanella, "*Characterisation of soot in oil from a gasoline direct injection engine using Transmission Electron Microscopy,*" *Tribol. Int.*, 2015, doi: 10.1016/j.triboint.2015.01.025.

[201] S. Choi and H. Seong, "*Oxidation characteristics of gasoline direct-injection (GDI) engine soot: Catalytic effects of ash and modified kinetic correlation,*" *Combust. Flame*, vol. 162, no. 6, pp. 2371–2389, 2015, doi: https://doi.org/10.1016/j.combustflame.2015.02.004.

[202] C. K. Gaddam and R. L. Vander Wal, "*Physical and chemical characterization of SIDI engine particulates,*" *Combust. Flame*, 2013, doi: 10.1016/j.combustflame.2013.05.025.

[203] K. O. Lee, H. Seong, S. Sakai, M. Hageman, and D. Rothamer, "*Detailed Morphological Properties of Nanoparticles from Gasoline Direct Injection Engine Combustion of Ethanol Blends,*" *SAE Tech. Pap. 2013-24-0185*, 2013, doi: https://doi.org/10.4271/2013-24-0185.

[204] U. Mathis, R. Kaegi, M. Mohr, and R. Zenobi, "*TEM analysis of volatile nanoparticles from particle trap equipped diesel and direct-injection spark-ignition vehicles,*" *Atmos. Environ.*, 2004, doi: 10.1016/j.atmosenv.2004.04.016.

[205] S. Choi and H. Seong, "*Oxidation characteristics of gasoline direct-injection (GDI) engine soot: Catalytic effects of ash and modified kinetic correlation,*" *Combust. Flame*, vol. 162, no. 6, pp. 2371–2389, 2015, doi: https://doi.org/10.1016/j.combustflame.2015.02.004.

[206] K. Lee, H. Seong, W. Church, and S. McConnell, "*Examination of particulate emissions from alcohol blended fuel combustion in a gasoline direct injection engine,*" *Proc. 8th Int. Conf. Model. Diagnostics Adv. Engine Syst. COMODIA 2012*, pp. 305–310, 2012, doi: 10.1299/jmsesdm.2012.8.305.

[207] M. Wentzel, H. Gorzawski, K.-H. Naumann, H. Saathoff, and S. Weinbruch, "*Transmission electron microscopical and aerosol dynamical characterization of soot aerosols,*" *J. Aerosol Sci.*, vol. 34, no. 10, pp. 1347–1370, 2003, doi: https://doi.org/10.1016/S0021-8502(03)00360-4.

[208] N. Serhan, A. Tsolakis, and F. J. Martos, "*Effect of propylene glycol ether fuelling on the different physico-chemical properties of the emitted particulate matters: Implications of the soot reactivity,*" *Fuel*, vol. 219, pp. 1–11, 2018, doi: 10.1016/j.fuel.2018.01.065.

[209] K. Park, D. B. Kittelson, and P. H. McMurry, "*Structural properties of diesel exhaust particles measured by Transmission Electron Microscopy (TEM): Relationships to particle mass and mobility,*" *Aerosol Sci. Technol.*, 2004, doi: 10.1080/027868290505189.

[210] M. Wozniak, F. R. A. Onofri, S. Barbosa, J. Yon, and J. Mroczka, "*Comparison of methods to derive morphological parameters of multi-fractal samples of particle aggregates from TEM images,*" *J. Aerosol Sci.*, vol. 47, pp. 12–26, 2012, doi: 10.1016/j.jaerosci.2011.12.008.

[211] M. Lapuerta, F. Oliva, J. R. Agudelo, and A. L. Boehman, "*Effect of fuel on the soot nanostructure and consequences on loading and regeneration of diesel particulate filters,*" *Combust. Flame*, vol. 159, no. 2, pp. 844–853, 2012, doi: 10.1016/j.combustflame.2011.09.003.

[212] C. Wang-Hansen, P. Ericsson, B. Lundberg, M. Skoglundh, P.-A. Carlsson, and B. Andersson, "*Characterization of Particulate Matter from Direct Injected Gasoline Engines,*" *Top. Catal.*, vol. 56, no. 1–8, pp. 446–451, 2013, doi: 10.1007/s11244-013-9994-4.

[213] H. Seong, S. Choi, and K. Lee, "*Examination of nanoparticles from gasoline direct-injection (GDI) engines using transmission electron microscopy (TEM),*" *Int. J. Automot. Technol.*, vol. 15, no. 2, pp. 175–181, 2014, doi: 10.1007/s12239-014-0019-5.

[214] M. Bogarra, J. M. Herreros, A. Tsolakis, A. P. E. York, P. J. Millington, and F. J. Martos, "*Influence of on-board produced hydrogen and three way catalyst on soot nanostructure in Gasoline Direct Injection engines,*" *Carbon N. Y.*, vol. 120, pp. 326–336, 2017, doi: 10.1016/j.carbon.2017.05.049.

[215] Z. Wu, C. Song, G. Lv, S. Pan, and H. Li, "*Morphology, fractal dimension, size and nanostructure of exhaust particles from a spark-ignition direct-injection engine operating at different air–fuel ratios,*" *Fuel*, vol. 185, pp. 709–717, 2016, doi: 10.1016/j.fuel.2016.08.025.

[216] A. Liati, D. Schreiber, P. D. Eggenschwiler, Y. A. R. Dasilva, and A. C. Spiteri, "*Electron microscopic characterization of soot particulate matter emitted by modern direct injection gasoline engines,*" *Combust. Flame*, vol. 166, pp. 307–315, 2016, doi: 10.1016/j.combustflame.2016.01.031.

[217] Y. Luo, L. Zhu, J. Fang, Z. Zhuang, C. Guan, C. Xia, X. Xie, and Z. Huang, "*Size distribution, chemical composition and oxidation reactivity of particulate matter from gasoline direct injection (GDI) engine fueled with ethanol-gasoline fuel,*" *Appl. Therm. Eng.*, vol. 89, pp. 647–655, 2015, doi: 10.1016/j.applthermaleng.2015.06.060.

[218] C. Wang-Hansen, P. Ericsson, B. Lundberg, M. Skoglundh, P. A. Carlsson, and B. Andersson, "*Characterization of particulate matter from direct injected gasoline engines,*" 2013, doi: 10.1007/s11244-013-9994-4.

[219] A. Messerer, R. Niessner, and U. Pöschl, "*Comprehensive kinetic characterization of the oxidation and gasification of model and real diesel soot by nitrogen oxides and oxygen under engine exhaust conditions: Measurement, Langmuir–Hinshelwood, and Arrhenius parameters,*" *Carbon N. Y.*, vol. 44, no. 2, pp. 307–324, 2006, doi: https://doi.org/10.1016/j.carbon.2005.07.017.

[220] C. Wang, H. Xu, J. M. Herreros, T. Lattimore, and S. Shuai, "*Fuel Effect on Particulate Matter Composition and Soot Oxidation in a Direct-Injection Spark Ignition (DISI) Engine,*" *Energy & Fuels*, vol. 28, no. 3, pp. 2003–2012, 2014, doi: 10.1021/ef402234z.

[221] J. Rodríguez-Fernández, M. Lapuerta, and J. Sánchez-Valdepeñas, "*Regeneration of diesel particulate filters: Effect of renewable fuels,*" *Renew. Energy*, vol. 104, pp. 30–39, 2017, doi: https://doi.org/10.1016/j.renene.2016.11.059.

[222] K. Yehliu, O. Armas, R. L. Vander Wal, and A. L. Boehman, "*Impact of engine operating modes and combustion phasing on the reactivity of diesel soot,*" *Combust. Flame*, vol. 160, no. 3, pp. 682–691, 2013, doi: 10.1016/j.combustflame.2012.11.003.

[223] J. Rodríguez-Fernández, M. Lapuerta, and J. Sánchez-Valdepeñas, "*Regeneration of diesel particulate filters: Effect of renewable fuels,*" *Renew. Energy*, vol. 104, pp. 30–39, 2017, doi: https://doi.org/10.1016/j.renene.2016.11.059.

[224] R. L. Vander Wal and A. J. Tomasek, "*Soot oxidation,*" *Combust. Flame*, vol. 134, no. 1–2, pp. 1–9, 2003, doi: 10.1016/S0010-2180(03)00084-1.

[225] R. L. Vander Wal and A. J. Tomasek, "*Soot nanostructure: dependence upon synthesis conditions,*" *Combust. Flame*, vol. 136, no. 1–2, pp. 129–140, 2004, doi: 10.1016/j.combustflame.2003.09.008.

[226] K. Al-Qurashi and A. L. Boehman, "*Impact of exhaust gas recirculation (EGR) on the oxidative reactivity of diesel engine soot,*" *Combust. Flame*, 2008, doi: 10.1016/j.combustflame.2008.06.002.

[227] R. L. Vander Wal and C. J. Mueller, "*Initial investigation of effects of fuel oxygenation on nanostructure of soot from a direct-injection diesel engine,*" *Energy and Fuels*, 2006, doi: 10.1021/ef060201+.

[228] J. Zhu, K. O. Lee, A. Yozgatligil, and M. Y. Choi, "*Effects of engine operating conditions on morphology, microstructure, and fractal geometry of light-duty diesel engine particulates,*" *Proc. Combust. Inst.*, vol. 30, no. 2, pp. 2781–2789, 2005, doi: 10.1016/j.proci.2004.08.232.

[229] R. L. Vander Wal and A. J. Tomasek, "*Soot nanostructure: dependence upon synthesis conditions,*" *Combust. Flame*, vol. 136, no. 1–2, pp. 129–140, 2004, doi: 10.1016/j.combustflame.2003.09.008.

[230] B. Apicella, A. Tregrossi, A. Ciajolo, J. Abrahamson, R. L. Vander Wal, and C. Russo, "*The Effect of Temperature on Soot Properties in Premixed Ethylene Flames,*" *Combust. Sci. Technol.*, vol. 191, no. 9, pp. 1558–1570, 2019, doi: 10.1080/00102202.2019.1566228.

[231] A. W. Kandas, I. Gokhan Senel, Y. Levendis, and A. F. Sarofim, "*Soot surface area evolution during air oxidation as evaluated by small angle X-ray scattering and CO 2 adsorption,*" *Carbon N. Y.*, vol. 43, no. 2, pp. 241–251, 2005, doi: 10.1016/j.carbon.2004.08.028.

[232] B. . Stanmore, J. . Brilhac, and P. Gilot, "*The oxidation of soot: a review of experiments, mechanisms and models,*" *Carbon N. Y.*, vol. 39, no. 15, pp. 2247–2268, 2001, doi: 10.1016/S0008-6223(01)00109-9.

[233] I. Morjan, I. Voicu, R. Alexandrescu, I. Pasuk, I. Sandu, F. Dumitrache, I. Soare, T. C. Fleaca, M. Ploscaru, V. Ciupina, H. Daniels, A. Westwood, and B. Rand, "*Gas composition in laser pyrolysis of hydrocarbon-based mixtures: Influence on soot morphology,*" *Carbon N. Y.*, vol. 42, no. 7, pp. 1269–1273, 2004, doi: 10.1016/j.carbon.2004.01.020.

[234] E. J. Barrientos, "*Impact of Oxygenated Fuels on Sooting Tendency and Soot Oxidative Reactivity with Application to Biofuels,*" Pennsylvania State University, 2014.

[235] C. J. Mueller, W. J. Pitz, L. M. Pickett, G. C. Martin, D. L. Siebers, and C. K. Westbrook, "*Effects of Oxygenates on Soot Processes in DI Diesel Engines: Experiments and Numerical Simulations,*" *SAE Tech. Pap. 2003-01-1791*, 2003, doi: 10.4271/2003-01-1791.

[236] E. J. Barrientos, "*Impact of Oxygenated Fuels on Sooting Tendency and Soot Oxidative Reactivity with Application to Biofuels,*" Pennsylvania State University, 2014.

[237] D. M. Smith and A. R. Chughtai, "*The surface structure and reactivity of black carbon,*" *Colloids Surfaces A Physicochem. Eng. Asp.*, 1995, doi: 10.1016/0927-7757(95)03337-1.

[238] I. A. Khalek, "*Particle Emissions from Direct Injection Gasoline Engines,*" *Technol. Today*, 2011.

[239] F. Catapano, S. Di Iorio, P. Sementa, and B. M. Vaglieco, "*Characterization of ethanol-gasoline blends combustion processes and particle emissions in a GDI/PFI small engine,*" *SAE Tech. Pap. 2014-01-1382*, 2014, doi: 10.4271/2014-01-1382.

[240] G. Karavalakis, D. Short, D. Vu, M. Villela, R. Russell, H. Jung, A. Asa-Awuku, and T. Durbin, "*Regulated Emissions, Air Toxics, and Particle Emissions from SI-DI Light-Duty Vehicles Operating on Different Iso-Butanol and Ethanol Blends,*" *SAE Int. J. Fuels Lubr.*, vol. 7, no. 1, pp. 2014-01–1451, 2014, doi: 10.4271/2014-01-1451.

[241] Y. Kobayashi and M. Arai, "*Characteristics of PM Exhausted from Pool Diffusion Flame with Gasoline and Surrogate Gasoline Fuels,*" *SAE Int. J. Engines*, vol. 9, no. 1, pp. 2015-01–2024, 2015, doi: 10.4271/2015-01-2024.

[242] W. Yinhui, Z. Rong, Q. Yanhong, P. Jianfei, L. Mengren, L. Jianrong, W. Yusheng, H. Min, and S. Shijin, "*The impact of fuel compositions on the particulate emissions of direct injection gasoline engine,*" *Fuel*, vol. 166, pp. 543–552, 2016, doi: 10.1016/j.fuel.2015.11.019.

[243] L. Chen and R. Stone, "*Measurement of enthalpies of vaporization of isooctane and ethanol blends and their effects on PM emissions from a GDI engine,*" *Energy and Fuels*, 2011, doi: 10.1021/ef1015796.

[244] R. Zhu, J. Hu, X. Bao, L. He, and L. Zu, "*Effects of aromatics, olefins and distillation temperatures (T50 & T90) on particle mass and number emissions from gasoline direct injection (GDI) vehicles,*" *Energy Policy*, vol. 101, pp. 185–193, 2017, doi: 10.1016/j.enpol.2016.11.022.

[245] F. Leach, R. Stone, and D. Richardson, "*The Influence of Fuel Properties on Particulate Number Emissions from a Direct Injection Spark Ignition Engine,*" *SAE Tech. Pap. 2013-01-1558*, 2013, doi: https://doi.org/10.4271/2013-01-1558.

[246] K. Aikawa and J. J. Jetter, "*Impact of gasoline composition on particulate matter emissions from a direct-injection gasoline engine: Applicability of the particulate matter index,*" *Int. J. Engine Res.*, 2014, doi: 10.1177/1468087413481216.

[247] J. Yang, P. Roth, H. Zhu, T. D. Durbin, and G. Karavalakis, "*Impacts of gasoline aromatic and ethanol levels on the emissions from GDI vehicles: Part 2. Influence on particulate matter, black carbon, and nanoparticle emissions,*" *Fuel*, vol. 252, pp. 812–820, 2019, doi: https://doi.org/10.1016/j.fuel.2019.04.144.

[248] E. J. Barrientos, J. E. Anderson, M. M. Maricq, and A. L. Boehman, "*Particulate matter indices using fuel smoke point for vehicle emissions with gasoline, ethanol blends, and butanol blends,*" *Combust. Flame*, vol. 167, pp. 308–319, 2016, doi: https://doi.org/10.1016/j.combustflame.2016.01.034.

[249] G. Karavalakis, T. D. Durbin, J. Yang, L. Ventura, and K. Xu, "*Fuel Effects on PM Emissions from Different Vehicle/Engine Configurations: A Literature*

Review," *SAE Tech. Pap. 2018-01-0349*, 2018, doi: https://doi.org/10.4271/2018-01-0349.

[250] Y. Shi, A. Cortes-Morales, and B. Taylor, "*Study of Gasoline Particulate Matter Index with Refinery Blends,*" *SAE Tech. Pap. 2018-01-0354*, 2018, doi: https://doi.org/10.4271/2018-01-0354.

[251] G. Karavalakis, D. Short, D. Vu, R. L. Russell, A. Asa-Awuku, H. Jung, K. C. Johnson, and T. D. Durbin, "*The impact of ethanol and iso-butanol blends on gaseous and particulate emissions from two passenger cars equipped with spray-guided and wall-guided direct injection SI (spark ignition) engines,*" *Energy*, 2015, doi: 10.1016/j.energy.2015.01.023.

[252] H. Liu, X. Ma, B. Li, L. Chen, Z. Wang, and J. Wang, "*Combustion and emission characteristics of a direct injection diesel engine fueled with biodiesel and PODE/biodiesel fuel blends,*" *Fuel*, vol. 209, pp. 62–68, 2017, doi: 10.1016/j.fuel.2017.07.066.

[253] P. Price, B. Twiney, R. Stone, K. Kar, and H. Walmsley, "*Particulate and Hydrocarbon Emissions from a Spray Guided Direct Injection Spark Ignition Engine with Oxygenate Fuel Blends,*" *SAE World Congr. Exhib.*, 2007, doi: 10.4271/2007-01-0472.

[254] J. M. Storey, T. Barone, K. Norman, and S. Lewis, "*Ethanol Blend Effects On Direct Injection Spark-Ignition Gasoline Vehicle Particulate Matter Emissions,*" *SAE Int. J. Fuels Lubr.*, vol. 3, no. 2, pp. 2010-01–2129, 2010, doi: 10.4271/2010-01-2129.

[255] Z. Zhang, T. Wang, M. Jia, Q. Wei, X. Meng, and G. Shu, "*Combustion and particle number emissions of a direct injection spark ignition engine operating on ethanol/gasoline and n-butanol/gasoline blends with exhaust gas recirculation,*" *Fuel*, 2014, doi: 10.1016/j.fuel.2014.04.052.

[256] M. M. Maricq, J. J. Szente, and K. Jahr, "*The impact of ethanol fuel blends on PM emissions from a light-duty GDI vehicle,*" *Aerosol Sci. Technol.*, 2012, doi: 10.1080/02786826.2011.648780.

[257] J. Cho, W. Si, W. Jang, D. Jin, C. L. Myung, and S. Park, "*Impact of intermediate ethanol blends on particulate matter emission from a spark ignition direct injection (SIDI) engine,*" *Appl. Energy*, 2015, doi: 10.1016/j.apenergy.2015.08.010.

[258] C. Wang, H. Xu, J. M. Herreros, J. Wang, and R. Cracknell, "*Impact of fuel and injection system on particle emissions from a GDI engine,*" *Appl. Energy*, 2014, doi: 10.1016/j.apenergy.2014.06.012.

[259] M. Storch, F. Hinrichsen, M. Wensing, S. Will, and L. Zigan, "*The effect of ethanol blending on mixture formation, combustion and soot emission studied in an optical DISI engine,*" *Appl. Energy*, 2015, doi: 10.1016/j.apenergy.2015.06.030.

[260] H. Seong, K. Lee, and S. Choi, "*Effects of Engine Operating Parameters on Morphology of Particulates from a Gasoline Direct Injection (GDI) Engine,*" 2013,

doi: https://doi.org/10.4271/2013-01-2574.

[261] Y. Gao, D. Kim, Y. Zhang, S. Kook, and M. Xu, "*Influence of ethanol blending ratios on in-flame soot particle structures in an optical spark-ignition direct-injection engine,*" *Fuel*, vol. 248, pp. 16–26, 2019, doi: https://doi.org/10.1016/j.fuel.2019.02.131.

[262] Y. Wang, X. Yu, Y. Ding, Y. Du, Z. Chen, and X. Zuo, "*Experimental comparative study on combustion and particle emission of n-butanol and gasoline adopting different injection approaches in a spark engine equipped with dual-injection system,*" *Fuel*, vol. 211, pp. 837–849, 2018, doi: https://doi.org/10.1016/j.fuel.2017.09.108.

[263] X. Gu, Z. Huang, J. Cai, J. Gong, X. Wu, and C. Lee, "*Emission characteristics of a spark-ignition engine fuelled with gasoline-n-butanol blends in combination with EGR,*" *Fuel*, vol. 93, pp. 611–617, 2012, doi: https://doi.org/10.1016/j.fuel.2011.11.040.

[264] T. Wallner and R. Frazee, "*Study of Regulated and Non-Regulated Emissions from Combustion of Gasoline, Alcohol Fuels and their Blends in a DI-SI Engine,*" *SAE Tech. Pap. 2010-01-1571*, 2010, doi: https://doi.org/10.4271/2010-01-1571.

[265] J. Turner, A. Lewis, S. Akehurst, C. Brace, S. Verhelst, J. Vancoillie, L. Sileghem, F. Leach, and P. P. Edwards, "*Alcohol fuels for spark-ignition engines: performance, efficiency and emissions effects at mid to high blend rates for binary mixtures and pure components,*" *Proc. Inst. Mech. Eng. Part D J. Automob. Eng.*, 2017.

[266] P. Geng, H. Zhang, and S. Yang, "*Experimental investigation on the combustion and particulate matter (PM) emissions from a port-fuel injection (PFI) gasoline engine fueled with methanol–ultralow sulfur gasoline blends,*" *Fuel*, vol. 145, pp. 221–227, 2015, doi: 10.1016/j.fuel.2014.12.067.

[267] X. Wang, Y. Ge, L. Liu, Z. Peng, L. Hao, H. Yin, Y. Ding, and J. Wang, "*Evaluation on toxic reduction and fuel economy of a gasoline direct injection-(GDI-) powered passenger car fueled with methanol–gasoline blends with various substitution ratios,*" *Appl. Energy*, vol. 157, pp. 134–143, 2015, doi: https://doi.org/10.1016/j.apenergy.2015.08.023.

[268] J. Qin, X. Li, and Y. Pei, "*Effects of Combustion Parameters and Lubricating Oil on Particulate Matter Emissions from a Turbo-Charged GDI Engine Fueled with Methanol/Gasoline Blends,*" *SAE Tech. Pap. 2014-01-2814*, 2014, doi: https://doi.org/10.4271/2014-01-2841.

[269] C. Paladpokkrong, D. Liu, Y. Ying, W. Wang, and R. Zhang, "*Soot reduction by addition of dimethyl carbonate in normal and inverse ethylene diffusion flames: Nanostructural evidence,*" *J. Environ. Sci.*, vol. 72, pp. 107–117, 2018, doi: https://doi.org/10.1016/j.jes.2017.12.016.

[270] K. Choi, J. Kim, A. Ko, C.-L. Myung, S. Park, Y. Lee, J. Park, and S. K. Han, "*Evaluation of Time-Resolved Nano-Particle and THC Emissions of Wall-Guided GDI Engine,*" *SAE Tech. Pap. 2011-28-0022*, 2011, doi:

https://doi.org/10.4271/2011-28-0022.

[271] C. Farron, N. Matthias, D. E. Foster, M. Andrie, R. Krieger, P. Najt, K. Narayanaswamy, A. Solomon, and A. Zelenyuk, "*Particulate Characteristics for Varying Engine Operation in a Gasoline Spark Ignited, Direct Injection Engine,*" 2011, doi: 10.4271/2011-01-1220.

[272] A. Berndorfer, S. Breuer, W. Piock, and P. Von Bacho, "*Diffusion Combustion Phenomena in GDi Engines caused by Injection Process,*" *SAE Tech. Pap. 2013-01-0261*, 2013, doi: https://doi.org/10.4271/2013-01-0261.

[273] M. Zhang, W. Hong, F. Xie, Y. Su, L. Han, and B. Wu, "*Experimental Investigation of Impacts of Injection Timing and Pressure on Combustion and Particulate Matter Emission in a Spray-Guided GDI Engine,*" *Int. J. Automot. Technol.*, vol. 19, no. 3, pp. 393–404, 2018, doi: 10.1007/s12239-018-0038-8.

[274] B. S. Higgins, C. J. Mueller, and D. L. Siebers, "*Measurements of Fuel Effects on Liquid-Phase Penetration in DI Sprays1,*" *SAE Tech. Pap. 1999-01-0519*, 1999, doi: https://doi.org/10.4271/1999-01-0519.

[275] J. Su, W. Lin, J. Sterniak, M. Xu, and S. V. Bohac, "*Particulate matter emission comparison of spark ignition direct injection (SIDI) and port fuel injection (PFI) operation of a boosted gasoline engine,*" *ASME 2013 Intern. Combust. Engine Div. Fall Tech. Conf. ICEF 2013*, 2013, doi: 10.1115/ICEF2013-19157.

[276] Y.-Q. Pei, J. Qin, and S.-Z. Pan, "*Experimental study on the particulate matter emission characteristics for a direct-injection gasoline engine,*" *Proc. Inst. Mech. Eng. Part D J. Automob. Eng.*, vol. 228, no. 6, pp. 604–616, 2014, doi: 10.1177/0954407013493899.

[277] I. Arsie, S. Di Iorio, and S. Vaccaro, "*Experimental investigation of the effects of AFR, spark advance and EGR on nanoparticle emissions in a PFI SI engine,*" *J. Aerosol Sci.*, 2013, doi: 10.1016/j.jaerosci.2013.05.005.

[278] F. Xie, W. Hong, Y. Su, M. Zhang, and B. Jiang, "*Effect of external hot EGR dilution on combustion, performance and particulate emissions of a GDI engine,*" *Energy Convers. Manag.*, vol. 142, pp. 69–81, 2017, doi: 10.1016/j.enconman.2017.03.045.

[279] M. Costa, F. Catapano, P. Sementa, U. Sorge, and B. M. Vaglieco, "*Mixture preparation and combustion in a GDI engine under stoichiometric or lean charge: an experimental and numerical study on an optically accessible engine,*" *Appl. Energy*, 2016, doi: 10.1016/j.apenergy.2016.07.089.

[280] T. Lattimore, C. Wang, H. Xu, M. L. Wyszynski, and S. Shuai, "*Investigation of EGR Effect on Combustion and PM Emissions in a DISI Engine,*" *Appl. Energy*, vol. 161, pp. 256–267, 2016, doi: 10.1016/j.apenergy.2015.09.080.

[281] T. Lattimore, C. Wang, H. Xu, M. L. Wyszynski, and S. Shuai, "*Investigation of EGR Effect on Combustion and PM Emissions in a DISI Engine,*" *Appl. Energy*, vol. 161, pp. 256–267, 2016, doi: 10.1016/j.apenergy.2015.09.080.

[282] M. Bogarra, J. M. Herreros, C. Hergueta, A. Tsolakis, A. P. E. York, and P. J.

Millington, "*Influence of Three-Way Catalyst on Gaseous and Particulate Matter Emissions During Gasoline Direct Injection Engine Cold-start,*" *Johnson Matthey Technol. Rev.*, vol. 61, no. 4, pp. 329–341, 2017, doi: 10.1595/205651317X696315.

[283] R. W. Schefer, D. M. Wicksall, and A. K. Agrawal, "*Combustion of hydrogen-enriched methane in a lean premixed swirl-stabilized burner,*" *Proc. Combust. Inst.*, vol. 29, no. 1, pp. 843–851, 2002, doi: https://doi.org/10.1016/S1540-7489(02)80108-0.

[284] P. Saxena and F. A. Williams, "*Testing a small detailed chemical-kinetic mechanism for the combustion of hydrogen and carbon monoxide,*" *Combust. Flame*, vol. 145, no. 1, pp. 316–323, 2006, doi: https://doi.org/10.1016/j.combustflame.2005.10.004.

[285] J. E. Dec and E. B. Coy, "*OH Radical Imaging in a DI Diesel Engine and the Structure of the Early Diffusion Flame,*" *SAE Tech. Pap. 960831*, 1996, doi: https://doi.org/10.4271/960831.

[286] D. B. Kittelson, U. Patwardhan, D. Zarling, D. Gladis, and W. Watts, "*Issues associated with measuring nothing or almost nothing: Real-time Measurements of Metallic Ash Emissions from Engines,*" *Cambridge Part. Meet.*, 2013.

[287] L. Chen, R. Stone, and D. Richardson, "*Effect of the valve timing and the coolant temperature on particulate emissions from a gasoline direct-injection engine fuelled with gasoline and with a gasoline–ethanol blend,*" *Proc. Inst. Mech. Eng. Part D J. Automob. Eng.*, vol. 226, no. 10, pp. 1419–1430, 2012, doi: 10.1177/0954407012444966.

[288] S. Samuel, A. Hassaneen, and D. Morrey, "*Particulate Matter Emissions and the Role of Catalytic Converter During Cold Start of GDI Engine,*" *SAE Tech. Pap. 2010-01-2122*, 2010, doi: https://doi.org/10.4271/2010-01-2122.

[289] T. Shimoda, Y. Ito, C. Saito, T. Nakatani, Y. Shibagaki, K. Yuuki, H. Sakamoto, C. Vogt, T. Matsumoto, Y. Furuta, W. Heuss, P. Kattouah, and M. Makino, "*Potential of a Low Pressure Drop Filter Concept for Direct Injection Gasoline Engines to Reduce Particulate Number Emission,*" *SAE Tech. Pap. 2012-01-1241*, 2012, doi: 10.4271/2012-01-1241.

[290] K. Ogyu, T. Ogasawara, Y. Nagatsu, Y. Yamamoto, T. Higuchi, and K. Ohno, "*Feasibility Study on the Filter Design of Re-Crystallized SiC-GPF for TWC Coating Application,*" *SAE Tech. Pap. 2015-01-1011*, 2015, doi: 10.4271/2015-01-1011.

[291] S. Spiess, K. F. Wong, J. M. Richter, and R. Klingmann, "*Investigations of emission control systems for gasoline direct injection engines with a focus on removal of particulate emissions,*" *Top. Catal.*, vol. 56, no. 1–8, pp. 434–439, 2013, doi: 10.1007/s11244-013-9992-6.

[292] P. Rounce, A. Tsolakis, P. Leung, and A. P. E. York, "*A Comparison of Diesel and Biodiesel Emissions Using Dimethyl Carbonate as an Oxygenated Additive,*" *Energy & Fuels*, vol. 24, pp. 4812–4819, 2010, doi: 10.1021/ef100103z.

[293] M. E. Bardin, E. V Ivanov, E. J. K. Nilsson, V. A. Vinokurov, and A. A. Konnov, "*Laminar Burning Velocities of Dimethyl Carbonate with Air,*" *Energy & Fuels*, vol. 27, no. 9, pp. 5513–5517, 2013, doi: 10.1021/ef401108a.

[294] O. P. Bhardwaj, F. Kremer, S. Pischinger, B. Lüers, A. F. Kolbeck, and T. Koerfer, "*Impact of Biomass-Derived Fuels on Soot Oxidation and DPF Regeneration Behavior,*" *SAE Int. J. Fuels Lubr.*, vol. 6, no. 2, pp. 505–520, 2013, doi: https://doi.org/10.4271/2013-01-1551.

[295] K. Kondo Aizawa, T., Kook, S., Pickett, L., "*Uncertainty in sampling and TEM analysis of soot particles in diesel spray flame,*" *SAE Tech. Pap. 2013-01-090*, 2013, doi: https://doi.org/10.4271/2013-01-0908.

[296] M. Lapuerta, R. Ballesteros, and F. J. Martos, "*A method to determine the fractal dimension of diesel soot agglomerates,*" *J. Colloid Interface Sci.*, vol. 303, no. 1, pp. 149–158, 2006, doi: 10.1016/j.jcis.2006.07.066.

[297] S. J. Harris and M. M. Maricq, "*Signature size distributions for diesel and gasoline engine exhaust particulate matter,*" *J. Aerosol Sci.*, vol. 32, no. 6, pp. 749–764, 2001, doi: https://doi.org/10.1016/S0021-8502(00)00111-7.

[298] K. O. Lee, R. Cole, R. Sekar, M. Y. Choi, J. Zhu, J. Kang, and C. Bae, "*Detailed characterization of morphology and dimensions of diesel particulates via thermophoretic sampling,*" *SAE Tech. Pap. 2001-01-3572*, 2001, doi: 10.4271/2001-01-3572.

[299] H. J. Seong and A. L. Boehman, "*Evaluation of Raman Parameters Using Visible Raman Microscopy for Soot Oxidative Reactivity,*" *Energy & Fuels*, vol. 27, no. 3, pp. 1613–1624, 2013, doi: 10.1021/ef301520y.

[300] H. M. Cho and B. Q. He, "*Spark ignition natural gas engines-A review,*" *Energy Convers. Manag.*, 2007, doi: 10.1016/j.enconman.2006.05.023.

[301] P. V Puzinauskas, B. D. Willson, and K. H. Evans, "*Optimization of Natural Gas Combustion in Spark-Ignited Engines Through Manipulation of Intake-Flow Configuration,*" *CEC/SAE Spring Fuels Lubr. Meet. Expo.*, 2000, doi: https://doi.org/10.4271/2000-01-1948.

[302] F. A. Ayala, M. D. Gerty, and J. B. Heywood, "*Effects of Combustion Phasing, Relative Air-fuel Ratio, Compression Ratio, and Load on SI Engine Efficiency,*" *SAE Tech. Pap. 2006-01-0229*, 2006, doi: https://doi.org/10.4271/2006-01-0229.

[303] K. Komiyama and J. B. Heywood, "*Predicting NOx Emissions and Effects of Exhaust Gas Recirculation in Spark-Ignition Engines,*" 1973, doi: https://doi.org/10.4271/730475.

[304] M. Abián, S. L. Silva, Á. Millera, R. Bilbao, and M. U. Alzueta, "*Effect of operating conditions on NO reduction by acetylene–ethanol mixtures,*" *Fuel Process. Technol.*, vol. 91, no. 10, pp. 1204–1211, 2010, doi: https://doi.org/10.1016/j.fuproc.2010.03.034.

[305] D. E. Hinkle, W. Wiersma, and S. G. Jurs, *Applied statistics for the behavioral*

sciences, vol. 663. Houghton Mifflin College Division, 2003.

[306] M. K. Balki, C. Sayin, and M. Canakci, "*The effect of different alcohol fuels on the performance, emission and combustion characteristics of a gasoline engine,*" *Fuel*, vol. 115, pp. 901–906, 2014, doi: 10.1016/j.fuel.2012.09.020.

[307] A. Elfasakhany, "*Performance and emissions analysis on using acetone–gasoline fuel blends in spark-ignition engine,*" *Eng. Sci. Technol. an Int. J.*, vol. 19, no. 3, pp. 1224–1232, 2016, doi: 10.1016/j.jestch.2016.02.002.

[308] C. Esarte, M. Abián, Á. Millera, R. Bilbao, and M. U. Alzueta, "*Gas and soot products formed in the pyrolysis of acetylene mixed with methanol, ethanol, isopropanol or n-butanol,*" *Energy*, vol. 43, no. 1, pp. 37–46, 2012, doi: 10.1016/j.energy.2011.11.027.

[309] W. Sun, B. Yang, N. Hansen, and K. Moshammer, "*The influence of dimethoxy methane (DMM)/dimethyl carbonate (DMC) addition on a premixed ethane/oxygen/argon flame,*" *Proc. Combust. Inst.*, vol. 36, no. 1, pp. 449–457, 2017, doi: 10.1016/j.proci.2016.06.145.

[310] I. Abdul-Khalek, D. Kittelson, and F. Brear, "*The Influence of Dilution Conditions on Diesel Exhaust Particle Size Distribution Measurements,*" *SAE Tech. Pap. 1999-01-1142*, 1999, doi: 10.4271/1999-01-1142.

[311] S. L. Von Der Weiden, F. Drewnick, and S. Borrmann, "*Particle Loss Calculator - A new software tool for the assessment of the performance of aerosol inlet systems,*" *Atmos. Meas. Tech.*, vol. 2, no. 2, pp. 479–494, 2009, doi: 10.5194/amt-2-479-2009.

APPENDIX 1: DATA ACQUISITION CHANNELS

[1] Dynamometer and Engine Control (10 Hz)	
Engine speed	rpm
Engine load	Nm
Engine coolant temperature	°C
Charge air temp	°C
Oil temperature	°C
Temp - Intake Manifold	°C
Exhaust temperature (Pre-turbo)	°C
Exhaust temperature (Pre-TWC)	°C
Exhaust temperature (Post-TWC)	°C
Intake air temperature	°C
EGR temperature	°C
Fuel temperature	°C
Fuel Mass Flow	kg/h
Ambient Pressure	bar

[2] LabVIEW data acquisition (0.5° CAD)	
Cylinder pressure	bar

[3] LabVIEW data acquisition (1 Hz)	
GPF Inlet Pressure	mbar
GPF Outlet Pressure	mbar

[2] ECU Parameters (10 Hz)	
Engine speed	rpm
Throttle plate position	%
Throttle pedal position	%
IVO timing	°aTDC
EVC timing	°aTDC
Waste-gate duty cycle	%
Injection timing	°bTDC
Injection duration	ms
Ignition timing	°bTDC
Ignition dwell	ms
Engine temperature	°C
Oil temperature	°C
Charge air temperature	°C
Fuel temperature	°C
Charge Air pressure	mbar
Oil Pressure	MPa
Fuel Pressure	MPa
Mass air flow	kg/h
Oxygen sensor (HEGO)	V

Data channels acquired by [1] CADET PC, [2] DAQ PC1 and [3] DAQ PC2

APPENDIX 2: INSTRUMENTATION MEASUREMENT ACCURACY

Instrument	Range	Accuracy
Rheonik RM015 Coriolis Mass Fuel Flow Meter	0 to 20 kg/h	±0.12%
Dynamometer Load Cell	0 to 1000 N	±0.05% FS
AVL GM12D Pressure Transducer	0 to 200 bar	±0.3% FS
Variohm EPT3100 pressure Transducer	0 to 4 bar (absolute)	±0.5 %
TSI 3969 SMPS	0 to 107 particles/cm^3	± 10% < 5 x 10^4 particles / cm^3 ± 20% < 10^7 particles/cm^3
MKS 2030 Multigas FTIR	10 ppb to 100 %	10 to 100 ppb
AVL Digas 440		
O_2	0 to 22 %	< 2 % ± 0.1 % ≥ 2 % ± 5 %
Perkin Elmer Pyris 1 TGA		
Mass	Up to 1300 mg	± 2 μg
Temperature	50 °C to 1500 °C	± 5 °C
Renishaw inVia Raman Spectroscopy	200 nm to 2200 nm	< ± 0.01 cm^{-1}

APPENDIX 3: AUTHOR PUBLICATIONS AND AWARDS

Publications

1. J.H.Chan, A.Tsolakis, J.M.Herreros, K.X.Kallis, C.Hergueta, S.Sittichompoo and M.Bogarra "*Combustion, Gaseous Emissions and PM Characteristics of Dimethyl-Carbonate (DMC)-Gasoline Blend on Gasoline Direct Injection (GDI) Engines*", *Fuel*, vol. 263, pp. 116742 2019, DOI: https//doi.org/10.1016/j.fuel2019.115742. (Published)

2. J.H.Chan, A.Tsolakis, J.M.Herreros and K.X.Kallis, "*Investigation of Combustion, Gasesous Emissions and PM Characteristics with Air-Fuel-Ratio on Gasoline Direct Injection (GDI) Engines*". (Future Publication)

3. J.H.Chan, A.Tsolakis, J.M.Herreros and K.X.Kallis, "*GPF Performance of Aftertreatment Architectural Configurations on Gasoline Direct Injection (GDI) Engines*". (Future Publication)

Awards and Scholarship

University of Birmingham, School of Engineering Postgraduate Scholarship 2016

APPENDIX 4: ADDITIONAL INFORMATION

In-House MATLAB Script

Pixel Calculation

```
  n=0;
DataFileName = [DataFilePre '_' num2str(D)];
im = imread([DataFilePre '_' num2str(D) '.png']);
if size(im,3)==3
   im=rgb2gray(im);
else
   im=im2uint8(im);
end
disp([DataFilePre '_' num2str(D) ' Loaded'])
dp=dpv(D);
dp0=dp*s1(D)/s2(D);
Lw1=size(im,1);
Lw2=1;
Ww1=size(im,2);
Ww2=1;
sumcent=0;
Areasqf=2E70;

im2=im;
```

Centroid Calculation

```
s = regionprops(im,'centroid');
centroids = cat(1, s.Centroid);
centx=centroids(:,1);
centy=centroids(:,2);
centx(isnan(centx))=[];
centy(isnan(centy))=[];
centxt=mean(centx);
centyt=mean(centy);
```

Binarization and Project Area Calculation

```
for i=1:size(im,1)
      for j=1:size(im,2)
         if im(i,j,:)~=255
            sumcent=(norm([i j]-[centxt centyt]))^2+sumcent;
               im2(i,j,1)=0;
          end
       end
 end

im2=~im2;
n=sum(im2(im2==1));
```

Appendix 4: Additional Information

Minimum Bounding Rectangular Calculation

```
for anglexs=0:2:355
    im3=imrotate (im2,anglexs);
    Lw1=size(im3,1);
    Lw2=1;
    Ww1=size(im3,2);
    Ww2=1;

    for i=1:size(im3,1)
       for j=1:size(im3,2)

        if im3(i,j,:)==
              if Lw1>=
                 Lw1=i;
              end
              if Lw2<=
                 Lw2=i;
              end
              if Ww1>=
                 Ww1=j;
              end
              if Ww2<=j
                 Ww2=j;
              end
         end
       end
    end

    asq=Lw2-Lw1;
    bsq=Ww2-Ww1;
    Areasq=asq*bsq;
       if Areasq < Areasqf
            Areasqf=Areasq;
            anglef=anglexs;
            Lw=asq;
            Ww=bsq;
       end
end
imf=imrotate(im2,anglef);
imwrite(imf, ([DataFilePre '_minarea2' num2str(D) '.png']));
```

Number of Primary Particles (np_0) Calculation

```
Pixar=Pixarv(D);
numpart=(n/(pi/4*dp^2))^1.09;
Projarea=n*Pixar;
numpartf=ceil(numpart);
```

Radius of Gyration (R_g) Calculation

```
Rg=nthroot(1/n*sumcent,2);
Rgnm=nthroot(1/n*sumcent,2)*s1(D)/s2(D);
```

Appendix 4: Additional Information

Roof Form Factor (RFF) Calculation

```
im2=im2bw(im2);
image3=imfill(im2,'holes');
image4=edge(image3,'roberts');
perim=sum(image4(image4==1));
RFF=nthroot(4*pi*n/perim^2,2);
imwrite(image4, ([DataFilePre '_perim' num2str(D) '.png']));
```

```
if D == DataFileNumEnd

    MSExcelTitle{1} = 'Filename';
    MSExcelTitle{2} = 'num of part';
    MSExcelTitle{3} = 'Rg(nm)';
    MSExcelTitle{4} = 'dp0';
    MSExcelTitle{5} = 'RFF';
    MSExcelTitle{6} = 'L';
    MSExcelTitle{7} = 'W';
    MSExcelTitle{8} = 'Df';

end
```